Pettigrew, T.L., Casey, J.F., Miller, D.J., et al., 1999
*Proceedings of the Ocean Drilling Program, Initial Reports* Volume 179

# 4. HAMMER DRILL SITE (1104 AND 1106) AND SITE 1105[1]

Shipboard Scientific Party[2]

## HAMMER DRILL-IN CASING SYSTEM CONCEPT ENGINEERING: TESTING ON THE SOUTHWEST INDIAN RIDGE

### Introduction

Since the inception of the Deep Sea Drilling Project (DSDP) and its successor, the Ocean Drilling Program (ODP), one of the principal objectives of the science community has been to penetrate an entire section of oceanic crust to reach the crust/mantle boundary. This objective has proven to be a difficult engineering task from the initial efforts of ocean drilling to the present. Attempts to initiate and drill holes in young, highly fractured basaltic rock with little or no sediment cover have proven unsuccessful (e.g., Legs 106, 109, 142). However, efforts to initiate deep basement holes with considerable sedimentary cover have proven successful in yielding more stable holes. For example, Hole 504B reached a depth in excess of 2100 m before the hole was lost to further penetration. Approximately two-thirds of the crust below, however, remained unsampled, as did much of the drilled crust because of low recovery.

Following this and other attempts at total crustal penetration, new strategies were adopted based on successful drilling in tectonic windows into peridotite during Leg 109 along the Mid-Atlantic Ridge near the Kane Transform (MARK Area; Detrick, Honnorez, Bryan, Juteau, et al., 1988) and into gabbroic rocks during Leg 118 near the Atlantis II Transform on the Southwest Indian Ridge (SWIR; Robinson, Von Herzen, et al., 1989). This new approach involved total crustal penetration by a strategy called offset drilling, in which tectonically exposed lower

[1]Examples of how to reference the whole or part of this volume.
[2]Shipboard Scientific Party addresses.

Ms 179IR-104

crustal and upper mantle sections were targeted. By drilling multiple long holes laterally offset in the same region, different levels of the crust and upper mantle could be sampled. Using these laterally offset holes presumably would allow a composite section of the oceanic crust to be constructed, once correlated. Subsequently, this approached was used during Legs 147 (Hess Deep; Gillis, Mével, Allan, et al., 1993) and 153 (MARK Area; Cannat, Karson, Miller, et al., 1995) and again during Leg 176 (Atlantis II Transform; Dick, Natland, Miller, et al., 1999).

With the exception of Hole 735B drilled during Leg 118 and 176 (1508 m of total penetration), which was initially spudded using a guide base on an highly unusual wave-cut platform along the Atlantis II Fracture Zone in the Southwest Indian Ocean, other ODP igneous legs conducted in young terrane, where there is little to no sedimentary cover, have been successful only in penetrating and coring to about 200 meters below the seafloor (mbsf) or less. They have also been characterized by far less recovery than experienced during Legs 118 and 176. Experience gained from the two legs that directly followed the inception of offset drilling strategy, Legs 147 (Hess Deep; Gillis, Mével, Allan, et al., 1993) and 153 (MARK region; Cannat, Karson, Miller, et al., 1995), indicates that the current hard-rock guide base design is not optimal for establishing boreholes in fractured igneous rock environments with moderate slopes and little or no sediment cover. These are typical environmental conditions for mid-ocean ridge and fracture-zone drilling targets. Thinly sedimented slopes that are covered with debris or rubble are also commonly encountered in young terrane at mid-ocean ridges. These areas have proven especially problematic from an engineering point of view because of the difficulties in keeping a stable open hole for deepening.

Even with these formidable engineering and technical problems, the scientific objective of total crustal penetration or developing a composite section by drilling offset holes in the ocean crust remains one of the highest priority thematic objectives of ODP. Therefore, new hardware and techniques need to be developed to establish boreholes in these environments to meet the scientific objectives of hard-rock drilling. The tool with the most promise of dramatically increasing ODP's ability to establish a borehole in hard-rock environments is the hammer drill-in casing system (HDS). Thorough testing of this tool during Leg 179 before its general deployment in an actual hard-rock leg should increase the likelihood of success in the future. Therefore, the engineering portion of Leg 179 was dedicated solely to testing a hammer drill-in casing system in a fractured hard-rock environment. Tests were conducted along a transverse ridge adjacent to the Atlantis II Transform fault, which offsets the Southwest Indian Ridge. The hammer-drill test sites are located near the highly successful Hole 735B (Fig. **F1**). This region was chosen for the tests because of its well known geological framework and the fact that it possesses an uncommon combination of hard-rock drilling targets, including shallow to deep-water exposures in both flat and highly sloped environments.

F1. Satellite altimetry free-air gravity map displaying the SWIR, the AII F.Z., and the location of Hole 735B, **p. 73.**

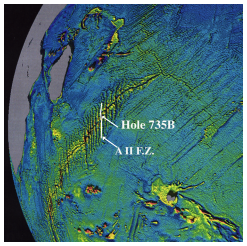


## Background of the Hammer Drill-In Casing System

Drilling and coring operations in fractured hard rock must overcome many challenges not confronted in piston coring operations. These can be summarized as initiating the borehole, stabilizing the borehole, and establishing reentry capability. Until a drilling/coring bit can gain purchase, because it is not stabilized by sediment, it tends to chatter across

the surface of a hard-rock outcrop. Difficulty initiating a hole is exacerbated if the drilling target is on a slope. Rubble from the seafloor, drill cuttings, and material dislodged from the borehole wall must continually be removed; however, the size and density of this material complicates this task. Because of bit wear in hard rock, deep penetration (beyond a few tens of meters) absolutely requires the ability to perform multiple entries into a borehole. The ideal system for drilling in hard-rock environments would disregard local topographic variation, seafloor slope, and thickness of sediment cover or talus accumulation. Such a system should initiate a hole, then simultaneously deepen the hole and stabilize the upper part of the hole with casing. This requires the bit to cut a hole with a greater diameter than the casing and then to be withdrawn through the casing string. The casing in turn would facilitate hole-cleaning operations by elevating the annular velocity of the drilling fluid and would ease reentry operations by eliminating the possibility of offsets in the borehole wall (ledges or bridges). Finally, this ideal system would leave behind a structure to simplify the required multiple reentries.

The hammer drill-in casing system is composed of a hydraulically actuated percussion hammer drill, a casing string or multiple casing strings, a free-fall deployable reentry funnel, and a casing hammer. Once the casing string has been drilled into place and the reentry funnel installed, the drilling assembly is unlatched from the casing string and removed. The borehole is left with casing and a reentry funnel in place. If required, the casing string may be cemented in place, and multiple casing strings may be installed in the same borehole.

This type of HDS is currently being used in Iceland to install large diameter 18⅝-in casing more than 100 m deep in fractured basalt. Unfortunately, the Icelandic system is pneumatically driven and, thus, is not suited for use in deep water. However, a hydraulically actuated hammer drill, suitable for use by ODP, is currently under development in Australia. ODP is assisting in the development of this hammer drill and has incorporated it into the HDS.

A viable HDS would (1) eliminate the need for any form of independent seafloor structure such as the hard-rock base, (2) allow spudding boreholes on much steeper slopes than can be achieved using an independent seafloor structure, (3) reduce sensitivity to thin sediment cover, debris, or rubble lying on the spudding surface, and (4) reduce dependency on precise site surveys.

ODP initiated its HDS project in 1994 with a worldwide industry survey of the available hammer-drill technology, techniques, and equipment. In July 1996, ODP was invited to visit an Iceland Drilling Company drill site where 11¾-in casing was being drilled into fractured basalt using a pneumatic hammer drill. It was determined that similar techniques could be employed by ODP. However, because of the water depths typically associated with ODP legs, the pneumatic hammer drill would have to be replaced with a hydraulic, or water, powered hammer drill. Further industry surveys resulted in locating SDS Digger Tools, Canning Vale, Western Australia, which had a 6-in prototype water-powered hammer drill that was ready for commercialization. Discussions with SDS Digger Tools resulted in an agreement between the company and ODP to work together to scale up the existing 6-in water hammer to a size suitable for drilling in 16-in casing.

To test the general concept, in August 1996, a field test of the existing SDS Digger Tools 6-in water hammer was carried out. The field test was successful in drilling 7-in casing into black granite in a quarry.

Since SDS Digger Tools was not in the business of making underreaming hammer-drill bits, in September 1996 the decision was made to use underreaming hammer-drill bits manufactured by Holte Manufacturing, Eugene, Oregon, U.S.A. Holte Manufacturing has been in the business of drilling in casing into hard fractured rock for many years, in many locations around the world, using pneumatic hammer drills.

In October 1996, SDS Digger Tools presented the option to ODP of using an existing prototype 12¼-in water hammer. The 12¼-in water hammer could be used to drill in 13⅜-in casing and would cost less to complete development than developing an entirely new hammer capable of drilling in 16-in casing. Therefore, the decision was made to change the prototype HDS from 16-in casing to 13⅜-in casing and to employ the SDS Digger Tools prototype 12¼-in water hammer. In January 1997, ODP engineers traveled to Perth, Australia, to witness bench testing of the prototype SDS 12¼-in water hammer. The bench test was successful, and the project was continued based on the 12¼-in water hammer drill.

The 12¼-in water hammer was field tested in black granite in April 1997. Although the field tests, from a drilling standpoint, were successful, it was determined that the hammer closing forces were too high for safe operation from the drillship. A redesign of the 12¼-in water hammer was undertaken by SDS to lower the closing forces. A second round of field tests was carried out with a modified 12¼-in water hammer in September 1997 at Rogaland Research Center, Stavanger, Norway. The results of the second field test indicated that the closing forces were now in an acceptable range for use by ODP.

During development of the 12¼-in water hammer drill by SDS Digger Tools, ODP/TAMU (Texas A&M University) developed the supporting hardware required for the HDS system. This hardware included a hydraulically actuated casing running tool, a modified 13⅜-in casing hanger, a bearing assembly between the modified casing hanger and casing string, and a free-fall reentry cone. The bearing assembly between the modified casing hanger and casing string was added to allow the drilling assembly to rotate independently of the casing string. The free-fall reentry cone was designed to be assembled around the drill pipe and dropped to the seafloor, coming to rest on the modified 13⅜-in casing hanger. Besides making reentry easier, the free-fall reentry cone locks out the bearing between the casing hanger and casing string. Locking out the bearing is required for installation of other casing strings using conventional ODP casing running tools, which must be rotated to latch and release. The HDS running tool, hanger bearing, and free fall-reentry cone were assembled and fit tested at ODP/TAMU in March 1998. All of the HDS equipment was shipped to Cape Town, South Africa, in April 1998 for testing at sea during Leg 179.

## Hammer Drilling Engineering and Scientific Objectives

There were three primary objectives for the hammer drill-in casing evaluation. The first objective was to determine the operational characteristics of the hammer drill. The hammer drill was thoroughly tested on land before it was deployed at sea; however, it was difficult to simulate the shipboard deployment environment. Thus, during Leg 179 the hammer was deployed by itself for evaluation prior to using the entire hammer drill-in casing system. The second phase of testing would involve determining the viability of the hammer drill-in casing system.

Once the shipboard operational characteristics of the hammer drill were established, the complete hammer drill-in casing system would be deployed for evaluation. Three boreholes in increasingly difficult environments were envisioned to completely test the equipment. Finally, our third test phase would involve determining the maximum allowable slope for hammer-drill operations. The proposed drilling plan addressed the minimum requirements to evaluate the potential of a hammer drill-in casing system. No coring was specifically planned; however, we did envision the possibility of attempting recovery of at least two cores through the established boreholes.

Initially, we planned to deploy the hammer drill on top of the wave-cut platform. Our projected site, based on the Leg 118 seafloor survey, was in an area of very thin (<1–2 cm) sediment cover ~75 m west of Hole 735B in ~730 m of water. Once shipboard operational parameters were determined, we intended to assemble and deploy the entire hammer-drill system and attempt to set and recover, if possible, 40–60 m of casing string at the same location. Pending successful completion of the casing installation at our first site, we planned to establish cased holes in deeper water and eventually on a sloped surface.

## Modification of the Cruise Objectives

The sea trials for the hammer drill-in casing system took place near Site 735 along the Atlantis II Transform adjacent to the SWIR (Fig. **F1**). There were some difficulties in maintaining the original 15-day schedule for the hammer-drilling tests. First, the *JOIDES Resolution* was delayed before leaving port because of a major repair to the drill string guide horn damaged in a previous leg. The ship departed Cape Town on 21 April, more than 6 days late. Second, a delayed shipment of hammer bits and drill-in casing supplies had not reached the ship before the *JOIDES Resolution* left Cape Town. These materials had to be sent to the *Resolution* while on station near Hole 735B, but the resupply ship did not arrive until 10 May, ~8 days after supplies on hand for the hammer-drilling tests were exhausted. Thus, before the hammer supplies arrived, only 3 days of hammer tests were completed at Site 1104 before hammer supplies were exhausted (see **"Operations,"** p. 14). The scheduled 15 days of tests had to be suspended in order to await transfer of the parts by a resupply ship from Reunion Island. A contingency plan had been developed in the event of catastrophic failure of the HDS. Implementation of this contingency plan included rotary coring time at Site 1105, which lies ~1.2 km east-northeast of Site 735B on the Atlantis Bank. This unexpected result of the leg resulted in extensive coring in the gabbroic massif exposed near Site 735B. Because of lost operational days and a further failure in transfer of all materials from the resupply ship because of agitated seas, serious compromises were made to the HDS testing and planned experiments, as well as to drilling originally scheduled for the Ninetyeast Ridge Observatory (NERO) site on the second part of the leg. In all, ~ 17 days of operational time out of an original 26 days devoted to the primary objectives of the leg (hammer tests and NERO) were lost as a consequence of these delays. The hammer tests were resumed on 11 May, but only for a 2-day period at Site 1106, where three alternate bit designs were tested (see **"Operations,"** p. 14).

## Tectonic Setting of the Atlantis Bank and Drill Sites, Southwest Indian Ridge

Hole 735B, the hammer test sites (Sites 1104 and 1106), and Site 1105 lie on or adjacent to the Atlantis Bank. This platform is located to the east of the north-south–trending Atlantis II Transform (Figs. F1, F2), which offsets the SWIR in a left-lateral sense by a distance of 199 km (Engel and Fisher, 1975). The transform lies between 31°50′S and 33°40′S along ~57°E. The age offset is ~20 Ma, and the slip rate along the transform is ~0.8 cm/yr (Fisher and Sclater, 1983; Dick et al., 1991c). Because of the slow spreading rates of the SWIR segments to the north and south, the rift valleys adjacent to the transform and the transform valley itself are characterized by strong relief.

Dick et al. (1991b) presented the first detailed multibeam map of the Atlantis II Transform and adjacent ridge-transform intersections (RTIs). The multibeam map of the transform and a 3-D shaded relief image (Figs. F2, F3) are reproduced here based on the original site-survey digital data (kindly provided by H. Dick). These figures display the major morphotectonic features of the Atlantis II Transform. As originally described by Dick et al. (1991c), these features include two RTIs, with well-developed nodal basins, inner corner highs, and more subdued outer corners of the rift valley; the transform valley; transverse ridges east and west of the transform valley; and two median tectonic ridges near the axis of the transform valley.

Both RTIs to the north and south display asymmetric rift valleys with inside corner highs, outer corner lows, and nodal deeps at the RTIs. RTIs (e.g., see Searle and Laughton, 1977; Fox and Gallo, 1984; Tucholke and Lin, 1994). In the case of the northern RTI of the Atlantis II Transform, the relief of the inner rift valley wall is nearly double that of the outer rift valley wall.

Asymmetric rift valleys along slow-spreading centers, especially those near RTIs, have been interpreted to result from long-lived low-angle detachment faults. These detachments are thought to dip from the inner corner rift valley wall into the subsurface below the rift valley. The inner corner is envisioned as the unroofed footwall block of crustal penetrating and long-lived low-angle detachment faults (Karson and Dick, 1983; Karson et al., 1987; Karson, 1990). The outer corner is envisioned as the hanging-wall block. Detailed studies have shown that the inner corner of many rift valley walls may be largely composed of deep-seated plutonic or ultramafic rocks (e.g, Karson et al., 1987; Dick et al., 1991c; Karson and Winters, 1992; Cannat and Casey, 1995).

The SWIR lies at the extremely slow end of the spreading rate spectrum and is likely to be characterized by low magma supplies and smaller crustal thicknesses (e.g., Reid and Jackson, 1981). The inner walls of the Atlantis Transform, which represent the crust generated at the inner corners of the RTIs, have been extensively dredged, and the results show that peridotite (43%) and gabbro (24%) dominate the recovery (Dick et al., 1991a, 1991c). It has also been recognized that compositions of mid-ocean-ridge basalts (MORB) and peridotites from these dredge rocks indicate low degrees of partial melting (Johnson and Dick, 1990, 1992). These factors support the notion that the crust of the inner corners of the RTIs may be thin and may commonly represent sites where spreading was not accommodated principally by magma addition but by mechanical extension for long periods of time. Low-angle detachment faulting is regarded as the principal mechanism for accommodating extension. The northern and southern RTIs of the

F2. Bathymetry of the Atlantis II transform fault, p. 74.

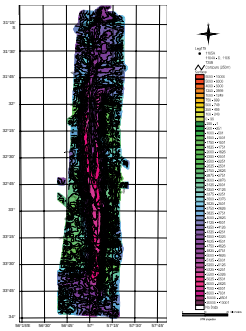

F3. Three-dimensional image of the Atlantis II transform fault, p. 75.

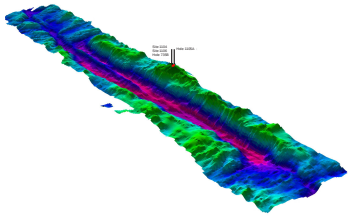

Atlantis Transform are likely sites in which low-angle detachment faulting and unroofing (Fig. F4) lead to exposure of deep crustal and serpentinized upper mantle rocks that are transported from the ridge axis along the transform valley and adjacent crust (Dick et al., 1991c).

There are two median tectonic ridges in the center of the transform valley (Dick et al., 1991c). In the northern half of the transform, there is a prominent median tectonic ridge that reaches 1.5 km above the transform valley floor on either side (Figs. F2, F3). It extends 110 km and plunges to the south terminating at 31°54′S. A second less prominent median tectonic ridge extends from the southern RTI to ~33°38′S. It extends ~99 km and reaches an elevation of ~250 m above the transform valley floor. The origin of median tectonic ridges have been interpreted to be associated with changes in plate motion that result in modification of the position of the principal transform deformation zone from one side of the transform valley to the other as the two RTIs are approached (Dick et al., 1991c).

Other striking features of the Atlantis Transform include two transverse ridges that lie at the top of both walls of the transform. The transverse ridges are greatly elevated with respect to the floor of the transform and the adjacent nontransform crust. Dick et al. (1991c) tentatively estimated the transverse ridges stand ~1 km above the adjacent nontransform seafloor. The ridges form prominent features that extend from the inner corner highs along the length of the active transform. Each transverse ridge consists of a series of alternating highs and lows with up to 2.5 km of relief in a longitudinal direction parallel to each transverse ridge.

The Atlantis Bank exposes gabbroic rocks that were drilled within Hole 735B during Legs 118 and 176 and in Hole 1105A of Leg 179. It is situated astride the eastern transverse ridge of the transform (Figs. F5, F6) and therefore originated at the northern RTI. Hole 735B (Robinson, Von Herzen, et al., 1989) is located 18 km west of the present-day axis of the north-south Atlantis II Transform on the Atlantis Bank. The bank is the shallowest part of the transverse ridge (Fig. F3) and is thought to represent a wave-cut platform (Dick et al., 1991c), which exposed gabbroic rocks sometime during the massif's transport to its present position along the Atlantis II Transform. This likely occurred during unroofing at the seafloor along the footwall of a long-lived normal detachment fault and formation of the rift valley inner corner high at ~11.5 Ma. It, subsequently, became part of the eastern transverse ridge (see Fig. F4). The Atlantis Bank shallows to just under 700 m, whereas the adjoining Atlantis II transform reaches a maximum depth of 6480 m. The bank is ~9 km long in a north-south direction and 4 km wide. The top of the bank is nearly flat and has proven to represent an excellent surface for both bare-rock and guide-base spudding. There was 500 m of gabbroic rock cored from Hole 735B with >86% recovery during Leg 118 (Robinson, Von Herzen, et al., 1989). In 1997, during Leg 176, Hole 735B was deepened to >1.5 km below seafloor with similarly high recovery (Dick, Natland, Miller, et al., 1999). This represents the deepest penetration of any hole drilled into an oceanic gabbroic section. The seismic velocity structure of the massif has been investigated by Muller et al. (1997) and shows that the Moho is >5 km beneath the massif. The nature of the oceanic seismic crust/mantle boundary is unknown, but the tentative velocities at the base of the crustal section appear lower than typical mantle velocities. The massif is characterized by low-relief exposures of gabbroic rocks on the top of the bank, but dredges of serpentinized peridotite have also been reported from the transform valley

F4. Schematic model showing the mechanism of exposure of gabbroic rock at Site 735, p. 76.

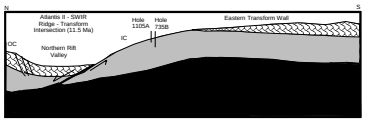


F5. Detailed bathymetry of the Atlantis Bank adjacent to the Atlantis II transform fault, p. 77.

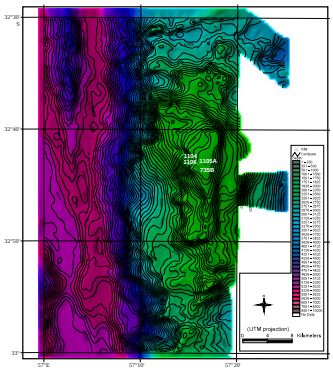

F6. Three-dimensional shaded-relief image of the Atlantis Bank along the wall of the Atlantis II transform fault, p. 78.

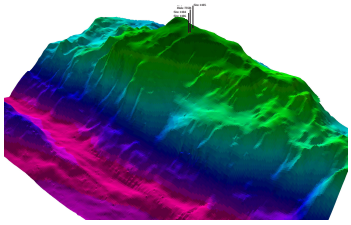

wall adjacent the Atlantis Bank at a water depth of ~4382 m water depth (Dick et al., 1991c). Thus, beneath the gabbroic massif of the Atlantis Bank, the Moho could represent an hydration boundary between serpentinized and unhydrated mantle assemblages. The age of the massif is ~11.5 Ma, based on isotopic dating and magnetic anomaly data over the Atlantis Bank (Stakes et al., 1991; Dick et al., 1991c).

Hammer-drilling tests were to be conducted in the general vicinity of previously drilled Hole 735B to the east of the Atlantis II Transform on the Atlantis Bank because of ideal logistical considerations. The test sites required a range of conditions from flat, bare rock outcrops to both bare rock and thinly sedimented or rubble-covered basement targets on slopes of varying inclination. This range of conditions was necessary to fully estimate the HDS capabilities in the range of operating conditions expected during hard-rock legs. The region surrounding the Atlantis Bank provides an extreme range of water depths from 700 m to more than 6 km and provides a variety of spudding surfaces ranging from relatively level massive outcroppings with clean surfaces to severely sloped, talus-covered surfaces. The first set of hammer holes were attempted directly adjacent to Hole 735B on the wave-cut platform at Sites 1104 and 1106, whereas subsequent hammer drilling was to occur on the slopes adjacent to the platform.

## Previous Results from Hole 735B

Results from Hole 735B have shown that drilling deep into the gabbroic sections of the oceanic crust can be accomplished under the right conditions. Previous drilling in the region during Leg 118 (Natland et al., 1991; Dick et al., 1991a) has shown that the core consists of foliated metagabbro near the surface (Unit I, 0–37.41 mbsf), olivine gabbro (Unit II, 37.41–170.22 mbsf), followed downward by olivine gabbro with disseminated oxide gabbro (Unit III, 170.22–223.57 mbsf), massive oxide gabbros (Unit IV, 223.57–274.06 mbsf), massive olivine gabbro (Unit V, 274.06–382.40 mbsf), and olivine gabbro, oxide gabbro and troctolites (Unit VI, 382.40–500.70). The deeper penetration of Leg 176 to ~1500 m depth (Dick, Natland, Miller, et al., 1999) will add to this stratigraphic succession, but the shallowest part of the section will be of particular interest during Leg 179 because it may cover part the same stratigraphic interval as that anticipated in coring Hole 1105A. The most distinctive unit in Hole 735B is Unit IV, which consists of massive oxide gabbros. Unit IV also shows an elevated magnetic susceptibility signature when compared with the units above and below (Pariso et al., 1991).

The bulk rock and mineral geochemistry in the upper 500 m of the section (Bloomer et al., 1991; Natland et al., 1991; Dick et al., 1991a; Hebert et al., 1991; Ozawa et al., 1991) shows that the section has a wide range of geochemical signatures from very primitive (bulk rock Mg# of 0.80–0.88) to very fractionated (bulk rock Mg# of 0.23–0.30). In general, the bulk and mineral chemistries of the samples clearly show two groupings that broadly divide the oxide gabbro or gabbronorite and the olivine gabbros. Olivine gabbros show primitive bulk rock and mineral compositions, whereas oxide gabbros tend to show more fractionated mineral chemistry. Both groupings overlap in a downhole plot but are clearly distinctive trends. Both Hebert et al. (1991) and Ozawa et al. (1991) show that the olivine gabbro samples can be divided into two units downhole. One from 0–270 m and the other from 270–500 m. Each unit shows a trend from somewhat more primitive mineral chem-

istries at the base to more fractionated upward. This type of cryptic chemical variation in the olivine gabbros is what would be expected of cyclic units caused by fresh influxes of primitive magma followed by fractionation (e.g., Irvine, 1979; Komor et al., 1985). The reset at 270 m to a higher Mg# could be interpreted to mark a major fresh input of primitive magma. Superimposed on this major reset are finer scale cyclic cryptic chemical variations (Hebert et al., 1991), which are not as well defined because of the scale of sampling. Each reset generally yields higher Mg# in clinopyroxene and olivine and higher An content of plagioclase.

The oxide gabbros and gabbronorites over the same stratigraphic intervals show the opposite trend. Instead of becoming more fractionated upward in each cycle, the well-defined upper trend becomes more primitive from 270 mbsf upward (Ozawa et al., 1991; Hebert et al., 1991). The lower unit, although more poorly defined, also becomes more primitive upward. This provides an overall downhole trend, which is an inverse olivine gabbro trend. The oxide gabbros, although abundant higher in the section, also become scarcer lower in the hole. Dick et al. (1991a) interpret the oxide gabbros and more fractionated rocks to represent the products of evolved intercumulus melts. Hebert et al. (1991), however, emphasize that there is a continuum of mineral compositions between oxide gabbro and olivine gabbro. The bimodal distribution of rock types and mineral chemistries over the same stratigraphic interval, however, is somewhat unique.

Magmatic, crystal-plastic, and brittle structures have been documented throughout the core. Most of the core intervals are free of significant crystal-plastic deformation and may or may not be characterized by weak magmatic foliations and fabrics (Cannat, 1991). There are many inclined ductile shear zones with normal shear sense (Cannat, 1991). These appear more prevalent near the top of the hole. Cataclastic zones and brittle faults have also been noted. Of particular note is the strong correlation between zones of crystal-plastic deformation and oxide-rich gabbros (Natland et al., 1991; Dick et al., 1991c; Cannat et al., 1991).

Metamorphism in core from Hole 735B ranged from static to dynamic (Stakes et al., 1991; Kempton et al., 1991; Alt and Anderson, 1991). Dynamically metamorphosed rocks generally showed the highest temperature alteration and include granulites with largely anhydrous assemblages to amphibolites with brown to green amphibole. Amphibolite gneisses were documented at the top of the hole. Statically metamorphosed rocks show high (>600°C) to moderate temperature (440°–600°C) alteration, the latter usually associated with fractures filled by vein material. Low-temperature smectite, zeolite, calcite, and prehnite were noted along fractures and represent latest alteration. Oxygen and Sr isotope data generally suggest low water-rock ratios during alteration (Kempton et al., 1991; Stakes et al., 1991).

Paleomagnetic studies of the core indicate that the core is reversely magnetized and that samples have consistently undergone an ~20° rotation because the magnetic inclination is steeper than would be expected for the region (Pariso et al., 1991). In addition, the presence of oxide-rich gabbro and its magnetic signature suggests that the gabbros may represent an important source component for marine magnetic anomalies (Pariso et al., 1991; Dick et al., 1991c).

## Contingency Hole 1105A and Objectives

The selection of a location for Site 1105 was aided by a site survey cruise of the *James Clark Ross,* which was conducting bathymetric, magnetic, and sampling surveys of the Atlantis Bank as the *JOIDES Resolution* arrived. Data transfer between the *James Clark Ross* and the *JOIDES Resolution* allowed an adequate site to be chosen for drilling, which was a considerable distance from Hole 735B. The site had to meet certain requirements because we chose not to employ a hard-rock guide base to achieve maximum penetration in the short time available. The site was at the crest of the Atlantis Bank where the surface relief was minimal. We achieved a bare-rock spud by using a tricone bit and drilled to ~15 mbsf. A modified free-fall funnel was installed, and drilling into gabbroic rock commenced.

The site is close to a ridge-axial trend with respect to Hole 735B but more distal from the north-south Atlantis II Transform, which lies directly to the west of Hole 735B. The site was chosen to avoid a duplication of Hole 735B core by drilling at proximal Site 1104, where the hammer tests were conducted for the first 3 days. At the same time, we tried to utilize Hole 735B as a reference section to attempt to accomplish the following objectives:

1. Reconstruct the detailed pseudostratigraphy of the gabbroic section of the oceanic crust displaced 1.2 km from reference Hole 735B to compare with previous results.
2. Attempt to laterally correlate large-scale igneous units, structural features, and geophysical characteristics over the broader distance represented by the offset in Holes 1105A and 735B in a direction that was nearly parallel to the former ridge axis.
3. Constrain the overall crustal architecture, igneous history, structure, and structural history of the massif exposed on the platform.
4. Constrain the detailed cryptic chemical and mineralogic variations in an oceanic layered gabbroic complex to test models of magma evolution and magma-chamber geometries.
5. Complete a successful suite of logs, including Formation MicroScanner (FMS), in a gabbroic section to understand the geometry of igneous layering and to characterize the geophysical characteristics of the gabbroic section as a whole.

If successful, the correlation experiment could yield a minimum measure of the dimensions of subaxial magma chamber systems and continuity of structure and metamorphic processes along the strike of the ridge axis at very slow-spreading centers. If correlations are unsuccessful, the scale of the experiment will place limits on the dimensions of igneous units, the former size of continuous magma chambers, and the continuity of structures. Correlation will be attempted on the basis of detailed and integrated data sets including core descriptions and subsequent shore-based laboratory analyses to establish cryptic chemical and mineralogical variations, as well as alteration and structural profiles of the core. Data from a full logging program will also be used in the correlation attempts.

The axial thermal structure (Kuznir and Bott, 1976) along mid-ocean ridges is likely to vary significantly as a function of spreading rates and proximity to hot spots. Based on the ability to image crustal level magma chambers using seismic methods, fast-spreading centers are

usually considered to maintain small, but likely steady-state magma chambers (e.g., Detrick et al., 1987; Harding et al., 1990; Sinton and Detrick, 1992), whereas slow spreading center data has not yet suggested any semblance of steady-state chambers (Fowler, 1976; Fowler, 1978; Nisbet and Fowler, 1978; Detrick et al., 1990). It should be noted that the seismic results used at fast-spreading centers having lower bathymetric relief are not directly comparable in resolving power to those at high relief, slow-spreading mid-ocean ridges. In addition, refraction studies along slow-spreading ridges have resolved lower velocity crust along the rift valley (Purdy and Detrick, 1986). Overall, however, the data indicate that the plutonic foundations of slow-spreading crust are likely to be created by solidification of smaller ephemeral magma chambers, the size and dimensions of which we have little direct information (Fig. **F7**). Most investigators place the maximum size of slow-spreading magma chambers at <1–2 km (e.g., Nisbet and Fowler, 1978; Detrick et al., 1987).

Drilling into tectonic windows of the plutonic portion of the ocean crust with a dense closely spaced array of holes that cover a substantial depth range is likely the only viable method in attempting to map and firmly establish the dimensions and nature of transient magma chambers at slow-spreading centers. Where several holes have been drilled into tectonic windows (e.g., MARK and Hess Deep), the shallow depths of penetration, the recovery rates, and/or lateral distances between holes were generally not conducive to lateral correlation of sections. The only hole to date that has achieved significant penetration into the plutonic crust, as well as an exceptionally high recovery rate (86%), is Hole 735B along the SWIR, which was recently deepened and achieved penetration depths of 1508 mbsf during Leg 176 (Dick, Natland, Miller, et al., 1999). The core from Hole 735B provides the first almost-continuous section of oceanic gabbros sampled by ocean drilling. During Leg 179, we had the opportunity to drill and core a hole at a moderate distance of 1.2 km from Hole 735B in an attempt to laterally correlate units between holes. Whereas the depth of penetration was modest (158 mbsf) compared to that of Hole 735B, the recovery rate was nearly identical.

Ophiolite sections are generally regarded as representative of obducted segments of oceanic crust derived from or incorporated into a forearc setting before their obduction onto continental crustal blocks (Dewey, 1976; Casey and Dewey, 1984). Their exact origin is problematic because of trace element signatures in volcanics that generally indicate an arc tectonic environment, although the same signature has recently been observed along a mid-ocean ridge (the Chile Rise) by Klein and Karsten (1995). Without addressing these uncertainties, it is sufficient to say that it is likely that classic ophiolite sequences, including pillow lavas, sheeted dikes, gabbroic rocks, and ultramafic tectonites, represent some type of ocean crust and mantle formed in extensional environments that may have similarities to mid-ocean ridges. Thus, analogies with the plutonic sections of ophiolites may indeed help in deciphering the nature of the plutonic foundations of oceanic crust, especially when our view is limited to the scale of a borehole core.

The overall stratigraphy of ophiolite plutonic sections is very well summarized from base to top by many studies (e.g., Coleman, 1977; Dewey and Kidd, 1977; Casey et al., 1981). The plutonic stratigraphy of ophiolites is generally defined by the composition of the cumulates and the presence or absence of fine-scale igneous layering (centimeter to

F7. Typical ophiolite stratigraphy juxtaposed against predictions of geophysical studies of slow-spreading ridges, **p. 79.**

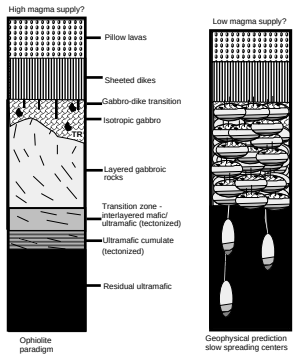

meter scale). Generally, at the base it consists of what is thought to represent an ultramafic cumulate section directly above depleted mantle residual harzburgite or less depleted lherzolite. This is followed upward by a strongly interlayered mafic and ultramafic transition zone, followed by a layered gabbro section, an isotropic gabbro section, and commonly a dike-gabbro transition (see Fig. F7). These definitions are somewhat simplified and at times misleading. The most strongly layered rocks (centimeter to meter scales) are at the base of the plutonic section, which consists of ultramafic and transition zone cumulates that are commonly tectonized, and lowermost part of the layered gabbro section. In general, as one progresses upward through the layered gabbro section, the intervals of monotonous nonlayered gabbros between finely (centimeter to meter scale) interlayered gabbroic rocks increase until strongly layered gabbros disappear. The zone of nonlayered gabbros at the top of the plutonic section is called the isotropic gabbros, but they are hardly isotropic. They are simply nonlayered but commonly contain faint banding and significant variations in grain size and modal mineralogy. They are also characterized by the highest oxide abundances and contain intrusive bodies of trondhjemite and other felsic rocks, as well as scarce to abundant crosscutting diabase dikes.

In sections below the isotropic gabbro, which show layering, lateral continuity of the fine-scale igneous layering is generally lacking, and the layers tend to pinch out over lateral distances equivalent to outcrop scales. This is unlike continental layered intrusions where, in general, lateral continuity of layering on a kilometer scale is well demonstrated and where, rarely, a single layer can be followed for more than 25 km (e.g., Irvine, 1979). These types of scales of lateral continuity are never approached in the case in ophiolite plutonic sections. The fine-scale (centimeter to meter scale) layers in ophiolites cannot be followed laterally for more than ~100–200 m and commonly much less because they pinch out. There are larger scales of layering, as much as 40 to 200 m, that can be traced laterally for kilometers and can be correlated from one section to the next (e.g., Casey et al., 1981; Casey and Karson, 1981; Komor et al., 1985); however, the fine-scale layering on the scale observed in oceanic gabbroic core is generally the laterally discontinuous type within each distinctive unit. The fine-scale layers are also characterized by variable orientations in ophiolites with inclinations that range from paleohorizontal to paleovertical (Dewey and Kidd, 1977; Casey and Karson, 1981; Smewing, 1981; Casey et al., 1983). Similar dipping layers have been observed in ODP cores (e.g., Cannat, Karson, Miller, et al., 1995).

The large-scale units defined in ophiolites generally consist of interlayered intervals with distinctive rock types, such as troctolite, pyroxenite, or oxide gabbro. In addition, the broad-scale map unit contacts between isotropic gabbro, layered gabbro, transition zone, and ultramafic cumulates can be traced laterally. These units, however, typically show extreme variation in thickness. (Casey et al., 1981). For example, the ratio between layered gabbros and isotropic gabbros in a crustal section can change significantly along strike by up to a factor of 3 or 4. Over a scale of several kilometers, the isotropic gabbro section can be the dominant part of the gabbroic interval or can be almost nonexistent.

In summary, the lack of lateral continuity of fine-scale layering in the oceanic crust, but improved continuity for larger scale units, should be expected in the oceanic crust. Another characteristic of ophiolites is the

lateral heterogeneity of broad-scale unit thicknesses. Likewise, this may be a typical feature in the oceanic crust.

How the ophiolite model (Fig. F7) of the plutonic section fits with the pseudostratigraphy predicted by small ephemeral chambers, which might exist at slow-spreading magma-starved ridge segments, is not exactly known. Primitive mantle-derived MORB magmas forming discrete magma chambers in the crust should generate the same type of cumulates observed in ophiolites or layered intrusions but within each small intrusion. The crystallization sequence of MORB magmas should generate dunite cumulates, followed by troctolites, olivine gabbros, gabbros, oxide gabbros or gabbronorites, and, finally, felsic rocks within each small magma body as it fractionates from primitive MORB (Fig. F7). Alternatively, magmas fractionate olivine in the colder upper lithospheric mantle beneath slow-spreading centers and arrive at crustal levels after fractionating enough olivine to only generate gabbroic rocks at crustal levels (Cannat and Casey, 1995; Niu, 1997; Cannat et al., 1997; Casey, 1997; Niida, 1997). This, however, is inconsistent with the fact that picritic basalts with only olivine and spinel on the liquidus are known to pass through the subaxial plumbing system and erupt along some mid-ocean ridges (Melson and O'Hearn, 1986; Natland, 1990; Perfit et al., 1996). Small ephemeral chambers beneath magma-starved slow-spreading centers like the SWIR might predict a complex stratigraphy of mixed ultramafic, gabbroic, and felsic rocks solidified in each small chamber repeating itself within a stratigraphic section cored through the crust. They also should show many crosscutting igneous intrusions and relationships in order to feed magma chambers at different levels in the crust, sheeted dikes, and pillow lavas above. This model is similar to the sill model proposed for the Oman ophiolite (Boudier et al., 1996), but the model predicts that the lower crust should be riddled with vertical feeder dikes, as well as sill systems, to feed multiple chambers in the plumbing system (Fig. F7). Sinton and Detrick (1992) propose that the subaxial regions of slow-spreading centers represent crystal mushes with variable amounts of melt porosity, through which magma is delivered from the mantle to the surface. This mechanism would tend to reduce lithologic and chemical variability within the mush zone because melt delivered by porous flow will continually react with the crystalline material through which it passes.

Drilling during Legs 118 and 176 provides the most extensive drill core yet recovered from a plutonic section generated at a slow-spreading center. Drilling during Leg 179 at Site 1105 provided the first samples and logging information of an offset hole necessary to attempt to laterally correlate sections of the plutonic crust for distances >1 km. Although Hole 1105A is more limited in penetration, it provides internal checks that help constrain the results from each of the holes drilled on the Atlantis Bank.

## Summary

Investigations carried out in the region of the Atlantis Bank along the Atlantis II transform have been extensive and represent the location of the deepest penetration yet by ODP into the plutonic foundations of oceanic crust. This site provides an ideal location to test a new engineering approach to bare rock drilling in hard-rock terrane on the ocean floor. The investigations carried out during Leg 179 will attempt to improve the ability of the drillship to spud and create stable holes in hard-rock environments with a new hammer drill-in casing system. In

addition, contingency rotary coring in the region of the Atlantis Bank will attempt to refine models of the architecture of the plutonic foundations of the ocean crust by drilling in gabbroic rock offset by 1.3 km from reference Hole 735B.

# OPERATIONS

## Hammer Drill System Components

The HDS tested during Leg 179 was a concept assembly comprised of seven basic components: (1) an underreaming bit, (2) a water hammer, (3) a jet sub, (4) a running tool, (5) a hanger bearing assembly, (6) a reentry cone, and (7) the casing string (Fig. F8). The overall HDS is an adaptation of similar hammer drill systems used on land, in particular by the geothermal industry. However, some fundamental aspects of the HDS had to be changed, or added, for deployment at sea.

F8. Schematic diagram of water hammer drill-in casing system deployment, p. 80.

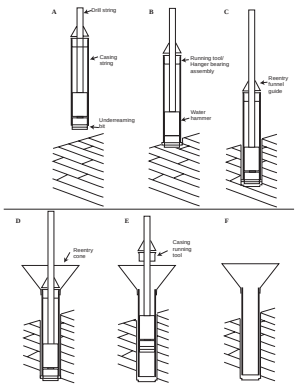


### Hammer Drill Underreaming Bits

Hammer drill bits drill by crushing rock under extremely high point loads using hemispherical tungsten carbide inserts (TCIs) as the cutters. The cutters are driven into the rock with each impact of the hammer, thus chipping a small portion of the rock with each blow. The bits are rotated slowly, ~20 rpm, to index the cutters between impacts of the hammer. Underreaming bits are required to open the borehole large enough for the casing to follow behind the drill bit as the hole is being drilled. The underreaming bits are designed to collapse to a small enough overall outside diameter to be pulled up through the casing string once the casing has been emplaced.

There were two basic designs of underreaming bits used during Leg 179. Both types were direct adaptations of land-based hammer drill underreaming bits currently used in industry. The first type is called a concentric underreaming bit (CUB; Fig. F9) and is a relatively new development in the hammer drill industry. The CUB has a pilot bit, ~12¼ in in diameter, sized such that it will pass through a 13⅜-in casing string. Immediately above the pilot bit are three underreaming arms that are retracted and expanded by rotating the drill string left or right, respectively. When retracted, the underreamer arms close to the same outside diameter as the pilot bit (12¼-in). When expanded, the underreaming arms open to an effective diameter of 14¾-in, thus creating a large enough borehole for 13⅜-in casing to pass through. The advantage of the CUB is that the underreaming arms ream ~84% of the borehole circumference with each stroke of the hammer. Based on data collected from land-based operations, the CUB has proven to drill faster and last longer than conventional eccentric underreaming bits.

F9. Schematic drawings of hammer drill concentric and eccentric underreamer bits, p. 81.

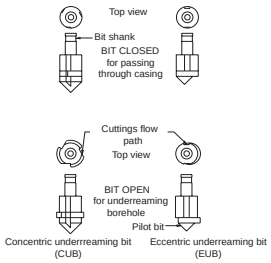


The second type of underreaming bit used during Leg 179 is called an eccentric underreaming bit (EUB; Fig. F9). In the EUB the underreamer and the pilot bit are one piece. The EUB is built such that when it is in the closed position, the pilot bit is off axis to the drill string and the overall effective diameter (12¼-in) of the bit is small enough to be pulled up through 13⅜-in casing. When opened, the pilot bit moves on axis with the drill string and the eccentric is moved outward to perform the underreaming. Thus, when open, the EUB has an effective diameter of 15 in and is capable of creating a borehole large enough for 13⅜-in casing to pass through. As with the CUB, the EUB is retracted

and expanded by rotating the drill string left or right, respectively. The EUB has been used for years in the land-based hammer drilling industry. The disadvantage to the EUB is that the eccentric only reams ~38% of the borehole circumference with each stoke of the hammer. Thus, the EUB drills slower and does not last as long as the CUB.

## Water-Powered Hammer Drill

The heart of the HDS is the water-powered hammer drill (Fig. F10). As the name implies, the water-powered hammer drill is driven by pumping water through the hammer. The basic operating mechanism is an internal reciprocating piston. On the upstroke, the piston is slowed and stopped by compressing water. On the downstroke, high-pressure water drives the piston down until it impacts the top of the bit. The high-energy impact is transmitted through the bit body to the TCIs, thus creating extremely high, virtually point, impact loads on the rock.

Another feature of the hammer drill is a bypass mechanism that allows the driller to flush the borehole with high-viscosity mud without activating the hammer. When weight is applied to the hammer with the bit set on bottom, the bit shank moves upward, closing the bypass and diverting all flow through the hammering mechanism. When the bit is pulled clear of bottom, the bit shank is allowed to move downward, opening the bypass and diverting all of the flow around the hammering mechanism so that the hammer stops operating when not in contact with bottom.

The water hammer used during the testing during Leg 179 is a proprietary product of SDS Digger Tools, Pty., Ltd., 49 Vulcan Road, Canning Vale, Western Australia 6155 (telephone (09) 455 4433; fax (09) 455 4399). Specific operational parameters of the water hammer can be obtained by contacting SDS Digger Tools.

F10. Schematic drawing of the SDS water hammer drill, p. 82.

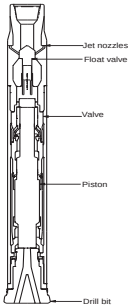


## Jet Sub

A special jet sub (Fig. F10) replaced the conventional water hammer top sub. The jet sub has receptacles for three nozzles capable of diverting part of the flow down the drill string and up the outside of the drill string at high velocities. When assembled in the complete HDS, the jet sub is placed ~2 m up inside the casing. While drilling in casing with the HDS, the cuttings are brought up the inside of the casing through the annular space formed by the casing inside diameter and the drilling assembly outside diameter. The jet sub is used to increase the velocity of the cuttings-laden water moving up the casing and out of the hole for more efficient hole cleaning.

## Running Tool

When casing is conventionally drilled in with hammer drills on land, individual joints of casing are added to the overall casing string at the surface as the casing string is being drilled in. Unlike the conventional land-based hammer drill-in casing systems, the HDS, because it is to be deployed in deep water, requires that the entire casing string be made up as a single assembly with the HDS and lowered to the seafloor. Thus a special running tool, which becomes an integral part of the drilling assembly, is required to support the casing string as it is lowered to the seafloor and drilled into place. The running tool must also be able

to unlatch from the casing string and be removed with the drilling assembly, thus leaving the drilled in casing fully open for reentry.

The HDS running tool employs a triangular cross section body (Fig. F11). The flats of the triangle provide flow paths for the cuttings to be circulated out of the hole while drilling. At each of the points of the triangle are latch dogs that, when extended, lock into mating grooves in the casing hanger. The latch dogs are held out, in the locked position, by a shifting sleeve inside the running tool body. To unlatch the running tool from the hanger bearing latch body, the shifting sleeve must be moved downward, out from underneath the latch dogs, thus allowing them to retract into the running tool body.

A special tool called a go-devil (Fig. F12) is used to move the running tool shifting sleeve. At the time when the running tool is unlatched from the casing hanger, the drill-string heave compensator is in operation and thus it is not safe to access to the drill-string bore to insert the go-devil. To get around this problem, there is a hydraulically actuated ball valve, on top of the top drive, which is normally opened and closed when retrieving core barrels during routine coring operations. When the HDS is deployed, the go-devil is placed on top of the ball valve, with the ball valve closed. To deploy the go-devil, the driller opens the ball valve, from the safety of the driller's shack, allowing the go-devil to fall into the drill string. Once the go-devil is inside the drill string, it is pumped down the drill string until it comes to rest on top of the running tool shifting sleeve. After the go-devil has landed on the shifting sleeve, the drill-string pressure is increased to ~600 psi until the shifting sleeve overcomes a snap ring and moves downward, releasing the latch dogs. After confirming the running tool has been unlatched from the casing hanger, the driller increases the drill-string pressure to ~1800 psi, shear releasing another sleeve inside the go-devil, which also moves downward and opens a circulation path to the hammer and borehole once again.

F11. Schematic drawing of the HDS running tool, p. 83.

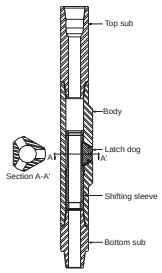


F12. Schematic drawing of the HDS go-devil, p. 84.

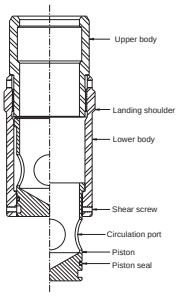


## Hanger Bearing Assembly

A hanger bearing design was incorporated into the casing hanger to allow the drilling assembly and integral running tool to rotate relative to the casing string while supporting the weight of the casing string (Fig. F13). During the drilling-in process, as the casing enters the borehole, the bearing assembly enables the casing to stop rotating, even though the drilling assembly is still being rotated. By doing so, the total torque required to drill the casing in is reduced. Also, whatever torque is produced is a direct response from the bit, thus giving the driller direct feedback regarding torque on bit.

F13. Schematic drawing of the HDS hanger bearing assembly, p. 85.

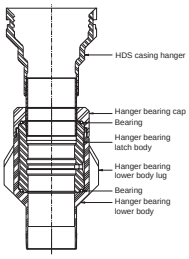


## Casing String

As mentioned previously, unlike conventional land-based hammer drill in casing techniques where the individual joints of casing are added to the string as it is being drilled in, the entire HDS casing string must be made up as part of the overall HDS assembly. The top of the HDS casing string must be compatible with other standard ODP casing tools and hangers. So, a standard ODP casing hanger is slightly modified by adding a hanger bearing assembly and shortening the casing pup joint for the HDS. For added protection at the bottom of the casing string, a hardened casing shoe is welded to the end, or shoe joint. The

hardened casing shoe is more collapse- and abrasion-resistant than the casing itself.

### Reentry Cone

A reentry cone was added to the HDS assembly to aid reentry to the borehole and to defeat the hanger bearing assembly (Fig. F14). The vibration-isolated television (VIT) camera is used to locate specific spud targets when spudding with the HDS. Because the VIT uses the drill string as a guide and must pass over the HDS assembly, the reentry cone can not be in place, on top of the HDS, while drilling in. Therefore, the HDS reentry cone was designed to be deployed after the casing has been drilled into place. The reentry cone is split into two halves and is attached around the drill string, while the drill string is still attached to the casing string, and free-fall deployed. The falling reentry cone comes to rest on top of the HDS casing hanger. As the reentry cone is falling, a guide on top of the HDS running tool centers the reentry cone with respect to the drill-string axis so that the body of the reentry cone passes over the outside of the casing hanger and extends down to the hanger bearing assembly housing. Special lugs inside the reentry cone body, near the top, land on top of the casing hanger, thus preventing the reentry cone from dropping below the casing hanger.

The standard ODP casing tools latch and unlatch by rotating the drill sting left and right respectively. Because the HDS hanger bearing allows the casing hanger to rotate relative to the casing string, it must be locked out for standard ODP casing tools to be used during subsequent operations at an HDS installation. The HDS reentry cone also provides a mechanism for locking out the hanger bearing assembly. The special lugs that land on top of the casing hanger also lock into the bypass flow grooves in the body of the casing hanger, thus preventing rotation between the casing hanger and the reentry cone. There is another set of lugs inside the reentry cone, near the bottom, that engages lugs on the outside of the hanger bearing housing, thus preventing rotation of the reentry cone with respect to the hanger bearing housing. Therefore, rotation of the hanger relative to the casing string is prevented.

F14. Schematic drawing of the HDS reentry cone assembly, p. 86.

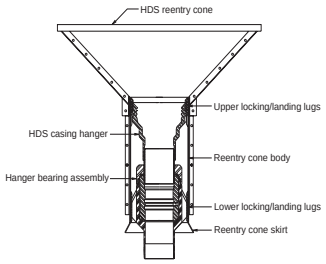


## Summary of Leg 179 Engineering and Drilling Operations

### Port Call: Cape Town, South Africa

While in port, we learned that the surface freight that contained many parts of the hammer drill system shipment would not arrive before the ship got under way. A quick inventory of HDS equipment already on board was made. The following HDS items were identified as being in the delayed surface shipment:

Three double-pin crossover subs (OG0709; NC 70 × NC 70). One crossover sub OG0725 (NC 70 pin × 6⅝-in full hole modified [FHM] box) was modified into one double-pin crossover sub OG0709 (NC 70 × NC 70) at a local machine shop in port.

Two HDS hanger bearing lower bodies (OJ5010). There was one HDS hanger bearing lower body on board. It was not possible to fabricate replacement HDS hanger bearing lower bodies in port or on board ship.

Three HDS hanger bearing caps (OJ5012). One HDS hanger bearing cap was fabricated at a local machine shop in port.

Two complete HDS reentry cone assemblies (OJ5014). It was not possible to fabricate a complete HDS reentry cone assembly in port or on board ship.

One HDS reentry cone (OJ5015). One drill-in casing reentry funnel (OJ4852) was modified into one HDS reentry cone. With one HDS reentry cone body (OJ5016) on board, one complete HDS reentry cone assembly (OJ5014) was fabricated on board ship.

Two 13⅜-in ST-L flush joint casing lift subs (OH5159). Two 13⅜-in ST-L flush joint pin connections were cut off of two damaged joints of 13⅜-in ST-L flush joint casing and modified into two 13⅜-in ST-L flush joint casing lift subs. Note: these are not certified lift subs and were destroyed after completion of the hammer drill testing.

Three 13⅜-in buttress casing collars. The 13⅜-in buttress casing collar is used to cross over from the HDS hanger bearing lower body to the 13⅜-in ST-L flush joint casing string via a double-pin casing crossover sub (13⅜-in buttress × 13⅜-in ST-L). There were no 13⅜-in buttress casing collars on board or available in port. The buttress pin connection was cut off the only HDS hanger bearing lower body on board. One double-pin casing crossover sub was cut in half and the 13⅜-in ST-L pin connection welded onto the HDS hanger bearing lower body, thus eliminating the need for the 13⅜-in buttress casing collar.

Four 9½-in drill collar lift subs (OD0208). The 9½-in drill collar lift sub was replaced by one crossover sub (OG0725; NC 70 pin × 6⅝-in FHM box) and one 8¼-in drill collar lift sub (OD0200), which were on board. There were only two crossover subs OG0725 on board after one was modified into a double-pin sub (OG0709). So, only two 9½-in drill collar lift subs were available.

Two 9½-in drill collar bail-type lift nubbins (OG0245). Fortunately the 9½-in drill collars came with cast steel thread protectors of the bail type so they could be used in place of the lift nubbin. Note: the cast steel thread protectors are not certified and should not be used routinely as lift nubbins.

Three 13⅜-in Holte hardened casing shoes. The 13⅜-in hardened casing shoes could not be fabricated in port or on board ship.

Two 13⅜-in HDS modified casing hangers. The 13⅜-in HDS modified casing hangers could not be fabricated in port or on board ship. One 13⅜-in HDS modified casing hanger was on board, allowing for one casing deployment.

Two HDS hanger bearing latch bodies (OJ5009). The HDS hanger bearing latch body could not be fabricated in port or on board ship. One HDS hanger bearing latch body was on board, allowing for one casing deployment.

## Transit: Cape Town to Site 1104

During the transit from Cape Town to Site 1104, the SDS water hammer drill was picked up and deck tested on 28 April. The test assembly consisted of an SDS concentric underreaming bit, SDS 12¼-in water hammer, SDS jet sub, with three blank nozzles installed, and the required crossover subs to the top drive. After making up the assembly, the bit breaker was placed on top of some dunnage and rubber matting on the rig floor. The bit was then lowered into the bit breaker and 5000 lb applied to the bit via the top drive. The mud pump was engaged, and the flow rate slowly increased to 75 gpm at 700 psi, when the hammer first began to cycle. As the flow rate was increased the hammer cycled

intermittently and erratically. The flow rate was increased to 375 gpm at 1770 psi, and the hammer began to cycle more evenly. The flow rate was increased to 400 gpm at 1900 psi and the hammer cycled smoothly. The hammer was cycled for several minutes before the flow rate was reduced to 240 gpm at 900 psi. The hammer was then cycled for a few minutes more before the pump was shut down.

It was theorized that the initial erratic behavior of the hammer was caused by air in the pumping system and excess grease left in the hammer from assembly. To test the theory, the mud pump was once again engaged and the flow rate slowly increased to 75 gpm at 270 psi, and the hammer began cycling very smoothly. To create a baseline pressure vs. flow-rate curve, the flow rate was increased in 50-gpm steps, and the corresponding pressure was recorded. Large vibrations were noted in the stand pipe and derrick, presumably from pressure pulse reflections from the hammer traveling back to the pump (Table T1).

T1. Hammer deck test data, Site 1104, p. 165.

Also during the transit, a frequency analyzer was assembled on board to monitor the hammer-induced pulsation frequency in the stand pipe as an aid in determining when the hammer was cycling. Although the initial frequency spectrum recorded was not a clear indication of when the hammer was operating, the voltage output spectrum from the pressure transducer installed in the stand pipe gave a good indication of when the hammer was cycling.

It is interesting to note that later in the hammer drill tests, additional filtering that made the frequency spectrum more prominent was added to the frequency analyzer. The frequency spectrum indicated a notable peak at ~30 Hz, the known operating frequency of the hammer. However, there was an even more prominent peak at ~60 Hz that was believed to be an indication of the power stoke of the hammer at 30 Hz, plus the return pulse as the hammer piston moved upward at 30 Hz and 180° out of phase, essentially doubling the frequency to 60 Hz. The increased amplitude of the 60-Hz signal may indicate that more energy is transmitted up the stand pipe by the hammer piston upstroke than is reflected by the power stroke when the piston moves downward. This further supported the theory that the stand-pipe vibrations were indeed caused by hammer-induced pressure pulse reflections traveling back to the pump.

## Site 1104

A positioning beacon was deployed at 1925 hr on 29 April, establishing Site 1104. The hammer drill was prepared for deployment for the first series of spudding and drilling tests without casing. The bottom-hole assembly (BHA) used for the HDS testing was made up of SDS concentric bit 1, a hammer drill, a jet sub, a crossover sub (OG0726), four 9½-in drill collars (OG0244), a crossover sub (OG0725), one 8¼-in drill collar (OL1040), one tapered drill collar (OG0300), six joints of 5½-in drill pipe (OG0052), and a crossover sub (OG1010) to 5-in drill pipe.

The BHA was tripped to the seafloor and the camera deployed for a seafloor survey. The point of reference for the survey was the hard-rock guide base at Hole 735B. Once Hole 735B was located, the ship was offset ~75 m west to the primary HDS testing site, where massive, sediment-free outcrop was observed. However, based on the most recent survey information received from H.J.B. Dick aboard the *James Clark Ross* (pers. comm., 1998), a second test site was explored ~200 m northwest of Hole 735B. Massive, sediment-free outcrop was also observed at the second site, and the decision was made to begin the hammer drill

testing at the second site. For better positioning of the ship, a second positioning beacon was deployed at 0224 hr on 30 April.

### *Site 1104 Spud Test*

Water depth was determined to be 740 meters below rig floor (mbrf) by drill-pipe measurement. With the camera deployed and no rotation of the drill string, several spud tests were conducted (Table T2). The hammer performed well during the spud tests, and the decision was made to recover the camera and move on to the drilling tests.

T2. Hammer drill spud test data, Site 1104, p. 166.

### *Hole 1104A*

Hole 1104A was spudded at 0620 hr on 30 April, with an SDS underreaming bit (Table T3). The pointed pilot bit did not skid as the hole was initiated. However, it is suspected that the bit heaved off bottom occasionally, thus starting a new hole. Only enough weight on bit (WOB), ~8000 to 10,000 lb, was applied to the hammer to keep the bit on bottom and the hammer bypass closed. It appeared that once the pilot bit was below the seafloor, the hammer performed better. Heave constantly caused the hammer bypass to open, causing the hammer to stop cycling and then restart. After ~1 m penetration the torque increased and became erratic. Excessive vibration in the stand pipe and derrick was noted.

T3. Hammer drill drilling test data, Hole 1104A, p. 167.

After ~45 min of hammering and 1.5 m penetration, the bit was pulled clear of the seafloor with a slight overpull of 10,000 to 15,000 lb. The camera was deployed to observe the borehole, which was found to be a clean symmetrical circle in the rock outcrop. The bit was set back on the seafloor, and while maintaining WOB, the camera was retrieved in preparation for another drilling test.

### *Hole 1104B*

With the camera back on board, Hole 1104B was spudded at 0830 hr on 30 April (Table T4). The water depth was determined to be 739 mbrf by drill-pipe measurement. The hammer began cycling smoothly as the flow rate was slowly increased with no rotation of the drill string. After a few minutes of spudding, the top drive was engaged to begin rotation of the drill string. Excessive vibration in the stand pipe and derrick were once again noted. At 0900 hr on 30 April, the rig air pop-off valve failed and drilling had to be stopped, while the bit remained in the hole. The pop-off valve was soon isolated and drilling resumed. Torque soon increased and became erratic. The hammer bypass was constantly opened, presumably by heave, causing the hammer to stop cycling and then restart. At 1130 hr on 30 April, after hammering for ~2½ hr with 1.5 m penetration, the bit became stuck. The bit was freed at 1150 hr on 30 April, and kept on bottom as the camera was deployed to observe the bit and borehole. The bit was pulled clear of the seafloor at 1230 hr on 30 April and appeared to be intact. The borehole was somewhat oval shaped, presumably from being spudded on a slope.

T4. Hammer drill drilling test data, Hole 1104B, p. 168.

The bit was set back on the seafloor, and while WOB was maintained the camera was retrieved in preparation for spudding Hole 1104C. With the camera back on board, the pump was engaged, and the flow rate slowly increased (Table T5), but the hammer would not cycle. The hammer was pulled clear of the seafloor to open the bypass and be flushed. However, similar results occurred when the bit was set back on the seafloor, closing the bypass. The standby pump (1) was engaged to make sure a problem with the pumps did not exist. The same pressure drops

T5. Hammer drill drilling test data, Hole 1104C, p. 169.

vs. flow rates were recorded, and the hammer did not cycle. The hammer and bit were retrieved for inspection.

Once back on board, the hammer was disassembled and it was determined that the hammer valve had cracked, allowing fluid to bypass it and thus preventing the hammer from cycling. It is theorized that the pressure transients across the valve created by the constant opening and closing of the hammer bypass may have been the cause of the cracking. A new valve was installed in the hammer, and the hammer was deck tested. The hammer was cycled for ~6 min at 100 gpm and 330 psi and at 200 gpm and 560 psi, with no problems. The pressure vs. flow rate curve was the same as for the new hammer, possibly indicating that no appreciable wear had occurred on the piston or other internal parts of the hammer during the two previous runs. The SDS CUB was not reusable. The TCIs on all three of the underreaming arms were sheared or broken off, except for the last one on each of the trailing edges (Fig. F15). Heavy abrasion was also observed on the surfaces of all the underreaming arms. The pilot bit was in good shape, except for one chipped TCI.

F15. SDS concentric underreamer bit 1, p. 87.

T6. Hammer drill drilling test data, Hole 1104C, p. 170.

### *Hole 1104C*

With a new bit (SDS CUB 2) installed on the refurbished hammer, the BHA was tripped back to the seafloor. The camera was deployed and a spudding location chosen. The bit was set on the seafloor and, while maintaining WOB, the camera was retrieved. Once the camera was back on board, Hole 1104C was spudded at 0105 hr on 1 May (Table T6). The water depth was established at 739 mbrf by drill-pipe measurement. The pump was engaged and the flow rate increased slowly with 5 to 10 rpm drill-string rotation. After ~10 min of drilling and 0.5 m penetration, there was a pressure loss observed, presumably from the hammer bypass opening, and the flow rate was slowed. The flow rate was once again increased with normal pressure vs. flow rate correlation, and the hammer restarted smoothly.

After ~30 min of drilling with 0.5 m penetration, the bit heaved off bottom, causing the hammer to stop, and the flow rate was reduced. It was thought that the bit may have heaved out of the hole and a new hole started as the flow rate was increased and the hammer restarted. Almost immediately the torque increased and became erratic. The drill-string rotation was erratic, from 10 to 50 rpm, as a result of slip stick. The hammer had to be stopped and restarted several times because of high torque buildup resulting in top-drive stalling.

At 0225 hr on 1 May, a 2-in nipple on the stand-pipe manifold failed because of the vibration in the stand pipe. Drilling had to be stopped so that the pump could be shut down for manifold repair. The bit remained in the borehole while the manifold was repaired, and the camera was deployed. Near the hole with the bit in it, three other holes were observed, confirming that the bit had indeed heaved out of the hole and started new holes. The bit appeared to be 0.5 m below the seafloor. The camera was retrieved and, with the stand-pipe manifold repaired, drilling resumed at 0334 hr 1 on May.

The flow rate was slowly increased and the hammer began to cycle. Torque was low and erratic, but increasing. During rotation the drill string was sticking and slipping. The top drive stalled on several occasions, and the hammer was stopped and the torque released. Each time the hammer restarted without any problems. At 0410 hr on 1 May, the bit became stuck and may have heaved out of the hole as it was freed. Drilling resumed until 0425 hr on 1 May, when the stand-pipe trans-

ducer failed because of stand-pipe vibration. Because the pumps had to be shut down to remove the pressure transducer from the stand pipe for repair, the bit was pulled clear of the seafloor.

### *Hole 1104D*

The stand-pipe pressure transducer nipple was blanked, and Hole 1104D was spudded at 0445 hr on 1 May (Table T7). The water depth was determined to be 739 mbrf by drill-pipe measurement. The pump was engaged, and the flow rate slowly increased. The bit heaved off the seafloor several times, causing the hammer to stop and restart. The torque soon increased and became erratic, eventually stalling the top drive. At 0510 hr on 1 May, drilling was halted and the camera was deployed while the bit remained on the seafloor. It appeared that several new holes had been spudded because of the bit heaving out of the hole during spudding. At 0615 hr on 1 May, the bit was pulled clear of the seafloor and the camera retrieved. The bit was also retrieved for inspection because of a lack of penetration.

T7. Hammer drill drilling test data, Hole 1104D, p. 171.

Once on deck the bit was inspected revealing the leading two TCIs on each of the underreamer arms were sheared or broken off (Fig. F16). The gauge surfaces of the SDS bit 2 underreamer arms were not as heavily abraded as those on the SDS bit 1. Except for the pilot bit nose TCI having been sheared or broken off, the rest of the pilot bit appeared to be in good shape. The pilot bit nose TCI was probably damaged as the bit was heaved off the seafloor during spudding.

F16. SDS concentric underreamer bit 2, p. 88.

### *Hole 1104E*

It appeared that the underreaming arms were preventing the hammer drill from advancing the borehole. To test this theory, parts of the underreaming bits used during the previous tests were converted into a drilling bit.

*Bit Modification 1*. Using a torch, the underreaming arms of SDS bit 1 were trimmed such that when opened, they would not extend past the outside diameter of the pilot bit and driver. Upon reassembly of the bit, the modified underreamer arms, when opened, did not appear to be strong enough to withstand drilling in hard rock. Therefore, bit modification 1 was abandoned.

*Bit Modification 2*. The second attempt at modifying an underreamer bit into a drill bit involved removing the underreamer arms and pilot bit from SDS bit 1. The pilot bit shank was shortened such that when installed in the driver, the underreamer arm gap was closed. The pilot bit was then installed and welded directly to the driver. Unfortunately, the pilot bit cracked during the welding process, and the bit could not be deployed.

*Bit Modification 3*. The third attempt at modifying an underreamer bit into a drill bit involved replacing the pilot bit with the broken nose TCI on SDS bit 2 with a new pilot bit. The original, damaged underreaming arms from SDS bit 2 were left in place. However, the underreaming arms were welded in place in the closed position. Because the underreaming bit was fixed in the closed configuration, new waterways had to be cut through the toes of the underreaming arms, using a torch and grinder.

The modified SDS bit was made up to the hammer drill BHA and tripped to the seafloor. The camera was then deployed to locate a spud target. The modified bit was placed on the seafloor ~1 m from Holes 1104C and 1104D. Maintaining WOB, the camera was retrieved and Hole 1104E was spudded at 0140 hr on 2 May (Table T8). Water depth was established at 740 mbrf by drill-pipe measurement. The weather

T8. Hammer drill drilling test data, Hole 1104E, p. 172.

began to deteriorate, and the rig floor was experiencing 1 to 2 m heave, resulting in the WOB having to be increased to 10,000 to 12,000 lb to keep the bit on bottom and the hammer bypass closed.

The pump was engaged, and the flow rate slowly increased. The hammer cycled smoothly but there appeared to be ~100 psi less pressure at any give flow rate than in past tests. There was also a noticeable reduction in the vibration in the stand pipe and derrick. At ~0155 hr on 2 May, the hammer heaved off bottom, opening the bypass, and thus the hammer quit cycling and had to be restarted. The flow rate was increased slowly once again, and once again the hammer began to cycle.

After ~1 m penetration the torque began to increase and become erratic. Heave at the rig floor had increased to 3 m. The top drive stalled at 24,000 ft-lb. An overpull of 40,000 lb was applied to the bit without freeing it. The BHA was lowered to close the hammer bypass. The hammer was restarted and cycled at 400 gpm at 1720 psi. The pipe was worked again with up to 40,000 lb overpull, and still the bit could not be freed. Finally the drill string was rotated left, the direction one would normally rotate to close the underreaming arms, and the bit came free. It was assumed that the welds had failed, allowing the underreaming arms to open, so the bit was pulled clear of the seafloor and the camera was deployed to verify this. Once the camera had reached the end of the pipe, the underreamer arms could be seen clearly in the open position. The camera and BHA were retrieved for inspection. Once on deck, it was observed that every weld on the modified bit had failed, allowing the underreaming arms to open. Also, ~2 in of the leading edges of all three of the underreaming arms were broken off (Fig. **F17**). The pilot bit appeared to be in good condition.

F17. SDS concentric underreamer bit modification 3, **p. 89.**

## HDS Testing Hiatus: Site 1105

With no other hammer drill bits on board other than SDS concentric underreaming bits, the decision was made to suspend further HDS testing pending the arrival of a supply vessel, the *La Curieuse*, from Reunion Island. The lost surface shipment had been located, and critical items were diverted to Reunion Island for delivery to the drillship via the *La Curieuse.* Also, a flat-faced standard hammer drill bit was sent to Reunion Island by SDS for delivery to the drillship via the *La Curieuse.* While waiting for the arrival of the *La Curieuse,* the drillship was moved ~1 km northeast of Site 1104 where Site 1105 was established. Hole 1105A was drilled to a depth of 15 mbsf using a 14¾-in tricone drill bit. The hole was then cored to a depth of 158 mbsf with 82.8% recovery, using the rotary core barrel. After logging Hole 1105A, the drillship was moved back to Site 1104 in anticipation of the arrival of the *La Curieuse* and the resumption of hammer drill testing. A new beacon was dropped at Site 1104 at 1938 hr on 10 May, establishing Site 1106.

The *La Curieuse* arrived on location at 2045 hr on 10 May and requested that the off-loading of cargo and personnel wait until daylight. Rough seas and high winds prevented the off-loading from taking place the following day, 11 May. The sea state and winds had deteriorated further, and the forecast for the following 48 hr showed no signs of improvement. There were three hammer drill bits on board the *La Curieuse* that were critical to completion of the hammer drill tests, one Holte CUB, one Holte EUB, and one SDS flat-face drill bit.

The hammer drill bits were successfully transferred from the *La Curieuse* to the drillship by tying buoys onto the drill bits and dropping them over the side. The drillship was then maneuvered to catch the buoys, and the ship's crane was used to hoist the drill bits on board. Because it was too rough to attempt off-loading any other cargo or personnel, the *La Curieuse* was released to return to Reunion Island at 1000 hr on 12 May.

### *Hole 1106A*

A Holte CUB was made up to the SDS hammer drill, and using the same HDS BHA configuration as previously used, the assembly was lowered to the seafloor. The camera was deployed for a seafloor survey. The Site 1104 holes were quickly located. So as not to confuse the Site 1104 holes with the Site 1106 holes, the ship was offset ~20 m to the north on the same outcrop. It was theorized that the nose TCI damaged on the previous bit may have resulted from the bit heaving off the seafloor as we attempted to keep the bit in place on the seafloor during retrieval of the camera. The decision was made to spud Hole 1106A with the bit off bottom. Thus the camera was retrieved with the bit clear of the seafloor.

Once the camera was back on board, the pump was engaged and a flow rate of 200 gpm established. Circulation was maintained for several minutes to flush any air out of the system. While maintaining a 200 gpm flow rate, and no rotation of the drill string, at 1600 hr on 12 May, the bit was lowered to the seafloor and Hole 1106A was spudded (Table **T9**). The water depth was determined to be 740 mbrf by drillpipe measurement. The hammer began to cycle immediately and the flow rate was slowly increased. The heave at the rig floor was estimated to be 2 to 3 m and, as a result, the bit was pulled off bottom several times, causing the hammer to stop and restart. After ~10 min of drilling, penetration began to be made and the hammer operation settled out somewhat. Heave was still a major problem and, because of a cross swell, roll factored into the difficulties as well.

T9. Hammer drill drilling test data, Hole 1106A, **p. 173.**

The drill bit had penetrated ~0.5 m when the torque began to increase and become erratic. The weather was deteriorating, and heave at the rig floor resulted in constant stop-start problems with the hammer. Several yellow (2%) automatic station keeping (ASK) system alerts occurred, indicating the dynamic positioning (DP) system was having a hard time holding the ship on station in the increasing wind. The DP operators also reported that the noise from the hammer was occasionally interfering with the acoustics of the ASK system. After ~3 hr drilling and 2 m penetration, 1000 psi was lost and the hammer quit running. The pump was stopped and the backup pump (1) was engaged with similar results, indicating the problem was downhole. We suspended drilling operations and retrieved the hammer for inspection.

With the hammer and bit on deck at 2230 hr on 12 May, an inspection was carried out. The Holte CUB had suffered much the same damage as did the SDS bits (Fig. **F18**, bit shown before deployment). All of the TCIs on the underreaming arms, except for the last one on the trailing edges, were broken off. Also, four TCIs near the shoulder of the pilot bit were broken off as well. Disassembly of the hammer revealed the valve was cracked similarly to the first cracked valve. The other internal parts of the hammer appeared to be in good shape.

F18. Holte concentric underreamer bit, **p. 90.**

### *Hole 1106B*

A new valve was installed in the hammer, and a Holte eccentric underreaming bit was attached to the SDS hammer. The hammer and bit assembly was then deck tested. The hammer cycled immediately and was cycled for 6 min. The hammer and eccentric bit were made up to the HDS BHA and tripped to the seafloor. The camera was deployed to locate a spud site. After locating the spud site and with the bit off bottom, the camera was retrieved. The pump was engaged, and a flow rate of 150 gpm was established. At 0640 hr on 13 May, the bit was lowered to the seafloor and Hole 1106B was spudded (Table T10). The water depth was determined to be 741 mbrf by drill-pipe measurement. After tagging bottom, the flow rate was slowly increased. It appeared as though the bit may have skidded downhill ~0.5 m during spudding. The hammer began to cycle smoothly, and penetration was being made when the bit appeared to heave out of the hole and skid downhill ~1 m. The torque immediately increased and became erratic, causing the top drive to stall. Heave continuously opened the hammer bypass. After 1 hr of drilling with virtually no penetration, we stopped drilling and retrieved the bit for inspection.

T10. Hammer drill drilling test data, Hole 1106B, p. 174.

Inspection of the Holte EUB revealed similar wear patterns as observed on the concentric bits (Fig. F19). The outer edge of the eccentric bit was severely abraded and most of the TCIs on the outer edged of the eccentric bit were broken. Several TCIs on the pilot bit shoulder were also broken. The EUB was determined not to be usable.

F19. Holte eccentric underreamer bit, p. 91.

### *Hole 1106C*

The SDS flat-face drill bit (Fig. F20) was the last hammer drill bit on board to test. Although the aim of the HDS is to drill in casing, which requires an underreamer bit, the drill bit was deployed in an effort to prove that (1) the hammer drill could drill hard rock and (2) it was the premature deterioration of the underreamer arms that was preventing deep penetration. In anticipation of a long drilling run, the hammer drill was disassembled and a new cartridge was installed. The drill bit was attached to the refurbished hammer drill, and the assembly was deck tested. The hammer cycled perfectly and was run for ~2 min. We reduced the flow rate to 130 gpm and picked up the hammer to check the bypass, which opened as expected.

F20. SDS drilling bit, p. 92.

The drill bit and hammer drill were made up to the same HDS BHA and tripped to the seafloor. The camera was deployed to locate a specific spud site for Hole 1106C. After retrieving the camera, the pump was engaged at 150 gpm to flush air out of the system. While we maintained flow rate, the drill bit was set on the seafloor at 1840 hr on 13 May, and Hole 1106C was spudded (Table T11). Water depth was determined to be 742.5 mbrf by drill-pipe measurement.

After ~25 min of drilling and 1 m penetration, the pressure began to increase and the hammer began to cycle intermittently. The bit was raised off bottom to open the bypass and flush the hammer. When the bit was set back on bottom, the pressure again began to rise and the hammer still cycled intermittently. The back-up pump (1) was engaged and similar events occurred, indicating the problem was probably downhole. So, the hammer was retrieved for inspection. While the hammer was retrieved, the drill string stayed full of water. This was an indication that the hammer check valve was not allowing the water inside the drill string to drain out as it was retrieved.

T11. Hammer drill drilling test data, Hole 1106C, p. 175.

Once on deck, the hammer was disassembled for inspection. The initial cartridge was removed, and the coating on the piston appeared to

have chipped off. The piston was found to have galled to the lower bushing and was stuck in the full up position. With the piston being stuck in the full up position, the check valve was prevented from opening and the water could not drain from the drill string. The stuck piston was also thought to be the cause of the high operating pressure and intermittent cycling. The drill bit was found to be in good condition and reusable.

### *Hole 1106D*

The hammer was refurbished with another complete cartridge, and the same flat-faced drill bit was installed. The assembly was then deck tested, and the hammer performed as expected. The hammer and bit were then made up to the same HDS BHA and tripped to the seafloor. The bit was set on the seafloor, and at 0340 hr on 14 May, Hole 1106D was spudded (Table T12) with 2 m heave at the rig floor. The flow rate was slowly increased, and the hammer cycled normally.

T12. Hammer drill drilling test data, Hole 1106D, p. 176.

After ~4 min of drilling, the pressure began to rise and the hammer began to cycle intermittently. The flow rate was reduced to stop the hammer and then increased slowly to restart the hammer. As before, the pressure continued to rise and the hammer cycled intermittently. The bit was raised off the seafloor to open the bypass and flush the hammer. When restarted, the hammer once again operated intermittently at higher than normal pressure. It was assumed that the piston and lower bushing had galled again, so the hammer was retrieved for inspection.

Once on deck, the hammer was disassembled for inspection. The initial cartridge was removed and the coating on the piston once again appeared to have chipped off. The piston was found to have galled to the lower bushing and was stuck in the full up position. The extent of the galling did not appear to be as bad as that observed in the cartridge used in Hole 1106C. Once again, with the piston being stuck in the full up position, the check valve was prevented from opening, and the drill string had to be pulled full of water. The drill bit, however, was found to be in good condition and reusable.

### *Hole 1106E*

The hammer was rebuilt with the same piston and valve. However, the lower bushing used in Hole 1106C had been repaired in the ship's machine shop, and it was assembled in the hammer. The drill bit was still in good condition, so the hammer and drill bit were made up and deck tested. The hammer was cycled for 2 min at 200 gpm and 650 psi, which are nominal readings. A noticeable reduction in the stand-pipe and derrick vibrations was observed, even though the flow rates and corresponding pressures were consistent with those of a new hammer.

The bit and hammer were tripped to the seafloor with the same HDS BHA configuration. The pump was engaged at a low flow rate of 150 gpm to flush out any air in the system. After a few minutes of flushing, the bit was lowered to the seafloor and Hole 1106E was spudded at 1140 hr on 14 May (Table T13). The drilling depth was determined to be 741 mbrf by drill-pipe measurement. During this time, the average heave at the rig floor was estimated to be 3 to 4 m, with occasional 5-m heaves.

T13. Hammer drill drilling test data, Hole 1106E, p. 177.

After ~15 min of drilling, the hammer drill began to make significant penetration. Despite constant opening of the hammer bypass caused by heave, the hammer drill continued to advance the borehole. Torque was slightly erratic, ranging from 2500 to 5000 ft-lb for most of the drilling. Occasionally the top drive would stall. However, when this

happened, the hammer was allowed to keep cycling, and it soon drilled itself off, allowing the drill-string rotation to resume.

After ~1 hr, 40 min and 8 m penetration, the stand-pipe pressure transducer nipple failed because of stand-pipe vibration, and the pump had to be stopped to repair it. The bit was pulled 4.5 m off the bottom of the hole, with a momentary 20,000 lb overpull. Slow rotation of the drill string was maintained as the pump was shut down. The stand-pipe bull plug containing the pressure transducer was removed, and a blank bull plug was installed in its place. The repairs took ~5 min.

When the pump was engaged, little or no pressure was observed, consistent with pumping through open-ended drill pipe. The back-up pump (1) was engaged with similar results, indicating the problem was downhole. The drill string was then lowered in anticipation of tagging the bottom of the hole. After the end of the pipe had been lowered 4.5 m below the last TD of Hole 1106E, we decided to pull the bit clear of the seafloor and deploy the camera for observation.

Once the camera had reached the end of the pipe, it appeared as though all of the drill collars were still intact, and the crossover sub between the drill collars and the jet sub on top of the hammer could be seen. However, the jet sub, hammer, and bit could not be seen. The end of the pipe and the camera were lowered to survey the seafloor. Several boreholes were observed. One of the boreholes appeared to have something in it, but it could not be confirmed as being the hammer. The sea state at the time of the survey caused the view of the seafloor to move in and out of focus. A further survey of the seafloor did not reveal the hammer, so either the hammer was still in the hole, out of sight, or had dropped onto the seafloor and rolled downslope. The camera and drill string were then retrieved.

When the end of the drill string was retrieved, all of the drill collars and the crossover sub between the drill collars and the jet sub were recovered. The jet sub, hammer drill, and bit were missing. The pin connection on the bottom of the crossover sub showed signs of having pulled out of the box connection on top of the jet sub. Two theories have been put forth as to when the failure may have occurred. The first theory is that the jet sub box connection had been weakened or even split by the pounding the bit was taking as a result of the excessive heave during spudding. When the bit was pulled off bottom and the momentary 20,000 lb overpull was observed, the bit may have hung up on the borehole wall and the crossover sub pin may have pulled out of the weakened jet sub box. The second theory is that while waiting on the stand pipe to be repaired with the hammer heaving in the borehole, the BHA may have leaned over, causing the jet sub box to fail. By pulling the bit 4.5 m off the bottom of the hole, the jet sub was positioned at, or near, the seafloor, compounding the bending problem.

Although enough spare parts were on board to assemble a second hammer drill, the decision was made to halt the hammer drill testing because there were no more hammer drill bits available to be tested that would have increased the hammer drill test data base. Also, because of the weather conditions, lack of reentry hardware, time constraints, and high probability of loss of the fishing equipment, it was not thought prudent to attempt to fish for the lost hammer. The 9½-in drill collars used in the HDS BHA were inspected, with no cracks found, and laid down. The drillship was secured for sea and at 2312 hr on 14 May, the *JOIDES Resolution* got under way for the next site.

## Engineering Results and Accomplishments for Leg 179

Although the complete HDS test plan could not be conducted because of the premature failure of the underreaming bits, a great deal of data was collected and a much better understanding of the HDS as deployed at sea was gained. Of primary concern was the performance of the hammer. Considering the sea state during most of the test, the hammer performed quite well. It must be noted that the hammer used for the tests was designed for drilling a 12¼-in borehole and that during the testing it was used to drill a 14¾-in borehole, an ~45% larger hole, thus reducing the efficiency of the hammer. The water hammer was also designed to work at maximum efficiency with a 2250-psi pressure drop across the piston. Because of the excessive vibrations in the pumps and stand pipe, the maximum continuous pressure drop across the hammer piston that could be maintained was ~1750 psi, which further reduced the hammer's efficiency. However, in spite of the low hammer efficiency, a rate of penetration of 4.8 m/hr was achieved in Hole 1106E in massive gabbro, using a 12¼-in standard hammer drill drilling bit.

Further analysis of the underreaming bits is required. However, first impressions are that the BHA was leaning over during spudding during the early stages of drilling. Being composed of 9½-in drill collars, the BHA was very stiff and so, as the BHA leaned over from being placed in compression, it caused the underreaming bits to be rotated about the horizontal axis (perpendicular to the drill-string axis). This rocking of the underreaming bit in the hole during drilling probably caused extremely high loads to be placed on the low side of the bit underreaming arms. The high loads resulted in shearing off the TCIs and severely abrading the underreaming arms themselves. Once the TCIs were broken off of the underreaming arms, the arms acted much like a bearing, preventing further penetration by the bit.

It is encouraging to note that the pilot portion of all the underreaming bits came out of the hole in good condition, further indicating that the hammer drill can penetrate subsea hard-rock formations and that the premature failure of the underreamer arms is what prevented deep penetration by the bit. The standard hammer drill drilling bit used in Holes 1106C and 1106D showed no signs of wear when retrieved, plus the excellent penetration rate observed in Hole 1106E further indicates that the overloading of the underreaming arms was the cause of lack of penetration with the underreaming bits.

There were three primary problems associated with the hammer drill during the tests. Twice during the testing, the hammer internal control valve cracked, thus allowing pressure to escape past the valve, preventing the piston from cycling. Failure of the valve appears to have been from two causes. First, the valve has some ports in a highly stressed area, causing a definite stress riser in the valve body. Second, the hammer was constantly opened and closed because of heave. When this occurred, the pump could not be stopped in time to prevent the pressure drop across the valve from dropping to near zero and then almost instantaneously increasing to ~1750 psi. The combination of the stress riser and the pressure cycling probably caused the cracking to occur in the valves.

The second problem that occurred with the hammer drill during the tests was that on two separate occasions the piston began galling to the lower bushing. A hard coating had been applied to the piston where it passes through the lower bushing. A close tolerance fit is used in place

of a dynamic seal between the piston and lower bushing. It appears that the hard coating may have been spalling as a result of cavitation erosion. The small flakes of the hard coating appeared to be wedging between the piston and the lower bushing, causing the galling to occur. This theory will have to be studied further in a metallurgical laboratory. In any case, the galling resulted in sluggish and erratic operation of the hammer; thus, the hammer had to be retrieved and the piston and lower bushing had to be replaced each time the galling occurred.

The third problem with the hammer drill during testing was associated with the stroke length (40 mm) required to open the bypass, thereby stopping the hammer from cycling. This stroke may be too short for deployment of the hammer drill from a floating vessel. Adding to the problem is a piston effect on the bit caused by the pressure drop across the hammer acting on the bit shank cross section area. This piston effect causes the bit to be pumped downward, thus opening the bypass, as the hammer drills off or is raised off bottom. Once the bypass opens, the power fluid is diverted around the piston, preventing the hammer from cycling. Thus whenever a large heave occurs, which the heave compensator can not completely adjust for in the drill-string motion, the hammer bypass is opened and the hammer stops cycling. None of the seafloor hardware or casing running tools was deployed during the testing, so no data on the performance of this equipment was obtained. However, this equipment was assembled and fit tested without problem.

### Conclusions

The Leg 179 HDS tests were designed to be a test of the overall HDS concept in actual sea conditions. As such, the tests provided a wealth of data (Tables **T1, T14**) that, with further study, should provide a clear indication as to the direction in which the HDS development should proceed. The hammer drill itself shows great promise of being able to penetrate subsea hard-rock environments. Although the hammer drill performed well considering the sea state during the testing, a dialogue with the manufacturer will be established to address issues such as the short stroke length required to open and close the bypass, the valve cracking problem, and galling of the piston and lower bushing.

T14. Summary of Leg 179 hammer drill drilling tests, **p. 178.**

It is evident that the underreaming bits designed for conventional land-based hammer drill operations, such as those used during Leg 179, are not suitable for drilling in casing in offshore deep water with an unsupported BHA. Ideas for new design underreaming bits are already being formulated. The HDS casing running tools and reentry cone were not deployed during Leg 179. However, they were land tested before Leg 179, and no problems were encountered. So, at this time, no redesign of these tools is planned. In general, confidence remains high with the overall HDS. The benefits of the HDS to ODP and the science community as a whole are well worth continuing with the HDS development.

## IGNEOUS AND METAMORPHIC PETROLOGY AND GEOCHEMISTRY

### Introduction

The nature and evolution of the oceanic crust and spreading-center magma chambers are two of the most important issues in modern

marine geology. Considerable research efforts have been directed toward revealing the structure and constituents of the lower oceanic crust and understanding magma chamber processes at spreading centers. Models for the nature of oceanic magma chambers have traditionally been derived from studies of layered intrusions in orogenic and cratonic environments (Wager and Brown, 1967; McBirney, 1995; Cawthorn, 1996) and from ophiolitic complexes of uncertain provenances (e.g., Moores and Vine, 1971; Pallister and Hopson, 1981). However, recent geophysical surveys and dredging conducted at mid-oceanic ridges have greatly enhanced and completely transformed the way we view the nature of oceanic magma chambers, their solidification processes, and magma migration and its crustal interactions (e.g., Fox and Stroup, 1981; Bloomer et al., 1989; Meyer et al., 1989; Sinton and Detrick, 1992). Of particular relevance in this context have been ODP's drilling efforts into the lower oceanic crust, first at Site 735 near the Atlantis II Fracture Zone of the Indian Ocean during Leg 118 (Robinson, Von Herzen, et al., 1989), then in the Hess Deep of the Atlantic Ocean during Leg 147 (Gillis, Mével, Allan, et al., 1993), and, subsequently, near the Kane Fracture Zone of the Atlantic Ocean during Leg 153 (Cannat, Karson, Miller, et al., 1995). Recently, the *JOIDES Resolution* revisited the SWIR during Leg 176 in an attempt to deepen Hole 735B (Dick, Natland, Miller, et al., 1999) and was successful in penetrating to about 1500 mbsf with excellent recovery. During Leg 179, a 158-m section of oceanic gabbros was cored at Site 1105, which is offset ~1.2 km from Hole 735B. Hole 1105A provides the first opportunity to assess the lateral variability of magma-chamber processes in the region.

## Lithostratigraphy

The following overview of the petrology of the core recovered from Hole 1105A during Leg 179 is based on the initial visual core descriptions (VCDs) as well as examination of the available thin sections and chemical analyses performed on board during the leg. The large variability in modes, grain sizes, and textures within individual intervals necessitates that the reported characteristics are given as averages. For the same reason, the information obtained from individual thin sections and X-ray fluorescence analyses are not necessarily representative of the broader interval from which they were obtained.

The core was divided into 141 intervals based on variations in mineralogy, mineral mode, texture, and grain size as described in **"Igneous Petrology and Geochemistry,"** p. 3, in the "Explanatory Notes" chapter. The detailed information on these lithologic intervals is given in the VCDs. Gabbroic rocks constitute by far the majority of the recovered igneous lithologies (>99% by volume) with only a very minor component of felsic veins (<1%). The gabbroic rocks have mostly medium- to coarse-grained granular textures and display modal, textural, and grain-size variations. Regularly to irregularly developed igneous layering and rare laminations are present within intervals, and many of the interval contacts are marked by layer boundaries. The grain-size variation shows extreme ranges with pegmatitic gabbro in 2%, coarse-grained gabbro in 67%, medium-grained gabbro in 28%, and fine-grained gabbro in 3% of the core. Modally, the gabbroic rocks range from gabbro (36%), to olivine gabbro (43%), oxide gabbro (17%), oxide olivine gabbro (4%), and minor amounts of gabbronorite. The principal gabbroic rock types used in the description are defined based on the presence of olivine, orthopyroxene, and/or Fe-Ti oxide minerals

in proportions as defined in "Rock Classification," p. 4, in the "Explanatory Notes" chapter.

## Lithologic Units

The lithologic intervals have been grouped into summary units for the ease of description and to facilitate comparison with the core recovered during Leg 118 (Robinson, Von Herzen, et al., 1989; Dick et al., 1991a). The units are based on modal and grain-size characteristics and are illustrated in Figure F21. The downhole variations in modal composition and grain size are illustrated in Figures F22, F23, and F24.

### *Unit I*

Lithologic Unit I includes intervals 1 through 23 (15.00–48.14 mbsf, Sections 179-1105A-1R-1 to 7R-1) and is composed of 33.14 m of alternating gabbro, olivine gabbro, and oxide olivine gabbro (Fig. F21). The lower boundary is defined by the appearance of a higher proportion of oxide gabbro and is clearly revealed by the abrupt change in average magnetic susceptibility (Fig. F22). Medium- to coarse-grained oxide olivine gabbro (8%) is confined to the lower part of the unit and only is present in intervals 19 through 22 (37.48–38.40 mbsf, Sections 179-1105A-4R-4 to 5R-2). The rest of Unit I is composed of medium- to coarse-grained gabbro and olivine gabbro (92%).

Extensive grain-size variation is present within individual intervals and ranges from fine to medium (e.g., intervals 13 and 16) and medium to pegmatitic (e.g., intervals 1, 8, and 17). The dominant grain size is coarse grained (68%) with minor components of medium-grained (31%) and pegmatitic gabbro (1%). Unit I is characterized by anhedral to subhedral granular textures with olivine (1%–20%), plagioclase (50%–70%), and clinopyroxene (20%–30%; all in volume percent). Coarser grains of poikilitic clinopyroxene are commonly developed and include smaller grains of plagioclase. Fe-Ti oxides and sulfides are present in trace amounts in gabbro and olivine gabbro. Oxide olivine gabbro is characterized by irregularly distributed, interstitial, and disseminated Fe-Ti oxides and sulfides, which may be highly concentrated in localized patches and bands. These oxide-rich zones are commonly accompanied by ductile deformation and the development of a strong foliated fabric in places (see "Structural Geology," p. 48). Primary igneous layering is defined by irregular to gradational grain-size layering and less common weak modal layering. Igneous lamination is not commonly observed in Unit I despite the igneous textures of the rocks. Felsic veins constitute a very minor component (e.g., Sections 179-1105A-2R-3, 5R-2, and 6R-2; Fig. F25). Unit I shows only sporadically developed deformational foliation and alteration (Fig. F26).

### *Unit II*

Lithologic Unit II includes intervals 24 through 123 (48.14–136.38 mbsf, Sections 179-1105A-7R-1 to 26R-2) and is composed of 88.24 m of alternating gabbro, oxide gabbro, and olivine gabbro (Fig. F21). The lower boundary is defined by a decrease in the proportions of oxide-rich intervals (Fig. F22). Unit II is composed of medium- to coarse-grained oxide and oxide olivine gabbro (29%), gabbro (55%), and olivine gabbro (16%); there is no systematic distribution of the three main rock types. The main difference between Unit I and Unit II is a higher proportion of oxide gabbro in the latter.

F21. Summary of visually defined lithologic intervals and syntheses units of Hole 1105A, p. 93.

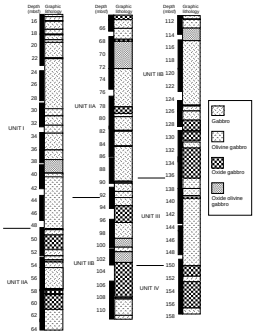


F22. The downhole variation in modal mineralogy of Hole 1105A as visually estimated during core description, p. 94.

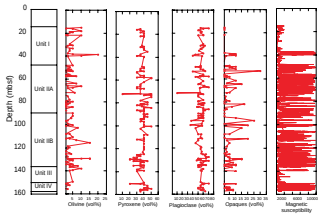


F23. The estimated downhole variation in maximum grain size in Hole 1105A, p. 95.

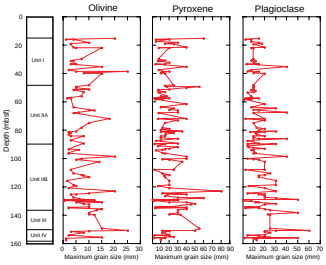


F24. The estimated downhole variation in the average grain size in Hole 1105A, p. 96.

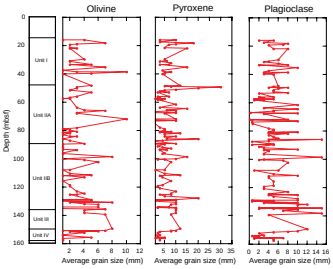

Similar to Unit I, many of the defined intervals have considerable grain-size variations from fine to medium (e.g., intervals 30, 38, 40, 42, 56, 77, 118, and 120), fine to coarse (e.g., intervals 89 and 99), medium to coarse (e.g., intervals 33, 39, 67, 70, 78, and 97), and coarse to pegmatitic (e.g., intervals 54, 65, 71, and 100). In addition, the average grain size in the lower part of the unit appears to be larger than in the upper part of the unit (Figs. F23, F24). This allows Unit II to be divided into two subunits. Subunit IIA is defined by intervals 24 through 78 (48.14–92.79 mbsf, Sections 179-1105A-7R-1 to 16R-2) and Subunit IIB by intervals 79 through 123 (92.79–136.38 mbsf, Sections 179-1105A-16R-2 to 26R-2). This subdivision corresponds well with the magnetic susceptibility measurements, which show a significant drop in average values at the interval 78/79 boundary (see "Physical Properties," p. 57). A reasonable breakdown of Unit II in grain-size categories, based on the estimated dominating lithologies, is for Subunit IIA fine (7%), medium (34%), coarse (56%), and pegmatitic (3%) and for Subunit IIB fine (1%), medium (23%), coarse (72%), and pegmatitic (4%), reflecting the increased grain size in the lower part of Unit II. Uniformly fine-grained gabbro intervals are evenly distributed through Unit II (e.g., intervals 32, 53, 55, 73, 75, 91, and 108).

The two main components of Unit II are oxide-poor gabbroic rocks and oxide-rich gabbroic rocks. Petrographically they are very similar to those found in Unit I. The gabbro and olivine gabbro intervals are composed of olivine (2%–20%), plagioclase (55%–70%), and clinopyroxene (20%–35%) with anhedral to subhedral granular and coarser poikilitic textures. Fe-Ti oxides are a minor component for all gabbro and olivine gabbro intervals. Oxide gabbro is typically composed of olivine (0%–15%), plagioclase (50%–60%), clinopyroxene (25%–40%), Fe-Ti oxides (5%–15%), minor amounts of sulfides, and, rarely, orthopyroxene and apatite. The mode of occurrence of the Fe-Ti oxides is very similar to that observed in Unit I. The Fe-Ti oxides are disseminated grains or grains concentrated in irregular seams. High concentrations of Fe-Ti oxides are commonly characterized by the development of foliated fabrics.

The primary igneous layering is mainly associated with extreme grain-size variation in addition to some modal variation that is not easily distinguished in hand specimen. Unambiguous igneous lamination is sporadic (Fig. F26). Felsic intrusive veins are less commonly observed in the lower part of the Unit (Fig. F25) with the notable exception of an aplitic felsic vein in interval 48. Fine-grained gabbro intervals are throughout Unit II (e.g., intervals 32, 53, 55, 73, 75, 91, and 108). Notable development of deformation and alteration effects are mainly restricted to intervals 76, 77, and 78.

### *Unit III*

Lithologic Unit III is composed of 14.22 m of gabbro (9%), olivine gabbro (88%), and minor amounts of Fe-Ti oxide gabbro (3%). The unit is defined by intervals 124 through 128 (136.38–150.60 mbsf, Sections 179-1105A-26R-2 to 29R-2; Fig. F21). The upper boundary is located at the bottom of lithologic interval 123 (136.38 mbsf) and is defined by an abrupt decrease in the modal abundance of Fe-Ti oxide as well as in the intensity of the magnetic susceptibility (Fig. F22). The lower boundary is located at the bottom of lithologic interval 128 (150.60 mbsf) and is defined by an increase in the modal abundance of Fe-Ti oxide and in the intensity of the magnetic susceptibility (Fig. F22). Unit III includes five lithologic intervals of which interval 126 (139.12–139.56 mbsf) is

F25. The downhole estimated alteration intensity and distribution of felsic veins, p. 97.

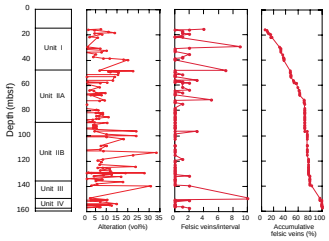


F26. The distribution of igneous laminations, modal and grain-size layering, crystal-plastic foliation fabric, and felsic veins, p. 98.

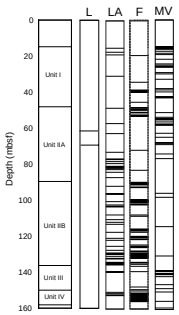

composed mainly of Fe-Ti oxide gabbro, whereas the other four intervals are olivine gabbro and olivine-bearing gabbro. As defined, Unit III is a sequence of dominantly olivine gabbro that is underlain and overlain by units characterized by a ubiquitous presence of oxide-rich gabbros. Because the rock types found in Unit III are similar to those in both Subunit IIB and Unit IV, the defined unit boundaries are without genetic connotations.

The principal rock types in Unit III are olivine gabbro and olivine-bearing gabbro. The olivine content ranges from 2% to 10% in visual modal estimates; interval 128 contains an accessory amount of olivine (2%), whereas intervals 124, 125, and 127 contain 10%, 5%, and 5%, respectively. Overall, the modal abundance of olivine appears to decrease downward in the unit. Most of the rocks are massive and coarse to pegmatitic in grain size with large, subhedral clinopyroxene oikocrysts (<55 mm) ubiquitously enclosing small euhedral plagioclase and more rarely subhedral olivine grains. The subhedral granular texture predominates throughout the unit. In some parts, gradational variations in mineral grain size (i.e., fining downward) are present with no clearly defined boundaries. In other areas, weak lamination, defined principally by alignment of elongated minerals, is developed.

A thin interval of Fe-Ti oxide-rich gabbro (interval 126) is present in Section 179-1105A-27R-1 (139.12–139.56 mbsf). This Fe-Ti oxide gabbro is highly variable in grain size (0.5–35 mm), is moderately to intensely altered with the formation of secondary plagioclase and green amphibole, and shows variably developed foliation. The Fe-Ti oxides are aggregates forming seams or irregular layers as well as separate grains with interstitial and irregular outlines. Fe-Ti oxide is closely associated with abundant apatite; this association can be seen in areas where the gabbros retain igneous textures. In contrast, apatite is noticeably lacking in the oxide-free olivine gabbros. This suggests that the Fe-Ti oxide-rich zones represent crystallization products of significantly more evolved magmas than those from which the olivine gabbros crystallized.

Felsic veins and alteration veins are not common in Unit III, although minor thin and discontinuous veins with narrow alteration zones are sporadic throughout the unit (Fig. **F25**). Mylonitic and porphyroclastic intervals are lacking in this unit.

### *Unit IV*

Lithologic Unit IV is the lowest unit of the core recovered at Hole 1105A (150.60–157.44 mbsf, Section 179-1105A-29R-2 to end of the core in Section 179-1105A-30R-3; Fig. **F21**). This unit represents a 21.06-m sequence in which Fe-Ti oxide-rich gabbro (37%) and gabbro (63%) intervals alternate. The Fe-Ti oxide-rich gabbro in Unit IV is generally similar to that in Unit III (e.g., interval 126), whereas the gabbro in Unit IV contains either an accessory amount of olivine (0.5%–3%) or completely lacks olivine. The contact with Unit III is marked by significant changes in mineralogy, texture, and physical properties as seen by an abrupt increase in the modal abundance of Fe-Ti oxide and in the intensity of the magnetic susceptibility (Fig. **F22**). The top 0.85 m of Unit IV (intervals 129, 130, and 131) are relatively massive, but the rest of the unit shows variably developed foliation. This weakly to moderately developed foliation persists throughout most of Unit IV and also distinguishes it from the previous unit.

The Fe-Ti oxide content in the oxide gabbro intervals of Unit IV ranges from 5% to 10% in visual modal estimates. The remainder of the

gabbroic rocks are mainly composed of plagioclase and clinopyroxene; the former generally exceeds the latter volumetrically. The oxide gabbros are in 0.15- to 1.18-m-thick intervals (intervals 129, 133, 135, 137, and 140). These gabbros are mostly fine to medium grained, but two coarse-grained intervals (129 and 133) occur with foliated and weakly banded structures accentuated by grain size and modal variations on a centimeter scale. Under the microscope, the banding is characterized by alternating coarser and finer grained layers that are accompanied by thin irregular seams of mafic minerals and/or Fe-Ti oxide minerals. The finer grained layers typically show porphyroclastic textures. The coarser grained layers are in most cases deformed to variable extents, but they retain igneous textures that are mostly subhedral granular. The banding may be relict magmatic modal variations, but the intense overprinted deformation prevents us from elaborating on such interpretations.

The gabbroic rocks in Unit IV are in 0.23- to 1.34-m-thick intervals (intervals 130, 131, 132, 134, 136, 138, 139, and 141). These gabbros contain only minor amounts of olivine and Fe-Ti oxides, or lack olivine, and are generally subhedral granular with sporadic subophitic intergrowth. Except for intervals 130, 131, and 141, which are composed of massive gabbros, the gabbros in Unit IV display variously developed foliation primarily defined by the preferred dimensional orientations of clinopyroxene and plagioclase grains or their recrystallized mineral aggregates. Despite the presence of deformation fabric, portions of these gabbro intervals commonly retain igneous textures. Felsic veins are rare, and thin alteration veins are not common, except in interval 141 (Fig. F25).

## Igneous Contacts and Layers

The nature of the contacts and the petrographic variability between and within individual intervals provides important constraints on the magmatic and tectonic history of Hole 1105A gabbros. In this section we review the findings from the visual inspection of the core and emphasize the primary igneous aspects. The deformational and structural aspects are dealt with in "Structural Geology," p. 48. The intervals were visually defined based on differences in grain size, modal content, texture, and structure. We discuss the most important types of contacts, but first briefly consider the forms of the contacts.

### Layer Contacts

The forms of contacts between intervals were defined as intrusive, planar, irregular, gradational, and tectonic. Of the 140 contacts described, 35% were not recorded because of breaks in recovery, 19% were classified as gradational, 38% as planar, 4% as irregular, and 4% as tectonic. None of the contacts was classified as intrusive. The clearly intrusive felsic veins were too small to be defined as individual intervals or lack preserved contacts. Fine-grained gabbro exists throughout the core as small intervals or as parts of intervals.

The tectonic contacts are either very sharp or irregular and are associated with the development of foliation and occasionally mylonitic fabrics (e.g., intervals 24 and 52). If it was possible to identify the original igneous contact, these were described accordingly and not as tectonic. Consequently, the contacts described as tectonic represent those for which the nature of the original igneous contacts could not be inferred.

The majority of the contacts are described as planar and are seen as a relatively abrupt changes in either grain size or modal composition. The gradational contacts show one rock type grading into another without a clearly defined interface on a scale of typically <1 cm. Such contacts may reflect differences in nucleation and growth rates. This simplistic view may require modifications for two reasons. First, it is possible that some contacts described as gradational result from late magmatic or subsolidus recrystallization. Second, melt migration within a semisolid crystal-liquid mush may significantly reshape primary igneous contacts. Such migrations may be driven either by liquid density relations, simple compaction, or deformation controlled compaction. It was argued by the Leg 118 participants that such melt migration could have played a major petrogenetic role at Site 735 (Robinson, Von Herzen, et al., 1989). The similarities in the contact types of the oxide-free and oxide-rich intervals from Hole 1105A do not suggest petrogenetic differences. Both groups have approximately constant planar/gradational abundance contact ratios (0.67/0.33).

## Igneous Lamination

Igneous lamination is defined by a magmatic planar alignment of the dominating primocrysts resulting in a relatively well-defined planar fabric to the rock. Well-developed and unambiguous igneous lamination has only been described from two oxide gabbro intervals in Unit II (intervals 43 and 51; Figs. F26, F27). At first sight, this result may be somewhat surprising in view of the plutonic nature of the gabbros. However, thin-section examinations suggest that lamination actually may be more common than indicated by the core descriptions. An example of a relatively well-developed lamination is illustrated in Figure F27 from a fine-grained olivine gabbro (interval 55; Section 179-1105A-12R-2) and is defined by the parallel alignment of plagioclase and mafic phases, including a distinct regular crystallographic alignment of plagioclase twin planes. Abundant examples of igneous lamination, however, are lacking based on thin-section descriptions.

F27. Igneous lamination in fine-grained olivine gabbro, p. 99.

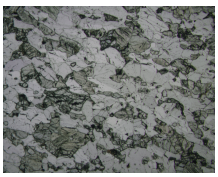

## Igneous Layering

The contacts of the intervals were visually characterized as mainly caused by modal, grain size, and textural differences, or a combination thereof. The summary of statistics for all intervals are (1) modal and grain-size change (58%), (2) grain-size, modal, and textural changes (23%), (3) grain-size change only (5%), (4) grain-size and textural changes (4%), (5) modal changes only (3%), (6) textural changes only (1%), and (7) layering contacts affected by ductile deformation (6%).

It is interesting that in excess of 80% of the contacts involve modal and grain-size changes typical of cumulate layering in continental basic intrusions and in ophiolites. The frequency of textural changes tends to increase with depth in the core. This can be correlated with a downhole increase in the proportion of pegmatitic to coarse grain sizes with depth (Figs. F23, F24). Figure F26 shows the recorded distribution of layering. It can be observed that well-documented layering is mainly concentrated in the upper part of Subunit IIA and in Subunit IIB and Unit IV.

## Modal Layering

A relatively nondistinct and commonly poorly defined modal layering characterizes 84% of the intervals with contacts described as either planar (67%) or gradational (33%). This type of layering is caused by gradational or abrupt changes in the mineral proportions, typically in the ratio between mafic and felsic minerals or by the appearance or disappearance of a phase (e.g., olivine and Fe-Ti oxide minerals). Such modal variations may give rise to alternating mafic- and felsic-rich layers or, in extreme cases, melanocratic and leucocratic layers. An example of this is seen in Figure F28A from a coarse-grained oxide gabbro (interval 89, Section 179-1105A-18R-2) as mafic layers composed of pyroxenes and oxide minerals that are separated by nearly monomineralic anorthositic layers a few centimeters thick. Another example is illustrated in Figure F28B where the mafic layer shows a finer scaled alternation between mafic and felsic parts, perhaps accentuated by deformation (interval 57, Section 179-1105A-13R-1). This type of layering is sporadic throughout the core and is not only confined to the interval contacts, but also down to a centimeter scale within individual intervals. This finer scaled layering appears to be generally similar to the layering used to define the individual intervals.

F28. Examples of modal layering, p. 100.

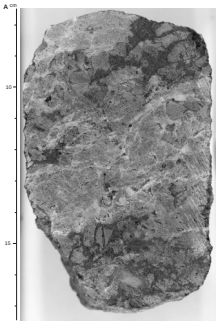

A significant part of the layering seen in the core is modally defined by the appearance or disappearance of a mineral phase not present in the layer above or below. Alternating gabbro and olivine gabbro intervals or layers represent examples of modal layering defined by the appearance or disappearance of olivine. The modal layering defined by the appearance or disappearance of Fe-Ti oxide minerals gives rise to alternating layers of olivine gabbro and oxide olivine gabbro or oxide gabbro down to a scale of decimeters. In addition, layering caused by modal variations in the amount of Fe-Ti oxide minerals appears on a small scale (centimeter–millimeter) as irregular layers or seams with high concentrations of Fe-Ti oxide minerals together with olivine and pyroxenes. These layers are mineralogically similar to gabbro in adjacent layers that have lower Fe-Ti oxide concentrations. This is illustrated in Figure F29, which shows a coarse-grained, oxide-bearing gabbro with an ~2-cm-thick central seam of highly concentrated Fe-Ti oxides (interval 71, Section 179-1105A-15R-1). Figure F28A illustrates an example with two seams of oxide gabbro separated by an oxide-bearing anorthositic band. Although the concentrations of Fe-Ti oxides may locally be high (75%), on the scale of an interval the concentrations may average only 2%, classifying some intervals as an oxide-bearing gabbro despite the local presence of Fe-Ti oxide gabbro bands (see "Igneous Lithology, Interval Definitions, and Summary," p. 6, in the "Explanatory Notes" chapter).

F29. Example of oxide layering, p. 102.

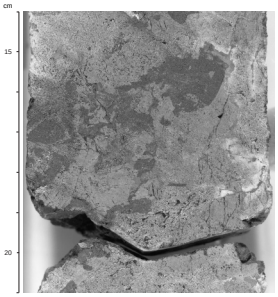

It is not possible, based on the present observations, to evaluate the origin(s) of the modal layering. Any model must explain both the alternating meter- to decimeter-scale layering as well as the finer scale layering mostly defined by the concentrations of the Fe-Ti oxides. Some of the available information indicates that redistribution of interstitial melt may have played a role either because of compaction or deformation. It is not clear whether a similar process can account for the meter-scale alternation of the two main components in the core (olivine gabbro and oxide olivine gabbro). A solution may be related to the magnitude and distance of migration of interstitial melt, either laterally or vertically, but in situ crystallization or gravitational and flow-controlled

crystal accumulation, sorting, as well as nucleation and growth-rate differentiating processes may also have played a role during solidification.

### Grain-Size Layering

The two most common changes of layer contacts are modal and grain-size changes. Grain-size layering is used to help define 90% of the intervals. The grain-size layering increases significantly in intensity downward in the core (Fig. F26) and may be related to an increase in the grain size and overall coarsening of the gabbros (Figs. F23, F24). This type of layering is defined by variation in grain size from typically medium- to coarse-grained and pegmatitic gabbro. An example of grain-size layering is shown in Figure F30. Typically, grain-size layering is seen as well defined, gradational to planar contacts with the coarser rocks occupying layers, patches, and pockets in finer grained rocks with perhaps limited lateral extent.

Fine-grained gabbro (or microgabbro) is present in most of the core as a minor component (4%), but it is also in layers and irregular pockets in coarser grained intervals. The fine-grained gabbros range in thickness from a few meters (interval 73, Section 179-1105A-15R-1) to <5 cm (intervals 32, 53, 55, 75, 91, 108, 134, and 138) and possess typically sharp contacts to the coarser grained gabbro (Fig. F31). They are most commonly olivine gabbros with equigranular textures showing rather sharp to irregular contacts and marginal coarsening of the fine-grained gabbro (Fig. F32).

Commonly, the grain-size layering is associated with textural changes from granular to inequigranular to poikilitic textures seen by the development of large clinopyroxene oikocrysts enclosing, or partially enclosing, plagioclase. Grain-size gradation within layers can be "normal" or "reverse." In general, the estimated maximum grain sizes are independent of rock type and increase for both plagioclase and pyroxene downward in the section (Figs. F23, F24). The fact that the dominating variability in the recovered core is related to variations in both modal abundances and grain size suggests that fluctuation in nucleation and growth rates were important during phase equilibrium changes and may have been controlled by fluctuation in the extent of magma mixing, compositional variability of a volatile component, and cooling rate.

## Magmatic Veins

Late magmatic veins of felsic material are present throughout most of the core and may represent a large compositional range including trondhjemite and diorite but are too thin to be defined as separate intervals. Despite their volumetrically minor importance, they are of considerable interest since they may represent the final product of magmatic differentiation. Felsic veins are particularly concentrated in the olivine gabbro and gabbro of Unit I and III (Figs. F25, F26). There are a few millimeter- to centimeter-thick veins with sharp and planar subparallel boundaries, which indicate intrusive relations, but irregular veins and patches are also common. A typical example is shown in Figure F33. Assimilation is sporadically suggested by included gabbroic material in some veins.

F30. Example of grain-size layering, p. 103.

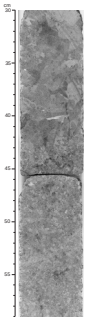

F31. Example of fine-grained oxide olivine gabbro alternating with coarse-grained oxide gabbro in deformed section, p. 104.

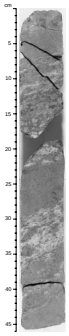

F32. Contact between fine-grained olivine gabbro with granular texture and a medium-grained olivine gabbro, p. 105.

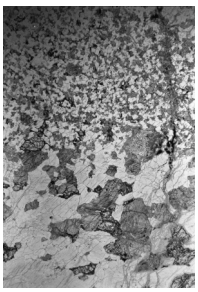

F33. Thin magmatic felsic vein with intruding gabbro, p. 106.

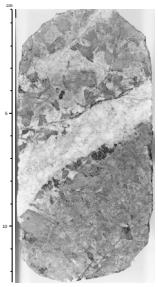

## Primary Petrography

Rock types are defined in "Rock Classification," p. 4, in the "Explanatory Notes" chapter. The main rock types are distinguished by variations in grain size and in the abundances of plagioclase, clinopyroxene, orthopyroxene, olivine, and Fe-Ti oxide. The term clinopyroxene is used for the entire compositional range of Ca-rich pyroxene; most of these are likely augitic pyroxenes, but their compositions are unknown. A minor amount of orthopyroxene is present in the Leg 179 gabbroic rocks, but pigeonite was not found despite being reported in a few cores from Leg 118 (Robinson, Von Herzen, et al., 1989). The relative abundance, modes, and grain-size variations of the main constituent minerals, based on VCDs, are presented in Figures F22, F23, F24, and F34.

A variety of gabbroic and metagabbroic rocks are recovered from Hole 1105A. Thin-section observations indicate that these include olivine gabbro (52%), gabbro (16%), oxide olivine gabbro (14%), oxide gabbro (16%), and oxide gabbronorite (2%). The proportions shown in parenthesis were obtained from the samples for which thin-section analyses were available and, therefore, are not identical to the visual estimates presented above. Obviously, the thin-section populations by no means accurately reflect the actual proportions of each rock type present in the core, but only give rough estimates of their proportions. In addition to these gabbroic rocks, felsic rocks are present as crosscutting veins in the core. We did not recover other types of gabbroic rocks such as troctolite, norite, and hornblende gabbro or any type of ultramafic rocks. Brown hornblende is ubiquitous throughout the core; it is found in >70% of the samples examined under the microscope, but its modal proportion is generally <1%–2% and never >10%. We found two highly olivine-rich samples (troctolitic gabbros) and one mafic mineral-poor sample (anorthositic gabbro); however, this is probably an artifact caused by either uneven distributions of minerals in coarse-grained rocks or small-scale layering. Olivine gabbro and olivine-bearing gabbro are by far the dominant rock types, constituting >70% of the recovered core.

Many of the gabbroic rocks display deformation textures ranging from weakly foliated to porphyroclastic or mylonitic (see "Structural Geology," p. 48). The gabbroic rocks with deformation and recrystallization textures represent >40% of the sample population examined under the microscope. This suggests that many of the gabbroic rocks in Hole 1105A are affected by deformation and recrystallization to various extents.

F34. Estimated modal variation on triangular diagrams, p. 107.

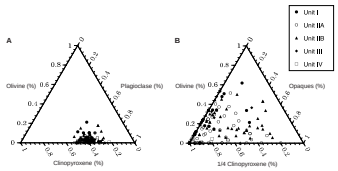


### Gabbro and Olivine Gabbro

Gabbro (<5% modal olivine) and olivine gabbro (>5% modal olivine) are the most abundant rock types distributed throughout the core. They are the main rock types in all of the lithologic units (Units I–IV). The primary mineral assemblages and modal compositions of gabbro and olivine gabbro are generally olivine (0%–30%), plagioclase (50%–70%), clinopyroxene (10%–40%), orthopyroxene (3%, found in one sample), trace amounts of primary brown hornblende, and opaque minerals (Fe-Ti oxide and sulfides). The modal proportions of olivine are generally <10%. These modal proportions were visually estimated under the microscope, coupled with point-counted modes from 25% of the thin sections. These modal estimates vary significantly because of both the

coarse-grained nature of the gabbros and the presence of modal layering (see "Igneous Contacts and Layers," p. 34). The gabbro and olivine gabbro are mostly medium to coarse grained but, in many cases, they are pegmatitic.

In general, the medium- and coarse-grained olivine gabbros have subhedral granular textures (Fig. F35). In some cases, these rocks are equigranular, but in others they are inequigranular with subhedral to anhedral, interlocking plagioclase and clinopyroxene crystals. Most of the coarse-grained and pegmatitic olivine gabbros, however, have poikilitic or subophitic textures in which large subhedral clinopyroxene oikocrysts enclose or partly enclose small euhedral to subhedral plagioclase and, to a much lesser extent, olivine (Figs. F36, F37). Although these rocks show pervasively igneous textures, deformation bands and undulatory extinction in olivine crystals (Fig. F38), and curved, tapering twin lamellae and undulatory extinction in plagioclase laths, are common (Fig. F39).

Plagioclase is found as euhedral to subhedral laths. These plagioclase crystals show weak compositional zoning, although it becomes difficult to recognize zoning in the deformed plagioclase crystals in which wavy extinction and deformation twins are commonplace. Symmetrical extinction angles obtained on the polysynthetic albite twins suggest that the compositional zoning of plagioclase is rather narrow, ranging from $An^{55}$ to $An^{65}$.

Olivine is present as rounded subhedral crystals or rounded anhedral crystals. The optic angles (2V) of olivine, estimated from interference figures of 70° to 80°, indicate relatively high magnesian compositions. Compositional zoning is not generally optically noted in olivine crystals; however, in one sample, a rounded, zoned olivine crystal enclosed in plagioclase has higher interference colors in the core than the rim with a fairly sharp interface. In several samples, we found a cluster of olivine crystals, which, as a whole, is similar to surrounding plagioclase and clinopyroxene crystals in grain size and appears to retain a single crystal outline (Fig. F39). In rare cases where olivine might have recrystallized, clusters of olivine crystals show a polygonal mosaic texture in which grain boundaries form 120° triple junctions. Olivine crystals generally display deformation bands and undulatory extinction even in gabbros that show typical igneous texture.

Clinopyroxene is present as prismatic to blocky, euhedral to anhedral crystals. Obvious compositional zoning of clinopyroxene is not detected under the microscope. Fine exsolution lamellae of orthopyroxene parallel to the c-axis are ubiquitously present in many clinopyroxene crystals. In several samples, clinopyroxene shows consertal intergrowth with adjacent clinopyroxene (Fig. F40. Some clinopyroxene crystals are clouded by acicular opaque minerals, which are aligned and regularly spaced. In one medium-grained gabbro (Sample 179-1105A-8R-1, 68–70 cm), we found orthopyroxene along with plagioclase, clinopyroxene, and olivine. This sample contains 2.8% modal Fe-Ti oxide (obtained by point counting). The orthopyroxene crystals are subhedral to anhedral with abundant, thin exsolution lamellae and blebs of clinopyroxene.

As noted previously, brown hornblende is an accessory mineral ubiquitous throughout the core (Fig. F41). It is mainly present as fringes to clinopyroxene crystals as well as patchy blebs inside clinopyroxene crystals. Less commonly, it also forms rims around Fe-Ti oxide and olivine. Brown hornblende crystals, in particular those that rim clinopyroxene, tend to be gradationally zoned toward green hornblende (i.e., those

F35. Fine-grained olivine gabbro with adcumulate texture, p. 108.

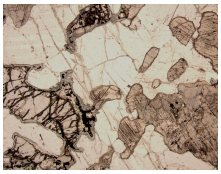

F36. Poikilitic clinopyroxene enclosing anhedral plagioclase grains in medium-grained olivine gabbro, p. 109.

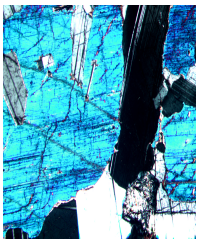

F37. Poikilitic clinopyroxene oikocrysts enclosing plagioclase laths, p. 110.

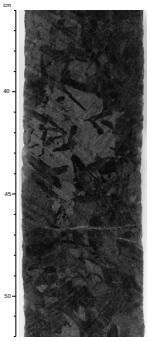

F38. Deformation bands in olivine in coarse-grained olivine gabbro, p. 111.

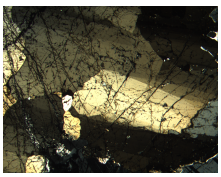

F39. Recrystallized granular aggregate of olivine in medium-grained olivine gabbro, p. 112.

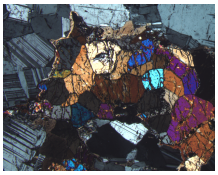

close to clinopyroxene are brown and gradually become greenish outward). Also, brown hornblende is generally replaced by fibrous, colorless amphibole (actinolite), which also replaces clinopyroxene. It is not certain whether this brown hornblende is a primary mineral. However, we believe that much of the brown hornblende is a primary igneous mineral for the following reasons:

1. If the brown hornblende is a metamorphic mineral, then anthophyllite, cummingtonite, or recrystallized olivine should be more common, replacing primary olivine and orthopyroxene. But these minerals are lacking in the Hole 1105A gabbros.
2. Brown hornblende is commonly one of late-stage magmatic precipitates formed from even "dry" tholeiitic magma.

Previous studies, however, have shown that extensive amounts of brown hornblende in porphyroclastic gneissic gabbro from Hole 735B could be related to high-temperature alteration (e.g., Stakes et al., 1991). As discussed in **"Alteration and Metamorphism,"** p. 42, some of the brown hornblende in the deformed gabbros from Hole 1105A also could be a product of high-temperature metamorphism. In a few medium-grained gabbro samples, vermicular, symplectic intergrowths of clinopyroxene and plagioclase along the grain boundaries can be found (Fig. **F42**).

Most of the fine-grained gabbros (microgabbro) are not truly igneous and apparently formed from coarser-grained gabbro by ductile to brittle deformation. There are, however, a few microgabbro samples that display truly igneous textures with a little or no sign of deformation. These microgabbros are anhedral granular with a relatively even distribution in grain sizes. Some of these display distinct igneous lamination defined by subparallel alignment of plagioclase and mafic minerals (Fig. **F27**). Obvious compositional zoning in these minerals is generally not optically detected, but, in rare cases, plagioclase displays a complex zoning pattern (Fig. **F43**).

## Oxide Gabbro, Oxide Olivine Gabbro, and Oxide Gabbronorite

Oxide gabbro (>5% modal Fe-Ti oxide; <5% modal olivine) and oxide olivine gabbro (>5% modal Fe-Ti oxide; >5% modal olivine) are the main rock types in lithologic Units II and IV; they are also present in subordinate amounts in lithologic Units I and III. The primary mineral assemblages and modal compositions of oxide gabbro and oxide olivine gabbro are generally olivine (0%–12%), plagioclase (50%–80%), clinopyroxene (5%–44%), orthopyroxene (0%–4%), opaque minerals (Fe-Ti oxides, sulfides; 5%–12%), and trace amounts of primary brown hornblende, apatite, and titanite. The modal compositions are visual estimates coupled with point counting of 25% of the thin sections. One oxide-rich gabbro sample contains orthopyroxene visually estimated as high as 5% (Fig. **F44;** Sample 179-1105A-22R-2, 74–78 cm).

Oxide gabbro and oxide olivine gabbro are in many respects similar to the gabbro and olivine gabbro described above, especially in terms of rock textures, mineral morphologies, and mineral intergrowth. Nonetheless, there are some distinct differences between these groups of gabbroic rocks from Hole 1105A. Most notable is the high content of Fe-Ti oxides in these gabbroic rocks when compared to the gabbros and olivine gabbros. Moreover, Fe-Ti oxide minerals are generally <0.5 mm in

F40. Consertal intergrowth of clinopyroxene in medium-grained olivine gabbro, **p. 113.**

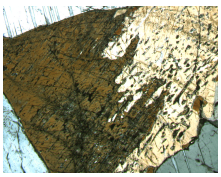

F41. Brown hornblende rim surrounding clinopyroxene and Fe-Ti oxides in pegmatitic gabbro, **p. 114.**

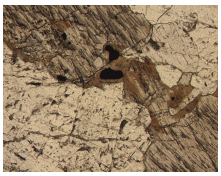

F42. Symplectic intergrowth between clinopyroxene and plagioclase in medium-grained granular gabbro, **p. 115.**

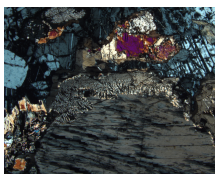

F43. Complex zoned plagioclase in otherwise adcumulate textured and laminated, fine-grained olivine gabbro, **p. 116.**

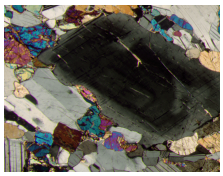

F44. Orthopyroxene with opaque inclusion in coarse-grained oxide- and olivine-bearing gabbronorite, **p. 117.**

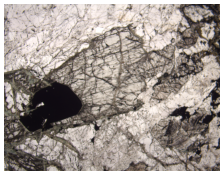

grain size in gabbro and olivine gabbro, whereas they are generally larger than this size and up to 10 mm in oxide gabbro and oxide olivine gabbro. In particular, they are present not only as single, interstitial fillings between larger silicates but as elongated aggregates forming seams and bands (Fig. F45). In several samples, we found apatite crystals in close association with Fe-Ti oxide seams (Figs. F46, F47). Where found, apatite generally ranges from 1% to 5% modal and contains saline fluid inclusions (Fig. F48). On board, XRF analyses indicated that some of these oxide-rich gabbros have $P_2O_5$ contents as high as 4 wt% (see "Geochemistry," p. 45). Apatite is characteristically absent from the gabbro and olivine gabbro samples examined under the microscope. The presence of considerable amounts of apatite is one of the significant features that characterizes the oxide-rich gabbros from Hole 1105A.

Leg 118 Shipboard Scientific Party (Robinson, Von Herzen, et al., 1989) noted the following petrographic characteristics that distinguish Fe-Ti oxide gabbro from other types of Hole 735B gabbro:

1. They contain calcium-poor pyroxenes (orthopyroxene and/or inverted pigeonite). Almost one-third of the iron titanium oxide gabbros contain inverted pigeonite, but this mineral is absent in other types of gabbro from Hole 735B.
2. Clinopyroxene usually has {001} exsolution lamellae, which are absent in other types of gabbro from Hole 735B.
3. Clinopyroxene commonly contains patches of orthopyroxene or inverted pigeonite, which show the same crystallographic orientation as exsolution in the host clinopyroxene.
4. Olivine is generally low in abundance (<2%), although a few olivine-rich Fe-Ti oxide gabbros are present.

The characteristics related to pyroxenes listed above are not generally applicable to the Leg 179 oxide-rich gabbros. Pigeonite is totally lacking in the thin sections of Leg 179 gabbros we examined, and orthopyroxene is present in only four out of 20 oxide-rich samples. This finding differs from the Leg 118 observation, in which the oxide-rich gabbros contained ubiquitous Ca-poor pyroxene. However, since we found orthopyroxene only in one oxide-poor gabbro sample, it appears that orthopyroxene tends to be associated with oxide-rich gabbros. In rarer cases, we found a clinopyroxene simply twinned on {100} with orthopyroxene lamellae leading to herringbone texture (Fig. F49), but it is not so common as in Hole 735B oxide gabbros. Olivine does appear to be generally low in abundance in the Leg 179 oxide-rich gabbros, but gabbros having ~5% modal olivine are not uncommon.

## Cumulate Nature of the Gabbros

There is little doubt that the gabbroic rocks recovered from Hole 1105A are igneous cumulates and composed of a framework of touching cumulus minerals concentrated through fractional crystallization (Irvine, 1982). Although the strongest support for this is provided by the whole-rock concentrations of major oxides and excluded trace elements (see "Geochemistry," p. 45), this also is in accordance with textural observations. The relatively unzoned nature of most cumulus phases and their granular interlocking textures suggest that the amount of postcumulus trapped melt is small and classify most of the gabbroic rocks as mesocumulates, adcumulates, and poikilitic adcumulates (or heteradcu-

F45. Interstitial Fe-Ti oxides and disseminated sulfide grains in an orthopyroxene-bearing oxide gabbro, p. 118.

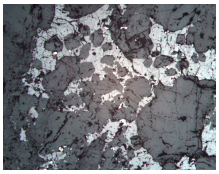

F46. Titanite adjacent to and intergrown with Fe-Ti oxide in medium-grained olivine-bearing oxide gabbro, p. 119.

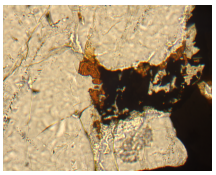

F47. Cluster of apatite included in amphibole and Fe-Ti oxide in coarse-grained olivine-bearing oxide gabbro, p. 120.

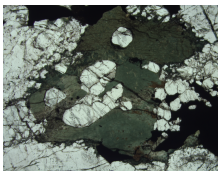

F48. Fluid inclusions with vapor bubble and halite daughter in apatite, p. 121.

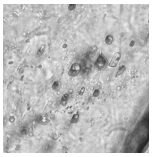

F49. Clinopyroxene with uncommon {001} exsolution lamella and twin-plane parallel to the c-axis in medium oxide gabbro, p. 122.

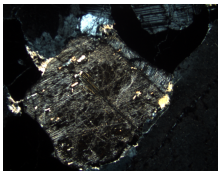

mulates; Wager et al., 1960; Irvine, 1982). The origin of the interstitial clinopyroxene and Fe-Ti oxide minerals found in many of the intervals in Hole 1105A is less certain, but they appear to have grown dominantly in equilibrium with the coexisting largely unzoned plagioclase and pyroxenes. Despite this, there is still some evidence for postcumulus trapped liquid crystallization. For example, in an anorthositic layer (interval 127 in 179-1105A-27R-3, 93–94 cm), clinopyroxene and olivine fill small interstices between large, euhedral to subhedral plagioclase crystals and may represent postcumulus crystallization. Well-developed evidence for interstitial crystallization (zoning and the appearance of low-temperature mineral phases) is observed in some thin sections but is not commonly found to characterize the gabbroic rocks of Hole 1105A. Additional support for the cumulate nature of the gabbros is provided by the modal layering (including monomineralic anorthositic layers) and the occasional preferred mineral orientations or lamination with plagioclase laths showing aspect ratios of ~1:4 roughly aligned subparallel to each other.

## Alteration and Metamorphism

The gabbroic rocks recovered from Hole 1105A were subjected to variable degrees of static hydrothermal alteration and, more remarkably, ductile to brittle deformation accompanied by recrystallization followed by later nonpervasive fracturing and felsic veining. These postmagmatic processes modify incipiently to almost completely or obliterate the original igneous texture (see **"Structural Geology,"** p. 48). As a result, the textures that display replacement of primary igneous minerals by secondary and metamorphic minerals or dynamic recrystallization of primary minerals are widespread throughout the core. Thin-section observation indicates that the gabbroic samples with no or only traces of secondary and/or metamorphic minerals constitute 18% of the total number of samples examined under the microscope. The remainder of the samples are altered or metamorphosed to various extents, ranging from 1% modal to as much as 30% modal secondary minerals (Fig. **F25**). It also appears from cursory inspection that the extent to which these gabbroic rocks are altered or metamorphosed is not closely related to the major igneous rock types such as gabbro, olivine gabbro, oxide gabbro, and oxide olivine gabbro, or to any specific lithologic unit described in **"Lithostratigraphy,"** p. 30. Instead, it appears to be largely related to the degree in which these rocks are deformed. Detailed petrologic studies of oceanic metagabbros have shown that metamorphic recrystallization is related to either deformation and/or interaction with seawater during cooling of the gabbroic sequence (e.g., Bonatti et al., 1975; Honnorez et al., 1984; Stakes et al., 1991). The alteration and metamorphism observed in Hole 1105A gabbroic rocks are generally in accord with this notion. On a mesoscopic scale, the gabbroic rocks that are altered or metamorphosed to lesser extents are typically massive, whereas those that are altered or metamorphosed to greater extents are foliated or banded. The textures of the massive gabbros grade from medium grained to pegmatitic and are generally subhedral granular and poikilitic; these massive rocks retain the igneous textures. The textures of the deformed gabbros grade from medium- to fine-grained porphyroclastic to fine-grained mylonitic. These porphyroclastic and mylonitic rocks generally no longer retain their original igneous textures (see **"Structural Geology,"** p. 48).

The minerals positively identified as secondary or metamorphic under the microscope include talc, serpentine, smectite, magnetite, calcite, epidote, chlorite, brown hornblende, green hornblende, actinolite, and plagioclase. In addition, orange-brown to pale greenish brown phlogopitic mica is found in a trace amount in one olivine gabbro sample. It is not certain, however, whether this mica is primary or secondary. The secondary and metamorphic mineralogy of the core is limited to <12 mineral species. This apparent simplicity in mineral assemblages is partly because the gabbroic samples from which thin sections were made were not taken from the late magmatic veins or their vicinities, and we only conducted optical determination of the minerals. It seems likely that more secondary and metamorphic minerals will be identified if further, more rigorous analyses are undertaken. There are three main styles of alteration and metamorphic recrystallization that can be distinguished mainly from textural relations and occurrences observed in the thin sections:

1. Metamorphic minerals that were formed through crystal-plastic deformation;
2. Secondary or metamorphic minerals that were formed by reaction of primary minerals with late magmatic fluids and/or seawater infiltrating along grain boundaries and open fractures under static conditions; and
3. Minerals that fill the veins related to late stage brecciation and felsic intrusion.

The metamorphic minerals that belong to the first category are those found in porphyroclastic and mylonitic gabbros. The fabrics of these rocks are described in detail in "Structural Geology," p. 48. In the porphyroclastic and mylonitic gabbros, relict plagioclase, clinopyroxene, olivine, and Fe-Ti oxides generally are porphyroclasts set in a finer grained, recrystallized mosaic dominated by plagioclase neoblasts. The plagioclase neoblasts are relatively strain free, commonly show sutured grain boundaries, and are easy to identify. Clinopyroxene appears to be more resistant to deformation, and olivine tends to be replaced with secondary minerals; therefore, these two minerals are less commonly found as neoblasts. There are, however, a few gneissic samples of tectonic origin, which display a fine-grained, subhedral equigranular texture with weak to strong foliation. The foliation is largely defined by the preferred dimensional orientation of plagioclase, clinopyroxene, orthopyroxene, and lenses of opaque minerals. The plagioclase crystals are relatively strain free, although some display undulatory extinction and deformation twins. In these samples, a minor amount of brown hornblende also is in close association with clinopyroxene and orthopyroxene. The two-pyroxene-bearing mineral assemblage indicates that they could have recrystallized at high temperatures (granulite-grade temperatures). Based on thin-section observation alone, however, we could not completely eliminate a possibility that some of these samples retain igneous remnants without recrystallization. If this is so, then these rocks simply represent weakly deformed noritic mineral assemblages. Further rigorous analysis is needed to resolve this ambiguity; tectonic and igneous textures apparently converge and become difficult to distinguish as the former is formed at increasing higher temperatures.

The secondary and metamorphic minerals that belong to the second category noted above include all the minerals previously mentioned. Neither zeolite group minerals nor prehnite were positively identified

in our examination of thin sections. Epidote is present, but it is only found in a trace amount in one sample. In most cases, this group of minerals fringe or completely replace the primary mafic minerals such as olivine and clinopyroxene and form pseudomorphs after these minerals. Fibrous actinolitic amphibole commonly fringes clinopyroxene; less commonly, greenish amphibole, which is either ferrous actinolite or common hornblende, does the same. Some of the greenish amphibole crystals are fibrous, but others are stocky, larger in grain size and show slight brownish tints. This variety of amphibole morphologies suggests the presence of various calcic amphiboles. Chlorite, smectite, and opaque minerals are present along with these amphiboles, replacing clinopyroxene. The pseudomorphs, after olivine, are generally composed of either (1) brown smectite + talc + magnetite, (2) brown smectite + talc + serpentine + magnetite, (3) talc + serpentine + chlorite + magnetite ± smectite or (4) brown smectite + talc + serpentine + magnetite ± actinolite. Opaque minerals and smectite commonly fill fractures and cleavages in olivine. It is noteworthy that clinopyroxene and olivine appear to be more susceptible to alteration or metamorphism under static conditions than plagioclase. Plagioclase alteration is restricted only to a slightly cloudy appearance with the formation of tiny clay minerals or to formation of chlorite, smectite, and/or colorless to greenish amphibole along microfractures and cracks. These fractures and cracks in plagioclase are commonly connected with the pseudomorphs after mafic primary minerals, and no crosscutting relation is observed between them. As for the minerals that belong to the third category, only VCD data are available at the moment. These data indicate that smectite-rich, amphibole + chlorite-rich, and calcite-rich veins are sparse throughout the core.

The alteration and metamorphic reactions in gabbroic intrusions at mid-oceanic ridge environments take place essentially during successive cooling stages (i.e., under a falling-temperature regime); thus, these processes are inherently retrogressive in nature. In continental gabbroic intrusions, reactions between primary magmatic minerals and the water-rich solutions that separate from the same magma at later stages during the process of crystallization are very common and are variously referred to as deuteric alteration or autometamorphism (e.g., Skaergaard intrusion). In fact, many of the petrographic features described above for Hole 1105A gabbroic rocks are virtually indistinguishable from those of deuteric alteration. However, oxygen isotope studies on Hole 735B metagabbros indicate that infiltrating seawater has played an important role in the alteration and metamorphic processes (Kempton et al., 1991). It is very likely that similar infiltration can be found at Site 1105.

The secondary and metamorphic mineral assemblages observed in Hole 1105A gabbroic rocks suggest that, overall, the pervasive alteration or dominant metamorphism probably took place under greenschist facies conditions. Basic rocks of the greenschist facies are characterized by the assemblage albite + epidote + chlorite + actinolite + titanite. In general, albite + epidote are ubiquitously found in the greenschist facies basic rocks in place of primary calcic plagioclase. As noted previously, epidote is conspicuously lacking in the Hole 1105A metagabbros, and plagioclase appears to be more resistant to alteration or metamorphism. Stakes et al. (1991) also reported that epidote is very rare at depths shallower than 150 mbsf in Hole 735B. This is perhaps one of the significant petrographic features that characterizes alteration and metamorphism at Sites 1105 and 735.

## Geochemistry

A set of 42 whole-rock samples was selected from Hole 1105A and analyzed by X-ray fluorescence for major elements (Si, Ti, Al, Fe, Mn, Mg, Ca, Na, K, and P) and selected trace elements (V, Cr, Ni, Cu, Rb, Sr, Y, Zr, and Nb). The results are shown in Table T15. The samples were selected to represent the main lithologies in the core and generally weighed 20–30 g. Sample preparation and analytical procedures and techniques are outlined in "Geochemistry," p. 6, in the "Explanatory Notes" chapter. Thin sections were prepared from splits of all samples for which XRF analyses were obtained.

The sampling was designed to characterize the main lithologies as well as to illuminate their downhole variation. The results are shown in Figure F50 for selected major elements and in Figures F51 and F52 for selected trace elements, as well as MgO and Mg#. The analyzed samples are identified in the figures according to the main lithologies as oxide gabbro (solid squares), olivine oxide gabbro (solid circles), gabbro (Xs), and olivine gabbro (open circles), based on thin-section examination of each sample analyzed. The analyzed trace elements are above the lower limit of detection, except for most of the Rb and some of the Nb determinations. Loss-on-ignition (LOI) values were generally <2% and reflect the low extent of alteration in the gabbros.

The high Mg/(Mg+Fe) ratios and low incompatible element abundances (e.g., $TiO_2$, $P_2O_5$, Y, and Zr) in the olivine gabbros and gabbros clearly identified these as cumulates when compared to typical Atlantis II Fracture Zone basalts (Natland et al., 1991). The low incompatible element contents, such as Nb, Zr, and Y, in most of the samples indicate that generally low amounts of intercumulus melt congealed within the cumulates, as also concluded by Natland et al. (1991) from a study of Hole 735B samples. The oxide gabbros and oxide olivine gabbros are compositionally highly variable in $Fe_2O_3$, $TiO_2$, and certain trace elements in comparison to the gabbros and olivine gabbros. Nevertheless, the relatively high $Fe_2O_3$, $TiO_2$, and $P_2O_5$ in some of the analyzed oxide gabbros indicate that they contain an overabundance of Fe-Ti oxide minerals and occasionally apatite in comparison to a melt composition, again indicating that these rocks are cumulate in origin rather than simply congealed melts.

The two main groups of gabbros (olivine gabbro and gabbros vs. oxide gabbros and oxide olivine gabbros) are for the most part clearly distinguished by their respective $TiO_2$ and $Fe_2O_3$ content (Fig. F50). However, these two groups are not clearly defined in terms of Mg/(Mg+Fe) ratio, and indeed there is overlap. The olivine gabbros and gabbros have Mg/(Mg+Fe) values between 0.4 and 0.8, $TiO_2$ generally <1.0 wt%, and $Fe_2O_3$ <10.0 wt%. In contrast, the oxide gabbros mostly have Mg/(Mg+Fe) values <0.5, $TiO_2$ >1.0 wt%, and $Fe_2O_3$ >10.0 wt%. These differences in Fe and Ti are a simple reflection of the modal variability in the content of Fe-Ti oxide minerals and do not necessarily reflect different parental magmas, although it may be the case for some of the oxide gabbros, based on geochemical and petrologic work on Hole 735B samples (Bloomer et al., 1991; Natland et al., 1991; Ozawa et al., 1991). In cores from Hole 1105A, there appears to be more of a continuum in magnesium numbers between the oxide gabbros and oxide-free gabbros indicating that the core contains a wide spectrum of fractionation extent over small vertical distances in the core. The findings at Site 1105 are consistent with the results obtained during Leg 118 (Robinson,

T15. Major oxide and trace element analyses of gabbros from Hole 1105A, p. 179.

F50. Downhole compositional variation in selected major oxides from Table T15, p. 123.

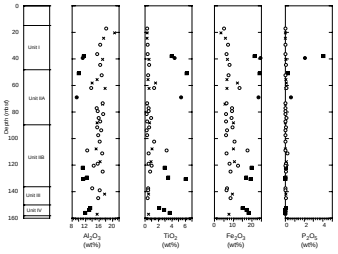

F51. Downhole compositional variation in selected trace elements from Table T15, p. 124.

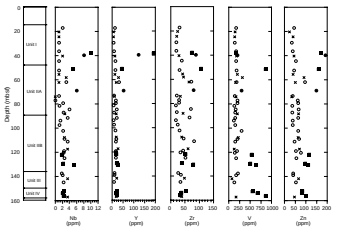

F52. Downhole compositional variation in compatible trace elements Ni and Cr, MgO, and Mg# from Table T15, p. 125.

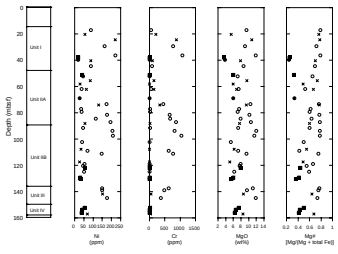

Von Herzen, et al., 1989) in the sense that both primitive and very evolved gabbroic rocks were recovered in close proximity to one another. One difference between the previous studies of Hole 735B and the present data from Hole 1105A is that some oxide gabbros contain very high $P_2O_5$ contents that may reach 4 wt% (e.g., Samples 179-1105A-4R-4, 57–62 cm, and 170-1105A-5R-1, 115–118 cm). Similar high $P_2O_5$ oxide gabbros were reported from the MARK region during Leg 153 at Site 922 (Shipboard Scientific Party, 1995). Such high concentrations indicate a maximum of ~10 wt% of modal apatite in the oxide gabbros and indicate a high extent of fractionation past apatite saturation.

The concentrations of some trace elements are positively correlated with the $TiO_2$, $Fe_2O_3$, and $P_2O_5$ contents (Fig. **F51**). For example, some of the oxide gabbros have relatively high concentrations of Nb, Y, Zr, and Zn (see Shipboard Scientific Party, 1995). Yttrium and to a lesser extent Nb show positive correlations with $P_2O_5$ concentrations, indicating that these elements in part may be controlled by the amount of apatite present. The elements Zr and Zn show good to poor positive correlation with $TiO_2$ and $Fe_2O_3$ and may reside in Fe-Ti oxide minerals, zircon, and sulfides. These correlations imply highly evolved residual melts and indicate that crystallization of Fe-Ti oxides, apatite, sulfides, zircon, and titanite were involved in the late stages of the differentiation and solidification processes.

The olivine gabbros of parts of Units I, II, and Unit III have relatively high concentrations of the compatible elements Ni and Cr that correlate with high MgO content but not with the Mg/(Mg+Fe) ratio (Figs. **F50, F52**). This may reflect relatively higher concentrations of modal olivine and pyroxene (or low plagioclase) in these intervals or significant changes in mineral compositions. It is also significant that for some incompatible trace elements, olivine gabbros of the oxide-rich Units II and IV tend to be relatively similar to the associated oxide gabbros (e.g., Zr and Ni).

It has been demonstrated that the variation in Mg/(Mg+Fe) for the olivine gabbros is a reflection of the compositional variation in the constituent minerals (i.e., olivine and clinopyroxene; Hebert et al., 1991, Bloomer et al., 1991; Dick et al., 1991a, 1992; Ozawa et al., 1991; Natland et al., 1991; Casey, 1997); therefore, the Mg/(Mg+Fe) ratio of whole-rock compositions can be used as a proxy for the cryptic variation in the mafic phases when Fe-Ti oxides are not present. Because the Mg/(Mg+Fe) ratio is calculated assuming that all iron is FeO, the presence of even small amounts of Fe-Ti oxides will lower the Mg/(Mg+Fe) ratio considerably and this no longer will reflect the mafic silicate mineral compositions.

The analyses of Hole 1105A cumulates illustrated in Figures **F50, F51,** and **F52** suggest a relatively variable Mg/(Mg+Fe) ratio for the olivine gabbros that appears to overlap with the Mg/(Mg+Fe) ratio of some oxide gabbros. In contrast, the oxide gabbros and olivine gabbros generally show a range of low ratios, reflecting their high Fe-Ti oxide modal abundances. The continuum in the range and overlap of compositions among olivine gabbros, gabbros, and oxide gabbros may suggest a common heritage for each group, but this tentative interpretation must await detailed cryptic mineral chemistry studies. The range of compositions sampled is relatively similar to previous results from Leg 118 (Robinson, Von Herzen, et al., 1989; Dick et al., 1991c) and Leg 153 (Cannat, Karson, Miller, et al., 1995; Casey, 1997). The stratigraphic

position of the Site 1105 gabbros, relative to the Site 735 gabbros, is at present uncertain and requires further detailed postcruise correlation efforts, but there may be significant overlap based on the initial attempts to correlate sections. There appears to be a relatively good correspondence between the results from Hole 1105A and the uppermost parts of Hole 735B in terms of Mg/(Mg+Fe) ratios and the presence of both primitive olivine gabbros and evolved oxide gabbros in close proximity over the same vertical intervals. Dick et al. (1991c) interpreted these two contrasting rock types to result from the mixing of primitive gabbros with highly fractionated oxide-rich intercumulus melts. The continuum of Mg/(Mg+Fe) ratios between oxide-free and oxide-bearing gabbros in Hole 1105A, however, was also noted for Hole 735B (Hebert et al., 1991). The question of the similar origin of both suites of rock clearly deserves very detailed studies of cryptic variation through the cumulate pile.

## Summary Discussion

Hole 1105A provides an important, but restricted, section through part of the lower oceanic crust. These results, together with a much more extensive coring from Hole 735B (Robinson, Von Herzen, et al., 1989), represent the most comprehensive sampling of an oceanic gabbroic complex to date. The previous study of these cores has contributed significantly to how we view magma chambers, their solidification processes, and their interaction with spreading ridge tectonics (e.g., Bloomer et al., 1991; Dick et al., 1991c, 1992; Ozawa et al., 1991; Natland et al., 1991).

The core obtained at Site 1105 is composed of a sequence of gabbro, olivine gabbro, oxide gabbro, and oxide olivine gabbro intervals that are grouped into four lithologic units. These intervals and units do not show mutual intrusive relationships and are considered to have been an integral part of a growing cumulus pile at the floor, roof bottom, or walls of a magma chamber (or multiple chambers). The gabbros at Site 1105 are dominantly typical adcumulates and heteradcumulates with some evidence for trapped liquid crystallization in the form of zoning in plagioclase. This indicates that some rocks solidified with significant trapped melt. Some incompatible trace element abundances are elevated over that expected for adcumulates and would suggest that a portion of the core contains significant amounts of formerly trapped melt that solidified in situ. In addition, sections of the core, which are highly deformed by ductile deformation, commonly mask evidence of mineral zonation because of the extreme strain in remnant porphyroclasts that leads to undulose extinction and recrystallization. Igneous lamination is scarce, but modally defined layers and variation are present throughout the core, particularly defined by changes in olivine and Fe-Ti oxide modal abundances. Nevertheless, a major criteria in defining igneous layering is grain-size variations from fine-grained to pegmatitic varieties of gabbroic rocks with gradational to planar interfaces seen on a centimeter to meter scales.

Some of the gabbroic rocks drilled at Site 1105 were subjected to crystal-plastic deformation to various extents and were locally dynamically recrystallized at temperatures possibly as high as granulite facies grade. Such plastically deformed zones within the gabbroic section may likely have provided pathways through which seawater infiltrated into the lower oceanic crust. In addition, gabbroic rocks were subjected to alter-

ation and metamorphism dominantly under greenschist facies conditions.

Despite their variability and cumulate nature, preliminary analysis of the Hole 1105A gabbros does not show a simple and systematic pattern of mineralogical and compositional variation with relative stratigraphic position. The core is composed of an intercalated interval or groups of intervals having distinct mineralogical and compositional ranges. One group is a relatively more primitive lithologic type composed of gabbro and olivine gabbro. The other group is an evolved lithologic type composed of oxide gabbro and oxide olivine gabbro. This spatial arrangement of the relatively primitive and evolved gabbros is very different from the systematic mineralogical and compositional variations commonly documented in gabbroic complexes in ophiolite and continental settings. Although the recovered rock types mimic the mineralogical variability and crystallization range expected in a fractionating basaltic magma chamber and there appears to be a compositional continuum, the close spatial arrangement of oxide gabbroic rocks and oxide-free gabbroic rocks does not lead to such a simple interpretation as classically portrayed in layered basic intrusions on land.

Despite their close association in the core and their contrasting mineralogical and compositional features, there is surprisingly limited evidence for interactions and mixing between the two compositional endmember components. The package of cumulates appears to have shared a common crystallization, postcumulus, and deformational history despite distinctly different parental liquid compositions (basalt and ferrobasalt). There is no conclusive evidence preserved in the Hole 1105A gabbros to indicate that the formation of the oxide gabbros postdates or is intrusive into the olivine gabbros. These findings are generally similar to the results obtained from Site 735 located only 1.2 km from Site 1105. Dick et al. (1991c) interpreted the intercalated oxide-rich and oxide-free gabbros to result from syntectonic differentiation caused by compaction of a partially molten olivine gabbro. They envisioned that intercumulus melt would migrate laterally and perhaps vertically into and along locally distributed ductile shear zones. This migrating melt would react with olivine gabbro, precipitate Fe-Ti oxide minerals, and finally solidify after cessation of deformation and thereby transform the olivine gabbro to ferrogabbro (Natland et al., 1991). Further studies of the 1105A core will be conducted to test the viability of such models.

# STRUCTURAL GEOLOGY

## Introduction

Seafloor spreading at slow-spreading centers such as the SWIR (0.8 cm/yr) is accommodated both by adding cross-sectional area to the crust via new magmatic material and by mechanical extension and deformation of the crust. During periods of high magma supply, spreading is probably dominantly accommodated by magmatic processes, whereas when magma supplies are low, spreading is accommodated dominantly by tectonic processes. The gabbroic massif exposed on the Atlantis Bank and drilled at Hole 1105A during Leg 179 formed along the ridge segment at the northern RTI of the Atlantis II Fracture Zone. The ridge segment is likely to have evolved in a magma-starved setting near the termination of the ridge axis at the transform. A large part of the extension was likely to have been accommodated by mechanical

extension. Thus, as gabbroic rocks solidified and cooled in the subaxial environment, fault and ductile shear zones were continuously forming in the new lithosphere as it was created. Subsequently, the gabbroic massif was unroofed and exposed to the seafloor, probably along a low-angle detachment fault at the northern RTI (Dick et al., 1991c) in a manner similar to the one proposed in the tectonic models for the MARK region south of the Kane Fracture Zone (Karson and Dick, 1983; Karson et al., 1987; Karson, 1990). After its initial exposure to the seafloor, the massif was transported to its present position northward along the transverse ridge directly to the east of the Atlantis II Transform during the last 11.5 m.y. (Dick et al., 1991b; Dick, Natland, Miller, et al., 1999). It has likely suffered further deformation by transform-related processes after being transported from the ridge axial environment in which it formed. Oceanic gabbroic rocks, such as those recovered from Hole 1105A, crystallized, compacted, solidified, and cooled over a range of temperatures and in two tectonic regimes (ridge and transform) leading to a variety of both ductile and brittle structures.

Hole 1105A penetrated to a depth of 158.00 m, and the cored interval measured 143 m starting at 15.0 mbsf. Core recovery included 118.43 m of gabbroic rocks for a total recovery of 82.82%. This high recovery provides a rather complete coverage of the rock types and pseudostratigraphy of the gabbroic section cored, as well as a detailed view of the structures in the gabbroic section. The rocks recovered in Hole 1105A record a wide variety of structural styles ranging from brittle to ductile. Each structure or structural interval in the core was logged in the structural geology log (see the **"Appendix"** contents list).

The discussion of structural observations in Hole 1105A proceeds from high- to low-temperature structures because the age progression in the deformational events represents a down-temperature retrograde tectonic history. This history is predicted by evolution of a plutonic assemblage originating in an RTI tectonic setting. Temperatures ranged from magmatic to seafloor temperatures during the massif's evolution and transport to its present position along the Atlantis II Transform Fault, which is about halfway between the two SWIR segments terminating the transform. At the highest temperature end of the spectrum, distinguishing between magmatic and dynamically metamorphosed rocks can be difficult (e.g., Thayer, 1963). In oceanic gabbros, the distinctions between igneous cumulate textures and dynamically recrystallized metamorphic texture are often blurred. This is because the gabbroic rocks solidify and cool in a deforming plate boundary zone, and most display at least some crystal-plastic microstructure. Deformation can initiate in a hypersolidus state before the last remaining liquid has solidified or just after complete solidification, when the rock is near magmatic temperatures (e.g., Cannat, 1991; Cannat et al., 1991). Textures can be annealed considerably and resemble igneous xenomorphic granular textures if cessation of deformation is at high subsolidus temperatures. There is commonly little distinction between the xenomorphic granular texture of many adcumulates and a granulitic gneissic texture when grains are coarse, equant, or polygonal, and these rocks lack strong tectonite foliations, even though the gneisses may have completely recrystallized under dynamic conditions. Another factor that compounds the confusion between magmatic and tectonic textures is that strain is typically localized in small intervals of the gabbro section. Transitions from completely undeformed magmatic textures and tectonite fabrics can occur rapidly at an interval contact or grade more subtly into the shear zone through an entire interval. These tec-

tonic boundaries are not at any regular intervals or spacing (see Fig. F26; "Igneous and Metamorphic Petrology and Geochemistry," p. 29). Lastly, recrystallization and metamorphism in oceanic gabbros are generally retrograde in nature, but if dynamic recrystallization takes place at high temperature near the solidus, the metamorphic mineralogy may be nearly identical to that of the original igneous rock. Generally, however, thin sections provide sufficient microstructural information to distinguish between magmatic and dynamically metamorphosed tectonite textures.

## Magmatic Textures and Fabrics

The majority of gabbroic rocks from Hole 1105A contain fine- to coarse-grained igneous or cumulate textures with random orientation of those primary igneous minerals. They are generally little affected or very weakly affected by crystal-plastic deformation (e.g., see Fig. F53). Some rare pegmatitic gabbros with random orientation textures are also present in the core. These random orientation textures are present even when there are inequant, elongate, or tabular igneous mineral habits, which are prerequisite for forming igneous lamination. Other rocks of gabbroic composition cored in Hole 1105A, however, show a distinct preferred dimensional orientation of those mineral grains that possess shape anisotropy. These preferred orientations can result from (1) crystal-plastic deformation or (2) the orientation of primary minerals above the solidus temperature by self-nucleation phenomenon, crystal accumulation, compaction, or reorientation by magmatic flow. Crystal-plastic and igneous fabrics are distinguished by the shapes and characteristics of the constituent minerals of the gabbroic rocks. The term igneous lamination is reserved for those rocks that show little to no evidence of crystal-plastic strain including distortion, stretching, or flattening of mineral grains, or evidence for grain-size reduction by dynamic recrystallization. In addition, definitive igneous textures or structures must be observed. For example, magmatic twins in plagioclase are readily distinguishable from their deformational tapered counterparts. Likewise, magmatic growth twinning {100} of augite is common in igneous samples and is a criteria for igneous origins because these twins will not form during dynamic recrystallization of pyroxene. Similarly, subhedral and euhedral shapes of plagioclase are common where intergrown subophitically or included as chadocrysts within pyroxene oikocrysts. Plagioclase also tends to display zoned rims that can be readily recognized to be of igneous origin.

The igneous origins of certain laminations or linear-preferred dimensional orientation are clear from the nature of the minerals displaying the fabric. In thin section, the characteristics of some rocks with magmatic laminations or lineations verify that shape-preferred orientation because of igneous processes exists locally in the section. These rocks are devoid or nearly devoid of recrystallization or other crystal-plastic deformation microstructure. For example, a fine-grained gabbroic rock displayed in thin section, Sample 179-1105A-12R-2, 50–53 cm (Figs. F54, F55), shows well-developed igneous lamination defined by the preferred dimensional orientation of tabular plagioclase and elongate pyroxene. There is some deformation twinning in plagioclase locally in the thin section, but most twinning is magmatic with straight margins of the twin plane and sharp blunt ends to each twin. Plagioclase displays distinct albite growth twins in most grains, and subhedral crystal shapes are common (e.g., Fig. F55). Plagioclase also shows core to rim

F53. Example of random orientation of coarse-grained and elongate subhedral plagioclase laths of igneous origin, p. 126.

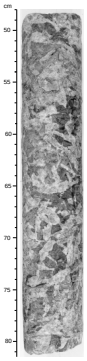

F54. An igneous lamination defined by the preferred dimensional orientation of elongate clinopyroxene and tabular plagioclase, p. 127.

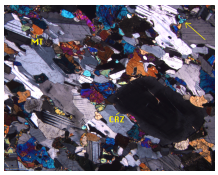

F55. Igneous lamination defined by the preferred dimensional orientation of elongate clinopyroxene and tabular plagioclase, p. 128.

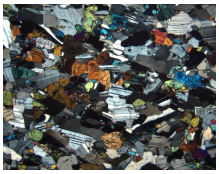

magmatic zoning and sometimes complex zoning (Fig. F54) demonstrating its igneous origin. Pyroxene also commonly shows {100} magmatic twinning parallel to the elongation direction (Fig. F54) and preservation of euhedral to subhedral shapes of included plagioclase (Fig. F56). Overall, the Hole 1105A core lacked significant evidence of magmatically aligned fabrics. Weak foliations of apparent ambiguous origin, which were noted in the VCDs, on further inspection under the microscope, generally consisted of crystal-plastic deformation fabrics. Fine-grained microgabbros tend to show more examples of magmatically aligned fabric when compared to their coarse-grained counterparts.

F56. Preservation of euhedral to subhedral grain shapes of plagioclase included within a clinopyroxene oikocryst, p. 129.

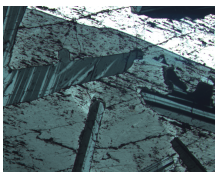

## Igneous Banding, Layers, and Interval Contacts

In general, igneous layers were observed throughout the core. Of 141 intervals defined in the core, ~30% of these display sharp, well-defined contacts. Igneous contacts consist of gradual or abrupt changes in modal mineralogy, modal proportions, grain size, and/or texture, or some combination of these (see "Igneous and Metamorphic Petrology and Geochemistry," p. 29). Other interval boundaries are structural in nature and mark boundaries between undeformed and ductilely deformed rocks. These boundaries can be abrupt with sharp shear-zone contacts between intervals of deformed rocks and intervals of undeformed rocks, or there may be a gradation with progressively increasing intensity of deformation and foliation as the high-strain portion of the shear zone is approached. For example, interval 179-1105A-29R-1, 95–118 cm (displayed in Fig. F57), shows a sharp, sheared contact between a coarse-grained gabbro above and a pegmatitic gabbro below. The contact is marked by a narrow ductile shear zone. On a smaller scale, igneous banding is present and consists of thin layers or bands that differ in lithology, modal proportions, grain size, and/or texture. All of these are less than several centimeters in thickness. Opaque-oxide mineral banding (discontinuous planar zones of oxide concentration) is the most common manifestation of banding and seems to reflect, in some cases, incursions of melts and their crystallization products into pre-existing cumulate gabbros with significant residual porosity. The orientation of oxide bands can locally lack consistency in the section, and the banding typically has irregular margins (e.g., see Fig. F58). It should be noted that, except for igneous contacts with felsic to leucocratic gabbro veins (see below), there are no igneous bands, layer, or interval contacts in which an intrusive contact with the adjacent gabbroic rock is clearly demonstrated. Lastly, the Formation MicroScanner (FMS) logs (see "Downhole Logging," p. 60) supports observations made in the core that the gabbroic section is strongly layered throughout and on a scale that ranges from meters to centimeters. FMS data also show, as in the core, that igneous layers have a significant range of dips (0°–75°), similar to dipping layers noted in ophiolite complexes (e.g., Casey and Karson, 1981).

F57. Ductile shear zone at a dipping contact between a coarse-grained gabbro and a pegmatitic gabbro, p. 130.

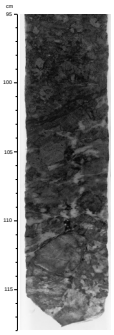

F58. Dipping oxide-mineral–rich band (interval ~66–71 cm) with up to 25%–30% opaque oxide minerals, p. 131.

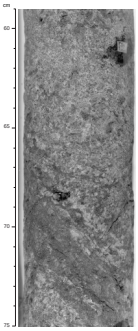

## Transitional Magmatic-Tectonite Textures

Most of the samples with igneous textures in Hole 1105A core are not completely free of at least some minor crystal-plastic deformation. Most commonly, deformation is restricted to mechanical plagioclase twins that are typically tapered and pinch out, undulose extinction of plagioclase, and some development of subgrain boundaries. Olivine is

also mildly strained and commonly kinked. Clinopyroxene tends to be undeformed in mildly strained rocks and retains obvious igneous textures. Plagioclase included within pyroxene is generally shielded from deformation typical of nonincluded plagioclase. The transition from igneous textures to crystal-plastic textures and fabrics is most commonly marked with the first appearance of thin bands (two to three grains thick) of plagioclase neoblasts along grain boundaries or subgrain boundaries (Fig. F59), abundant mechanical twinning of plagioclase, kinking, subgrain formation and rotation in olivine and plagioclase, and the appearance of serrated grain boundaries. These rocks, however, preserve much of their original igneous texture.

F59. Recrystallization of plagioclase neoblasts along subgrain boundaries in large plagioclase, p. 132.

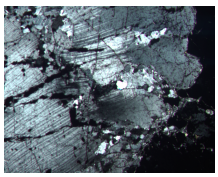

## High-Temperature Crystal-Plastic Fabrics

### *Equigranular Gneissic Textures*

Penetrative grain-size reduction in which all phases have undergone dynamic recrystallization to produce a finer grained, nearly equigranular gneissic mosaic texture with less than 0%–10% porphyroclasts is present locally in the section cored in Hole 1105A. This type of texture may be the highest temperature, lowest stress crystal-plastic textural type present because it implies a lack of significant ductility contrast between clinopyroxene, olivine, and plagioclase. The coarseness of the dynamically recrystallized plagioclase, olivine, and clinopyroxene implies higher temperature and lower stress conditions than porphyroclastic metagabbros with finer grain sizes. Each of the phases in the rock is dynamically recrystallized. The grain size of the recrystallization (average 0.75 mm) is not as fine as porphyroclastic rocks, and localization of grain-size reduction has not been as severe. The photomicrograph in Figure F60 of thin section 179-1055A-30R-2, 109–113 cm, shows an example of even dispersion of grain sizes in a dynamically recrystallized, fine-grained, gneissic gabbroic rock. The sample shows highly strained plagioclase (complex undulose extinction and subgrain structure) and moderately well-developed shape-preferred orientation. The fabric is defined by the preferred dimensional orientation of both plagioclase and clinopyroxene. Elongate aggregates of clinopyroxene and plagioclase also help to define the foliation.

F60. Even dispersion of grain sizes in a dynamically recrystallized fine-grained gneissic gabbroic rock, p. 133.

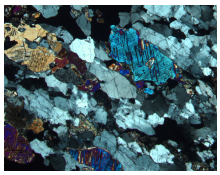

### *Porphyroclastic Textures and Fabrics*

Nonpenetrative grain-size reduction of minerals by dynamic recrystallization results in a strongly bimodal grain-size distribution. Grain-size reduction is present along anastomosing high-strain zones that outline porphyroclastic remnants of the original igneous rock. Porphyroclastic fabrics are defined by shape-preferred dimensional orientation of flattened and/or elongated pyroxene, olivine, or plagioclase porphyroclasts (e.g, see Fig. F61). Textures are characterized by bimodal grain sizes with finer grained polygonal neoblasts that often show less strain than porphyroclasts of the same phase. Grain-size reduction varies across individual shear zones and becomes more pronounced toward the center of the shear zone where the strain is the highest. Some highly localized deformation bands in the porphyroclastic rocks show extreme grain-size reduction (mylonitic bands). Porphyroclastic textures are present locally in much of the core, but appear to be more prevalent in the lower portion of the core (from below 90 mbsf). Examples of porphyroclastic textures are present in Sections 179-1105A-5R-1, 7R-1, 7R-2, 8R-1, 12R-1, 16R-1, 16R-2, 22R-1, 23R-1, 25R-1, 25R-3, 30R-1, and 30R-2. Where the minerals defining the fabric have elongated

F61. Strong crystal-plastic porphyroclastic foliation inclined ~30° in meta-oxide gabbros, p. 134.

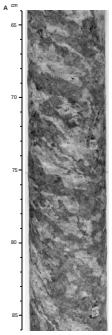

anhedral shapes with evidence of stretching and the development of asymmetric recrystallized tails, the structure is interpreted to be a crystal-plastic fabric. In core from Hole 1105A, porphyroclastic phases show different extents of crystal-plastic behavior. For example, plagioclase tends to be the most highly strained phase and one of the first to recrystallize to fine-grained neoblasts; olivine subsequently recrystallizes and finally, pyroxene. Pyroxene, which is rheologically the strongest of the three primary minerals under ductile conditions, may show little sign of deformation microstructure even though plagioclase and olivine are internally strained and/or dynamically recrystallized to fine-grained neoblasts. Largely strain-free pyroxene porphyroclasts commonly preserve chadocrysts or inclusions of euhedral to subhedral plagioclase, whereas the nonincluded plagioclase in the same rock has completely recrystallized under dynamic conditions (Figs. **F62, F63**). Pyroxene tends not to show significant strain when included in a matrix of opaque oxides, presumably because the oxides take up most of the strain as the weakest of all phases. In higher strain facies where clinopyroxene exceeds 50% of the rock, it does show higher strain and dynamic recrystallization, commonly in the form of mantles or asymmetric tails around the porphyroclasts. Most porphyroclastic clinopyroxenes are partially replaced by postkinematic patches of brown amphibole, indicating that some of the dynamic recrystallization ceased prior to alteration temperature ranging from 700°–900°C (Spear, 1981).

Because of the localized nature of the porphyroclastic textures, it is likely that most have formed along discrete ductile high-strain zones. A number of examples exist in the core in which porphyroclastic textures grade to porphyroclastic mylonite and to ultramylonite toward the center of a discrete shear zone where strains are high. Decimeter-thick mylonite zones with high oxide-mineral content were also observed in the core from ~53 and 71 mbsf (e.g., see Fig. **F64**). Other mylonites were observed on thin-section scales as discrete high-strain zones within porphyroclastic rocks and were generally marked by very fine-grained neoblast sizes (<0.03–0.01 mm). In general all of the porphyroclast phases are internally strained, bent, or kinked and may contain subgrains or intracrystalline fractures in the mylonites. Pyroxene, the strongest phase, is also generally affected by internal strain. In some shear zones, the crystal-plastic fabric shows a gradually changing orientation of the foliation away from the center of the shear zone, defining classic Ramsay-Ghram ductile shear-zone geometries. Shear criteria all yield normal displacement along inclined shear zones where measurements were possible.

## High-Stress Crystal Plastic Deformation and Strain Localization

As temperature decreased, ductile shear became more localized into narrower shear zones, some of which are on thin-section scales. Grain-size reduction is more pronounced, and coarse porphyroclastic textures give way to porphyroclastic mylonites, mylonites, and ultramylonites along narrow bands as the grain-size reduction becomes more pronounced (see Fig. **F64**). Porphyroclasts are more strongly deformed, and dynamic recrystallization is accompanied by the formation of microcracks (e.g., see Fig. **F65**). Plagioclase porphyroclasts tend to form elongate ribbons in the neoblastic matrix (Fig. **F66**). Olivine porphyroclasts tend to recrystallize to polygonal neoblasts, and clinopyroxene is

F62. Porphyroclastic oxide gabbro with two large clinopyroxene porphyroclasts, p. 137.

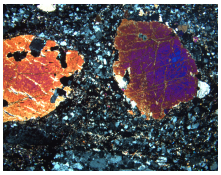

F63. Olivine and clinopyroxene porphyroclasts within a matrix of recrystallized plagioclase, p. 138.

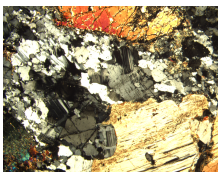

F64. Porphyroclastic oxide-bearing mylonites showing felsic layering. p. 139.

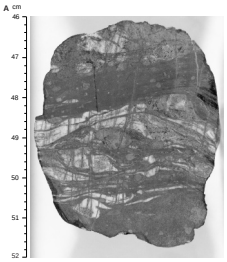

F65. Oxide-rich mylonite domain in contact with coarser porphyroclastic domain, p. 141.

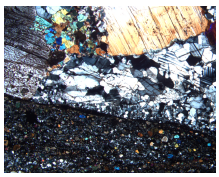

F66. Highly strained ribbon grains of plagioclase in mylonitic fine-grained matrix, p. 142.

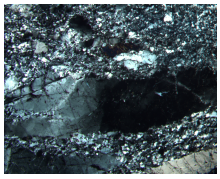

recrystallized as asymmetric tails or mantles around porphyroclasts (Fig. F67).

Oxide gabbros or oxide-bearing gabbros appear to localize strain on both a small and large scale. Good examples of strain localization occur at several interval boundaries throughout the core. For example, Section 179-1105A-25R-3 (Fig. F68) displays a contact between oxide gabbro and olivine gabbro. The oxide gabbro is generally dynamically recrystallized and possesses a porphyroclastic texture, but it also contains mylonitic bands. The olivine gabbro displays an igneous texture, but, immediately at the contact between olivine gabbro and oxide gabbro, rocks are affected by ductile deformation where oxides minerals are present.

In one of the oxide-rich mylonite zones, foliated oxide-free gabbro residing adjacent to undeformed gabbro has a porphyroclastic texture with strongly bimodal grain sizes. Clinopyroxene forms the major porphyroclastic phases, and plagioclase is dynamically recrystallized to finer neoblasts. An oxide band appears to localize mylonitic deformation as can bee seen in thin section (Fig. F69). Clinopyroxene porphyroclasts within the oxide-mineral matrix appear to be little strained, and this may indicate a high ductility contrast between the opaque oxides and the pyroxene, effectively shielding undeformed pyroxene porphyroclasts. Microfractures oriented at 35°–40° to the shear zone margins appear to be Riedel shears (Fig. F65). The effect of a migrating oxide-rich melt into the shear zone may be to localize the strain in the rheologically weak oxide-mineral–bearing regions. The fact that the host rock seems to be oxide free and deformed to a lesser extent than the oxide-rich region across an abrupt boundary may indicate that the oxide-rich melt invaded or infiltrated the shear zone after deformation was initiated. Once solidified, the oxide-mineral–rich intervals acted to localize deformation as the rheologically weakest part of the rock and focused ductile deformation, whereas the adjacent plagioclase had entered into the domain of brittle-ductile behavior (e.g., Riedel shears). Alternatively, as temperatures dropped and plagioclase and clinopyroxene increased in ductile strength, a contrasting and pre-existing oxide-rich zone localized strain to the rheologically weakest part of the rock.

Experimental data on the lower temperature ductility of opaque oxides supports the notion that opaque oxides will represent zones of strain localization during high to moderate temperature deformation. Whether the late-stage oxide-rich melts and their infiltration into gabbroic rocks initiated deformation or the solidified cumulus oxide minerals in the cumulates simply localized the strain in the weakest rheology as deformation proceeded is unknown. Given that oxides are likely to be ductile at lower temperatures than clinopyroxene, olivine, and plagioclase (Agar and Lloyd, 1997), it is unlikely that the distinction between hypersolidus or subsolidus initiation of the deformation can be assessed by microstructure. The deformation proceeds to the solid state and obliterates any evidence of hypersolidus deformation.

## Brittle Structures

The two classes of brittle structures recognized are (1) magmatic veins (MV) and (2) faults and fractures (F) and vein-filled fractures (AV). Each of these structures is indicated on the hard-rock VCDs.

F67. Clinopyroxene porphyroclast with asymmetric tails in mylonite, p. 143.

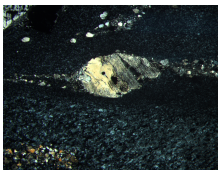

F68. Contact between intervals 115 and 116 showing mildly deformed gabbro adjacent to a strongly foliated oxide gabbro shear zone, p. 144.

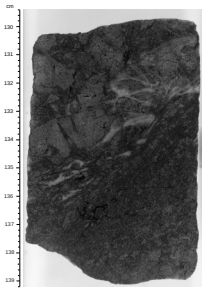

F69. Oxide-rich mylonitic domain with relatively strain-free small clinopyroxene porphyroclasts, p. 145.

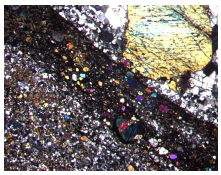

## Magmatic Veins

Brittle magmatic deformation is represented by the intrusion of veins of felsic compositions on a variety of scales. Veins range from 1 mm to ~3 cm in width. Their composition ranges from leucogabbro with assemblages of plagioclase + clinopyroxene ± brown hornblende to trondhjemite. The more silicic end-members are more common. Although numerous in some sections of the core (e.g., Sections 179-1105A-1R-1 to 1R-5, 6R-2 and 6R-3, 9R-1, 10R-1, and 27R-1 to 27R-4), they are volumetrically a small fraction of the total recovery. The downhole presence of veins are plotted in Figure F26 (see "Igneous and Metamorphic Petrology and Geochemistry," p. 29). Most veins are not affected by ductile deformation, especially the most felsic veins. However, there are some leucocratic gabbro veins that appear to have been affected by ductile deformation shortly after intrusion (Fig. F70). The strain appears localized in the vein and not in the country rock into which it intrudes. The clearest example is in Sample 179-1105A-4R1, 77–85 cm, in which crystal-plastic fabrics are oriented such that the foliation plane is parallel to the vein's margins. Veins have a range of orientations from near vertical to horizontal.

F70. Deformed leucocratic gabbro vein intruded into relatively undeformed gabbro, p. 146.

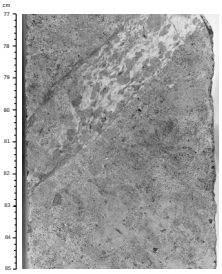

## Fractures and Alteration Veins

Most joints and fractures are filled by vein minerals along fracture walls, and they are logged in the Structural Geology spreadsheet as alteration veins and marked as AV on the core barrel sheets. There is significant variation in the density of veins throughout the section, but, in general, they tend to be scarcer in penetratively deformed sections of the gabbro (e.g., Sections 179-1105A-25R-1, 29R-1, and 30R-2,) and where the grain sizes are very coarse in undeformed gabbro (Sections 179-1105A-28R-1 and 4). Most of the veins observed are planar; however, curviplanar and irregular fractures were also observed. The majority of the planar fractures are characterized by actinolite and/or chlorite vein-fill mineral assemblages. These higher temperature veins have average dips of ~35°, but their dips range from 0°–80°. Most of the vein fill has extensional characteristics, but several veins displayed slickenfibers in the true-dip direction of the vein. The remainder of the veins also have variable dips and contain either higher temperature brown amphibole or lower temperature altered calc-silicate, carbonate, and smectite-zeolite.

In regions where smectite-calcite veins are in the core, the veins tend to be highly irregular, clustered, and wide (up to 0.4 cm), and the rocks appear altered and oxidized. Pieces 3, 4, and 5 of Section 179-1105A-21R-1 (~111 mbsf) and Pieces 1 and 2 of Section 26R-2 (~135–136 mbsf) were characterized by this type of alteration (Fig. F71A). Calcite veins were commonly partially open or consisted of calcite with well-developed crystal terminations grown into open vugs in veins (Fig. F71C). This evidence indicates that there may be active fluid flow through these fracture systems, and they may be associated with or found in the vicinity of active or recently active fault or fracture systems. Supporting this evidence of open subsurface fracture systems and currently active hydrological systems are temperature anomalies discovered in the borehole during logging at depths of ~104–105 and 135–136 mbsf, at or near the altered core regions. Although irregular in shape, these fractures are steeply dipping. This orientation may indicate that the deformation is transform related. Likewise, an open vertical fracture system

F71. Smectite-clay veins within fractures in oxidized core facies, p. 147.

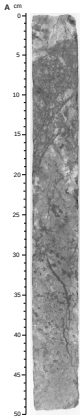

was observed in Section 179-1105A-16R-2 (~92 mbsf), where a subvertical fracture was imaged with FMS and a temperature anomaly was found during downhole logging (see "Downhole Logging," p. 60). These brittle structures appear to represent the latest features in the structural evolutionary scheme.

## Implications of Magnetic Data for Low-Temperature Structural Evolution

Preliminary magnetic data indicates that the core possesses a single coherent direction with an average inclination of ~69°. This value is uncorrected for borehole deviation measured at 3°. This is compared with an inclination of –52° expected for the site, significantly below the observed inclination. The difference of ~17° is larger than the discrepancy predicted by secular variation and plate movement in the last 11.5 m.y. As in Hole 735B paleomagnetic data, these results indicate a consistently reversed polarity for the section and may indicate a significant block rotation (~17°) of the gabbroic massif. The reversed polarity and proposed block rotation is strikingly similar to the block rotation of ~18° shown for Hole 735B gabbroic rocks (Pariso et al., 1991). The consistency of the magnetic inclination downhole suggests that any relative internal rotations along ductile shear zone in the section must have occurred before cooling below the blocking temperature for magnetite (~580°C) and are necessarily high temperature in origin. This is consistent with microstructural observations. In addition, gabbroic rocks from Holes 735B and 1105A have undergone approximately the same rotation after magnetic acquisition with little evidence of internal relative block rotation within the massif. This rotation is likely to have occurred during or after unroofing of the massif on the rift valley walls at the inner corner of the northern RTI and during the massif's subsequent transport along the transform. The steepening of the inclination would suggest a clockwise rotation along a low-angle normal detachment fault at the inner corner of the RTI (Fig. F72). This rotation is consistent with a low-angle normal fault detachment model for unroofing and exposure of the gabbroic massif at the seafloor.

F72. Schematic model of unroofing and exposure of the Atlantis Bank with tectonic rotation and steepening of magnetic inclination, p. 150.

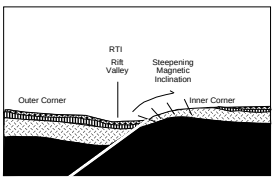


## Summary

The structure of the Hole 1105A core is complex, and structural styles and intensities range from ductile to brittle. Most of the gabbroic samples cored possess igneous textures, but several intervals of the core display crystal-plastic fabrics, and most samples display at least some crystal-plastic microstructure. Mylonitic zones with minimum thicknesses of 30 cm and characterized by high oxide-mineral content were observed at ~53 and 71 mbsf. Centimeter- to decimeter-thick zones of ductile shear that are coarser grained with porphyroclastic textures are restricted to the upper 90 m of core, whereas thicker zones (>1 m) of ductile deformation zones with weak to strong crystal-plastic fabrics become more prevalent at depths >90 mbsf. Some intervals of penetrative ductile deformation in the lower portion of the core exceed 2 m in thickness. Zones of ductile deformation are commonly oxide rich, as are the contact regions between undeformed and ductilely deformed gabbroic rocks, as if oxides lined the outer margins of ductile shear zones. Oxide gabbro-rich zones tend to be strain localizers based on the fact that many, but not all, of the crystal-plastic shear zones are rich in oxide minerals. Inclinations of the ductile foliations measured on the

core face vary from ~18° to 75° in the cored intervals and average ~30°–35°. Thin sections show a range of textures from strictly igneous to slightly deformed igneous, to dynamically recrystallized metamorphic textures with crystal-plastic fabrics. As deformation intensity increases, the effect can be most easily observed in plagioclase, where there is a progression from strain-free plagioclase, to plagioclase with deformation twins, undulose extinction, and kink bands, to dynamically recrystallized grains. Minor recrystallization of neoblasts along grain margins progresses to porphyroclastic textures with bimodal grain sizes and small neoblasts of plagioclase and highly strained and kinked plagioclase, pyroxene, or olivine porphyroclasts. Olivine is also likely to have recrystallized to neoblast grain sizes prior to pyroxene, which tends to be preserved as the dominant porphyroclastic phase unless the intensity of deformation is most severe.

Brittle fractures are generally filled with vein material such as actinolite and chlorite, but no large faults zones were recovered in the core. Smectite and calcite alteration veins are associated with oxidized gabbroic zones that may represent recently active fracture systems. Based on temperature, sonic, resistivity, and porosity logs, these fractures observed in the core may be associated with active shallow hydrological systems along the transform margin. There are several regions of low recovery, which could correspond to fault or fracture zones based on logging data.

Rotations associated with ductile shear zones within the section occurred before magnetic acquisition in the samples. However, magnetic measurements indicate that a late rotation of the gabbroic massif occurred at temperatures below ~580°C. This rotation is consistent with that determined at Hole 735B, indicating both sites show coherent behavior.

# PHYSICAL PROPERTIES

## Introduction

The study of the physical properties of gabbroic rocks from Hole 1105A is of significant value in understanding the evolutionary history of the Atlantis II Fracture Zone and in assessing the relative contributions of magmatic and tectonic processes to crustal evolution. Advantages of drilling along the Atlantis II Fracture Zone are that the geologic and tectonic frameworks are well established, previous drilling has been highly successful, and the water depth is shallow. Drilling operations during Leg 179 at Site 1105 were done in a water depth of ~695 m on a wave-cut platform devoid of the basaltic and diabasic carapace typical of a generic model of ocean crustal stratigraphy. Routine onboard measurements of physical properties included whole-core magnetic susceptibility, split-core magnetic intensity, inclination, and declination, as well as index properties on discrete minicore samples. These data can be examined as a function of lithology and alteration and can aid in the identification of boundaries between lithologies.

The physical properties of gabbroic rocks provide constraints for crustal model studies based on geophysical data. Measurements of the magnetic properties of these rocks are necessary to assess the contribution of lower crustal rocks to observed magnetic anomaly patterns, which form the basis of the universally accepted theory of plate tectonics advanced by Vine and Mathews (1963). Although many studies have

apportioned the primary source of these anomalies to the upper crustal extrusive basalts in the generic ocean crust model (e.g., Le Pichon and Heirtzler, 1968; Mckenzie and Sclater, 1971; Klitgord et al., 1975; and Patriat and Achache, 1984), recent paleomagnetic studies suggest that gabbroic rocks may provide a significant contribution to the magnetic anomaly signature (Kikawa and Pariso, 1991; Pariso et al., 1991).

## Magnetic Susceptibility

Continuous rock magnetic susceptibility measurements of 118 m of whole core were completed using the Bartington magnetic susceptibility meter with an 80-mm loop sensor. Measurements were made at 2-cm intervals. Several idiosyncrasies inherent in the data set archived in the JANUS database should be noted. First, the susceptibility meter saturates at values >10,000 SI. As a result, a value of 12,500 SI will show up in the database as 2,500 SI. Figure **F73** shows a continuous record of magnetic susceptibility measurements for the entire section cored at Hole 1105A. A simple filter, which removes anomalously low values on either side of values approaching the saturation limit of measurement, has been applied to the data in this plot. Additionally, measurements for Core 179-1105A-3R, 28.70–32.42 mbsf, are not included in the database because it was initially curated incorrectly, and the whole core was run through the MST with pieces out of order. However, using off-line reapportioning of the measurements, these data were reintegrated into data files used for additional processing (see Table AT4.XLS in the **"Appendix"** contents list).

It should be noted that the magnetic susceptibility measurements as recorded in the database have not been volume normalized. Most hard-rock cores (including all recovered during Leg 179) have an average radius of <58 mm and have irregular shapes and sizes. Additionally, the sphere of influence of the susceptibility loop is on the order of 10 cm. Therefore any measurement on a piece <10 cm long or at a location <5 cm away from the end of a piece will necessarily have a greater error than measurements on the central parts of continuous large pieces of core. Figure **F74** shows the whole-core magnetic susceptibility data after filtering for piece length. These data have been smoothed using a weighted moving average (dashed line).

As expected, the magnetic susceptibility data shows a marked correlation to macroscopic descriptions of the core. Intervals identified with abundant Fe-Ti oxide minerals in hand sample show a one-to-one correspondence with increased magnetic susceptibility. As an added benefit, using the magnetic susceptibility data as a proxy for oxide-mineral abundance, hence as an indicator of change in modal mineralogy, we can correlate and even refine locations of interval and unit boundaries in the core. The interval boundaries in the graphic lithology column on Figure **F74** were established based on petrographic criteria. The same interval boundaries are marked by a sharp increase or decrease in the magnetic susceptibility profile. An example of the utility of the magnetic susceptibility data is reflected in the position of the Subunit IIA/IIB boundary. From petrologic criteria, the boundary between these two subunits is gradational, marked by a gradual grain-size change and a gradual decrease in reported abundance of oxide minerals. However, in the magnetic susceptibility profile, there is a sharp decrease in the value of the core at 92.79 mbsf. This exact location in the core is described as the uppermost contact of a downward succession from gabbro, to olivine gabbro, to oxide-bearing olivine gabbro, to oxide olivine gabbro.

F73. Whole-core magnetic susceptibility measurements, **p. 151.**

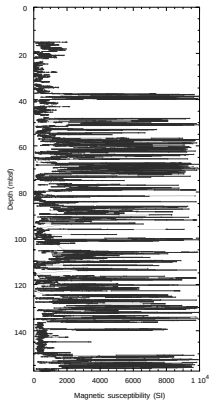


F74. Filtered whole-core magnetic susceptibility measurements, **p. 152.**

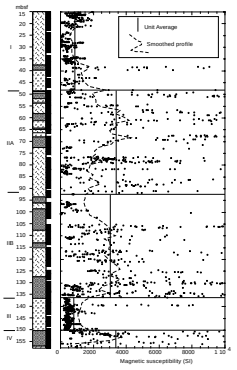

## Natural Remanent Magnetism

After splitting the cores, the archive section was passed through the shipboard cryogenic magnetometer. Continuous natural remanent magnetization (NRM) intensities, inclination, and declination were measured at 2-cm intervals. As with the whole-core data, some caution should be exercised in application of the split-core measurements. The response function of the superconducting quantum interface device (SQUID) sensors is subject to similar edge effects as the magnetic susceptibility loop. For these measurements, non-oriented pieces <10-cm long were removed from the archive half before measurement of NRM. The data have not, however, been filtered for the effects of piece ends or the gaps between pieces. Additionally, recent work on gabbroic rocks from the Atlantis II Fracture Zone (J. Gee, pers. comm., 1998) indicates the 20-mT demagnetization is insufficient to remove the drilling-induced radially oriented magnetic overprint. Table AT5.XLS (see the **"Appendix"** contents list) is a compilation of the NRM data from split-core measurements. Note that the only filtering applied to these data is removal of overlaps from cores with >100% curated recovery. Figure **F75** shows the relationship between declination, inclination, and intensity with depth. As with measurements from Leg 118 (Hole 735B), inclinations are mostly positive and steep. The small number of negative inclinations is almost certainly caused by unoriented pieces or small pieces, which were inadvertently flipped upside down. The simple arithmetic average of inclination values after 20-mT demagnetization is 67.4° (±19.8°), comparable to the 65° (±7°) calculated from shipboard data during Leg 118 (Robinson, Von Herzen, et al., 1989). The theoretical inclination of the site at 33°S is –52°, and the age of the oceanic crust is 11.75 Ma (magnetic Chron 5 $-r_{2n}$; Dick et al., 1991c). The observed inclinations are reverse in accordance with Chron 5, but steeper than the theoretical value. For a discussion of the steepening inclinations see **"Structural Geology,"** p. 48. Declination data should be examined with caution because the true azimuth of the cores is not fixed.

F75. Split-core measurements of natural remanent magnetization showing downhole variation in declination, inclination, and intensity, **p. 153.**

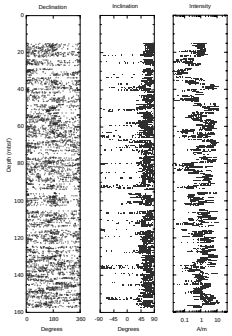


## Velocity Measurements

Compressional wave velocities ($V_p$) at ambient pressure and temperature were measured on 62 minicores from the Hole 1105A core. The measured velocities (see Table AT6 in the **"Appendix"** contents list) averaged 6.64 km/s and are comparable to the values for gabbroic rocks measured during Leg 118 (Shipboard Scientific Party, 1989) and are representative of seismic Layer 3. Figure **F76** shows the velocities measured relative to depth for the entire section sampled during Leg 179. The four major lithologies identified by macroscopic core description are all represented in the sample suite and have slightly different average $V_p$. Rocks characterized as gabbro and olivine gabbro have similar average $V_p$ (6.74 ± 0.04 and 6.70 ± 0.07 km/s, respectively). The amount of olivine is quite variable in these lithologies, although commonly 10% or less, and we would expect that because the plagioclase and clinopyroxene modal proportions are much higher and relatively constant that there is no significant variation in the $V_p$ of these lithologies. In contrast, the oxide gabbro and oxide olivine gabbro samples have markedly lower $V_p$ values (6.53 ± 0.76 and 6.59 ± 0.07 km/s, respectively). The lower velocity values can be attributed to the abundance of Fe-Ti oxide

F76. $V_p$ plotted as a function of depth for samples from Hole 1105A, **p. 154.**

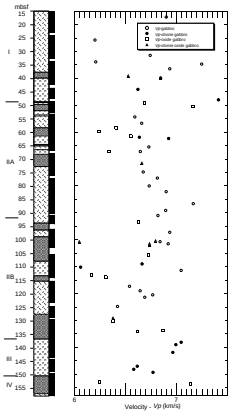

minerals, and the higher variability of values from the oxide gabbros is likely caused by the highly variable degree of alteration and variation in modal oxide abundance in these samples.

### Index Properties

Mass and volumetric measurements were made on 56 minicores representative of the various lithologies sampled from Hole 1105A (see Table AT7 in the "Appendix" contents list). The mean bulk density of all samples is 2.93 ± 0.15 g/cm. This compares with a mean bulk density of 2.97 ± 0.12 g/cm for samples from Leg 118. The mean porosity of the Leg 179 gabbroic rocks is 1.05 ± 0.49%, which is somewhat higher than the average porosity of samples from Leg 118 (0.64 ± 0.73%, Shipboard Scientific Party, 1989).

## DOWNHOLE LOGGING

### Operations

After reaching a depth of 158 mbsf on 9 May, preparations for logging began immediately (Table T16). The hole was conditioned and filled with freshwater gel mud with a density of 8.8 lb/gal, then the bit was released at the bottom of the hole. The pipe was pulled to 35.7 mbsf, and four tool strings were deployed on 10 May. The first tool string deployed was the sonic digital tool (SDT), dual induction tool (DIT), natural gamma-ray tool (NGT), and the temperature-logging tool (TLT). The second logging run consisted of the Formation MicroScanner (FMS) and NGT. The third tool string contained the hostile lithodensity sonde (HLDS), accelerator porosity sonde (APS), and the hostile natural gamma sonde (HNGS). The fourth and final tool string consisted of the borehole compensated sonic (BHC) and NGT. During each logging run, the wireline heave compensator (WHC) was turned on following the exit from pipe and used continuously while the tool strings were in open hole. Additionally, the drill pipe was pulled to a depth of 19.9 mbsf before tool string reentry into pipe during each run. Following data acquisition, log data was transmitted to the Lamont-Doherty Earth Observatory (LDEO) for depth and environmental correction processing and returned to the ship for use in this site chapter report.

T16. Operations summary for Hole 1105A, p. 183.

#### First Run: NGT-SDT-DIT-TLT

The tool string was assembled and lowered through the drill pipe at 10,000 ft/hr until the seafloor was reached at 714 mbrf. Following a 2-min interval of temperature tool equilibration, the tool string was lowered through the end of the drill pipe. The tool string was lowered to the total depth (TD) of 157 mbsf without difficulty and then pulled upward at a constant rate of 1800 ft/hr. During the first pass, the DIT and NGT yielded good data, whereas the SDT produced noisy data likely resulting from the excessive energy generated as the tool slid on the hard formation. In an attempt to improve the SDT signal, a second pass was made with the digital transmitter turned off and only the analog transmitter firing. The tool string was lowered to TD, logged upward to the seafloor depth, pulled from the hole, and dissembled. The SDT results were not improved during the second pass.

### Second Run: NGT-FMS

The NGT and FMS tool string was assembled and at the bottom of the hole in <3 hr after logging operations began. The tool string was pulled to the surface at the logging speed of 900 ft/hr for the first pass and 1800 ft/hr for the second pass. Maximum FMS gain settings of three were selected in anticipation of extremely resistive rocks. It was evident during both passes that excellent data were being acquired as many boundaries, fractures, and borehole features were clearly imaged. Furthermore, the logging speed of 1800 ft/hr did not have any affect on the FMS data, although the NGT data resolution may have been slightly degraded. Following the conclusion of the second pass, the tool string was pulled to the surface and disassembled.

### Third Run: HNGS-APS-HLDS

The gamma, porosity, and density tool string was run in the hole to TD and pulled upward at 900 and 1800 ft/hr during the first and second runs. During the first run, the gamma and porosity data appeared to be good, but the HLDS developed an intermittent data writing error. To correct the problem, the tool was lowered to the bottom of the hole, and a second pass was started with the APS powered down and a new surface telemetry control panel installed. The density tool response was normal for the duration of the logging run and good data were acquired.

### Fourth Run: NGT-BHC

A fourth run was attempted as a result of additional rig time becoming available. The BHC and NGT tool string was selected to acquire additional sonic data in light of the poor sonic data acquired by the SDT during run 1. One pass was made with the tool string from 157.6 to 11.3 mbsf and logged upward at 1200 ft/hr. Log data appeared to be of good quality during data acquisition. The high frequency noise and cycle skipping observed in the SDT measurement during run 1 were absent.

## Borehole Condition and Log Data Quality

A selection of logs acquired during Leg 179 is presented in Figures **F77, F78,** and **F79.** Their uppermost limit corresponds to the pipe depth and is indicated by the dashed horizontal line. Their lowermost limit represents the deepest depth achieved by the various tools (Fig. **F13,** p. 42, in the "Explanatory Notes" chapter). The diameter of Hole 1105A, as measured by the HLDS mechanical caliper (LCAL log, Fig. **F77**), varies between 10.0 and 14.2 in, with the largest diameters at 82.4 and 99.8 mbsf. The two caliper logs from the FMS illustrate two orthogonal dimensions of the borehole with depth. At 40.4, 80.6, and 98.6 mbsf, the borehole appears to be slightly elliptical in cross section with the difference between the two orthogonal measurements (logs C1 and C2) remaining under 1.6 in.

A general purpose inclinometry tool (GPIT) is routinely deployed with the FMS to provide accurate positioning of the string and to allow subsequent depth and azimuthal corrections on the acquired data. The GPIT utilizes a three-axis inclinometer and a three-axis magnetometer for the orientation and acceleration measurements. The borehole verti-

F77. Downhole logs for Hole 1105A, p. 155.

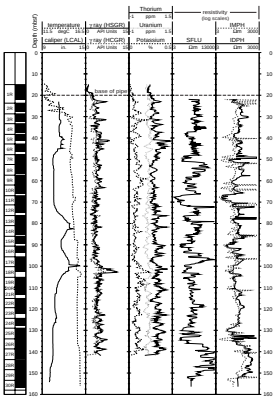

F78. Downhole logs for Hole 1105A, p. 156.

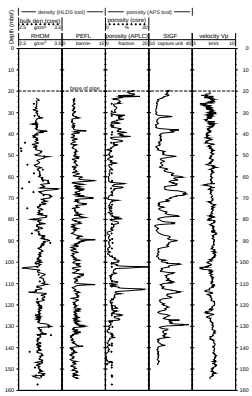

F79. Downhole logs for Hole 1105A, p. 157.

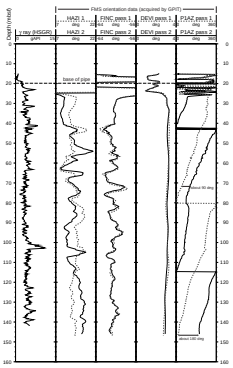

cal deviation, as measured by the GPIT, remains under 3.5° (DEVI, Fig. F79), and the absolute value of the magnetic field inclination fluctuates between 57.7° and 63.3° with a mean value of 60.6°. The field intensity is 0.37 A/m. Unlike the vertical hole deviation and magnetic field inclination curves, the hole azimuth logs (HAZI) do not overlap because both the acceleration and the magnetic field are used for the computation. HAZI fluctuates between N7E and N21E. The abundance of magnetic minerals in Hole 1105A likely has an influence on the azimuth measurements obtained with the GPIT magnetometer. Acute variations in the HAZI log correlate with small azimuthal shifts of the FMS image (<3°) and are within intervals <0.5 m long. However, considered on a 2-m scale and larger, the FMS orientation remains nearly constant and does not appear significantly affected by layers containing magnetite. Locally high abundances of magnetite induce only a slight fluctuation in the orientation of the local magnetic field, and the effect on the FMS pad orientation is likely to be limited. At this time, it is not possible to certify that the tool maintained true north as its reference when entering the borehole. Additional studies will be made postcruise to determine the true extent of mineralogic influence on the FMS azimuthal reference.

## Electrical Resistivity Measurements

Electrical resistivity measurements and images were obtained with the DIT and FMS, which record three different electrical logs and one type of formation image. The shallow (SFLU), medium (IMPH), and deep (IDPH) measurements given by the DIT are the only quantitative assessments of the formation's resistivity. Resistivities exhibit saturation where formation resistivity values are >1950 Ωm for IMPH and IDPH, and >9700 Ωm for SFLU. Minimum values for SFLU, IMPH, and IDPH are 4.1, 5.4, and 7.6 Ωm, respectively. Further deconvolution was performed by the Schlumberger engineer to enhance the logs' quality and vertical resolution. This additional phasor processing did not improve the abrupt variations and apparent saturation of the logs. Because the DIT was intended for use in lower resistivity rocks, the logs for this tool should be used with caution.

The quality of the FMS images from both passes is very good. As suggested, flushing the hole with resistive fresh water mud yielded an improved FMS response compared to the one observed during Leg 176 logging operations. The poor quality FMS images acquired during Leg 176 were attributed to the excessive resistivity contrast between the borehole fluid and the resistive rocks. If the resistivity contrast between the formations and the mud is too large, the FMS current will tend to flow into the borehole fluid rather than into the formation. Some vertical streaking in the FMS image occasionally is present at certain depths (e.g., pads 2 and 3 at 87 mbsf or pads 1 through 3 at 68 mbsf). This may be caused by mild fouling of some buttons by sticking mud. Additionally, a preferential path followed by the FMS appears to guide the pads. Below 83 mbsf, pad 1 of the second pass overlaps the measurement recorded by pad 3 of the first pass exactly. Then, between 80 and 83 mbsf, the FMS (second pass) rotated 90° clockwise (the caliper shows an increase of the diameter at this depth). Above 80 mbsf, pad 1 of the second pass overlaps the measurement recorded by pad 4 of the first pass (Fig. F79, track 5). Also note that the azimuth reference kept by the tool between 80 and 85 mbsf is the same within a few degrees (HAZI 1 and

HAZI 2 logs). This reference azimuth should not be confused with the rotation of the tool itself, given by pad 1 azimuth (P1AZ).

FMS images of Hole 1105A show layers of resistive rock with 1- to 6-m-thick conductive material at irregular intervals. Furthermore, resistive zones are intersected by a number of thin conductive features whose dip and approximated azimuth can be determined (e.g., Fig. F80). The conductive areas correlate quite well with the oxide and olivine oxide gabbro lithologic units defined in the core description. Conversely, the resistive intervals correspond to gabbro and olivine-bearing gabbro.

F80. FMS image over the depth interval 93–100 mbsf in Hole 1105A, p. 158.

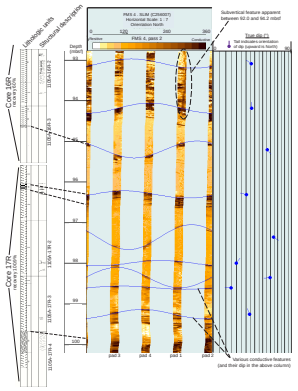

## Natural Gamma-Ray Measurements

The spectral gamma-ray logs were measured with both the NGT and HNGS tools. These tools have been used with the four logging strings for lithologic and depth correlation between the acquired logs. Despite the low overall radioactivity of the rocks encountered at Site 1105, the correlation between the natural gamma-ray logs is very good. The profiles obtained during the first run (Fig. F77) are likely to be more reliable as they were acquired at the low logging speed of 900 ft/hr and, hence, provided an improved statistical measurement. The total spectral gamma-ray (HSGR) varies from 0.35 to 10.7 API units with a mean value of 4.1 API units.

The uranium component of the spectral gamma measurement is observed to be negative at certain depths in the log. The negative uranium values can be correlated to intervals in the spectral log where the computed gamma-ray log, which is a measure of thorium and potassium contribution to the natural radioactivity, contains values which are greater than the HSGR values. This response can likely be attributed to tool design criteria where extremely low gamma counts associated with igneous rocks were not anticipated. The most significant variation observed on the HSGR log is at 102.6 mbsf and correlates with significant tool responses in velocity, porosity, and density measurements.

## Nuclear Measurements

The bulk density of the formation and the photoelectric factor (PEFL) were measured using the HLDS and are shown in Figure F78. Density values range from 2.6 to 3.4 g/cm³ with a mean value for the entire logged section of 3.0 g/cm³. The PEFL, which varies from 2.7 to 11.5 barns/e⁻, is often a good indicator of lithologic variations. For example, a surge of the PEFL at 61 mbsf corroborates a change in lithology from gabbro to oxide gabbro (see **"Igneous and Metamorphic Petrology and Geochemistry,"** p. 29). Peaks in the PEFL correlate well with changes between gabbro and oxide gabbro lithologies throughout the log, but not all lithologic boundaries are detected by the photoelectric index. Density values from discrete laboratory measurements show a good correlation with log measurements except between 43 and 75 mbsf, where they deviate.

The APS records a near/array porosity (APLC) and a far/near porosity (FPLC). The APLC is the primary porosity measurement because it is less influenced by changes in the density of the formation. The APLC in the logged section of the hole is 3.7%. Two distinct maxima are reached at 102.3 and 112.6 mbsf (Fig. F78). Respective porosities are 20.3% and 18.1%. High values may correspond to borehole washouts or fractures in igneous rocks and generally correlate with low peaks in the density

log. Local variations of the porosity log do not correlate well with discrete laboratory measurements. This may be caused by sampling bias because fractured intervals commonly result in poor recovery, and the rocks recovered have veins and fractures that are not often sampled for physical property measurements. The porosity log shows lower values and less variability at the depth intervals 48–62, 87–96, and 128–148 mbsf. The mean porosities and variances are 2.0% and 0.47, 1.6% and 0.13, and 1.5% and 0.84, respectively. They significantly vary in contrast with the mean porosities and variances at 19–48 mbsf (5.9% and 8.2), 62–87 mbsf (3.2% and 2.9), and 96–128 mbsf (4.7% and 10.0).

The APS sigma formation log (SIGF) measures the formation capture cross section of thermal neutrons. This measurement can be expressed in capture units and values for elements, minerals and rock types can be found in Schlumberger (1994; e.g., 7.0 for plagioclase feldspar, 21.5 for gabbro, 31.7 for olivine, and 112.1 for magnetite). The capture cross section is ~10 to 30 for most silicate minerals compared to >100 for Ti-Fe oxides. As expected, the correlation between SIGF peaks, and the conductive oxide-rich intervals of the FMS image are excellent. Figure **F81** compares SIGF directly to the geochemical data to confirm this pattern.

F81. Composite diagram of the first 90 mbsf, **p. 159.**

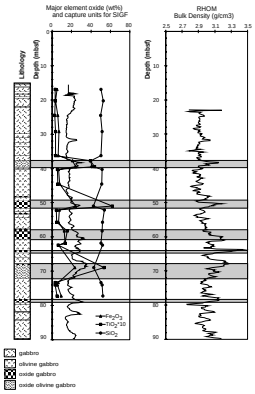


## Sonic Measurements

A second sonic tool deployment was made at this site to compensate for the poor quality logs provided by the SDT. The BHC was run and fortunately gave much better results (Fig. **F78**). The BHC gives only the interval transit time, or Delta T (DT) required for a compressional sound wave to travel through 1 ft of formation between two transmitters and four receivers. The mean DT value in Hole 1105A is 49 µs/ft and the corresponding velocities range from 4.2 to 6.9 km/s. The mean value for $V_p$ is 6.0 km/s. In the 20 to 30 mbsf range, the pipe interferes with the tool response and produces high amplitude variations of $V_p$. The $V_p$ processed for borehole effects exhibits slight trends, which can be described by linear best fit curves on the depth intervals 47–97 and 105–150 mbsf. These curves have respective slopes of 10.6/s and 15.8/s, and the respective average velocity differences between the beginning and the end of the intervals are 0.53 km/s and 0.71 km/s. Microcrack propagation caused by lithostatic pressure released as the cores equilibrate to sea-level pressures should lead to lower values of $V_p$ measured on board. This is not the case, but as for Hole 735B, the constant offset observed between logs and core data allows the logs to be used as proxies of the velocity through the formation.

## Temperature Measurements

Temperature measurements obtained with the TLT at Hole 1105A indicate an increasing hydrothermal gradient of 1°C/100 m. Perturbations in the hydrothermal gradient, seen as rapid increases in borehole fluid temperature, are clearly observed at 46–49, 68–70, 88, 96, 102–104, and 136 mbsf (Fig. **F77;** Note: the temperature log was not reprocessed or depth-shifted at LDEO). These easily distinguishable perturbations likely are a result of pumping the homogenous freshwater gel mud into the borehole and the subsequent borehole equilibration. As the borehole equilibrated to hydrostatic pressure and normalized temperature, water flowing from zones of secondary porosity may have

altered the temperature of the borehole fluid. The most notable example is at 102–104 mbsf, which represents a 0.6°C increase in borehole fluid temperature. Other in situ measurements at this interval confirm the existence of an enlarged borehole, increased porosity, and lower velocity zone, and the FMS log indicates features that may be interpreted as fractures. Furthermore, core recovery in this interval was low, only pebble- or gravel-sized material was recovered. Drilling notes indicate that the rate of penetration (ROP) increased and the seismic while drilling (SWD) signal dropped sharply as well. A similar response by all indicators may be seen at 96 m.

# SEISMIC WHILE DRILLING

## Hammer Drill Observations with an Ocean-Bottom Seismometer at Site 1104

At Hole 1104E tests were made of an SDS Digger Tools 12-in fluid hammer drill using an SDS concentric winged bit from 2140 to 2320 on 1 May. Two ocean-bottom seismometers (OBSs) were deployed at ~90 m (A4) and ~300 m (A8) from the test drilling site. Because of its high signal level, the drill-string accelerometer was not placed on the drill string, but recordings were made for 1.5 hr on the downhole measurement laboratory deck.

Figure F82 shows the 80-min interval from 2141 to 2300 covering the test, as recorded on the vertical component of OBS A4. The energy coupled to the ground varied greatly, depending on the fluid pressure (pumping rate) applied to the drill. The initial 10-min trace shows a gradual intensity increase as pumping pressure was increased to 1650 psi. At several points there were short, more intense intervals followed by the drill stalling. The increase in amplitude followed by stalling may have been caused by the heave of the ship. When not on bottom, the drill goes into bypass mode and resumes hammering when sufficiently loaded to close the bypass valve. The lower levels on the sixth trace (2231 to 2240) and the beginning of the eighth trace (2251 to 2254) may represent intervals in which the weight on bit was possibly too little or too great or drill orientation was incorrect for optimal coupling.

Figure F83 shows details of the waveform at 22:06:20 when the hammer drill stalled. The signal tapered off over 10 or more cycles. The signal appears to be richer in the second harmonic than the primary frequency (21 Hz) of the bit, or first harmonic.

F82. Vertical component of OBS A4's recording of the SDS 12-in fluid hammer drill with concentric winged bits, p. 160.

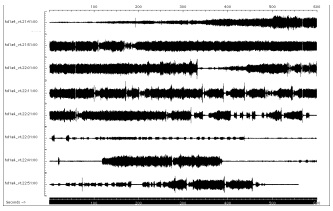

F83. The waveform at 22:06:20 on Figure F82, when the hammer drill stalled, plotted on two expanded scales, p. 161.

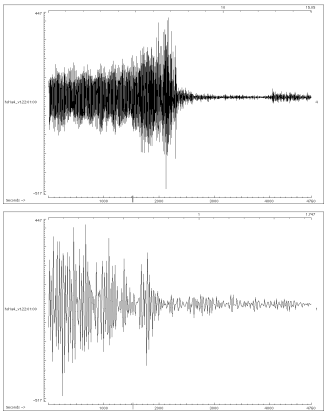

## SWD Experiments at Site 1105

While drilling at Hole 1105A, concurrent measurements of the accelerations of the drill string and of ground and water-borne seismic energy were made over four intervals totaling about 39 hr.

The hole was drilled with a four-roller-cone coring bit from 15 to 158 m; gabbro, olivine gabbro, and oxide gabbro were recovered. The majority of the drilled section was massive, but there were intervals showing deformation and/or alteration. A four-arm caliper log of the hole showed portions of it to have ellipticity of up to 25%. Observations were made for 54 m (34%) of the 158 m drilled. The data acquisition particulars are described in "Seismic While Drilling," p. 17, in the "Explanatory Notes" chapter. The accelerometer data are arbitrarily grouped in 30-min 4.464 MB files. Each 1-s record consists of 2480

bytes (400 samples per second, two bytes/sample, three channels, and an 80-byte ASCII header).

The two OBSs were deployed at ~1000 on 3 May and recovered at ~1330 on 10 May. The OBS data are recorded in one continuous 732-MB file (200 samples per second, two bytes/sample, three channels) for 7 days. The three channels consisted of a vertical geophone, a horizontal geophone, and a hydrophone. The OBS data concurrent with the accelerometer data were extracted from the two complete OBS data files, and converted into 40-s traces (SEGY format) for plotting and correlation purposes. The trace length was arbitrarily chosen. This produced working files consisting of 860, 908, 540, and 1215 records for each OBS (a total of 7046 traces).

Sample portions of these data time series and spectra were examined to (1) determine recording performance, (2) compare the signals between intervals of actual drilling and while the bit was raised during core retrieval, and (3) look for the anticipated spectral components relating to

1. Drill-string rotation rate (50 to 55 rpm with four roller cones);
2. Circulating pump (typically 80 strokes/min);
3. Drilling fluid circulation; and
4. Ship-generated noise (notably 15 Hz and harmonics from the 900 rpm of the ship's four running diesel engines).

Figure F84 compares samples of drill-string acceleration spectra during drilling and while the bit is raised during core recovery. The 0.68-Hz peak in the upper plot corresponds to the 41-rpm drill speed during core recovery. The 2.9-Hz peak in the lower plot appears to be the drill-string rotation rate (44 rpm) times the number of roller cones (four).

Figures F85 and F86 are the time series and spectra for two 31-s samples, the first while not drilling and the second while drilling. Note that the level while drilling is 1.5 to 3 times greater, depending on the component, than the level while not drilling. The cutting action of the bit produces more energy in the 8-to 40-Hz band. The spectral spikes at 15 Hz, the doublet at 29/30 Hz is ship engine noise. The 5- to 7-Hz peak in the seismometer traces, but not the hydrophone, is presently unexplained.

A comparison of the spectral responses between seismometer A4 and A8, both in deployment and then on the lab bench, indicates that seismometer A4 has less of the lower frequency response than A8.

F84. Amplitude spectra of drill-string accelerometer measurements at 35 mbsf, p. 162.

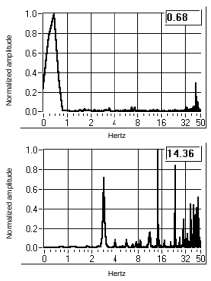


F85. Time series and spectra for a 31-s sample while not drilling in Hole 1105A, p. 163.

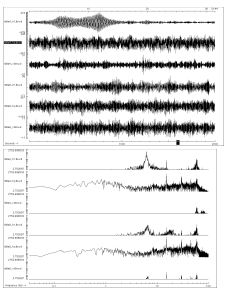

F86. Time series and spectra for a 31-s sample while drilling in Hole 1105A, p. 164.

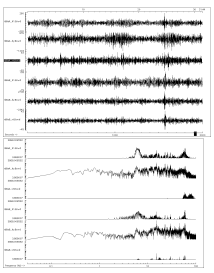

## Locating the OBSs on the Seafloor

The precise positioning capability of the ship allowed us to determine the bottom location of the OBSs with greater accuracy than is done in their customary use for refraction profiles. The ship is positioned with respect to a seafloor acoustic beacon (Datasonics model UAB-354M) using an array of three hydrophones, spaced about 24 and 30 m apart and lowered on rods 6 m below the ship. The OBSs descended at 0.8 m/s. After being released from their 45-kg anchor, the ascent rate of the OBSs was measured to be 1 m/s. Their positions on the seafloor were determined by using the dynamic positioning system to locate the ship 200 m east, north, west, and south of the hole and at the hole. At each position, we made slant-ranging measurements to the OBSs' transponder with a Benthos model DS-7000 acoustic deck unit. These ranges, together with the water depth at each OBS, allowed us to

calculate the horizontal locations. The 200-m offsets were determined by the amount that the dynamic positioning operators felt to be reliable.

At the second deployment in 700 m depth, OBS A4 was dropped 100 m north of the hole and landed at 60 m, 060° from the hole, 107 m to the southeast. OBS A8 was dropped 300 m north of the hole and landed 230 m north of the hole, 70 m to the south of the drop point. Drifts were both southerly and 15% and 12% of the water depth, respectively. The estimated precision is 20 m.

# REFERENCES

Agar, S.M., and Lloyd, G.E., 1997. Deformation of Fe-Ti oxides in gabbroic shear zones from the MARK area. *In* Karson, J.A., Cannat, M., Miller, D.J., and Elthon, D. (Eds.), *Proc. ODP, Sci. Results,* 153: College Station, TX (Ocean Drilling Program), 123–141.

Alt, J.C., and Anderson, T.F., 1991. Mineralogy and isotopic composition of sulfur in layer 3 gabbros from the Indian Ocean, Hole 735B. *In* Von Herzen, R.P., Robinson, P.T., et al., *Proc. ODP, Sci. Results,* 118: College Station, TX (Ocean Drilling Program), 113–126.

Bloomer, S.H., Meyer, P.S., Dick, H.J.B., Ozawa, K., and Natland, J.H., 1991. Textural and mineralogic variations in gabbroic rocks from Hole 735B. *In* Von Herzen, R.P., Robinson, P.T., et al., *Proc. ODP, Sci. Results,* 118: College Station, TX (Ocean Drilling Program), 21–39.

Bloomer, S.H., Natland, J.H., and Fisher, R.L., 1989. Mineral relationships in gabbroic rocks from fracture zones of Indian Ocean ridges: evidence for extensive fractionation, parental diversity, and boundary-layer recrystallization. *In* Saunders, A.D., and Norry, M.J. (Eds.), *Magmatism in the Oceanic Basins*. Geol. Soc. Spec. Publ. London, 42:107–124.

Bonatti, E., Honnorez, J., Kirst, P., and Radicati, F., 1975. Metagabbros from the Mid-Atlantic Ridge at 6°N: contact-hydrothermal-dynamic metamorphism beneath the axial valley. *J. Geol.,* 83:61–78.

Boudier, F., Nicolas, A., Ildefonse, B., 1996. Magma chambers in the Oman Ophiolite: fed from the top and the bottom. *Earth Planet. Sci. Lett.,* 144:239–250.

Cannat, M., 1991. Plastic deformation at an oceanic spreading ridge: a microstructural study of Site 735 gabbros (southwest Indian Ocean). *In* Von Herzen, R.P., Robinson, P.T., et al., *Proc. ODP, Sci. Results,* 118: College Station, TX (Ocean Drilling Program), 399–408.

Cannat, M., and Casey, J.F., 1995. An ultramafic lift at the Mid-Atlantic Ridge: successive stages of magmatism in serpentinized peridotites from the 15°N region. *In* Vissers, R.L.M., and Nicolas, A. (Eds.), *Mantle and Lower Crust Exposed in Oceanic Ridges and Ophiolites:* Dordrecht (Kluwer), 5–34.

Cannat, M., Karson, J.A., Miller, D.J., et al., 1995. *Proc. ODP, Init. Repts.,* 153: College Station, TX (Ocean Drilling Program).

Cannat, M., Lagabrielle, Y., Bougault, H., Casey, J., de Coutures, N., Dmitriev, L., and Fouquet, Y., 1997. Ultramafic and gabbroic exposures at the Mid-Atlantic Ridge: geological mapping in the 15 degrees N region. *Tectonophysics,* 279:193–213.

Cannat, M., Mével, C., and Stakes, D., 1991. Normal ductile shear zones at an oceanic spreading ridge: tectonic evolution of Site 735 gabbros (southwest Indian Ocean). *In* Von Herzen, R.P., Robinson, P.T., et al., *Proc. ODP, Sci. Results,* 118: College Station, TX (Ocean Drilling Program), 415–429.

Casey, J.F., 1997. Comparison of major- and trace-element geochemistry of abyssal peridotites and mafic plutonic rocks with basalts from the MARK region of the Mid-Atlantic Ridge. *In* Karson, J.A., Cannat, M., Miller, D.J., and Elthon, D. (Eds.), *Proc. ODP, Sci. Results,* 153: College Station, TX (Ocean Drilling Program), 181–241.

Casey, J.F., Dewey, J.F., Fox, P.J., Karson, J.A., and Rosencrantz, E., 1981. Heterogeneous nature of oceanic crust and upper mantle: a perspective from the Bay of Islands Ophiolite Complex. *In* Emiliani, C. (Ed.), *The Sea* (Vol. 7) *The Oceanic Lithosphere:* New York (Wiley), 305–338.

Casey, J.F., and Dewey, J.F., 1984. Initiation of subduction zones along transform and accreting plate boundaries, triple-junction evolution and forearc spreading centres—implications for ophiolitic geology and obduction. *Geol. Soc. London Spec. Publ.,* 13:269–290.

Casey, J.F., and Karson, J.A., 1981. Magma chamber profiles from the Bay of Islands ophiolite complex. *Nature,* 292:295–301.

Casey, J.F., Karson, J.A., Elthon, D., Rosencrantz, E., and Titus, M., 1983. Reconstruction of the geometry of accretion during formation of the Bay of Islands Ophiolite Complex. *Tectonics,* 2:509–528.

Cawthorn, R.G. (Ed.), 1996. *Layered Intrusions:* New York (Elsevier).

Coleman, R.G., 1977. *Ophiolites: Ancient Oceanic Lithosphere:* New York (Springer-Verlag).

Detrick, R.S., Buhl, P., Vera, E., Mutter, J., Orcutt, J., Madsen, J., and Brocher, T., 1987. Multi-channel seismic imaging of a crustal magma chamber along the East Pacific Rise. *Nature,* 326:35–41.

Detrick, R., Honnorez, J., Bryan, W.B., Juteau, T., et al., 1988. *Proc. ODP, Init. Repts.,* 106/109: College Station, TX (Ocean Drilling Program).

Detrick, R.S., Mutter, J.C., Buhl, P., and Kim, I.I., 1990. No evidence from multichannel seismic reflection data for a crustal magma chamber in the MARK area on the Mid-Atlantic Ridge. *Nature,* 347:61–64.

Dewey, J., 1976. Ophiolite obduction. *Tectonophysics,* 31:93–120.

Dewey, J.F., and Kidd, W.S.F., 1977. Geometry of plate accretion. *Geol. Soc. Am. Bull.,* 88:960–968.

Dick, H.J.B., Meyer, P.S., Bloomer, S., Kirby, S., Stakes, D., and Mawer, C., 1991a. Lithostratigraphic evolution of an in-situ section of oceanic Layer 3. *In* Von Herzen, R.P., Robinson, P.T., et al., *Proc. ODP, Sci. Results,* 118: College Station, TX (Ocean Drilling Program), 439–538.

Dick, H.J.B., Natland, J.H., Miller, D.J., et al., 1999. *Proc. ODP, Init. Repts.,* 176: College Station, TX (Ocean Drilling Program).

Dick, H.J.B., Robinson, P.T., and Meyer, P.S., 1992. The plutonic foundation of a slow-spreading ridge. *In* Duncan, R.A., Rea, D.K., Weissel, J.K., von Rad, U., and Kidd, R.B. (Eds.), *The Indian Ocean: A Synthesis of Results from the Ocean Drilling Program.* Geophys. Monogr., Am. Geophys. Union, 70:1–39.

Dick, H.J.B., Schouten, H., Meyer, P.S., Gallo, D.G., Berg, H., Tyce, R., Patriat, P., Johnson, K., Snow, J., and Fisher, A., 1991. Bathymetric map of the Atlantis II Fracture Zone, Southwest Indian Ridge. *In* Von Herzen, R.P., Robinson, P.T., et al., *Proc. ODP, Sci. Results,* 118: College Station, TX (Ocean Drilling Program), back pocket.

Dick, H.J.B., Schouten, H., Meyer, P.S., Gallo, D.G., Bergh, H., Tyce, R., Patriat, P., Johnson, K.T.M., Snow, J., and Fisher, A., 1991c. Tectonic evolution of the Atlantis II Fracture Zone. *In* Von Herzen, R.P., Robinson, P.T., et al., *Proc. ODP, Sci. Results,* 118: College Station, TX (Ocean Drilling Program), 359–398.

Engel, C.G., and Fisher, R.L., 1975. Granitic to ultramafic rock complexes of the Indian Ocean Ridge system, western Indian Ocean. *Geol. Soc. Am. Bull.,* 86:1553–1578.

Fisher, R.L., and Sclater, J.G., 1983. Tectonic evolution of the southwest Indian Ocean since the mid-Cretaceous: plate motions and stability of the pole of Antarctica/Africa for at least 80 Myr: *Geophys. J.R. Astron. Soc.,* 73:553–576.

Fowler, C.M.R, 1976. Crustal structure of the Mid-Atlantic Ridge crest at 37°N. *Geophys. J. R. Astron. Soc.,* 47:459–491.

Fowler, C.M.R, 1978. The Mid-Atlantic Ridge, structure at 45°N. *Geophys. J. R. Astron. Soc.,* 54:167–183.

Fox, P.J., and Gallo, D.G., 1984. A tectonic model for Ridge-Transform-Ridge plate boundaries: implications for the structure of oceanic lithosphere. *Tectonophysics,* 104:205–242.

Fox, P.J., and Stroup, J., 1981. The plutonic foundation of the oceanic crust. *In* Emiliani, C. (Ed.), *The Sea* (Vol. 7): The Oceanic Lithosphere: New York (Wiley), 119–218.

Gillis, K., Mével, C., Allan, J., et al., 1993. *Proc. ODP, Init. Repts.,* 147: College Station, TX (Ocean Drilling Program).

Harding, B.W., Storms, M.A., et al., 1990. *Proc. ODP, Init. Repts.,* 124E: College Station, TX (Ocean Drilling Program).

Hebert, R., Constantin, M., and Robinson, P.T., 1991. Primary mineralogy of Leg 118 gabbroic rocks and their place in the spectrum of oceanic mafic igneous rocks. *In* Von Herzen, R.P., Robinson, P.T., et al., *Proc. ODP, Sci. Results,* 118: College Station, TX (Ocean Drilling Program), 3–20.

Honnorez, J., Mével, C., and Montigny, R., 1984. Geotectonic significance of gneissic amphibolites from the Vema fracture zone, equatorial Mid-Atlantic Ridge. *J. Geophys. Res.,* 89:11379–11400.

Irvine, T.N., 1979. Rocks whose composition is determined by crystal accumulation and sorting. *In* Yoder, H.S. (Ed.) *The Evolution of the Igneous Rocks:* Princeton, NJ. (Princeton Univ. Press), 245–306.

Irvine, T.N., 1982. Terminology for layered intrusions. *J. Petrol.,* 23:127–162.

Johnson, K.T.M., and Dick, H.J.B., 1990. Episodicity in mantle melting inferred from peridotite trace element compositions. *Eos,* 71:1703.

Johnson, K.T.M., and Dick, H.J.B., 1992. Open system melting and temporal and spatial variation of peridotite and basalt at the Atlantis II fracture zone. *J. Geophys. Res.,* 97:9219–9241.

Karson, J.A., 1990. Seafloor spreading on the Mid-Atlantic Ridge: implications for the structure of ophiolites and oceanic lithosphere produced in slow-spreading environments. *In* Malpas, J., Moores, E.M., Panayiotou, A., and Xenophontos, C. (Eds.), *Ophiolites: Oceanic Crustal Analogues:* Proc. Symp. "Troodos 1987": Nicosia, Cyprus (Minist. Agric. Nat. Resour.), 547–555.

Karson, J.A., and Dick, H.J.B., 1983. Tectonics of ridge-transform intersections at the Kane Fracture Zone. *Mar. Geophys. Res.,* 6:51–98.

Karson, J.A., Thompson, G., Humphris, S.E., Edmond, J.M., Bryan, W.B., Brown, J.R., Winters, A.T., Pockalny, R.A., Casey, J.F., Campbell, A.C., Klinkhammer, G., Palmer, M.R., Kinzler, R.J., and Sulanowska, M.M., 1987. Along-axis variations in seafloor spreading in the MARK area. *Nature,* 328:681–685.

Karson, J.A., and Winters, A.T., 1992. Along-axis variations in tectonic extension and accommodation zones in the MARK area, Mid-Atlantic Ridge 23°N latitude: ophiolites and their modern oceanic analogues. *In* Parsons, L.M., Murton, B.J., and Browning, P. (Eds.), *Ophiolites and Their Modern Oceanic Analogues.* Geol. Soc. Spec. Publ. London, 60:107–116.

Kempton, P.D., Hawkesworth, C.J., and Fowler, M., 1991. Geochemistry and isotopic composition of gabbros from layer 3 of the Indian Ocean crust, Hole 735B. *In* Von Herzen, R.P., Robinson, P.T., et al., *Proc. ODP, Sci. Results,* 118: College Station, TX (Ocean Drilling Program), 127–143.

Kikawa, E., and Pariso, J.E., 1991. Magnetic properties of gabbros from Hole 735B, Southwest Indian Ridge. *In* Von Herzen, R.P., Robinson, P.T., et al., *Proc. ODP, Sci. Results,* 118: College Station, TX (Ocean Drilling Program), 285–307.

Klein, E.M., and Karstens, J.L., 1995. Ocean-ridge basalts with convergent-margin geochemical affinities from the Chile Ridge. *Nature,* 374:52–57.

Klitgord, K.D., Huestis, S.P., Mudie, J.D., and Parker, R.L., 1975. An analysis of near-bottom magnetic anomalies, sea-floor spreading and the magnetized layer. *Geophys. J. R. Astron. Soc.,* 43:387–424.

Komor, S.C., Elthon, D., and Casey, J.F., 1985. Mineralogic variation in a layered ultramafic cumulate sequence at the North Arm Mountain Massif, Bay of Islands Ophiolite, Newfoundland. *J. Geophys. Res.,* 90:7705–7736.

Kuznir, N.J., and Bott, M.H.P., 1976. A thermal study of the formation of ocean crust. *Geophys. J. R. Astron. Soc.* 47:83–95.

Le Pichon, X., and Heirtzler, J.R., 1968. Magnetic anomalies in the Indian Ocean and sea-floor spreading. *J. Geophys. Res.,* 73:2101–2117.

McBirney, A.R., 1995. Mechanisms of differentiation in the Skaergaard intrusion. *J. Geol. Soc. London,* 152:421–435.

McKenzie, D., and Sclater, J.G., 1971. The evolution of the Indian Ocean since the Late Cretaceous. *Geophys. J. R. Astron. Soc.,* 24:437–528.

Melson, W.G., and O'Hearn, T., 1986. "Zero-age" variations in the compositions of abyssal volcanic rocks along the axial zone of the Mid-Atlantic Ridge. *In* Vogt, P.R., and Tucholke, B.E. (Eds.), *The Western North Atlantic Region.* Geol. Soc. Am., Geol. of North Am. Ser., M:117–136.

Meyer, P.S., Dick, H.J.B., and Thompson, G., 1989. Cumulate gabbros from the Southwest Indian Ridge, 54°S–7°16′E: implications for magmatic processes at a slow spreading ridge. *Contrib. Mineral. Petrol.,* 103:44–63.

Moores, E.M., and Vine, F.J., 1971. The Troodos Massif, Cyprus and other ophiolites as oceanic crust: evaluation and implications. *Philos. Trans. R. Soc. London A,* 268:443–466.

Muller, M.R., Robinson, C.J., Minshull, T.A., White, R.S., and Bickle, M.J., 1997. Thin crust beneath Ocean Drilling Program Borehole 735B at the Southwest Indian Ridge? *Earth Planet. Sci. Lett.,* 148:93–107.

Natland, J., 1990. High level gabbros of the East Pacific Rise sampled by submersible at fault exposure in Hess Deep, Equatorial Pacific. *Eos,* 71:1647.

Natland, J.H., Meyer, P.S., Dick, H.J.B., and Bloomer, S.H., 1991. Magmatic oxides and sulfides in gabbroic rocks from Hole 735B and the later development of the liquid line of descent. *In* Von Herzen, R.P., Robinson, P.T., et al., *Proc. ODP, Sci. Results,* 118: College Station, TX (Ocean Drilling Program), 75–111.

Niida, K., 1997. Mineralogy of MARK peridotites: replacement through magma channeling examined from Hole 920D, MARK area. *In* Karson, J.A., Cannat, M., Miller, D.J., and Elthon, D. (Eds.), *Proc. ODP, Sci. Results,* 153: College Station, TX (Ocean Drilling Program), 265–275.

Nisbet, E.G., and Fowler, C.M.R., 1978. The Mid-Atlantic Ridge at 37° and 45°N: some geophysical and petrological constraints. *Geophys. J. R. Astron. Soc.,* 54:631–660.

Niu, Y. 1997. Mantle melting and melt extraction processes beneath ocean ridges: evidence from abyssal peridotites. *J. Petrol.,* 38:1047–1074.

Ozawa, K., Meyer, P.S., and Bloomer, S.H., 1991. Mineralogy and textures of iron-titanium oxide gabbros and associated olivine gabbros from Hole 735B. *In* Von Herzen, R.P., Robinson, P.T., et al., *Proc. ODP, Sci. Results,* 118: College Station, TX (Ocean Drilling Program), 41–73.

Pallister, J.S., and Hopson, C.A., 1981. Samail ophiolite plutonic suite: field relations, phase variation, cryptic variation and layering, and a model of a spreading ridge magma chamber. *J. Geophys. Res.,* 86:2593–2644.

Pariso, J.E., Scott, J.H., Kikawa, E., and Johnson, H.P., 1991. A magnetic logging study of Hole 735B gabbros at the Southwest Indian Ridge. *In* Von Herzen, R.P., Robinson, P.T., et al., *Proc. ODP, Sci. Results,* 118: College Station, TX (Ocean Drilling Program), 309–321.

Patriat, P., and Achache, J., 1984. India-Eurasia collision chronology has implications for crustal shortening and driving mechanism of plates. *Nature,* 311:615–621.

Perfit, M.R., Fornari, D.J., Ridley, W.I., Kirk, P.D., Casey, J., Kastens, K.A., Reynolds, J.R., Edwards, M., Desonie, D., Schuster, R., and Paradis, S., 1996. Recent volcanism in the Siqueiros transform fault: picritic basalts and implications for MORB magma genesis. *Earth Planet. Sci. Lett.,* 141:91–108.

Purdy, G.M., and Detrick, R.S., 1986. Crustal structure of the Mid-Atlantic Ridge at 23°N from seismic refraction studies. *J. Geophys. Res.,* 91:3739–3762.

Reid, I., and Jackson, H.R., 1981. Oceanic spreading rate and crustal thickness. *Mar. Geophys. Res.,* 5:165–172.

Robinson, P.T., Von Herzen, R., et al., 1989. *Proc. ODP, Init. Repts.,* 118: College Station, TX (Ocean Drilling Program).

Schlumberger, Inc., 1994. *Log Interpretation Charts:* Houston (Schlumberger).

Searle, R.C., and Laughton, A.S., 1977. Sonar studies of the Mid-Atlantic Ridge and Kurchatov fracture zone. *J. Geophys. Res.,* 82:5313–5328.

Shipboard Scientific Party, 1989. Site 735. *In* Robinson, P.T., Von Herzen, R., et al., *Proc. ODP, Init. Repts.,* 118: College Station, TX (Ocean Drilling Program), 89–222.

Shipboard Scientific Party, 1995. Site 922. *In* Cannat, M., Karson, J.A., Miller, D.J., et al., *Proc. ODP, Init. Repts.,* 153: College Station, TX (Ocean Drilling Program), 179–215.

Sinton, J.M., and Detrick, R.S., 1992. Mid-ocean ridge magma chambers. *J. Geophys. Res.,* 97:197–216.

Smewing, J.D., 1981. Mixing characteristics and compositional differences in mantle-derived melts beneath spreading axes: evidence from cyclically layered rocks in the ophiolite of North Oman. *J. Geophys. Res.,* 86:2645–2659.

Spear, F.S., 1981. An experimental study of hornblende stability and compositional variability in amphibolite. *Am. J. Sci.,* 281:697–734.

Stakes, D., Mével, C., Cannat, M., and Chaput, T., 1991. Metamorphic stratigraphy of Hole 735B. *In* Von Herzen, R.P., Robinson, P.T., et al., *Proc. ODP, Sci. Results,* 118: College Station, TX (Ocean Drilling Program), 153–180.

Thayer, T.P., 1963. Flow-layering in alpine peridotite-gabbro complexes. *Mineral. Soc. Am., Spec. Pap.* 1:55–61.

Tucholke, B.E., and Lin, J., 1994. A geological model for structure of ridge segments in slow spreading ocean crust. *J. Geophys. Res.,* 99:11937–11958.

Vine, F.J., and Matthews, D.H., 1963. Magnetic anomalies over oceanic ridges. *Nature,* 199:947–949.

Wager, L.R., and Brown, G.M., 1967. *Layered Igneous Rocks:* San Francisco (W.H. Freeman).

Wager, L.R., Brown, G.M., and Wadsworth, W.J., 1960. Types of igneous cumulates. *J. Petrol.,* 1:73–85.

**Figure F1**. Satellite altimetry free-air gravity map displaying the Southwest Indian Ridge, the Atlantis II Fracture Zone (AII F.Z.), and the location of Hole 735B.

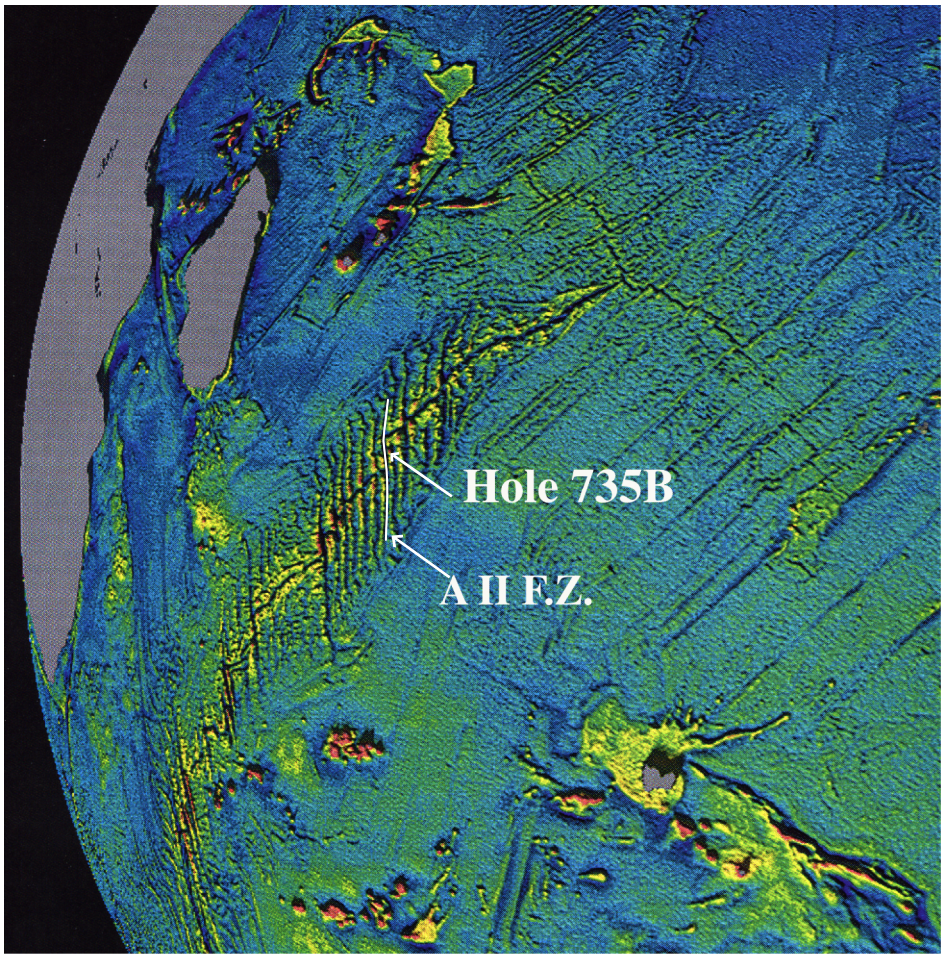

**Figure F2.** Bathymetry of the Atlantis II transform fault (Dick et al., 1991a) displaying the transform valley, transverse ridges, median tectonic ridge, and the northern and southern RTI. Solid circle marks the position of Hole 735B and Sites 1104–1106 atop the Atlantis Bank.

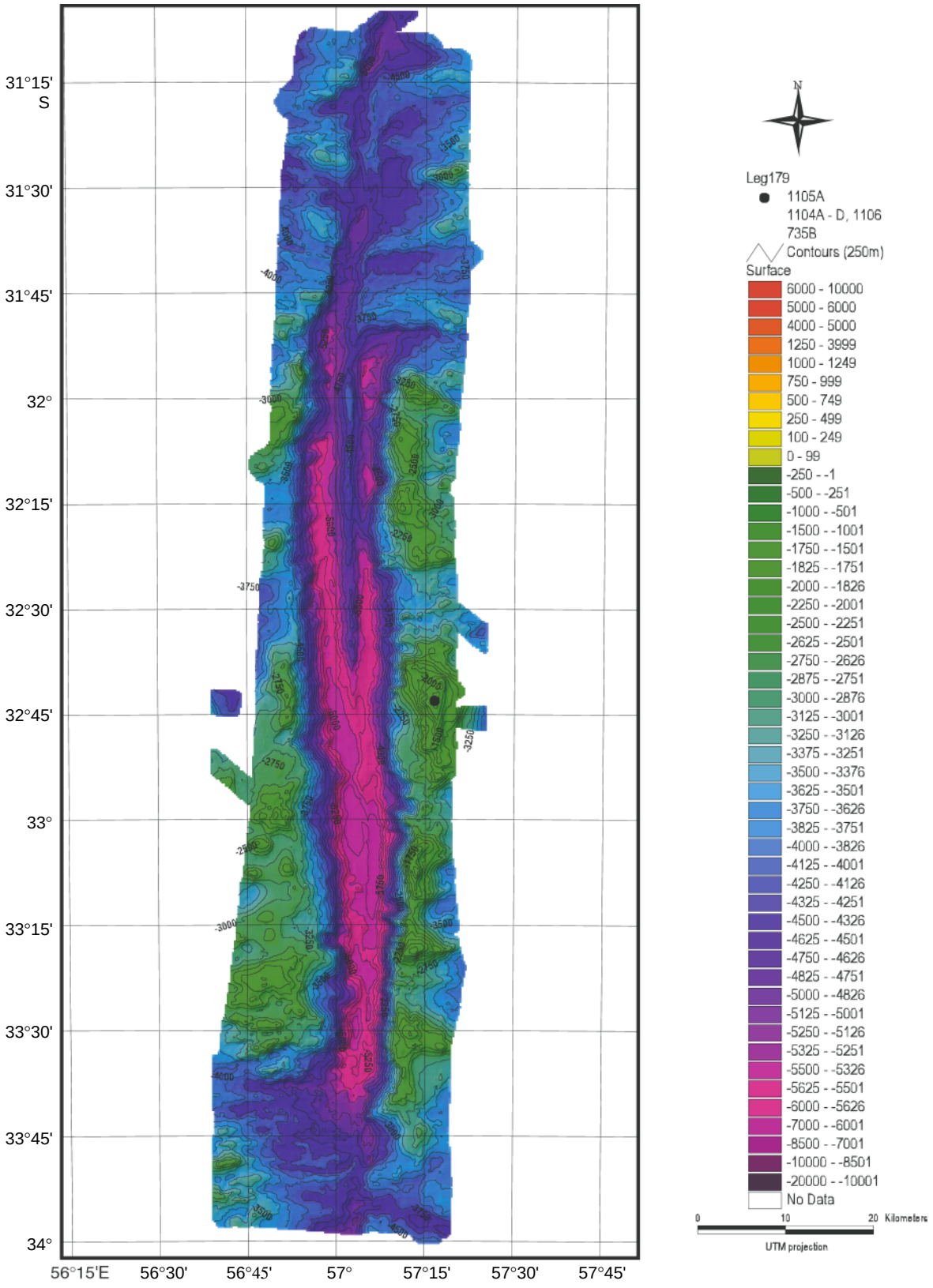

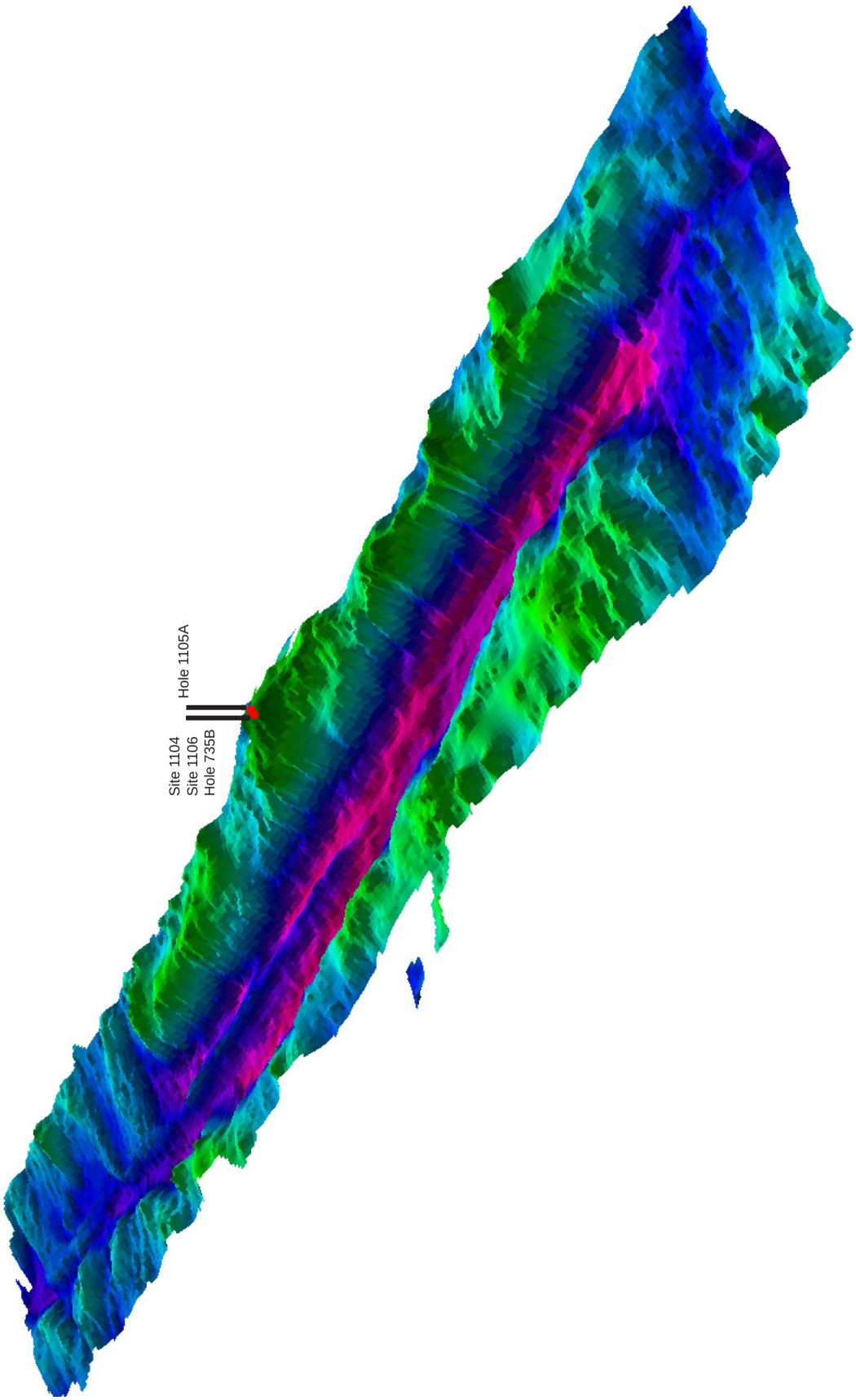


**Figure F3.** Three-dimensional image of the Atlantis II transform fault (multibeam data from Dick et al., 1991a) displaying the transform valley, transverse ridges, median tectonic ridge, and the northern and southern RTI. Solid lines mark the position of Holes 735B and 1105A and Sites 1104 and 1106 atop the Atlantis Bank.

**Figure F4.** Schematic model showing the mechanism of exposure of gabbroic rock at Site 735 on the Atlantis Bank. Exposure is interpreted to be caused by unroofing of the plutonic section on a low-angle detachment fault at the inner corner (IC) of the northern RTI between the Atlantis II Transform and SWIR (Dick et al., 1991b). The IC of the rift valley is the footwall and the outer corner (OC) is the hanging wall of a long-lived low-angle detachment that caused unroofing shortly after formation 11.5 Ma (Stakes et al., 1991).

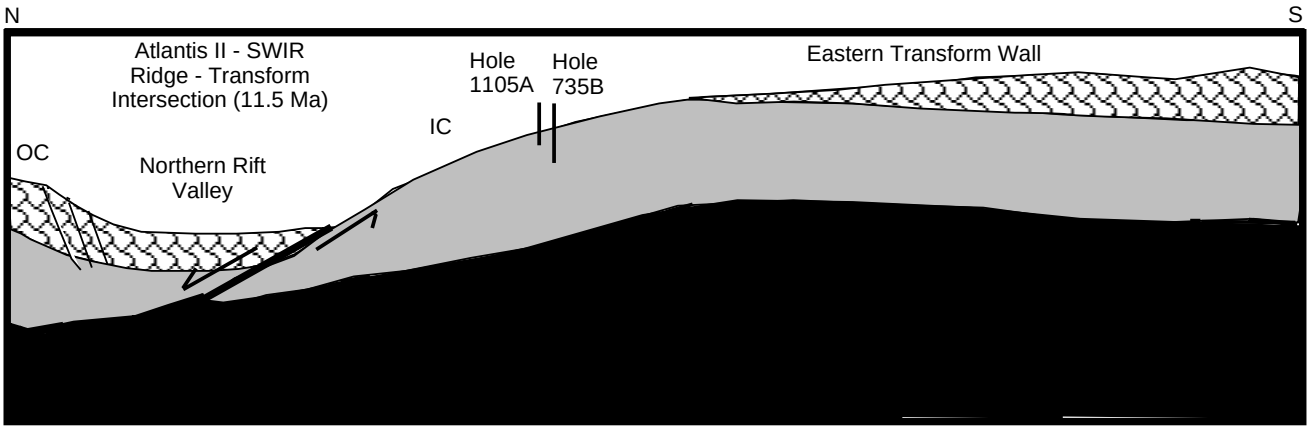

**Figure F5.** Detailed bathymetry of the Atlantis Bank adjacent to the Atlantis II transform fault (data from Dick et al., 1991a). The Atlantis Bank is interpreted to represent a wave-cut platform exposed at sea level sometime during its transport along the transform. Also shown are Sites 1104, 1105, and 1106 drilled during Leg 179 and Site 735 drilled during Legs 118 and 176.

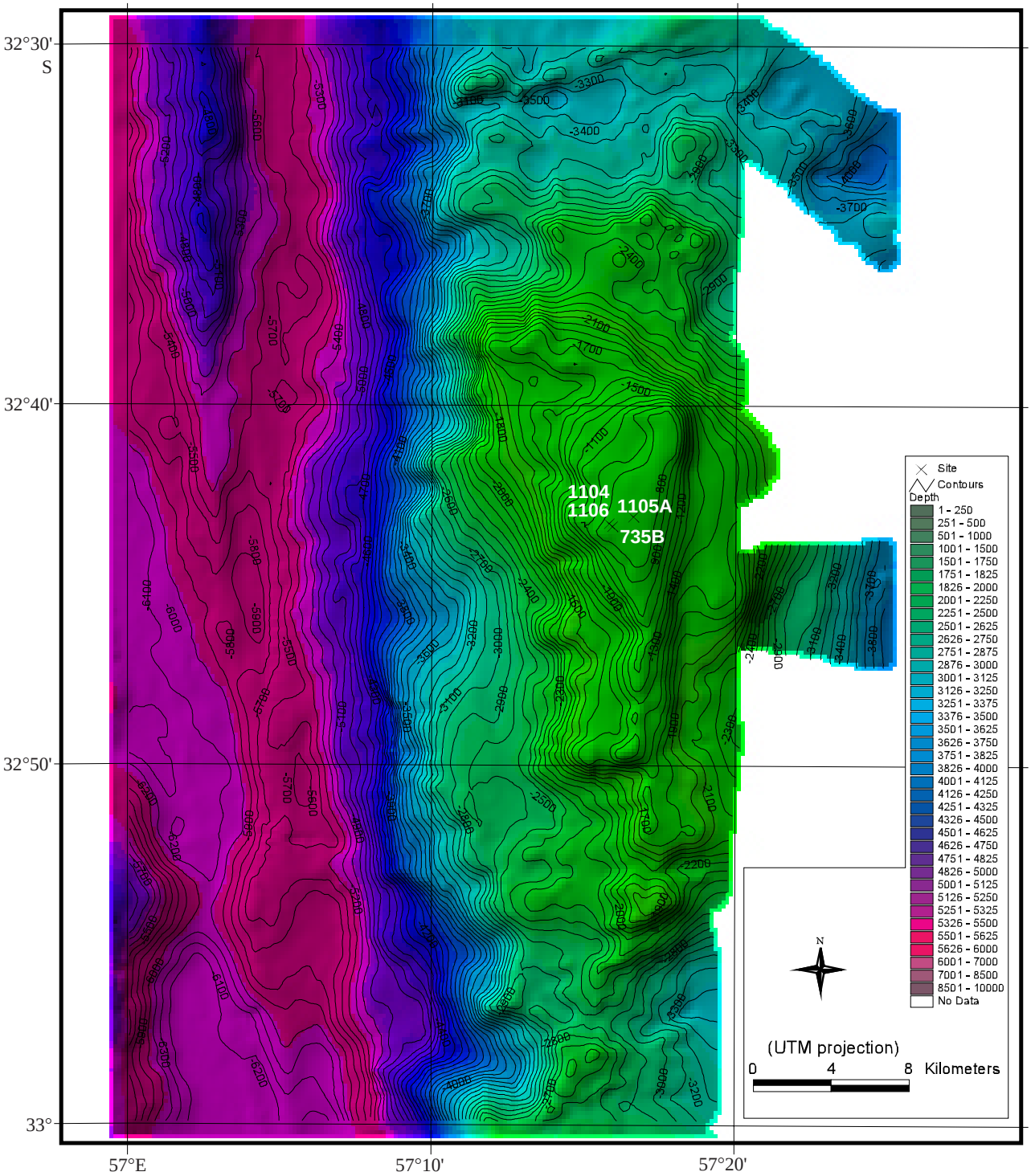

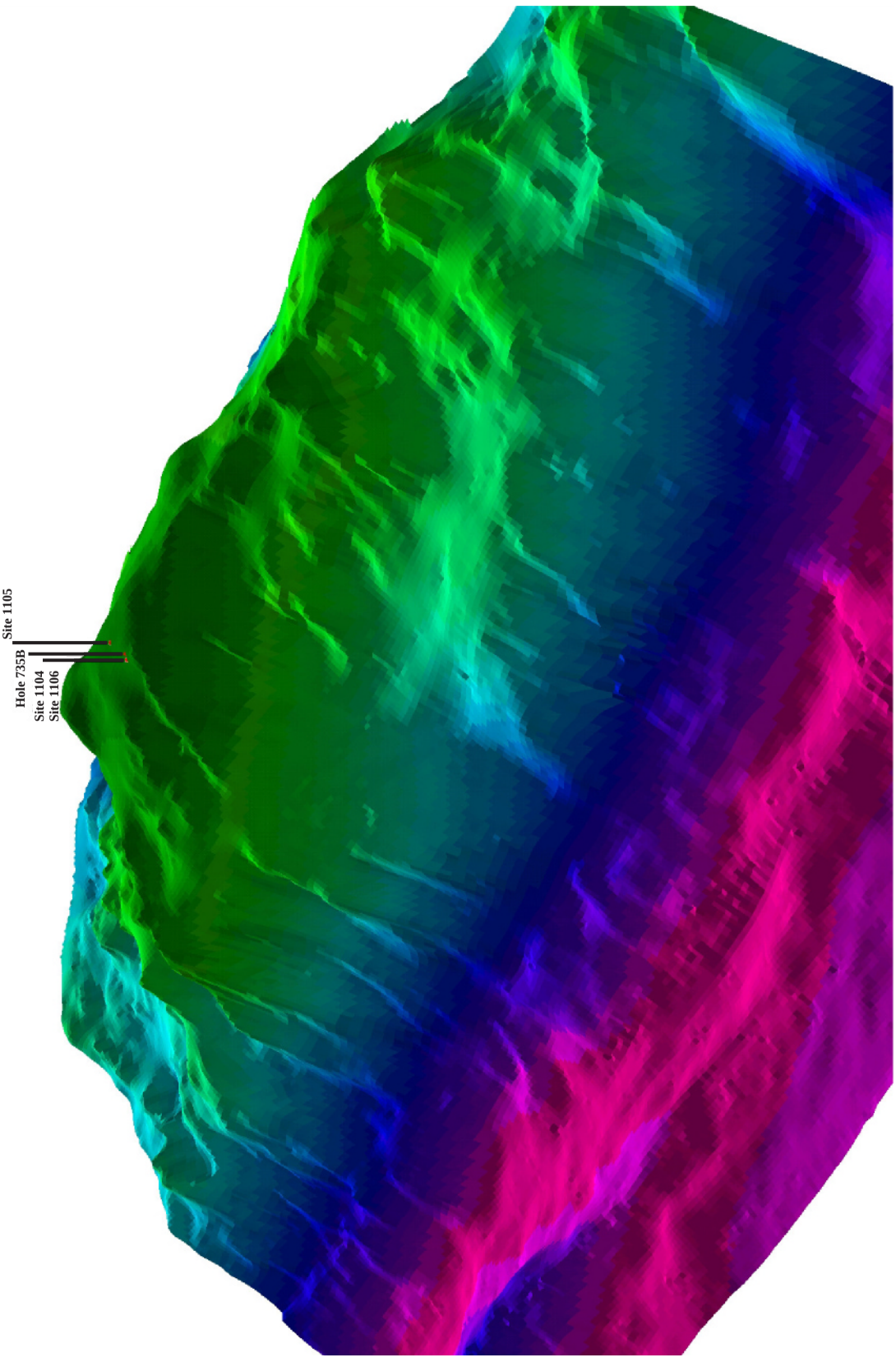


**Figure F6.** Three-dimensional shaded-relief image of the Atlantis Bank (looking northeast) along the wall of the Atlantis II transform fault (data from Dick et al., 1991a). The image shows Sites 1104, 1105, and 1106 drilled during Leg 179 and Hole 735B drilled during Legs 118 and 176. The image shows the transform valley, transverse ridges with the Atlantis Bank (highest region), and the termination of the median tectonic ridge in the axis of the transform valley.

**Figure F7.** Typical ophiolite stratigraphy (after Casey and Karson, 1981) juxtaposed against predictions of geophysical studies of slow-spreading ridges, which predict that the plutonic section is formed by the solidification of short-lived, small, ephemeral magma chambers. Such a model predicts a complex stratigraphy of stratiform intrusions or sill-like plutons (Boudier et al., 1996) with crosscutting igneous plutons that feed sheeted dikes and pillow lavas at the surface. In addition, the lithologic succession should show extreme heterogeneity as each magma body differentiates independently. TR = Trondhjemite intrusions.

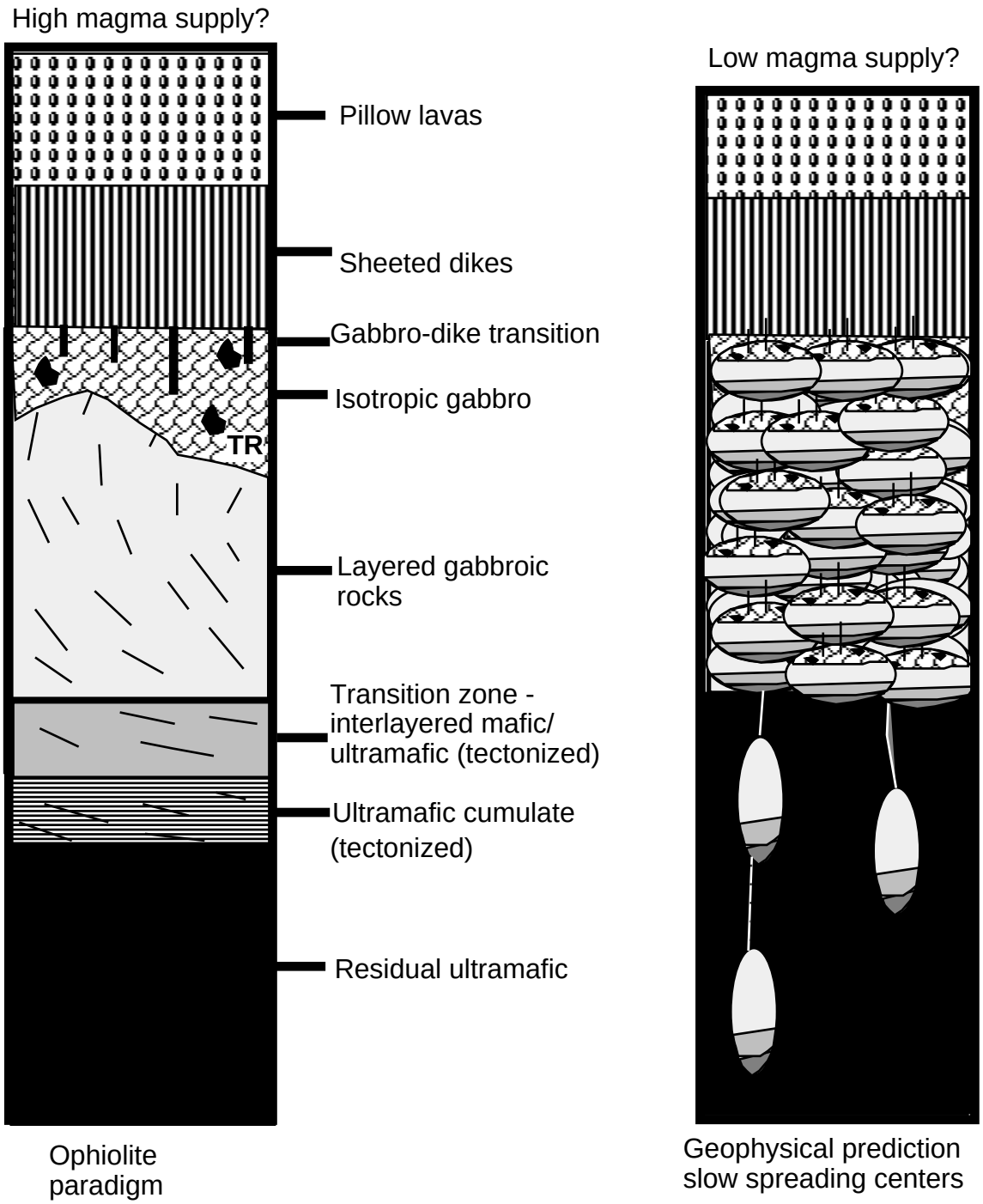

**Figure F8.** Schematic diagram of water hammer drill-in casing system deployment. **A.** Initial deployment. **B.** Spud hole and drill ahead. **C.** Disengage hydraulic hammer and circulate fluid. **D.** Install free-fall reentry funnel. **E.** Retract bit and release casing running tool. **F.** Recover hammer drill and leave a cased reentry hole on the seafloor.

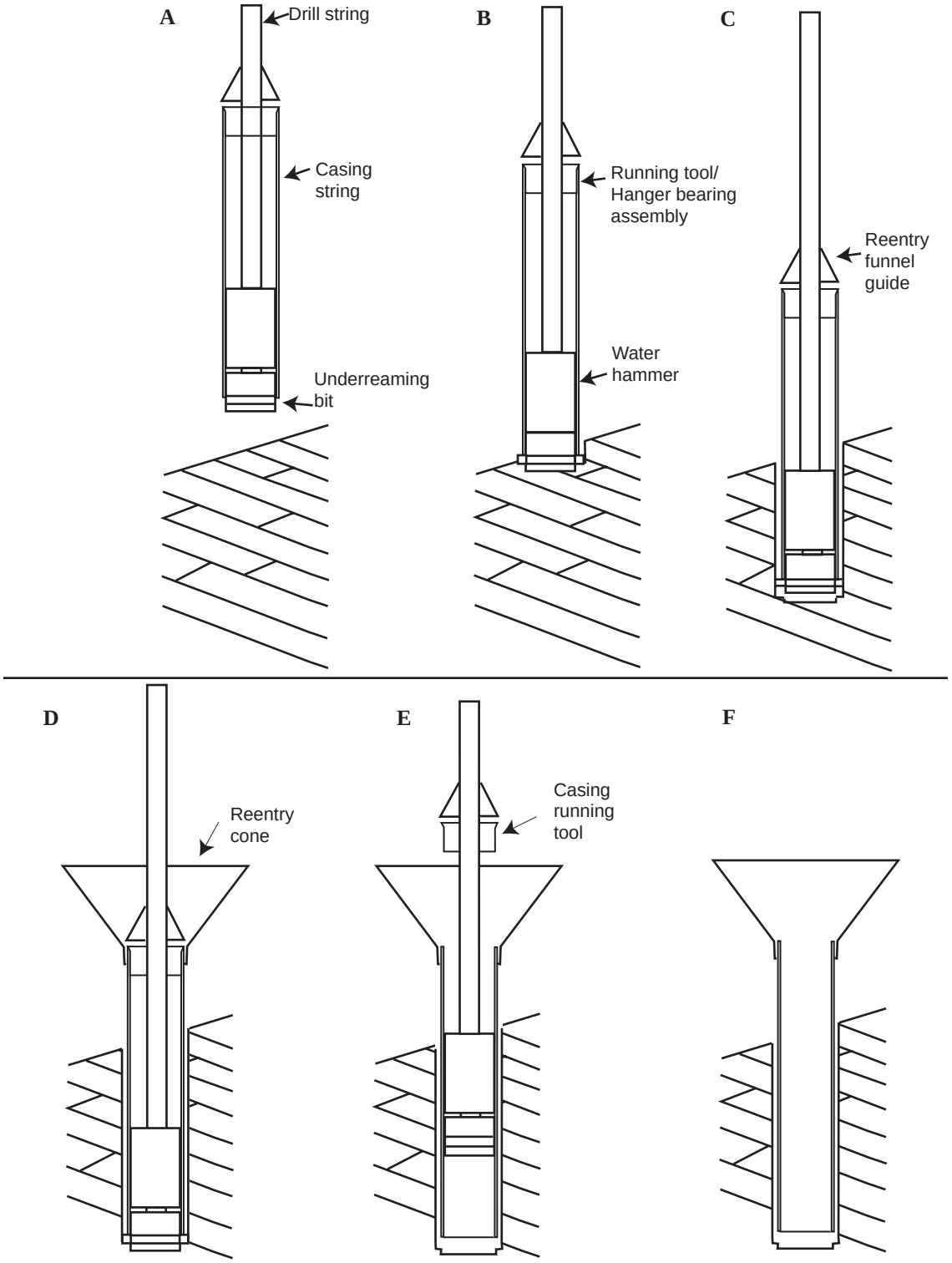

**Figure F9.** Schematic drawings of concentric and eccentric hammer drill underreamer bits.

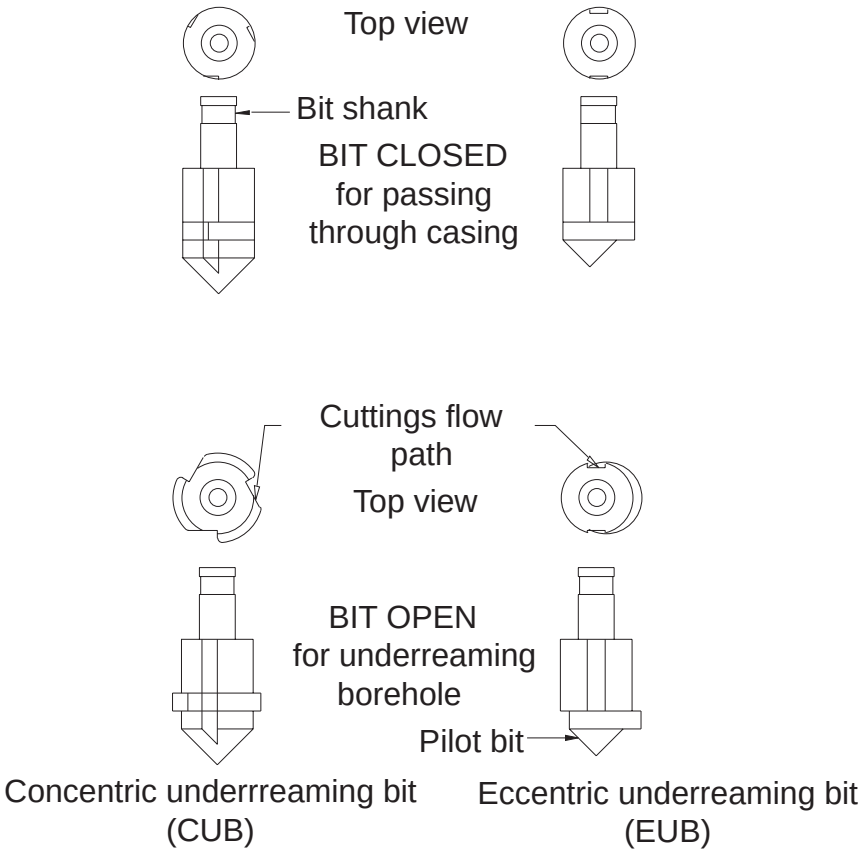

**Figure F10.** Schematic drawing of the SDS water hammer drill (courtesy of SDS Digger Tools, Pty., Ltd.)

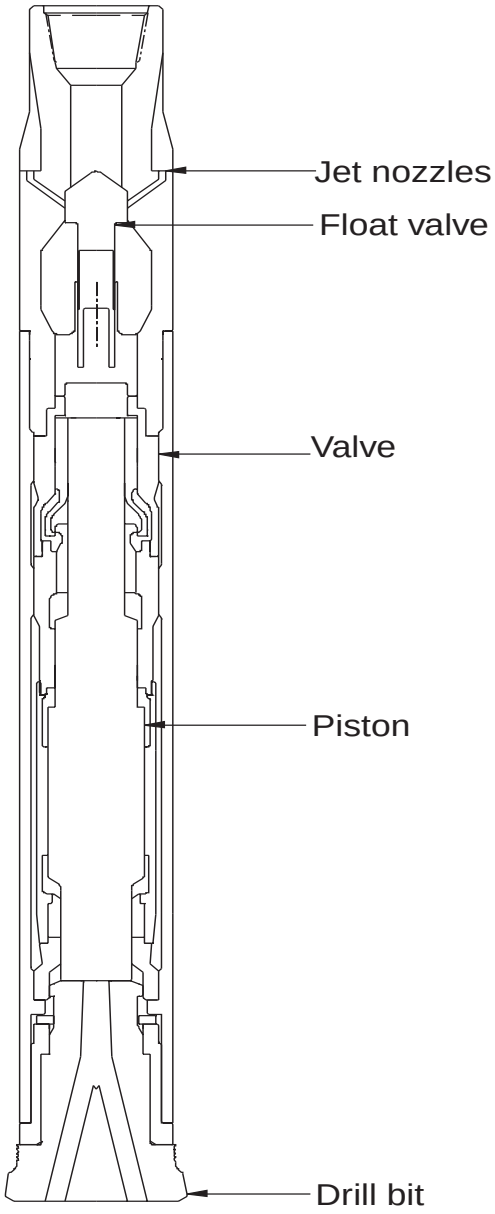

**Figure F11.** Schematic drawing of the HDS running tool.

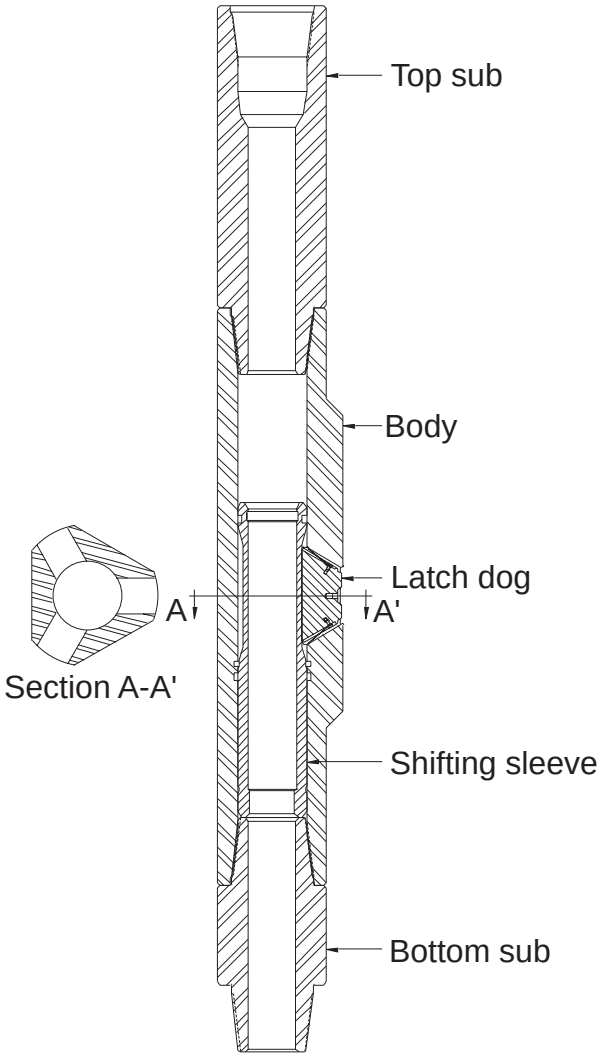

**Figure F12.** Schematic drawing of the HDS go-devil.

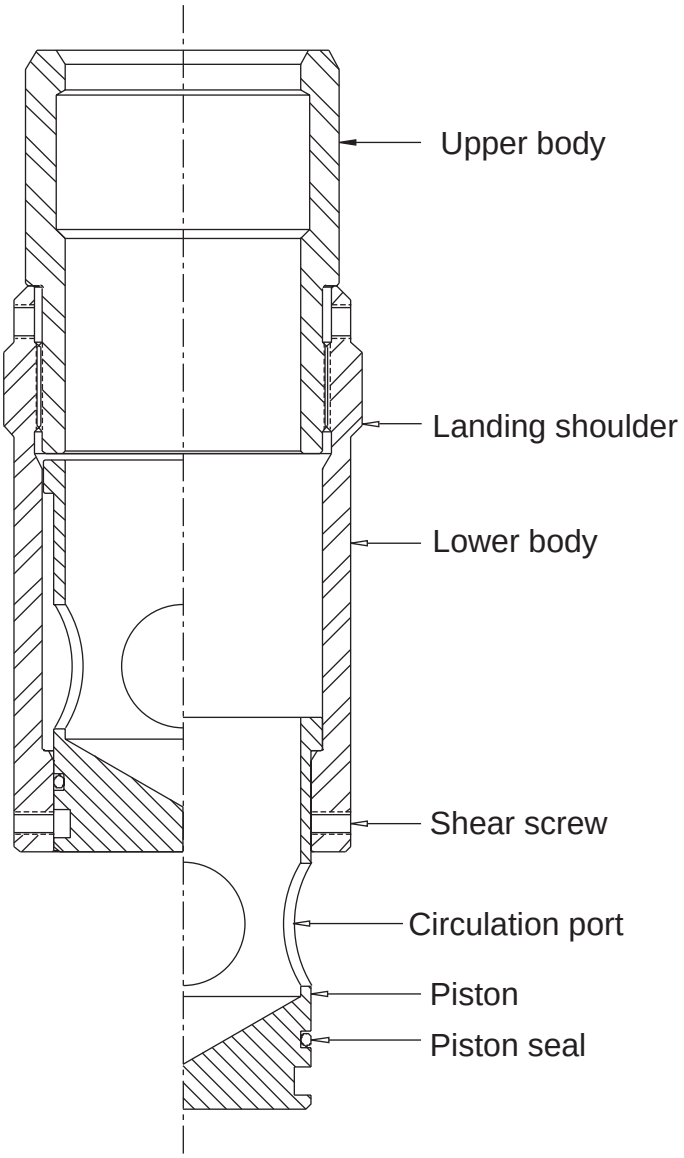

**Figure F13.** Schematic drawing of the HDS hanger bearing assembly.

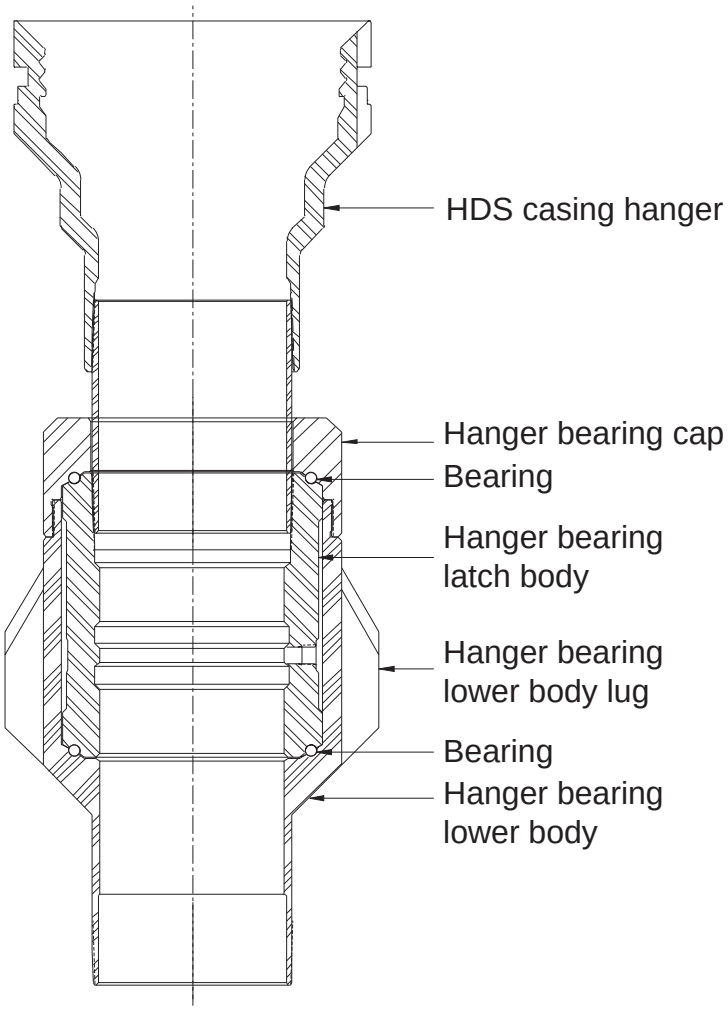

**Figure F14.** Schematic drawing of the HDS reentry cone assembly.

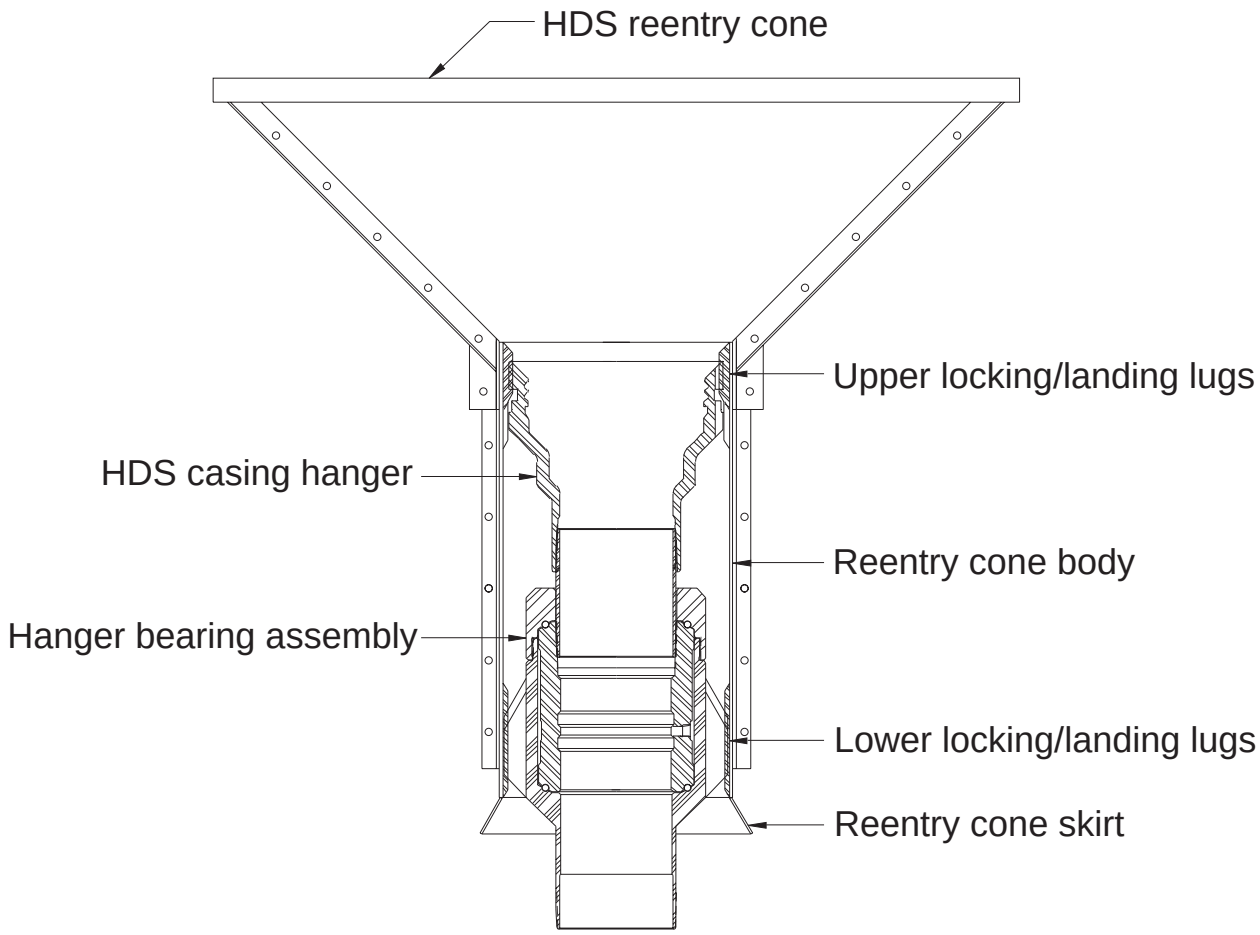

**Figure F15.** SDS concentric underreamer bit 1.

**Figure F16.** SDS concentric underreamer bit 2.

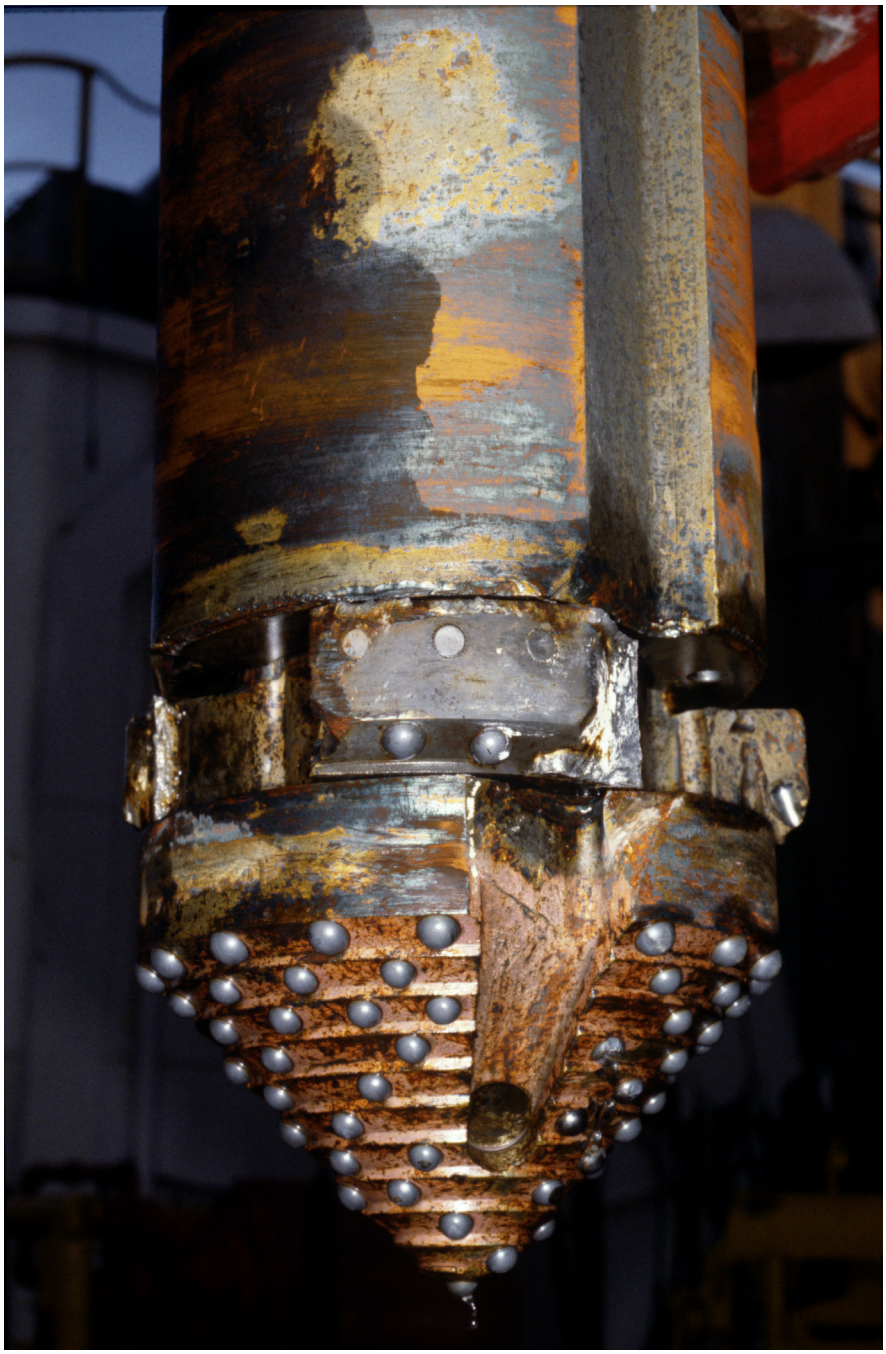

**Figure F17.** SDS concentric underreamer bit modification 3.

**Figure F18.** Holte concentric underreamer bit (before deployment).

**Figure F19.** Holte eccentric underreamer bit.

**Figure F20.** SDS drilling bit.

**Figure F21.** Summary of visually defined lithologic intervals and syntheses units of Hole 1105A as discussed in the text. Only the main lithologic rock types are illustrated.

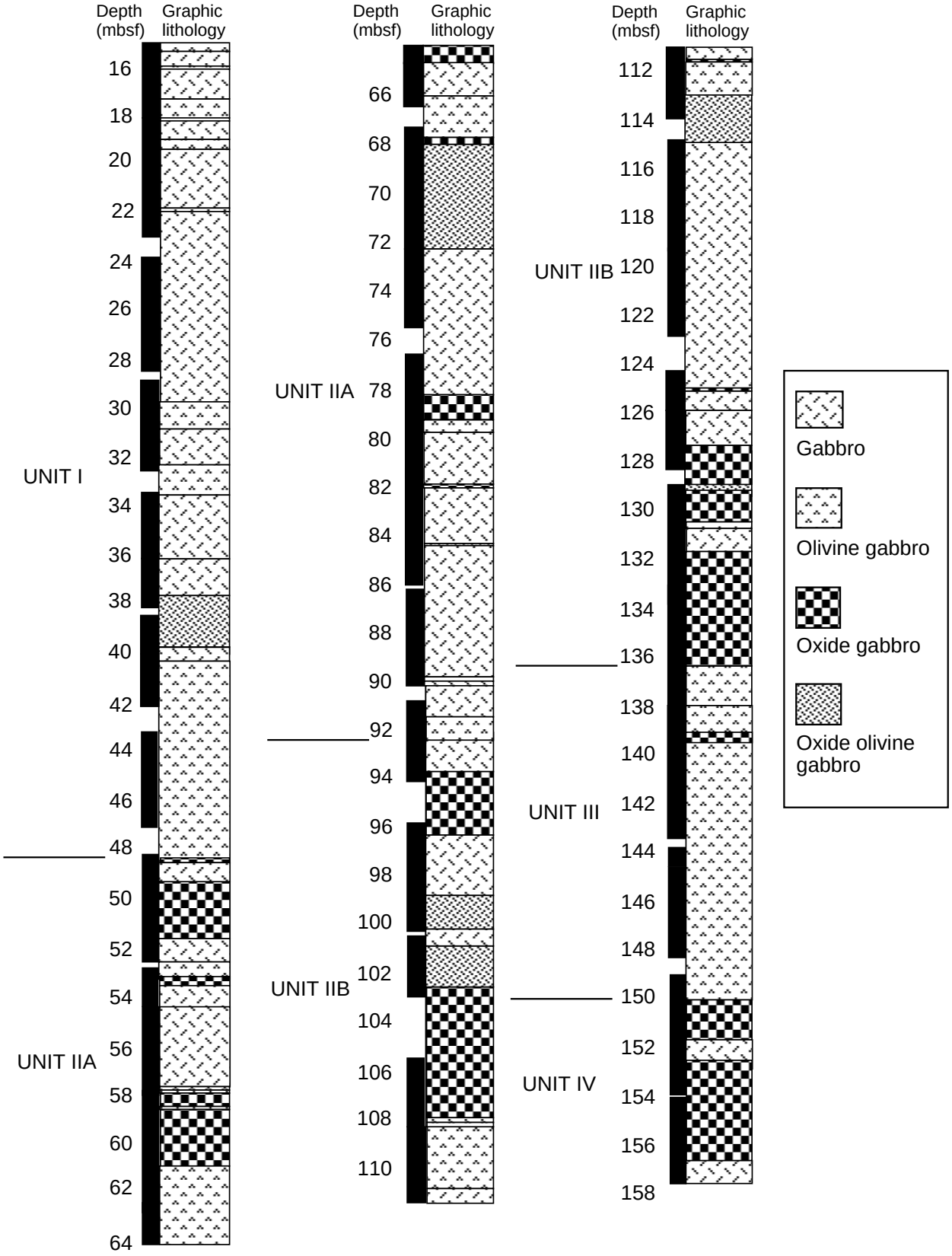

**Figure F22.** The downhole variation in modal mineralogy (in volume percent) of Hole 1105A as visually estimated during core description. The values represent averages of individual intervals. The magnetic susceptibility measured on the whole core is illustrated for comparison, particularly with Fe-Ti oxide contents and definition of unit boundaries (see **"Physical Properties,"** p. 57). Opaques include Fe-Ti oxides and sulfides.

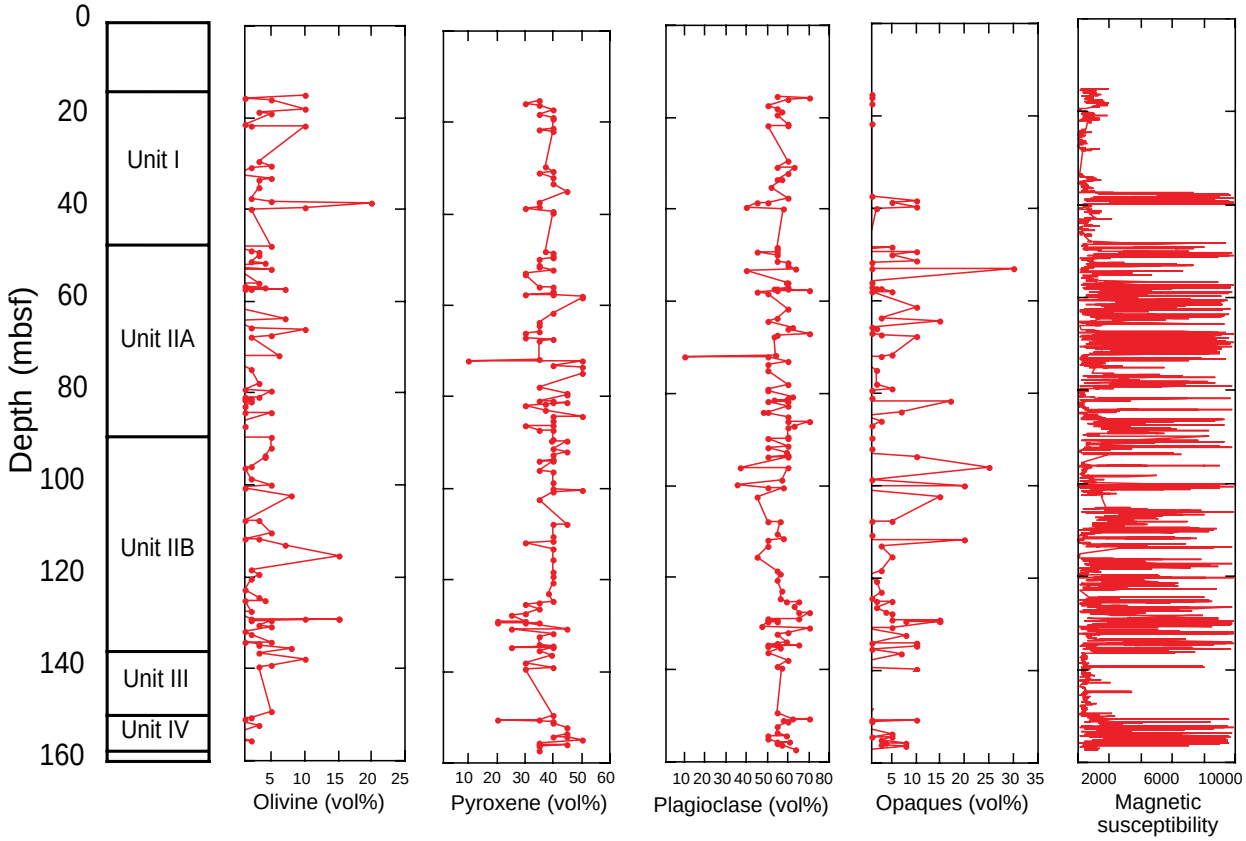

**Figure F23.** The estimated downhole variation in maximum grain size in Hole 1105A (in millimeters). The values are averages of individual intervals.

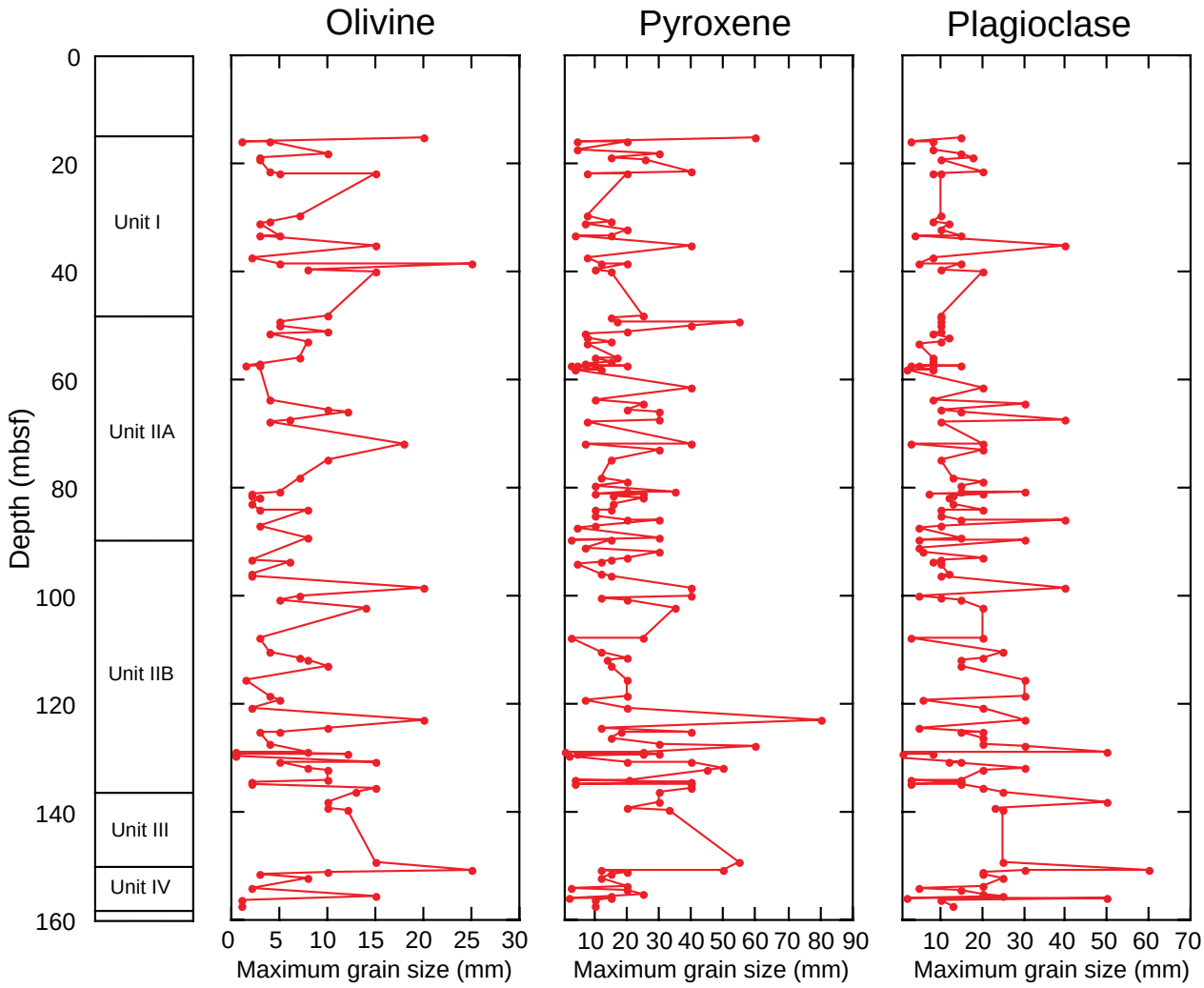

**Figure F24.** The estimated downhole variation in the average grain size in Hole 1105A (in millimeters). The values are averages of individual intervals.

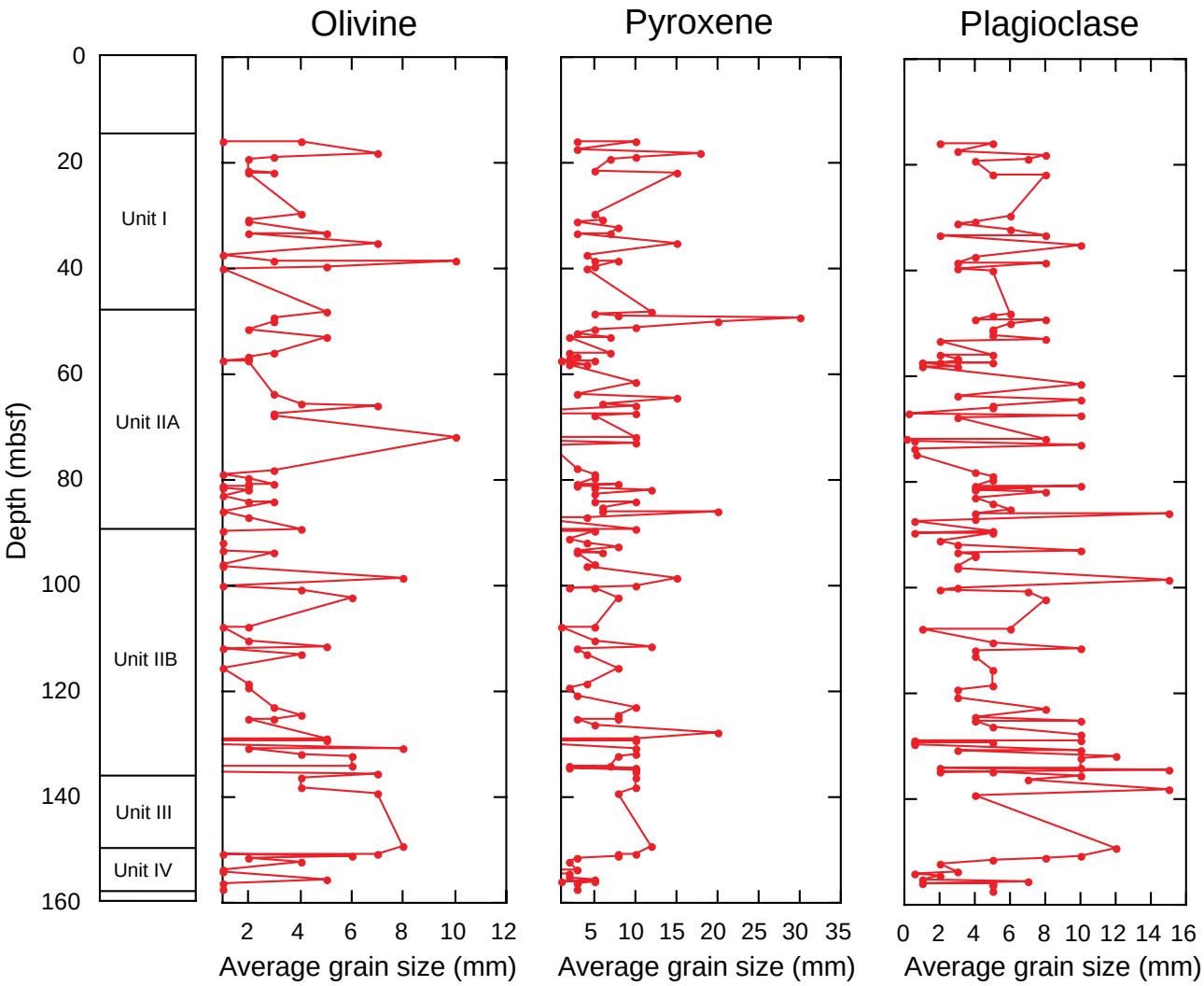

**Figure F25.** The downhole estimated alteration intensity (in volume percent) and distribution of felsic veins given as recorded number of veins per interval and as accumulative percentages.

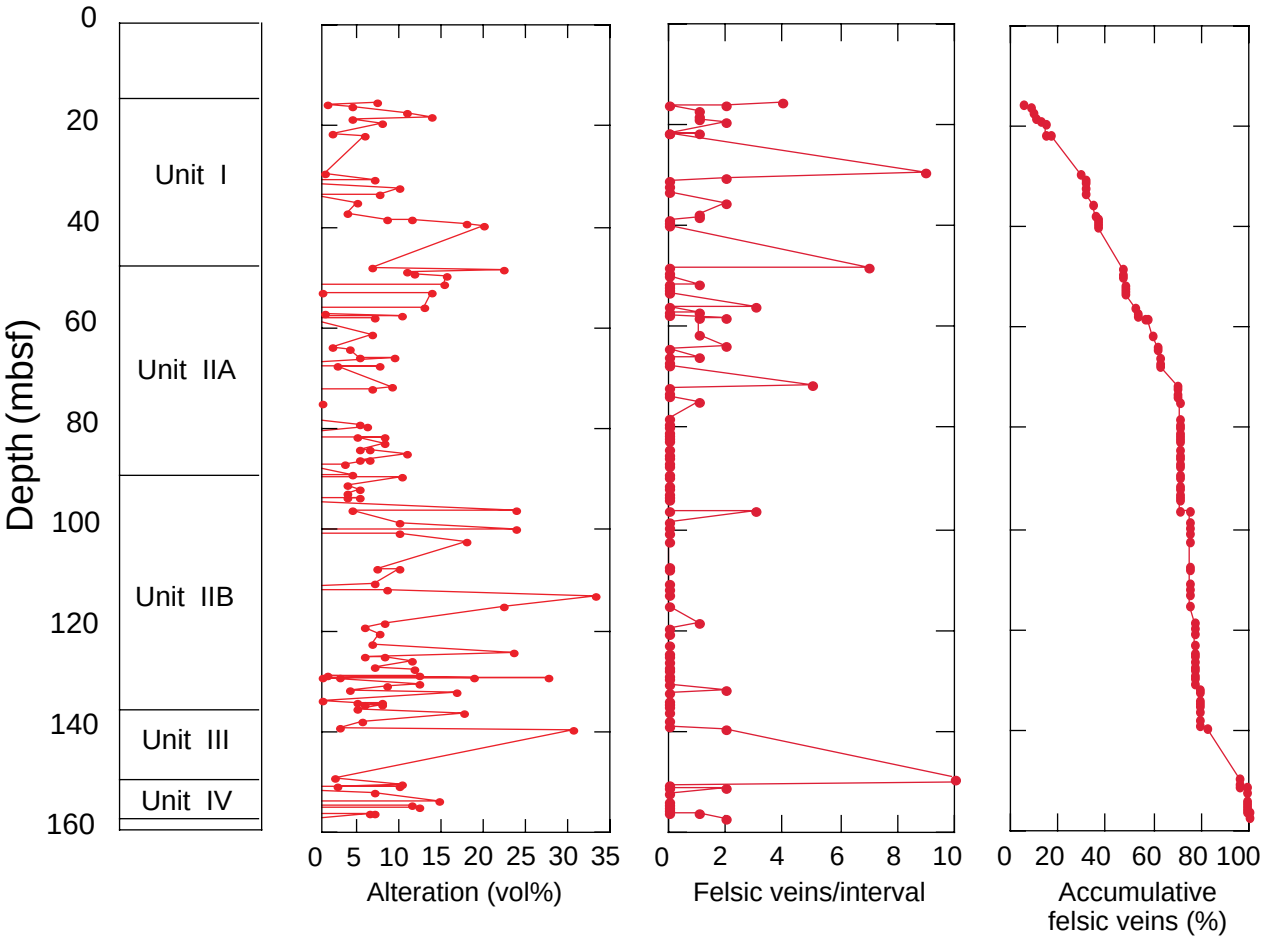

**Figure F26**. The distribution of igneous laminations (L), modal and grain-size layering (LA), crystal-plastic foliation fabric (F), and felsic veins (MV) in Hole 1105A.

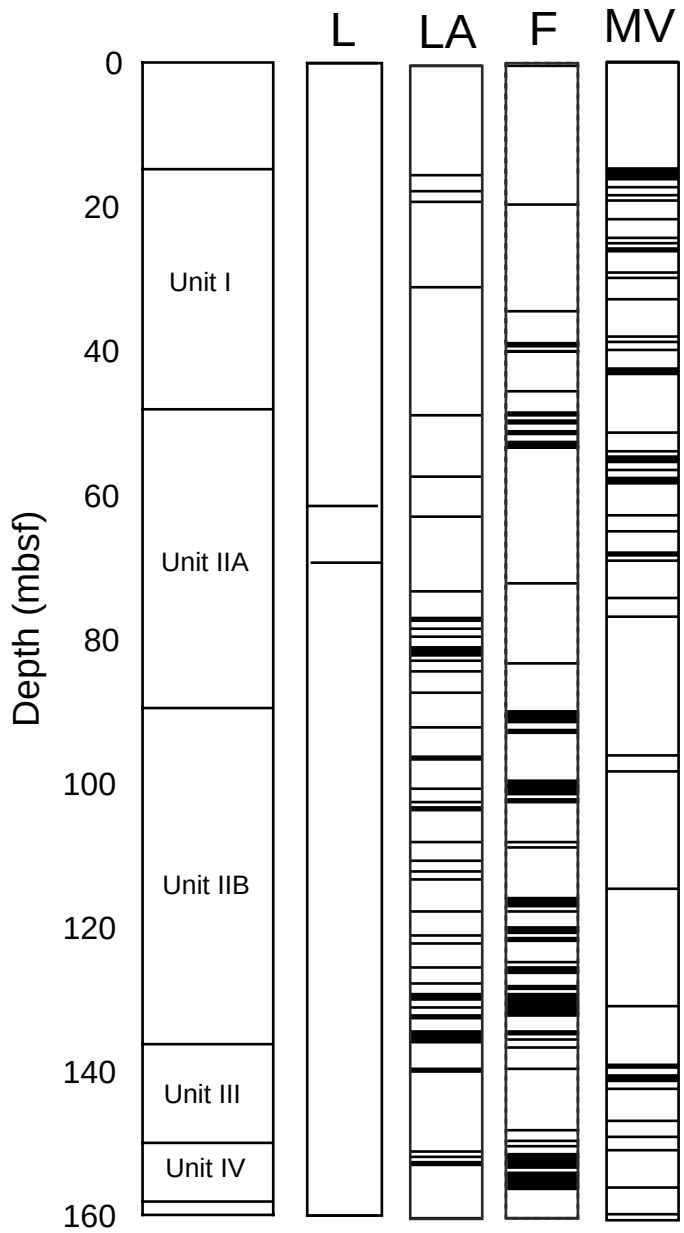

**Figure F27.** Digital photomicrograph showing igneous lamination in fine-grained olivine gabbro (interval 55, Sample 179-1105A-12R-2, 50–53 cm). Field of view = 5.5 mm, plane-polarized light.

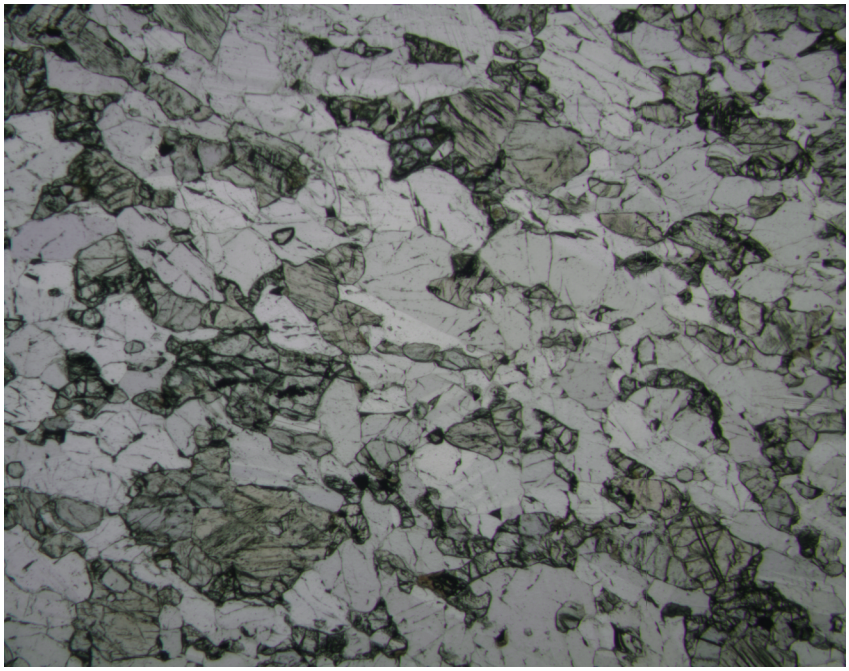

**Figure F28.** Examples of modal layering. **A.** Modal variation in the relative proportions of felsic and mafic components in oxide gabbro resulting in anorthositic layers separating oxide and pyroxene rich layers above and below (close-up core photograph of interval 89, 179-1105A-18R-2, 8–17 cm [Piece 2]). (Continued on next page.)

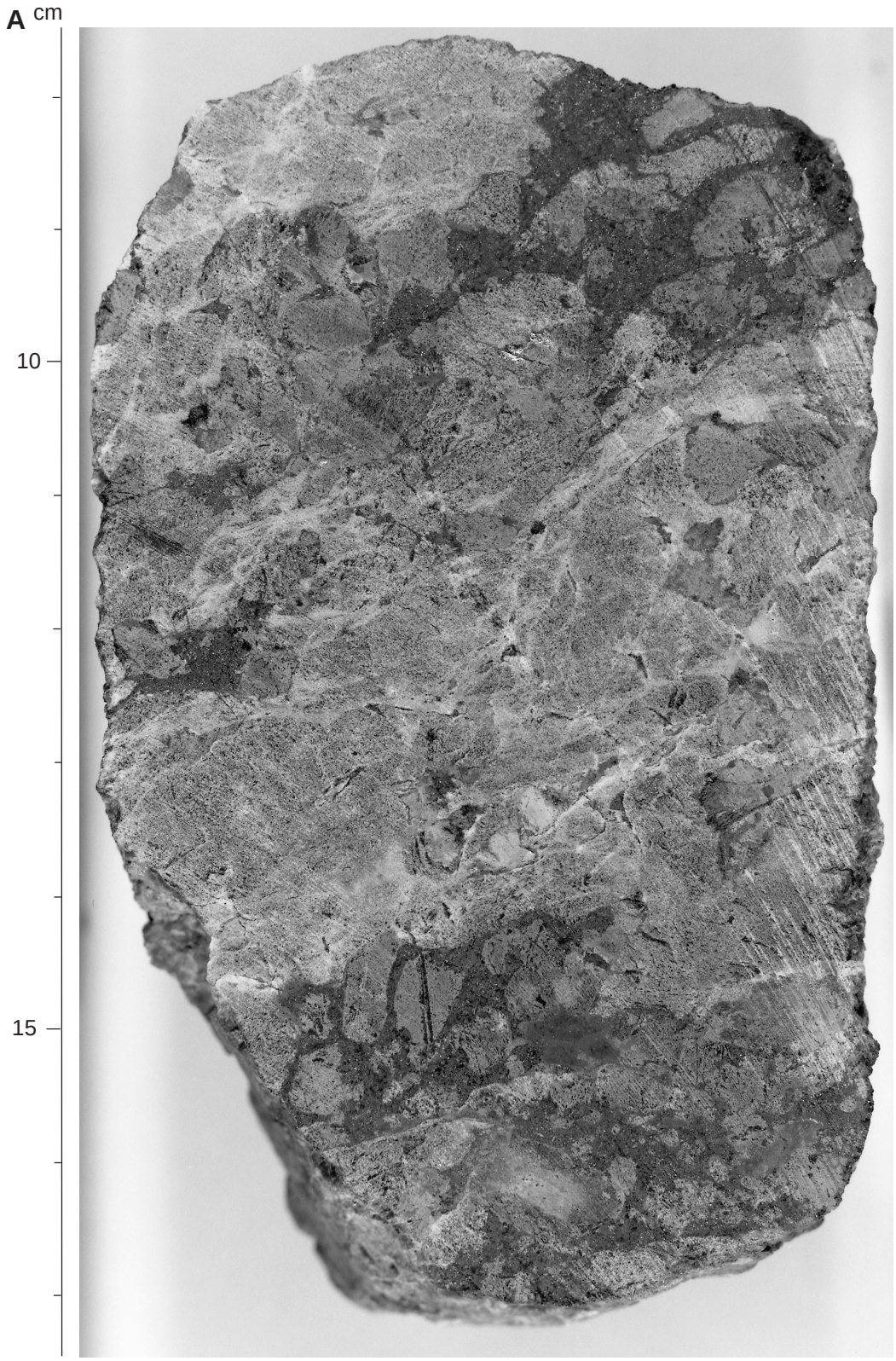

**Figure F28 (continued). B.** Layering showing modal variability in gabbro of felsic and mafic phases. Upper part of mafic layer slightly affected by deformation (close-up core photograph of interval 60, 179-1105A-13R-1, 59–75 cm [Piece 3C]). Also note prominent oxide gabbro layer at the base (interval 66–71) that parallels more subtle mafic-felsic layering above.

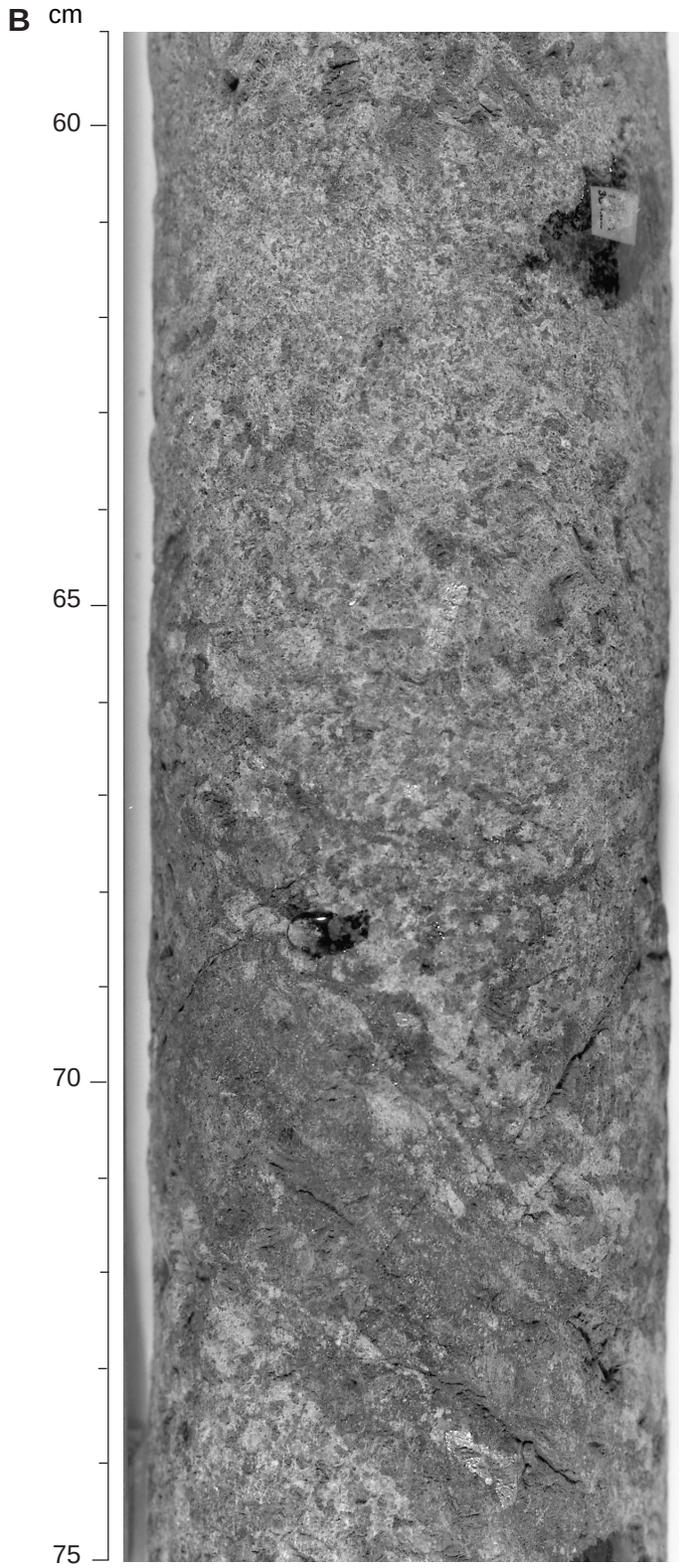

**Figure F29.** Example of oxide layering. Irregular layer with high concentration of Fe-Ti oxide minerals in coarse-grained gabbro (close-up core photograph of interval 71, 179-1105A-15R-1, 14–21 cm).

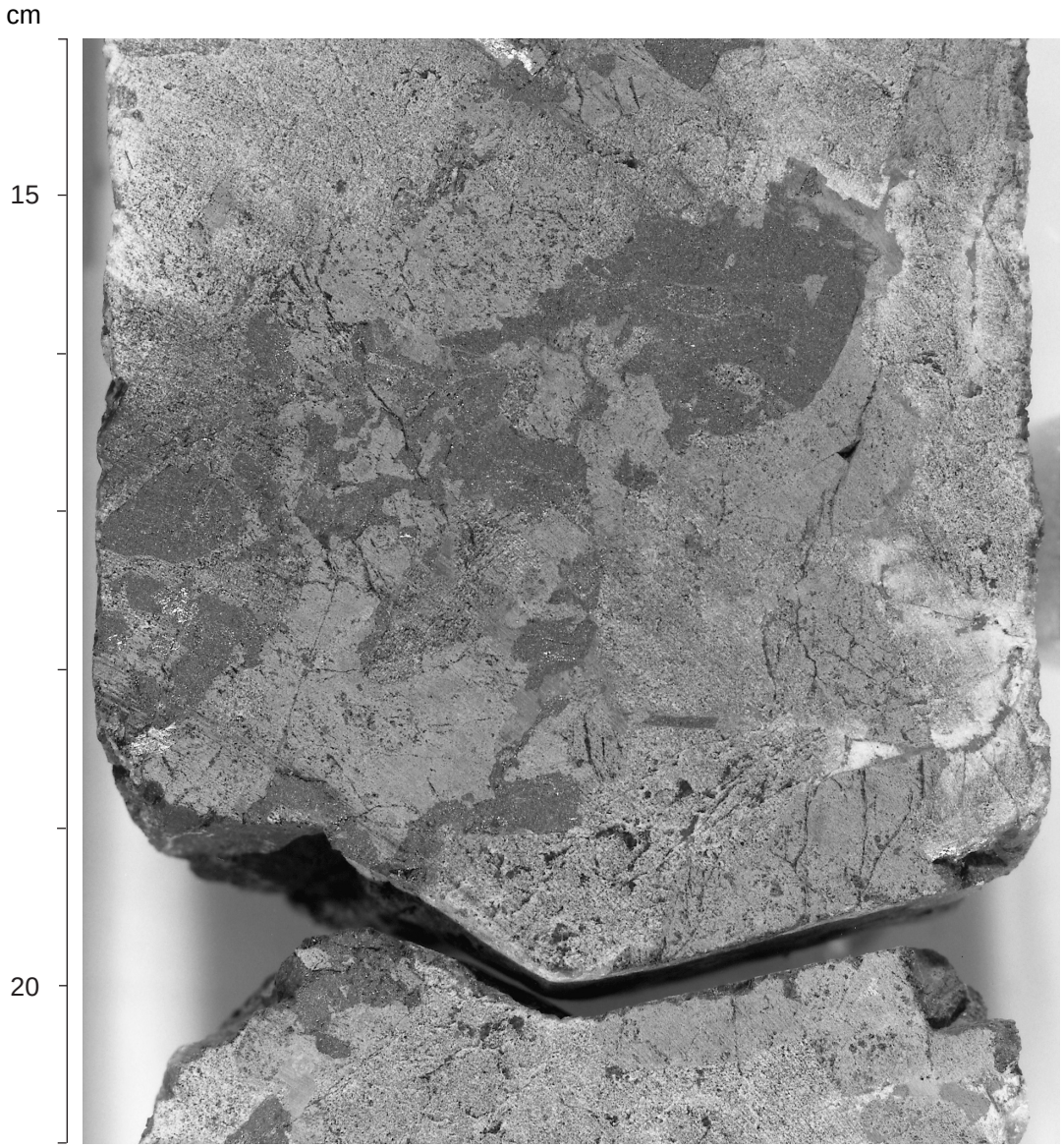

**Figure F30.** Example of grain-size layering. Planar interface between layers of massive medium-grained gabbro below massive coarse-grained gabbro (intervals 61 and 62, 179-1105A-13R-4, 30–59 cm, Pieces 3 and 4).

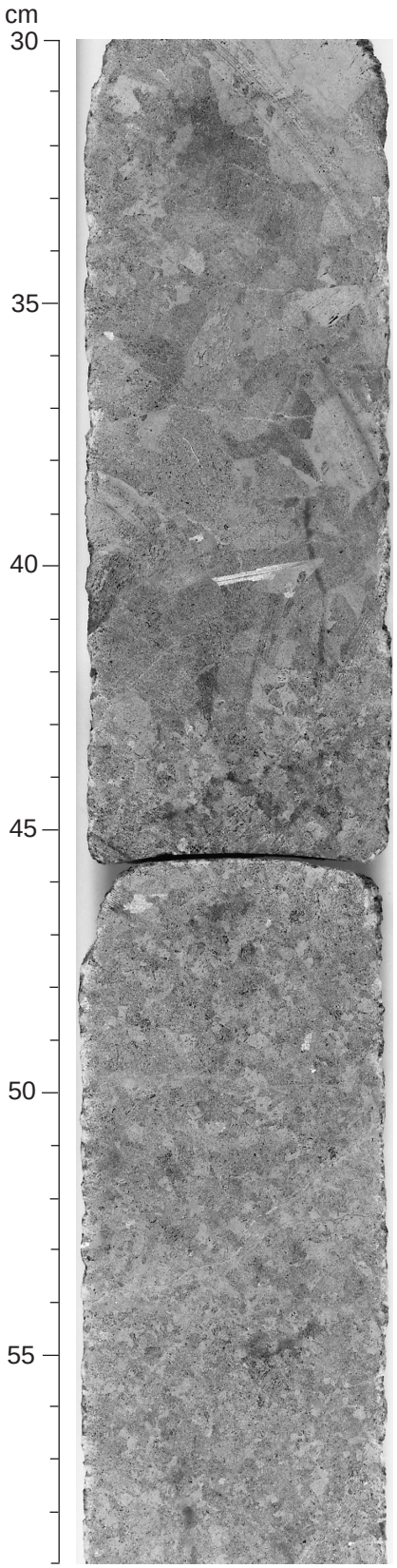

**Figure F31.** Example of fine-grained oxide olivine gabbro (dark) alternating with coarse-grained oxide gabbro (lighter bands) in deformed section (close-up core photographs of intervals 109–113, 179-1105A-25R-1, 0–46 cm).

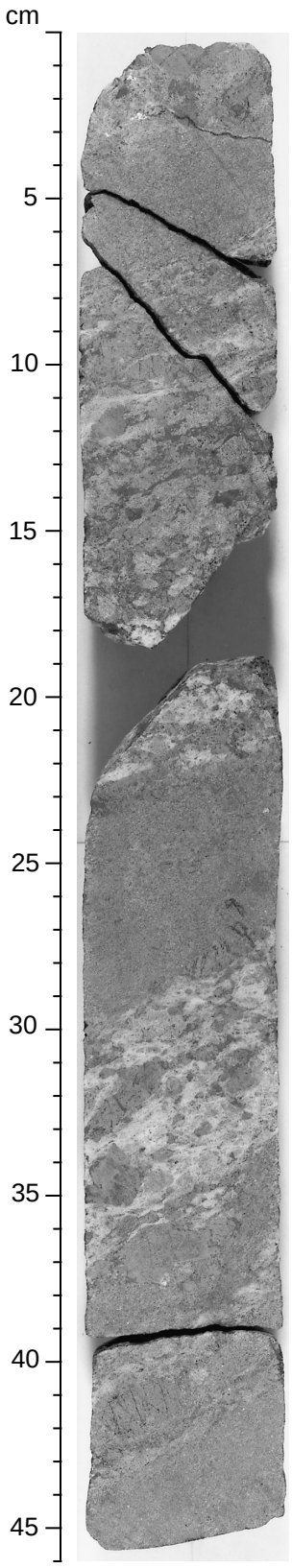

**Figure F32.** Photomicrograph of contact between fine-grained olivine gabbro with granular texture and a medium-grained olivine gabbro (Sample 179-1105A-13R-3, 24–26 cm). Plane-polarized light; long field of view = 23 mm.

**Figure F33.** Thin magmatic felsic vein with intruding gabbro (close-up core photograph of interval 6, 179-1105A-6R-3, 0.5–12.5 cm).

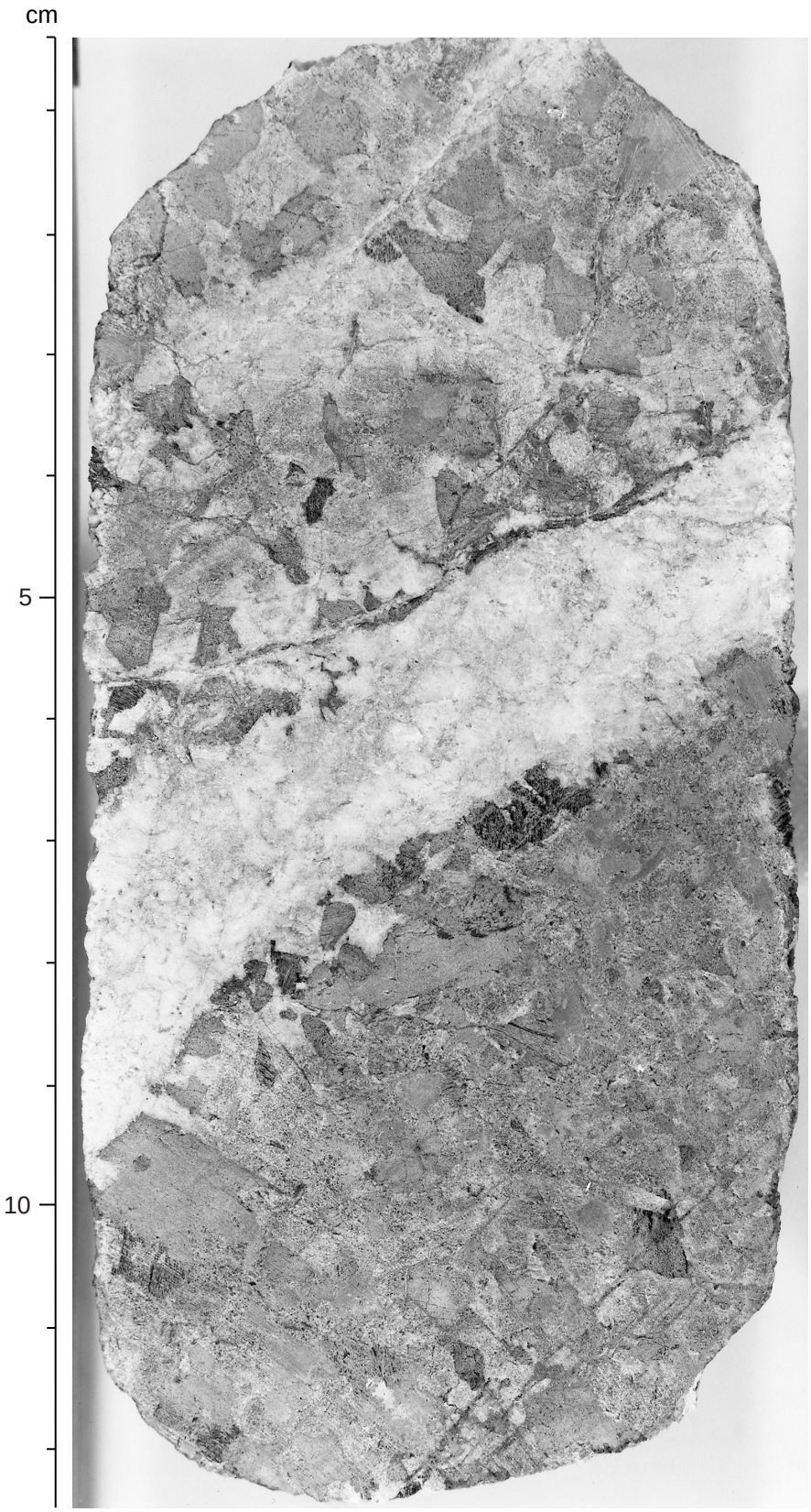

**Figure F34.** Estimated modal variation on triangular diagrams. **A.** Clinopyroxene-olivine-plagioclase. **B.** Clinopyroxene-olivine-opaques. Note that the scale for clinopyroxene has been divided by 4 in order to display variability in olivine and opaque minerals.

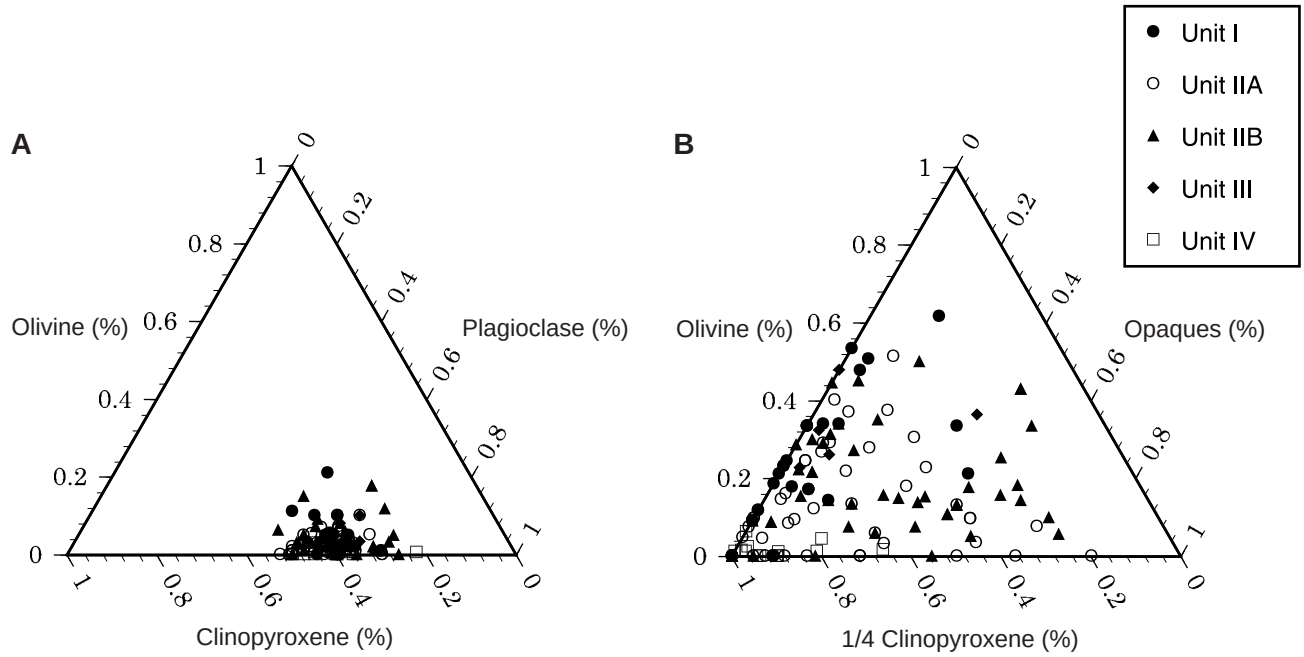

**Figure F35.** Digital photomicrograph of fine-grained olivine gabbro with adcumulate texture. Brown hornblende as rims around olivine (Sample 179-1105A-1R-2, 88–91 cm). Plane-polarized light; field of view = 2.75 mm.

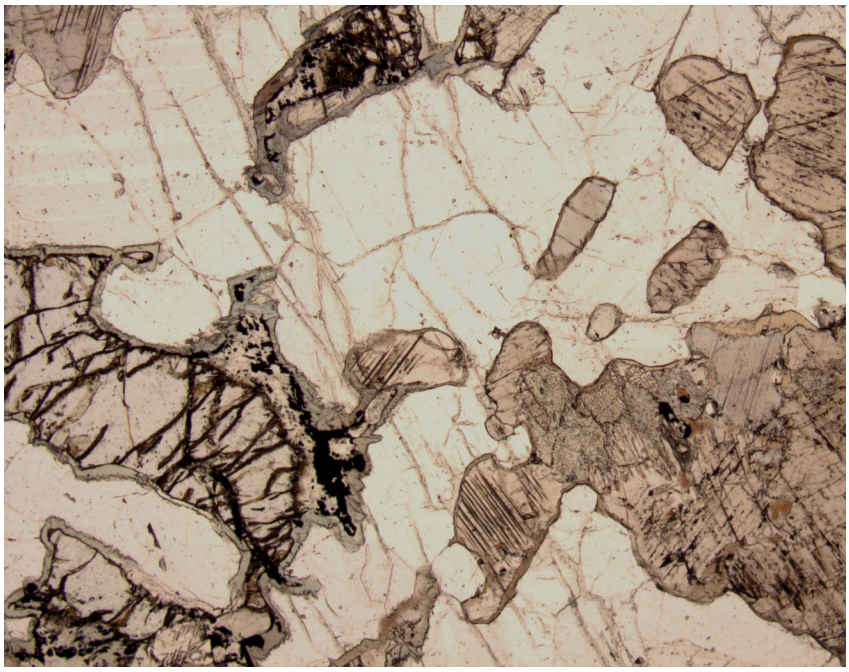

**Figure F36.** Digital photomicrograph of oikocrystic clinopyroxene enclosing subhedral plagioclase grains in medium-grained olivine gabbro (Sample 179-1105A-4R-3, 46–60 cm). Cross-polarized light; field of view = 5.5 mm.

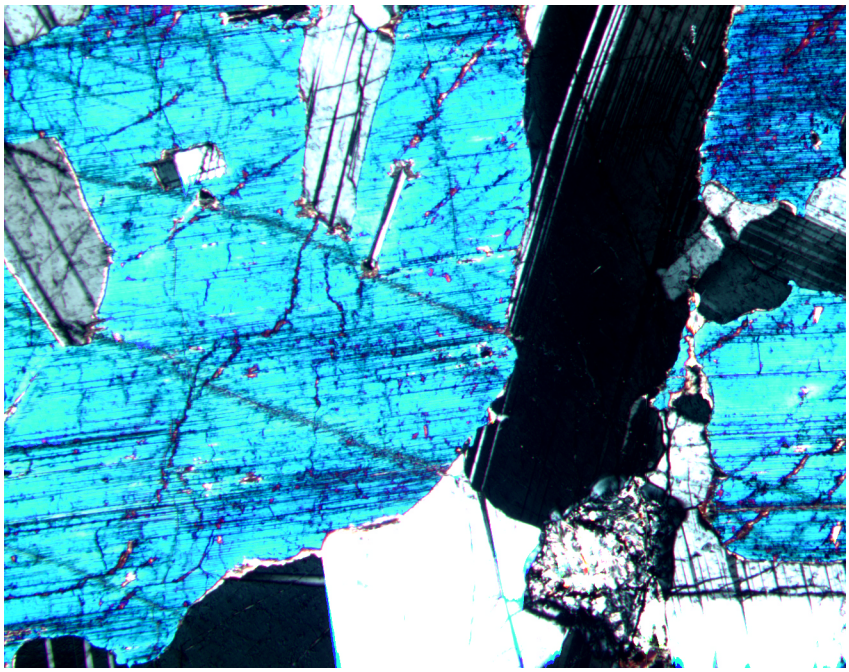

**Figure F37.** Close-up photograph illustrates poikilitic clinopyroxene oikocrysts enclosing plagioclase laths (interval 179-1105A-28R-2, 36–52 cm).

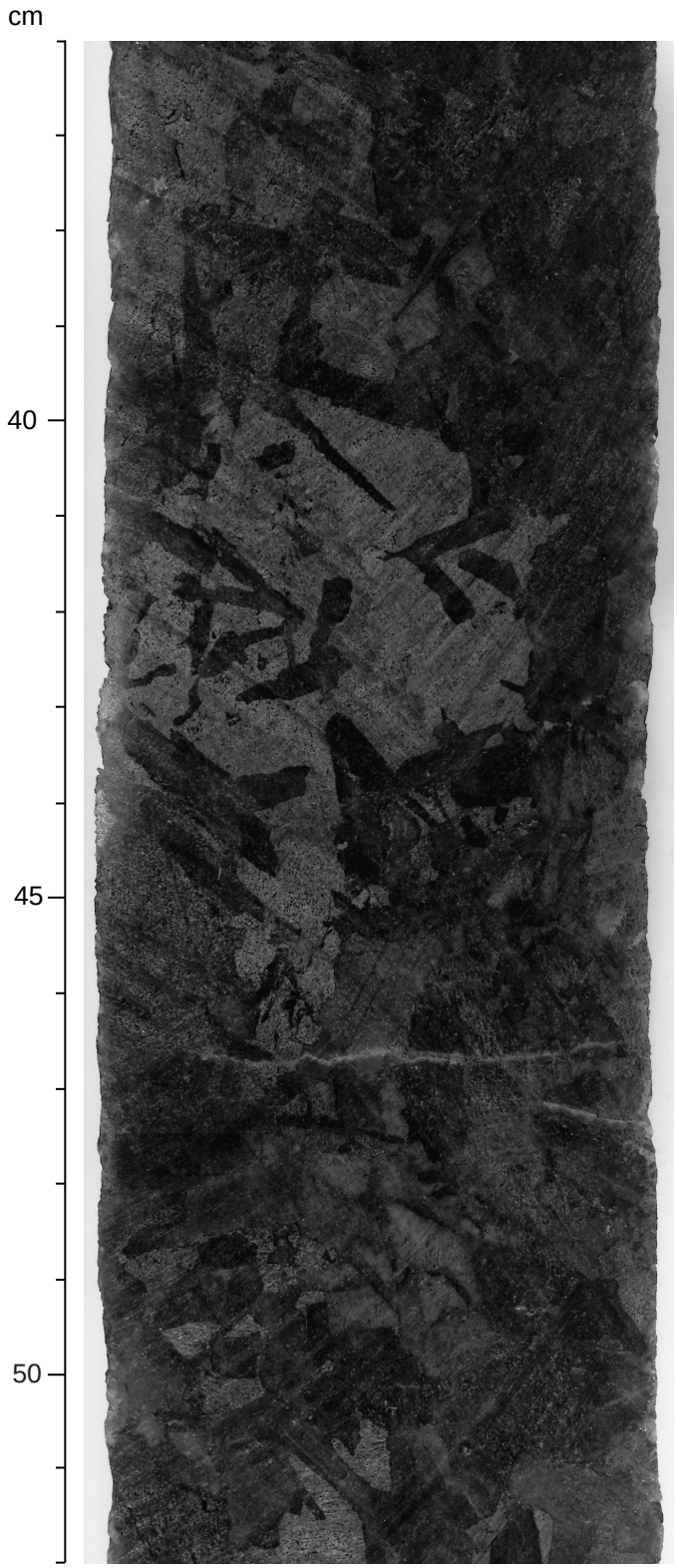

**Figure F38.** Digital photomicrograph of deformation bands in olivine in coarse-grained olivine gabbro (Sample 179-1105A-1R-4, 137–141 cm). Cross-polarized light; field of view = 5.5 mm.

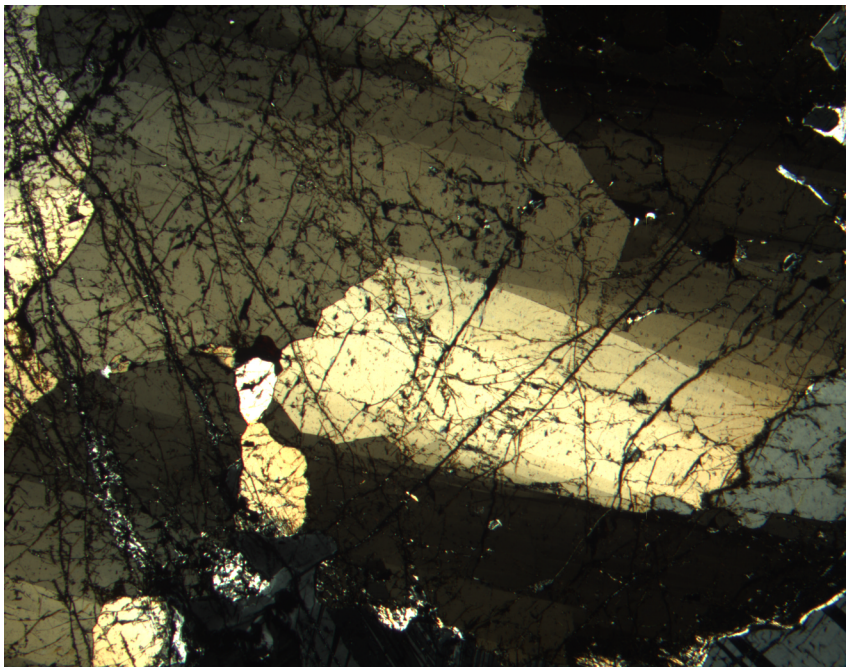

**Figure F39.** Recrystallized granular aggregate of olivine in medium-grained olivine gabbro (Sample 179-1105A-10R-1, 38–42 cm). Cross-polarized light; field of view = 2.75 mm.

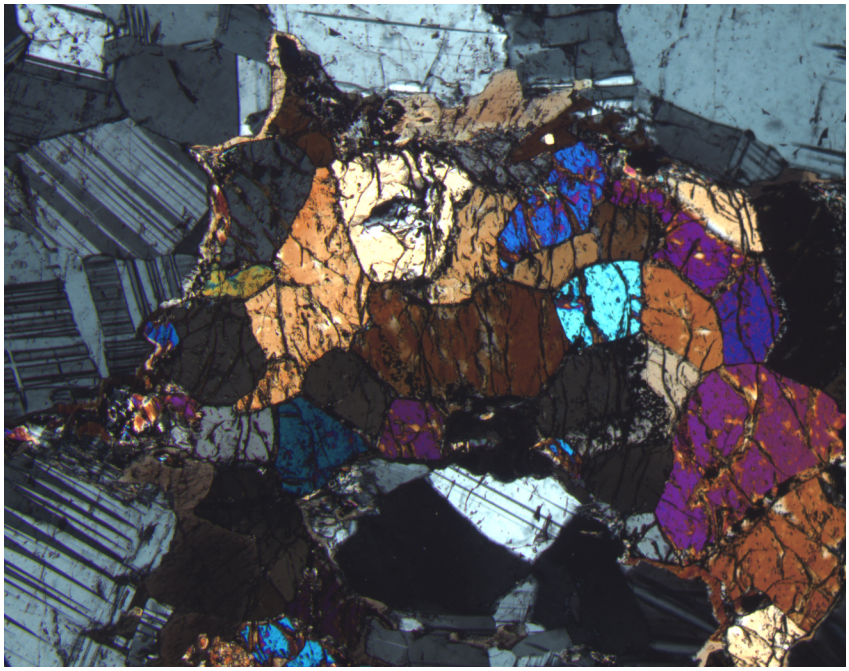

**Figure F40.** Digital photomicrograph of consertal intergrowth of clinopyroxene in medium-grained olivine gabbro (Sample 179-1105A-3R-1, 51–54 cm). Cross-polarized light; field of view = 2.75 mm.

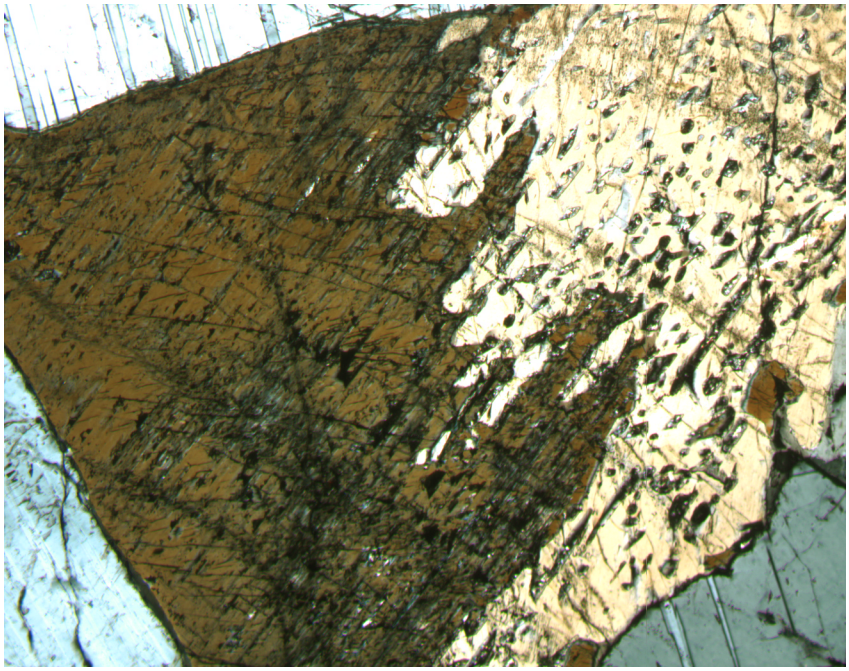

**Figure F41.** Digital photomicrograph of brown hornblende rim surrounding clinopyroxene and Fe-Ti oxides in pegmatitic gabbro (Sample 179-1105A-1R-4, 141–144 cm). Plane-polarized light; field of view = 1.4 mm.

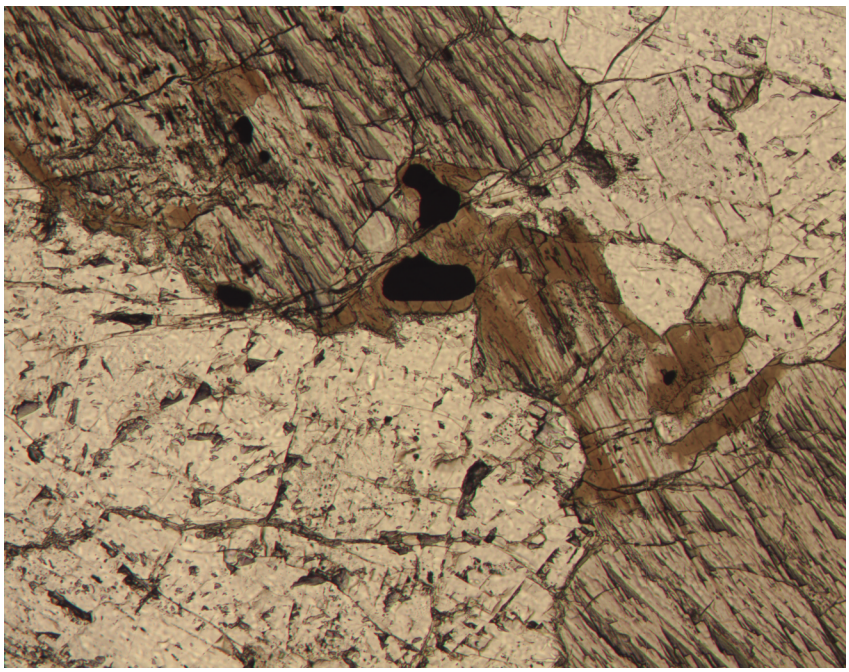

**Figure F42.** Digital photomicrograph showing symplectic intergrowth between clinopyroxene and plagioclase in medium-grained granular gabbro (Sample 179-1105A-8R-3, 53–56 cm). Cross-polarized light; field of view = 1.4 mm.

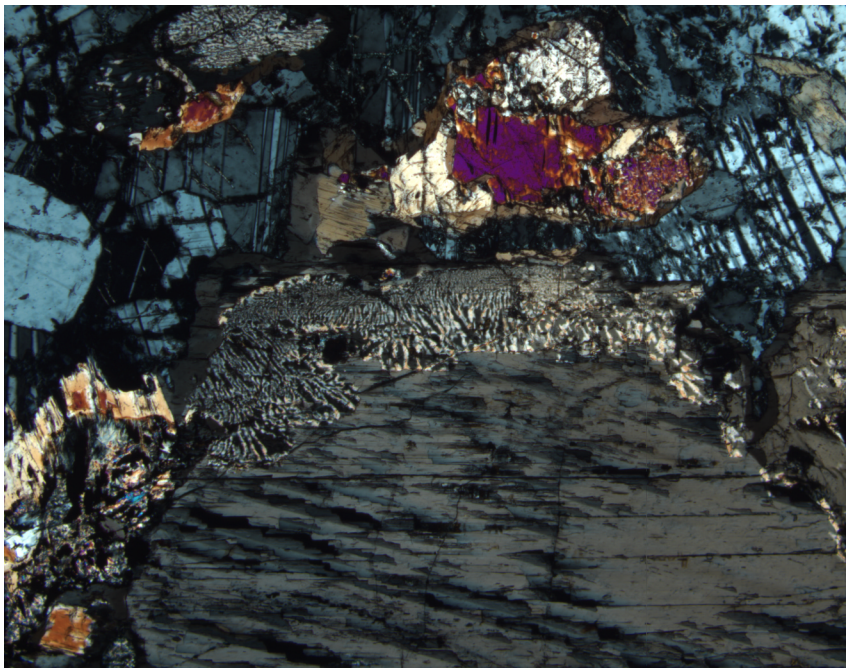

**Figure F43.** Digital photomicrograph showing complex zoned plagioclase in otherwise adcumulate textured and laminated, fine-grained olivine gabbro (Sample 179-1105A-12R-2, 50–53 cm). Same sample as illustrated in Figure F27. Cross-polarized light; field of view = 2.75 mm.

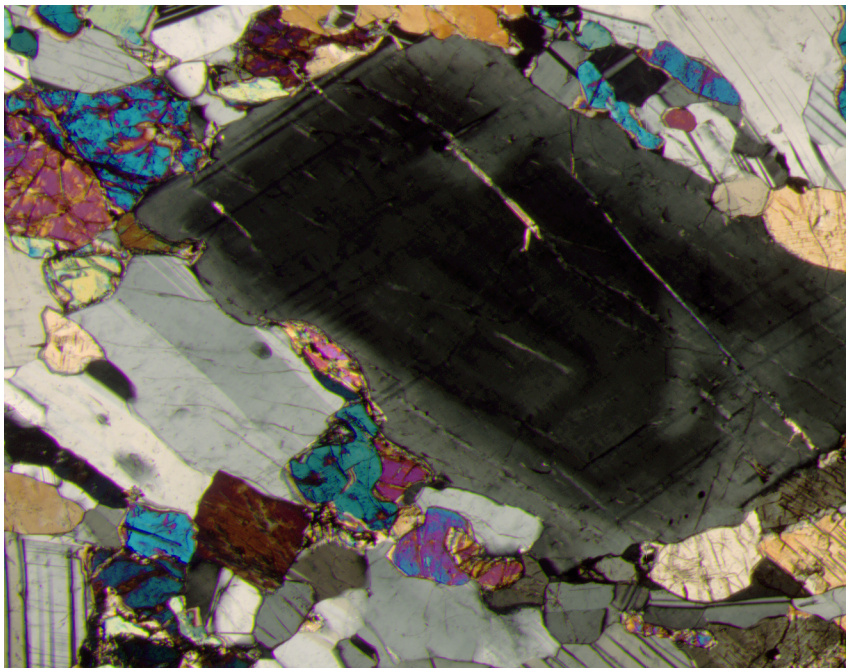

**Figure F44.** Digital photomicrograph showing an orthopyroxene with opaque inclusion in coarse-grained oxide- and olivine-bearing gabbronorite (Sample 179-1105A-22R-2, 74–78 cm). Plane-polarized light; field of view = 5.5 mm.

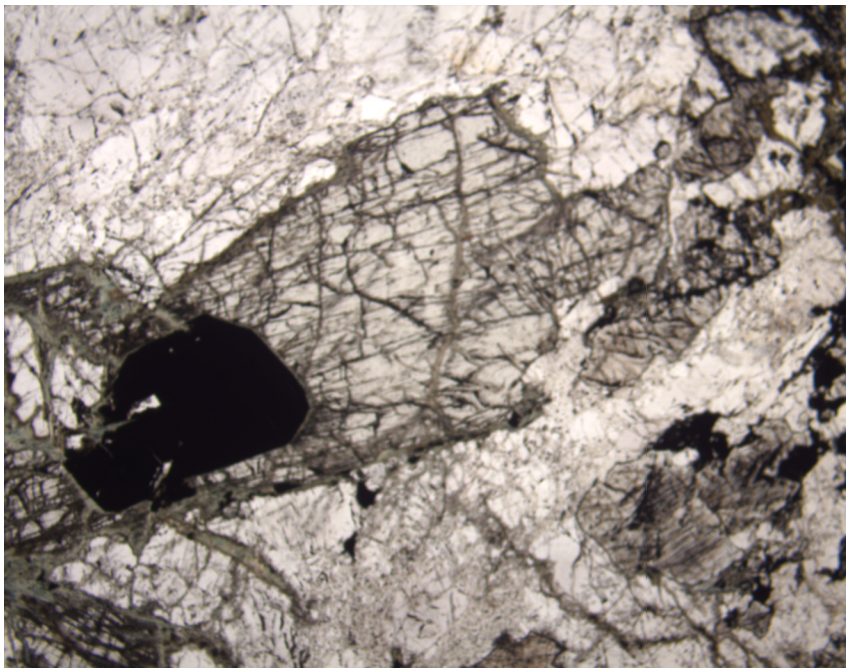

**Figure F45.** Digital photomicrograph of interstitial Fe-Ti oxides and disseminated sulfide grains in an orthopyroxene-bearing oxide gabbro (Sample 179-1105A-7R-3, 33–36 cm). Reflected light; field of view = 5.5 mm.

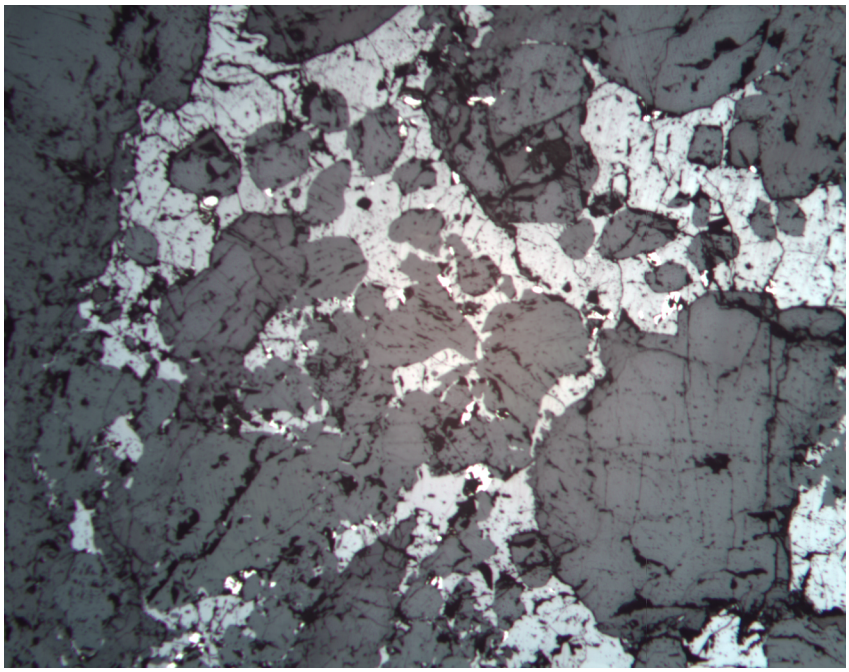

**Figure F46.** Digital photomicrograph of titanite (translucent, high relief) adjacent to and intergrown with Fe-Ti oxide in medium-grained olivine-bearing oxide gabbro (Sample 179-1105A-4R-4, 57–62 cm). Plane-polarized light; field of view = 35 µm.

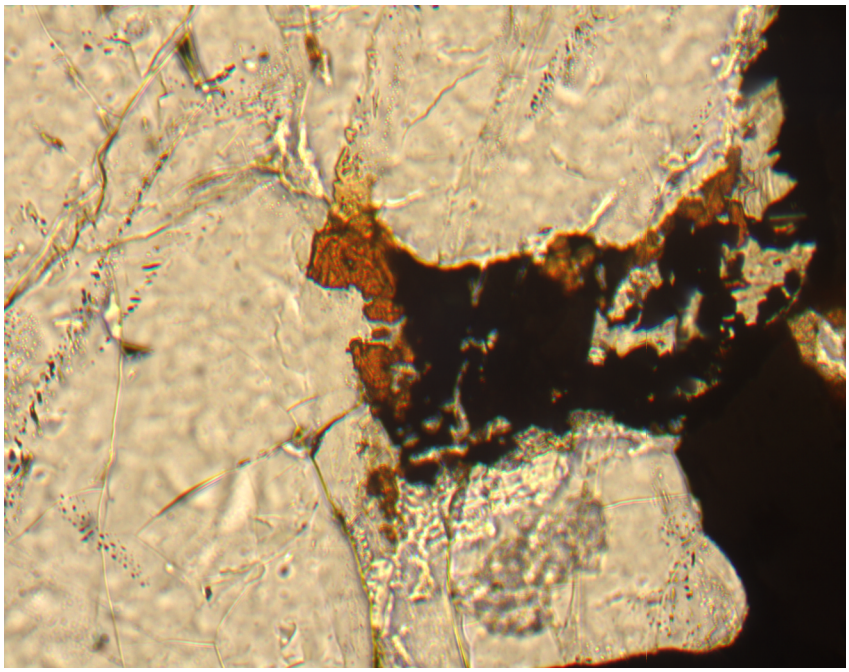

**Figure F47.** Digital photomicrograph of a cluster of apatite included in amphibole and Fe-Ti oxide in coarse-grained olivine-bearing oxide gabbro (Sample 179-1105A-4R-4, 57–62 cm). Plane-polarized light; field of view = 2.75 mm.

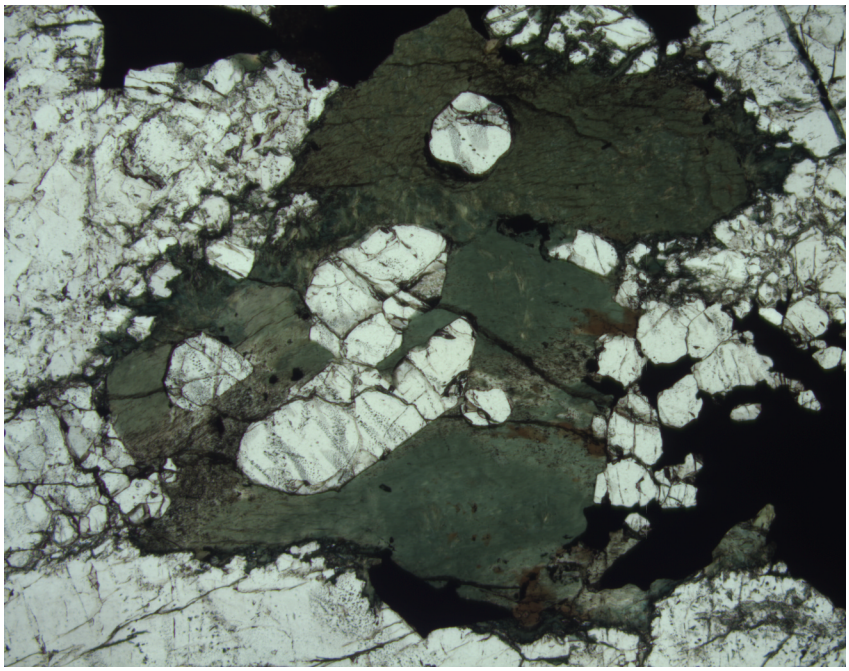

**Figure F48.** Digital photomicrograph of fluid inclusions with vapor bubble and halite daughter in apatite (Sample 179-1105A-4R-4, 57–62 cm). Plane-polarized light; field of view = 35 µm.

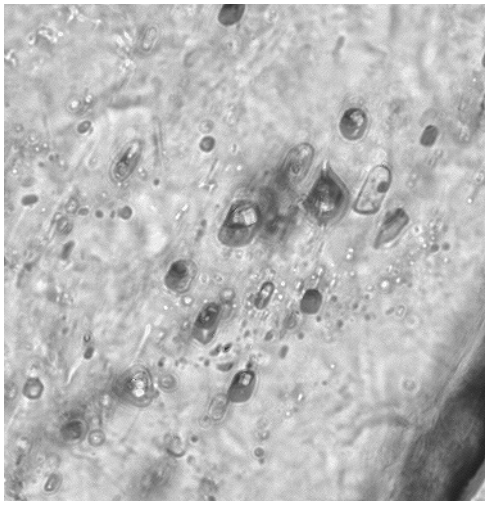

**Figure F49.** Digital photomicrograph of clinopyroxene with uncommon {001} exsolution lamella and twin-plane parallel to the c-axis in medium oxide gabbro (Sample 179-1105A-10R-2, 85–88 cm). The twin plane is located close to the opaque phase on the upper right of view and runs from the upper left to lower right. Most clinopyroxenes in Hole 1105A samples show exsolution along {100}. Cross-polarized light; field of view = 5.5 mm.

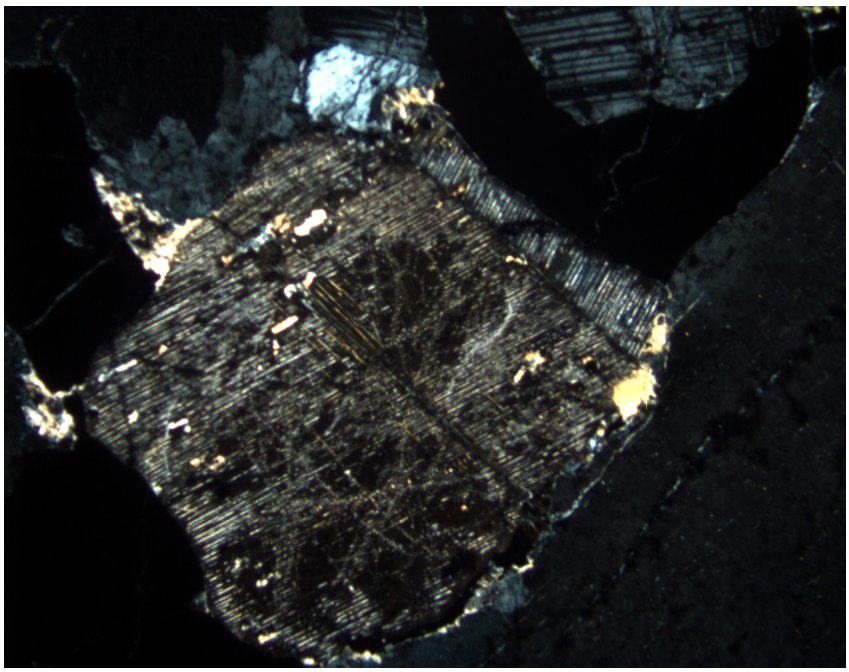

**Figure F50.** Downhole compositional variation in selected major oxides from Table T15. Solid squares = analyses from oxide gabbro, solid circles = oxide olivine gabbro, × symbols = gabbro, and open circles = olivine gabbro.

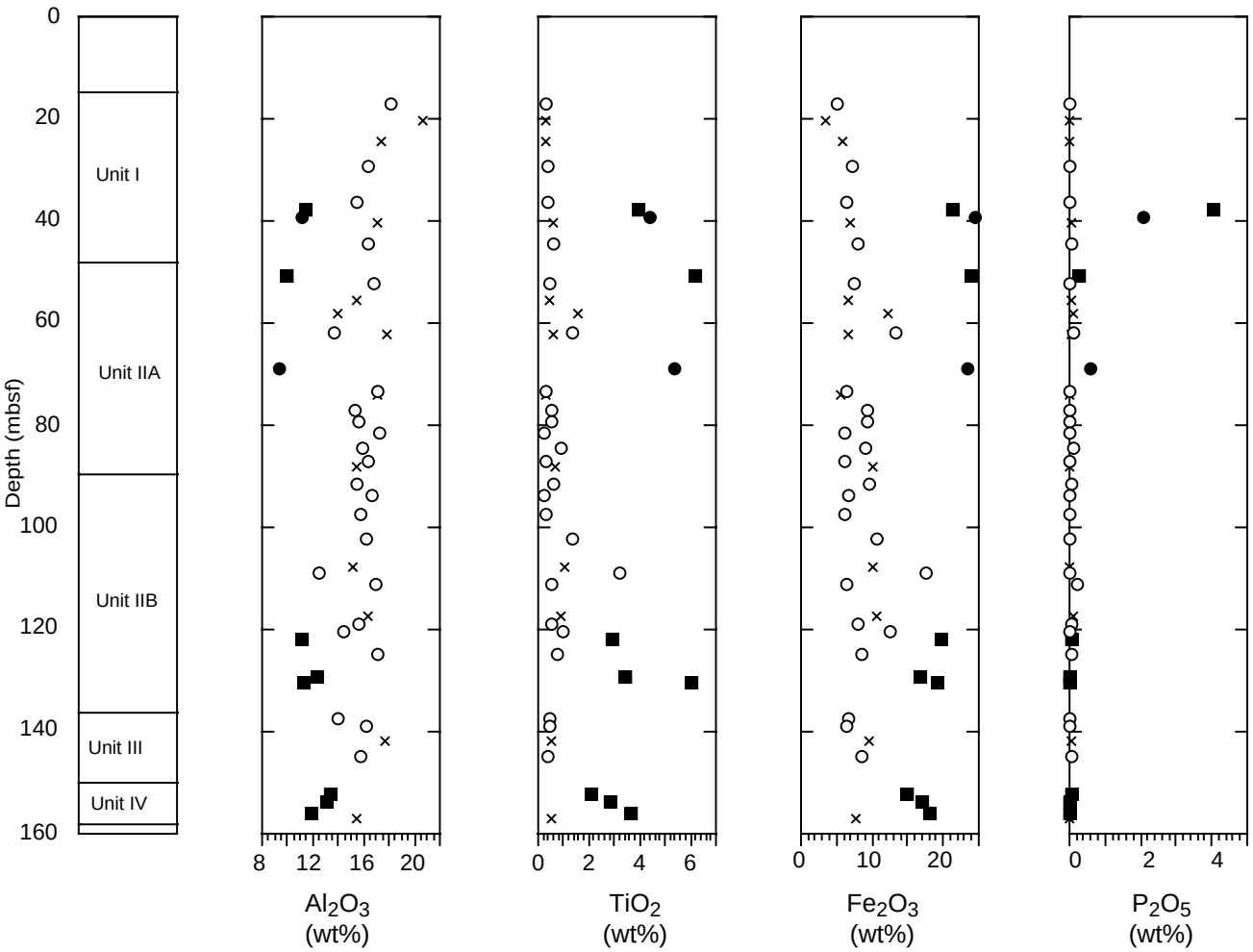

**Figure F51.** Downhole compositional variation in selected trace elements from Table T15. The Nb values shown for olivine gabbros are mostly at or below lower limit of detection. Symbols as in Figure F50.

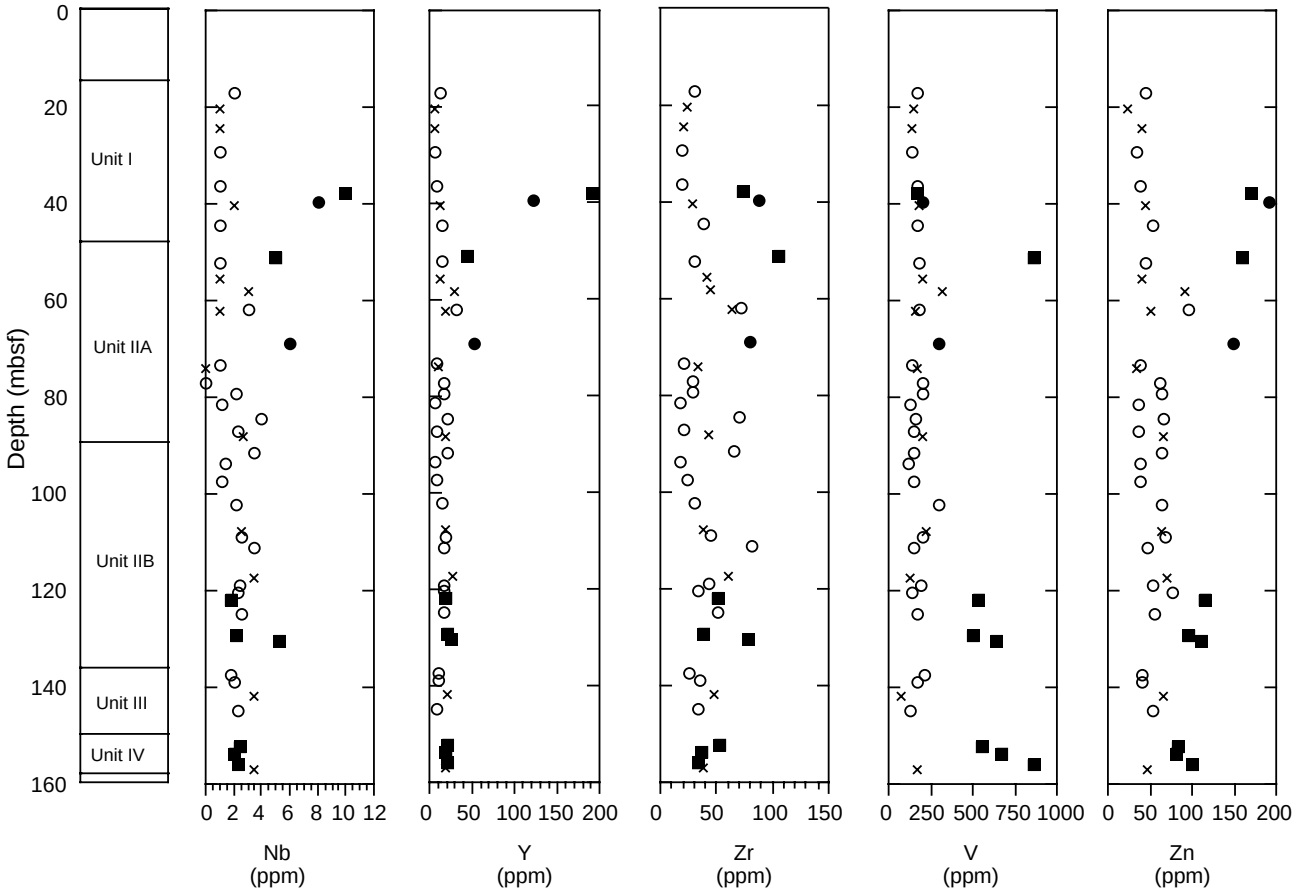

**Figure F52.** Downhole compositional variation in compatible trace elements Ni and Cr, MgO, and Mg# from Table T15. Symbols as in Figure F50.

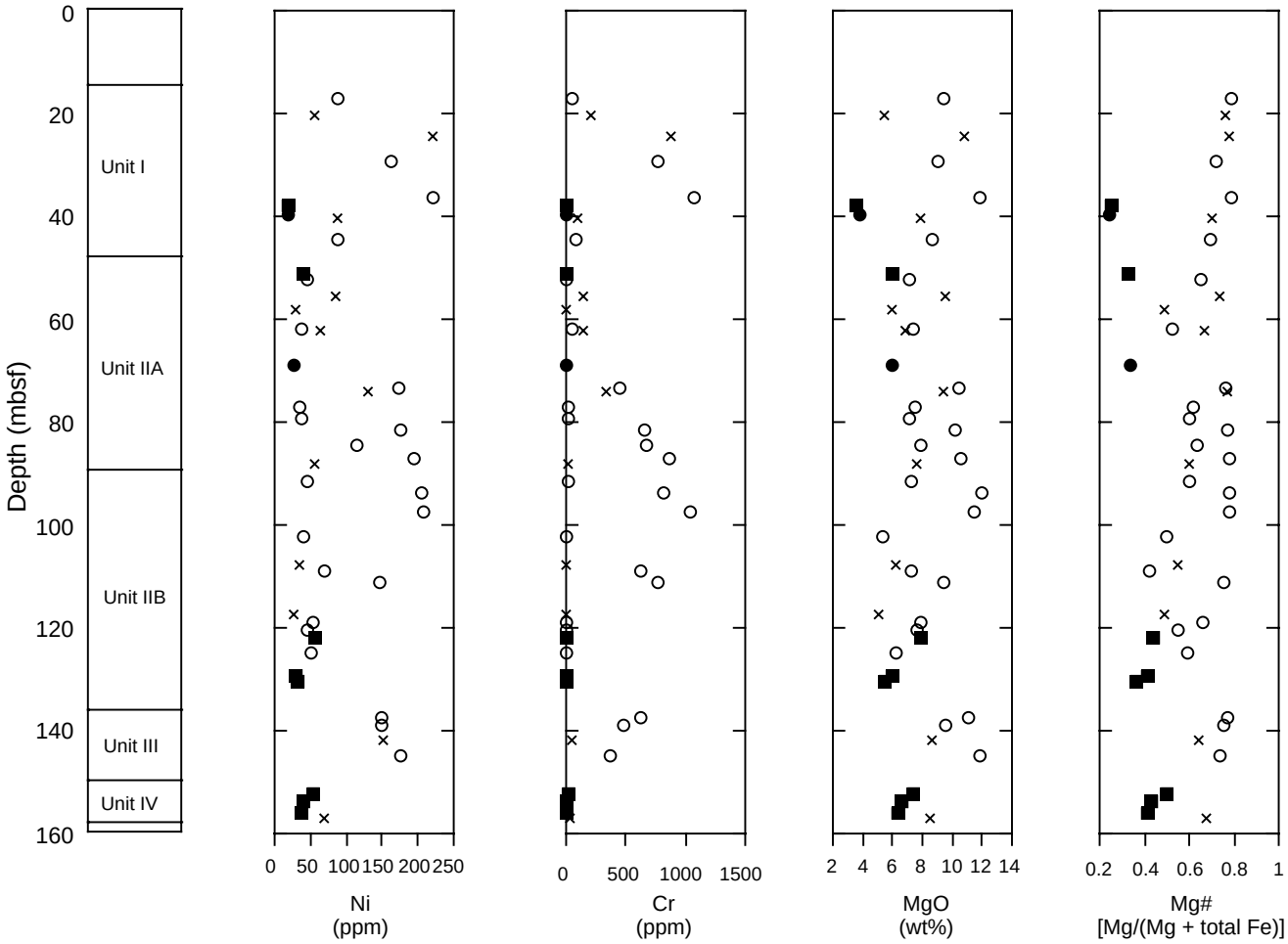

**Figure F53.** Close-up core photograph shows an example of random orientation of coarse-grained and elongate subhedral plagioclase laths of igneous origin with space-filling clinopyroxene. Note no sign of compaction of plagioclase laths or their preferred dimensional orientation, although strong shape anisotropy characterizes individual crystals (interval 179-1105A-25R-2, 48–81.5 cm).

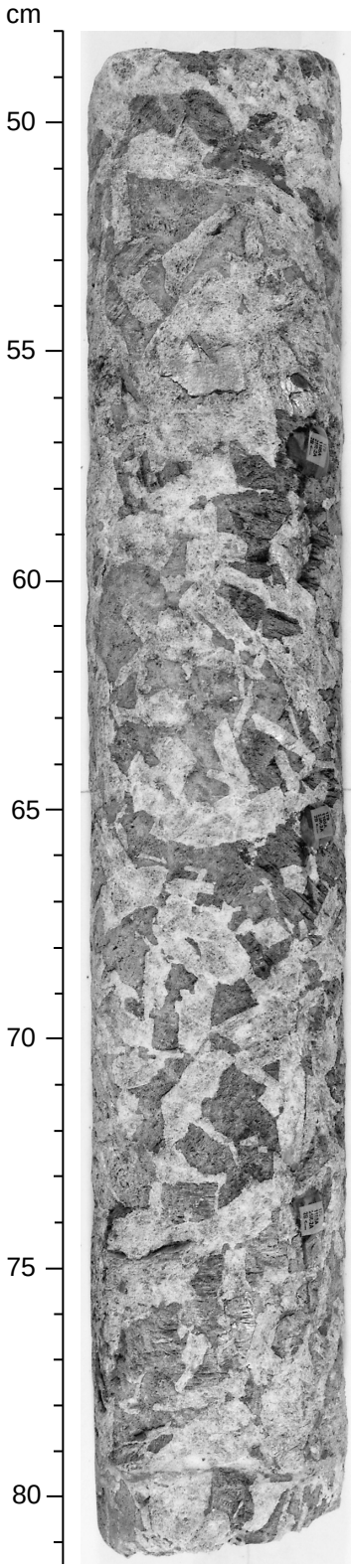

**Figure F54.** Digital photomicrograph of Sample 179-1105A-12R-2 (Piece 5, 50–53 cm), shows an igneous lamination defined by the preferred dimensional orientation of elongate clinopyroxene and tabular plagioclase. Lamination is oriented from upper left to lower right corner. Also note core-rim zoning in larger plagioclase (near extinction) and magmatic twins in clinopyroxene (upper left). Also note some plagioclase crystals contain deformation twins, which generally effect most igneous textures in cores from Hole 1105A (cross-polarized light; field of view = 5.5 mm).

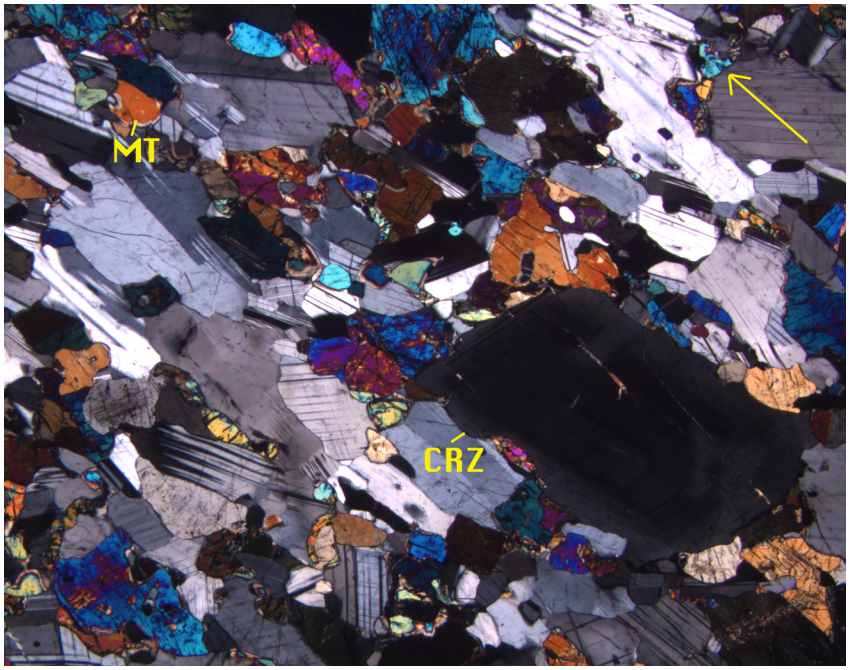

**Figure F55.** Digital photomicrograph of Sample 179-1105A-12R-2 (Piece 5, 50–53 cm), shows igneous lamination (approximately horizontal in photo) defined by the preferred dimensional orientation of elongate clinopyroxene and tabular plagioclase. Note albite and Carlsberg growth twins in plagioclase with blunt ends, which most commonly terminate at grain edges (cross-polarized light; field of view = 5.5 m).

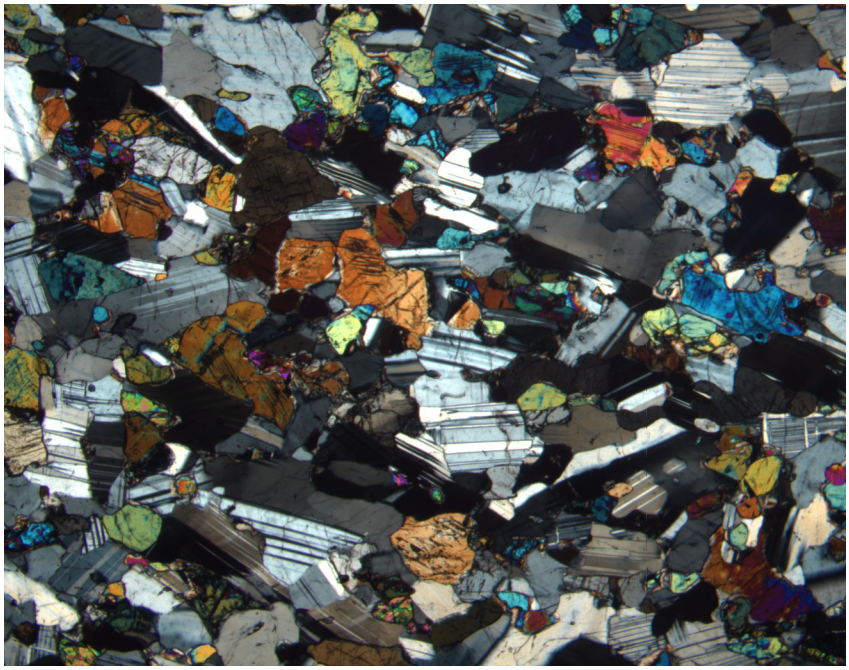

**Figure F56.** Digital photomicrograph of Sample 179-1105A-3R-2, 16–20 cm, showing preservation of euhedral to subhedral grain shapes of plagioclase included within a clinopyroxene oikocryst (cross-polarized light; field of view = 2.75 mm).

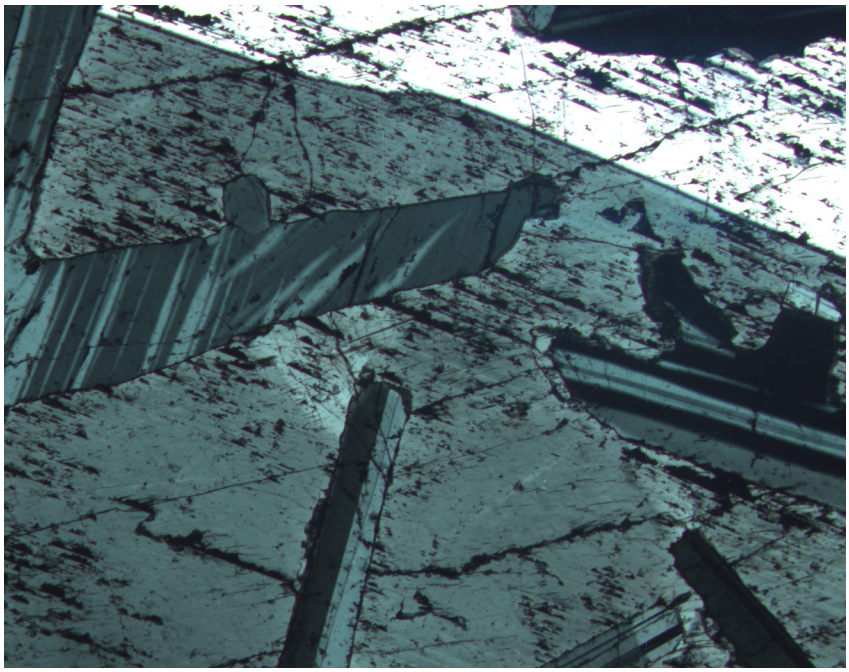

**Figure F57.** Ductile shear zone at a dipping contact between a coarse-grained gabbro and a pegmatitic gabbro at ~103 cm on the core face (close-up core photograph of interval 179-1105A-29R-1, 95–118 cm).

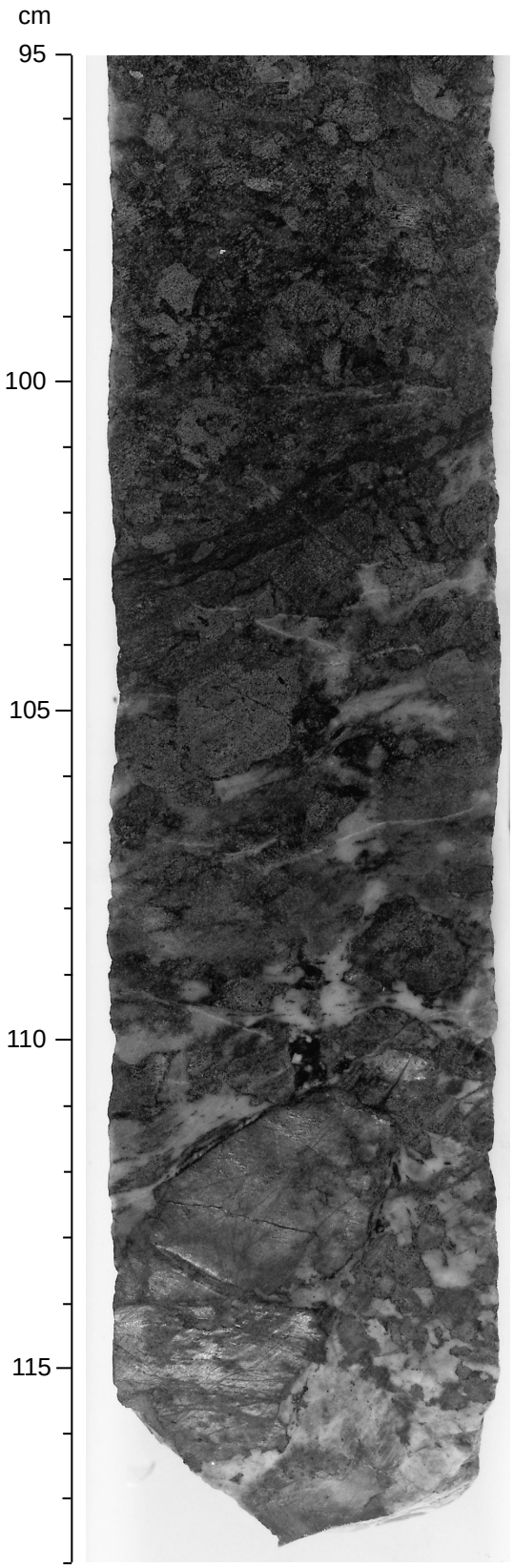

**Figure F58.** Dipping oxide-mineral–rich band (interval ~66–71 cm) with up to 25%–30% opaque oxide minerals. Note the irregular contact of the oxide band with the gabbro above and below (close-up core photograph of interval 179-1105A-13R-1, 59–75 cm).

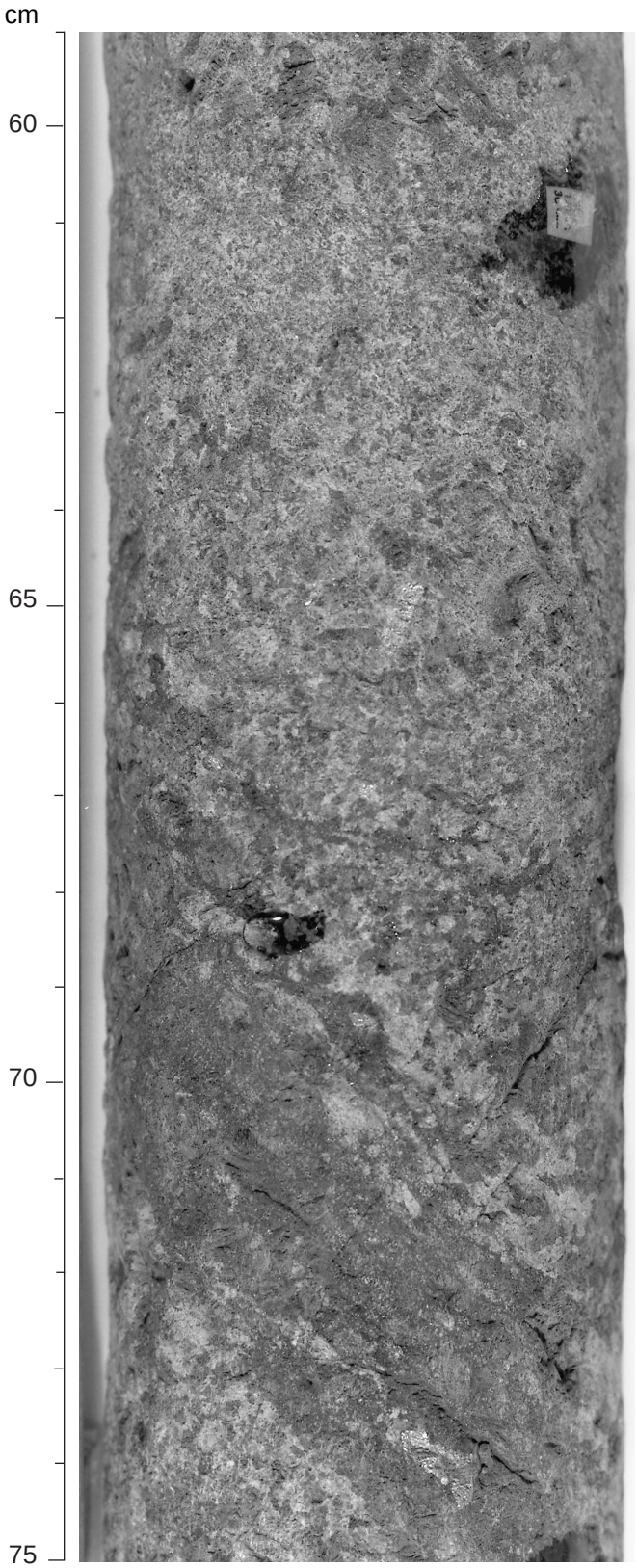

**Figure F59.** Digital photomicrograph of Sample 179-1105A-4R-4, 57–62 cm, shows recrystallization of plagioclase neoblasts along subgrain boundaries in large plagioclase at the initial stages of neoblast formation in a coarse-grained gabbro. Note plagioclase deformation twins and curvature into the recrystallization zone (cross-polarized light; field of view = 5.5 mm).

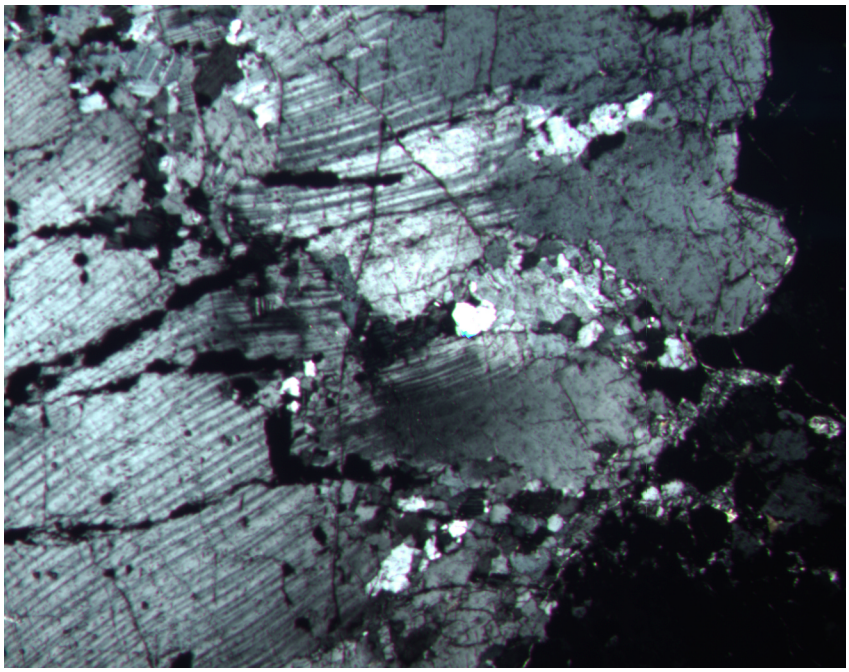

**Figure F60.** Digital photomicrograph of Sample 179-1105A-30R-2, 109–113 cm, shows even dispersion of grain sizes in a dynamically recrystallized fine-grained gneissic gabbroic rock. Note highly strained plagioclase (complex undulose extinction and subgrain structure) and well-developed foliation defined by the preferred dimensional orientation of both plagioclase and clinopyroxene. Foliation is oriented upper left to bottom right (cross-polarized light; field of view = 5.5 mm).

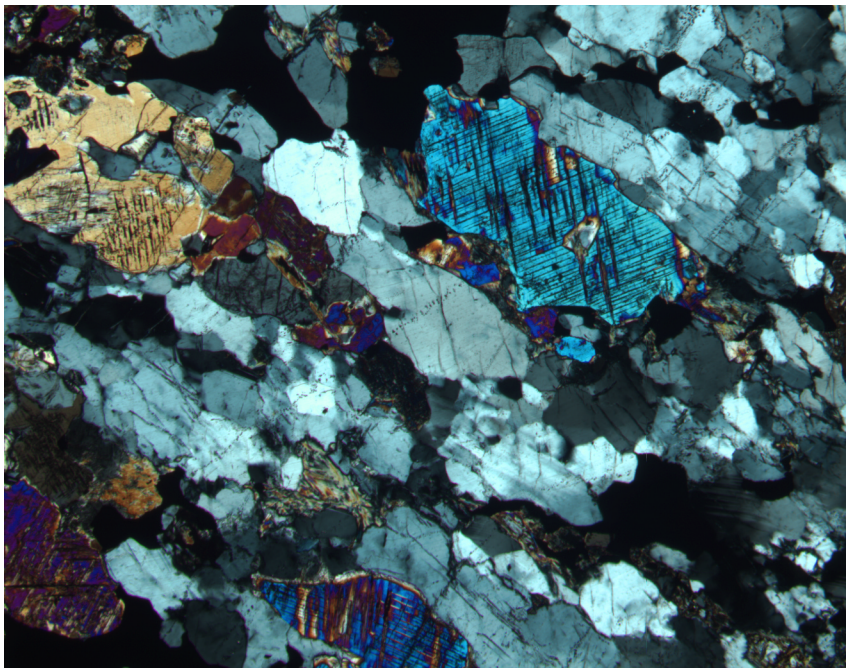

**Figure F61.** Close-up core photographs showing strong crystal-plastic porphyroclastic foliation inclined ~30° in meta-oxide gabbros. **A.** Interval 179-1105A-25R-1, 64–86 cm. (Continued on next two pages.)

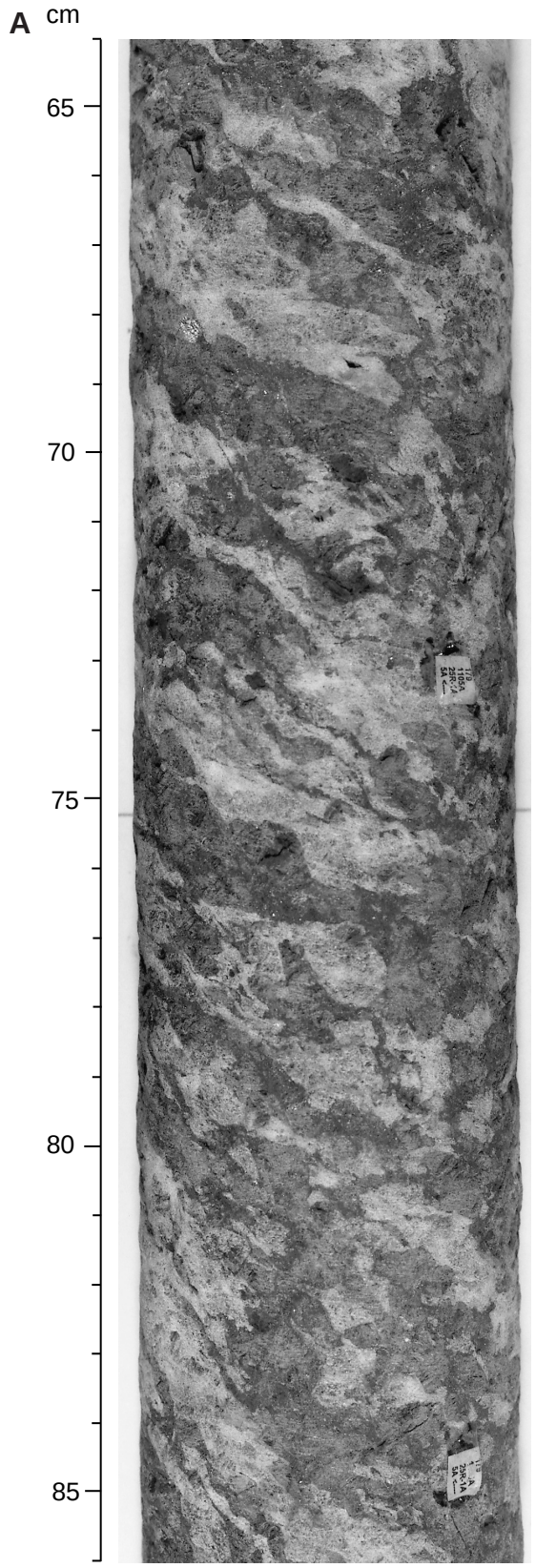

**Figure F61 (continued). B.** Interval 179-1105A-25R-1, 49–104 cm.

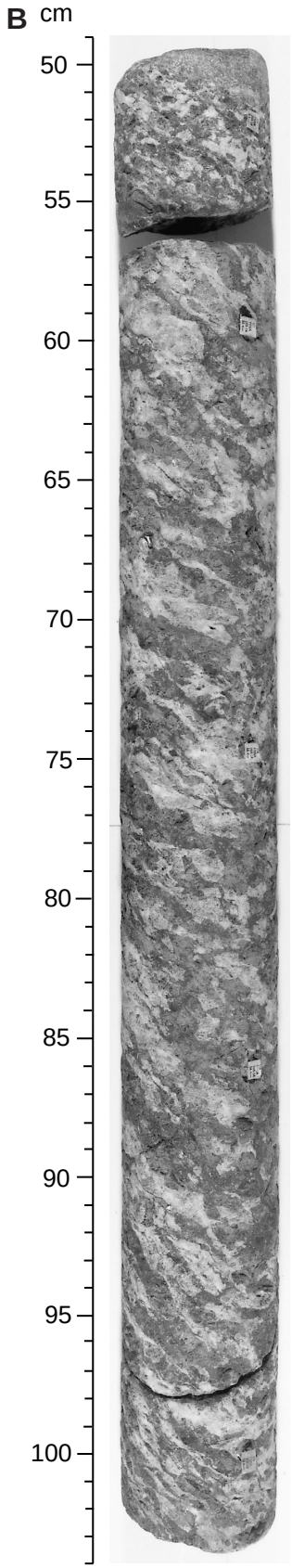

**Figure F61 (continued).** C. Interval 179-1105A-17R-4, 31–44 cm.

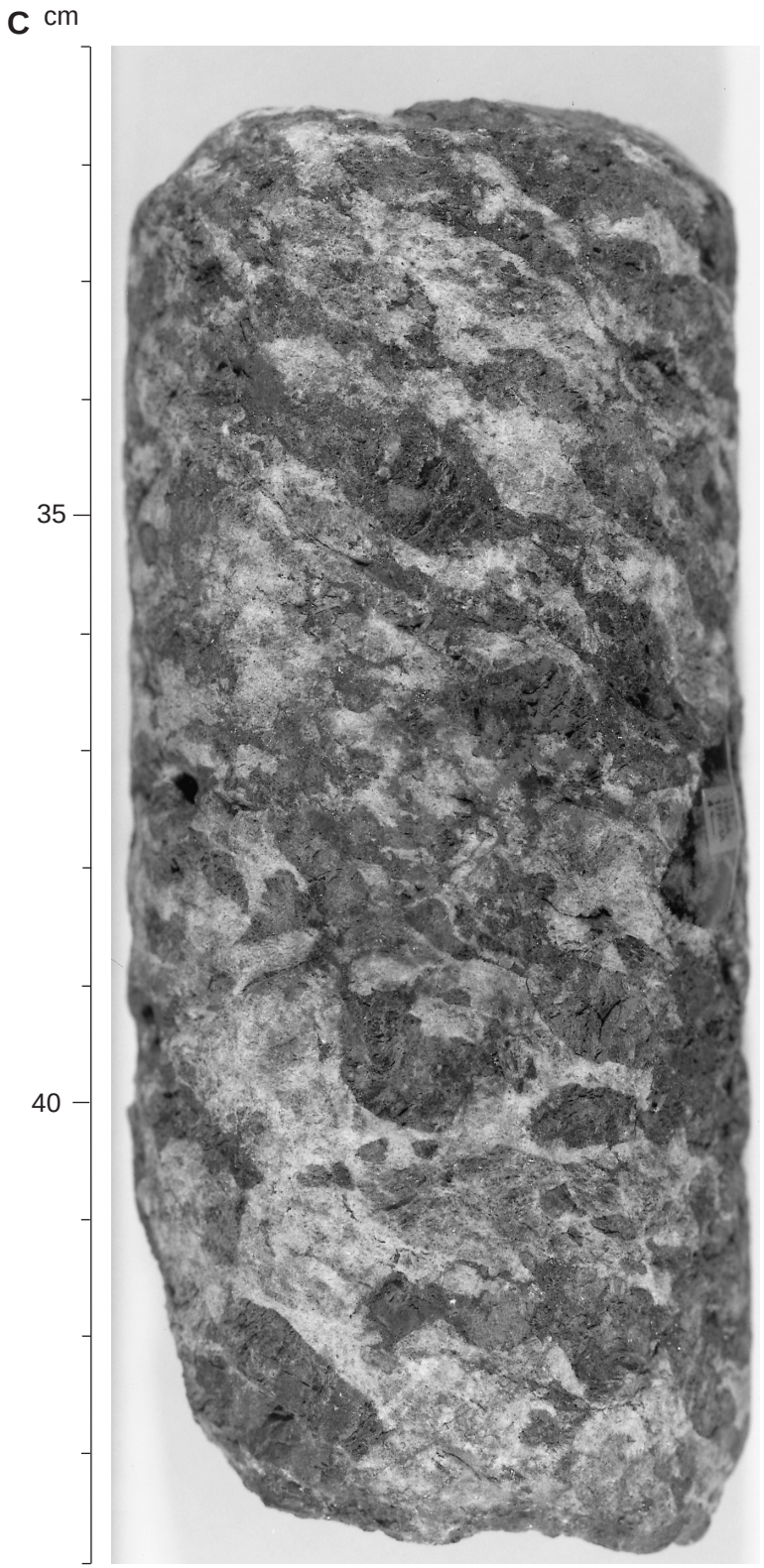

**Figure F62.** Digital photomicrograph of Sample 179-1105A-5R-1, 144–147 cm, displays porphyroclastic oxide-gabbro with two large clinopyroxene porphyroclasts that show little internal strain, yet plagioclase is completely recrystallized to fine-grained neoblasts, except for the subhedral plagioclase included in pyroxene, which was protected by from recrystallization (cross-polarized light; field of view = 5.5 mm).

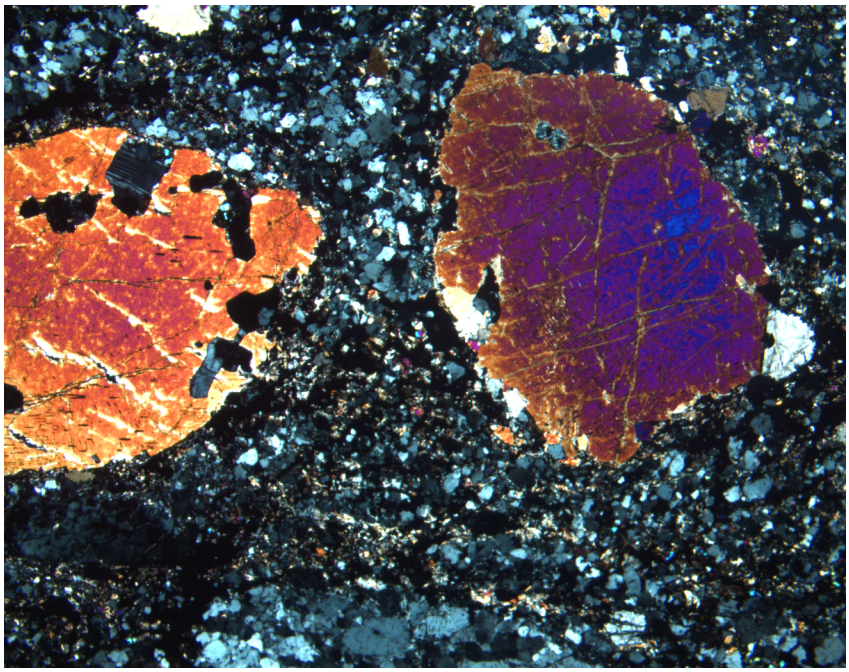

**Figure F63.** Digital photomicrograph of Sample 179-1105A-25R-3, 10–13 cm, displays olivine and clinopyroxene porphyroclasts within a matrix of recrystallized plagioclase. Olivine is highly strained and kinked, but clinopyroxene is mildly strained (cross-polarized light; field of view = 5.5 mm).

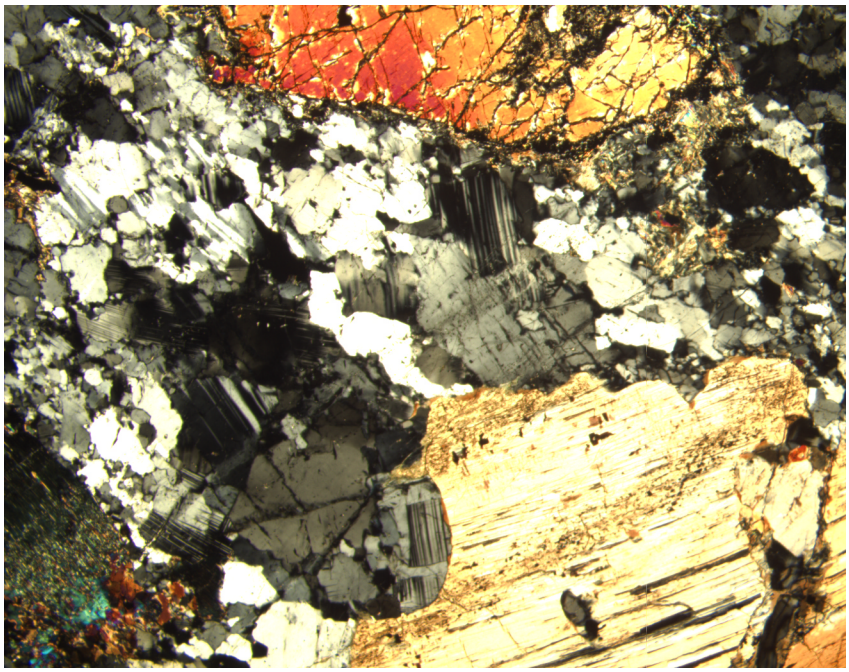

**Figure F64. A.** Porphyroclastic oxide-bearing mylonite showing felsic layering consisting of dynamically recrystallized plagioclase. Darker interlayered bands of recrystallized olivine and plagioclase with large and small porphyroclasts of clinopyroxene. Darkest band with small clinopyroxene porphyroclasts is rich in oxide minerals. Note vertical vein-filled fractures with actinolitic amphibole. Also note microfolds in felsic layers (interval 179-1105A-12R-1, 46–52 cm). (Continued on next page.)

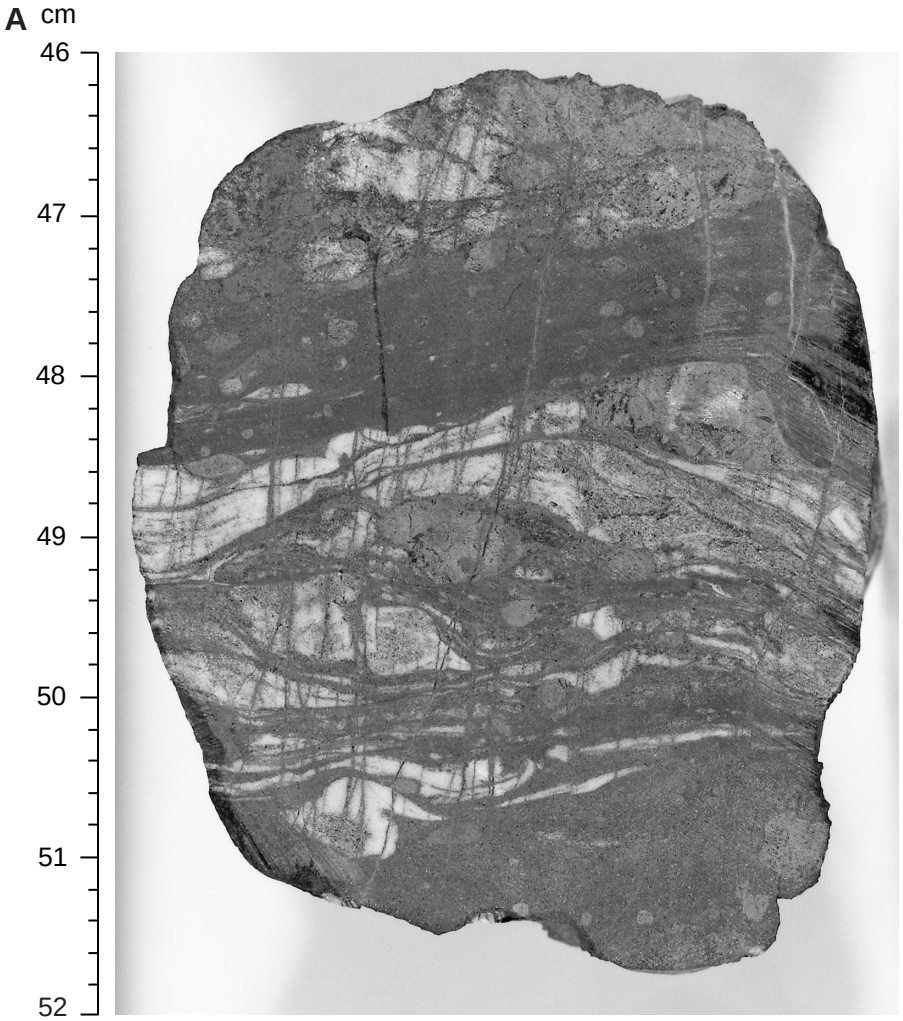

**Figure F64 (continued). B.** Similar layered mylonite from the same region of the core also showing microfolds of felsic bands and alternating pyroxene, oxide, and plagioclase-rich bands (interval 179-1105A-12R-1, 52–58 cm).

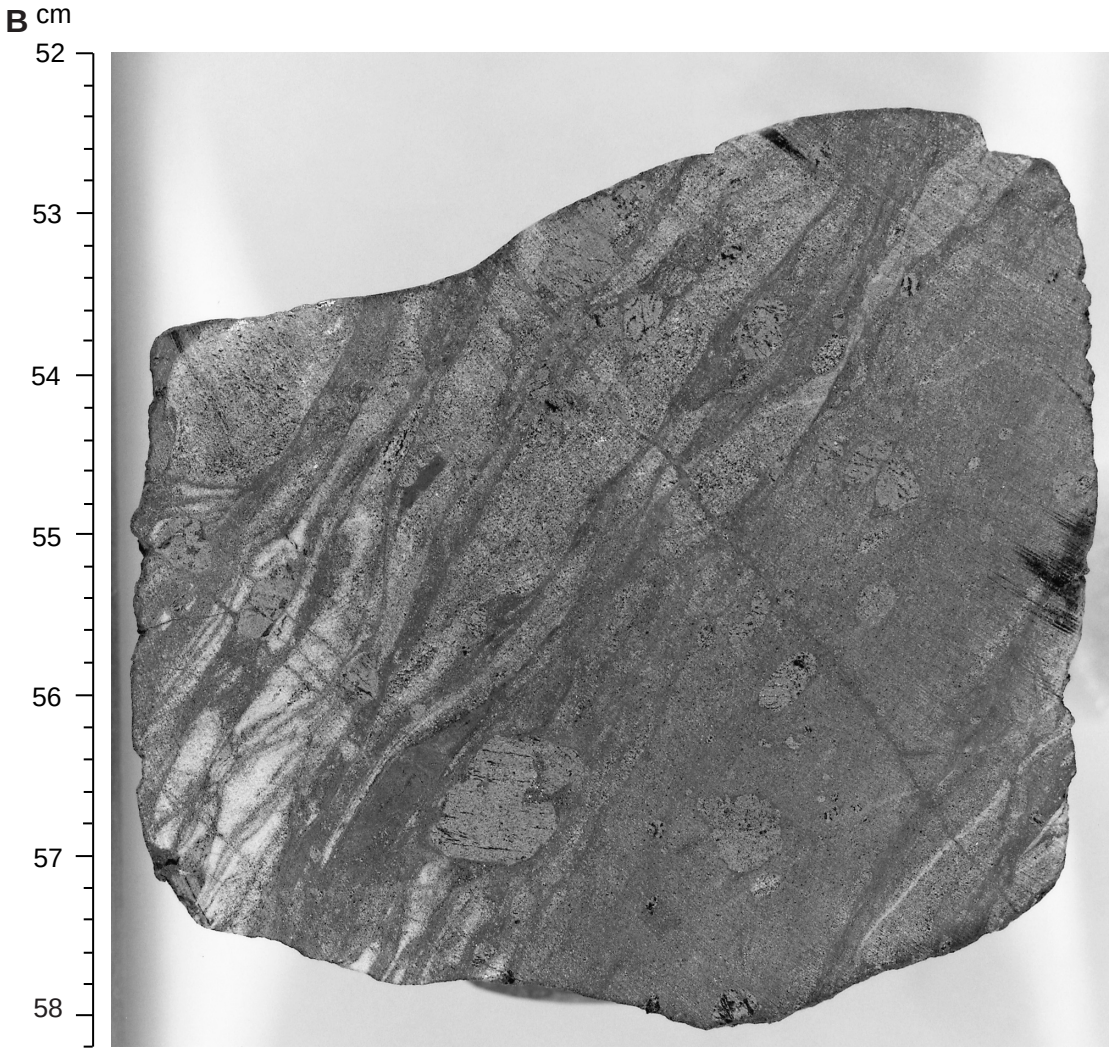

**Figure F65.** Digital photomicrograph of Sample 179-1105A-29R-1, 102–106 cm, shows a mylonite zone marked by oxide, a mylonite band, and a sharp contact between a coarser domain containing porphyroclastic textures with larger plagioclase neoblasts and a finer domain of mylonitic opaque oxide and plagioclase neoblasts surrounding small clinopyroxene porphyroclasts. An opaque oxide-rich zone shows its effect in localizing ductile strain. There is apparently a significant ductility contrast across the domain contact marked by the appearance of oxides. Coarser grained domains (coarser porphyroclastic texture) are affected by brittle synthetic or Riedel shears, which dissect neoblasts and porphyroclasts of plagioclase. Opaque oxide zones only show ductile deformation, and Reidels shears disappear into the oxide zone as they cross the domain contact. Also note dynamic recrystallization of clinopyroxene porphyroclasts in the coarser domain (cross-polarized light; field of view = 5.5 mm).

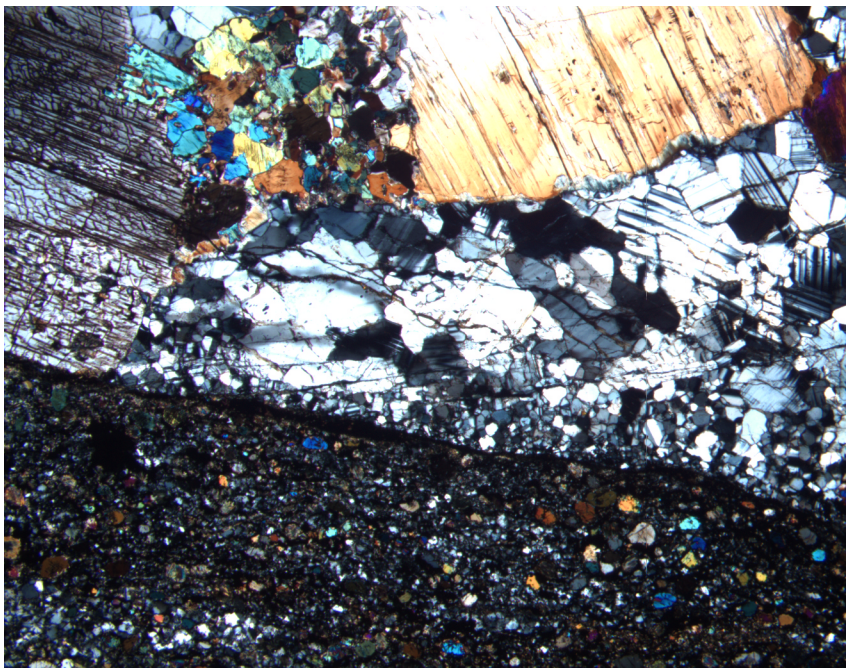

**Figure F66.** Digital photomicrograph of Sample 179-1105A-25R-3, 10–13 cm, shows highly strained ribbon grains of plagioclase in a mylonitic fine-grained matrix (cross-polarized light; field of view = 5.5 mm).

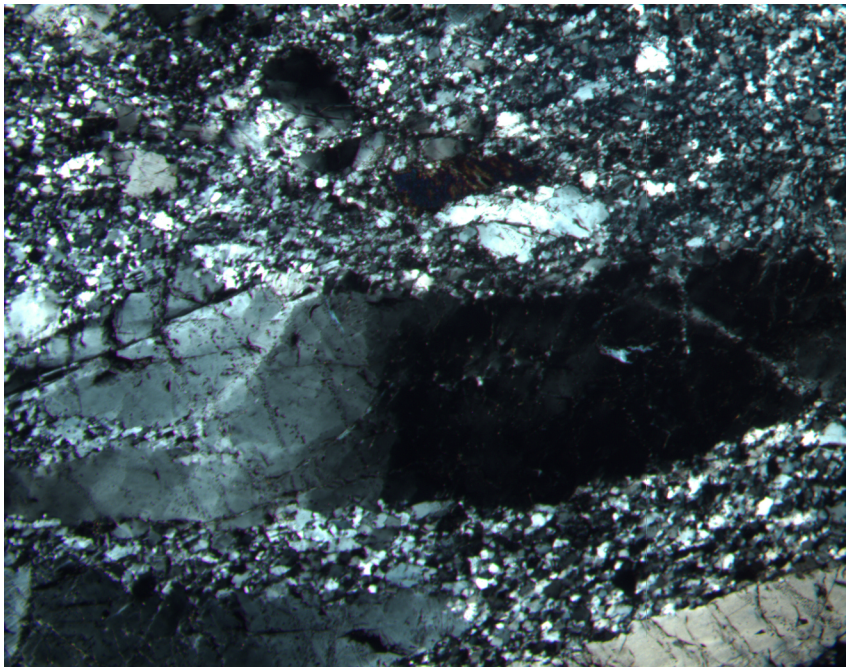

**Figure F67.** Digital photomicrograph of Sample 179-1105A-30R-2, 109–113 cm, showing a clinopyroxene porphyroclast in mylonite. The porphyroclast has asymmetric tails of neoblastic clinopyroxene and indicates a dextral sense of shear (cross-polarized light, field of view = 5.5 mm).

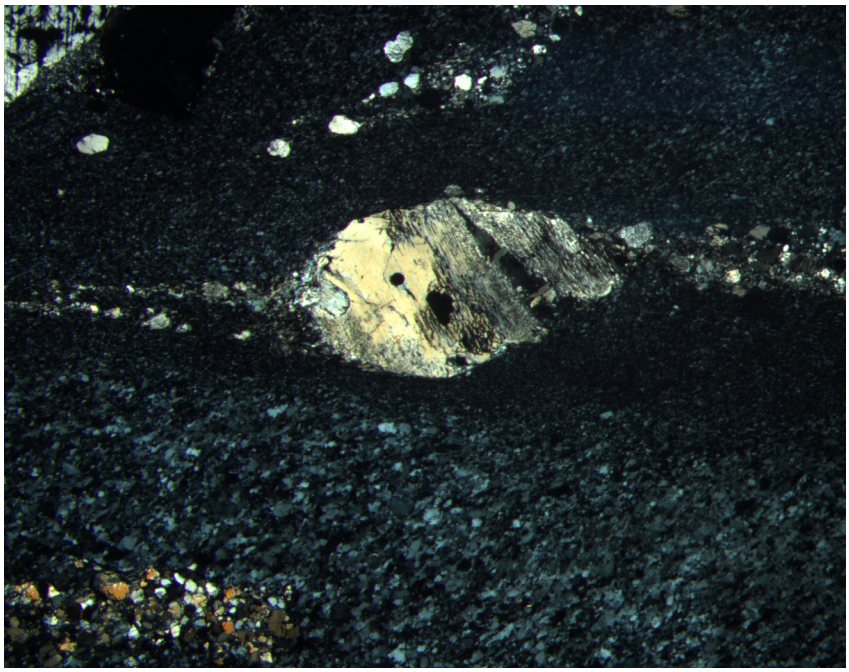

**Figure F68.** Close-up core photograph, interval 179-1105A-25R-2, 129.5–139 cm. Contact between intervals 115 and 116 showing mildly deformed gabbro adjacent to strongly foliated oxide gabbro shear zone. The contact is infiltrated by thin felsic veins that are most likely intruded syn-kinematically. The veins are most highly strained as they approach the margin of the oxide gabbro shear zone where strain is generally localized.

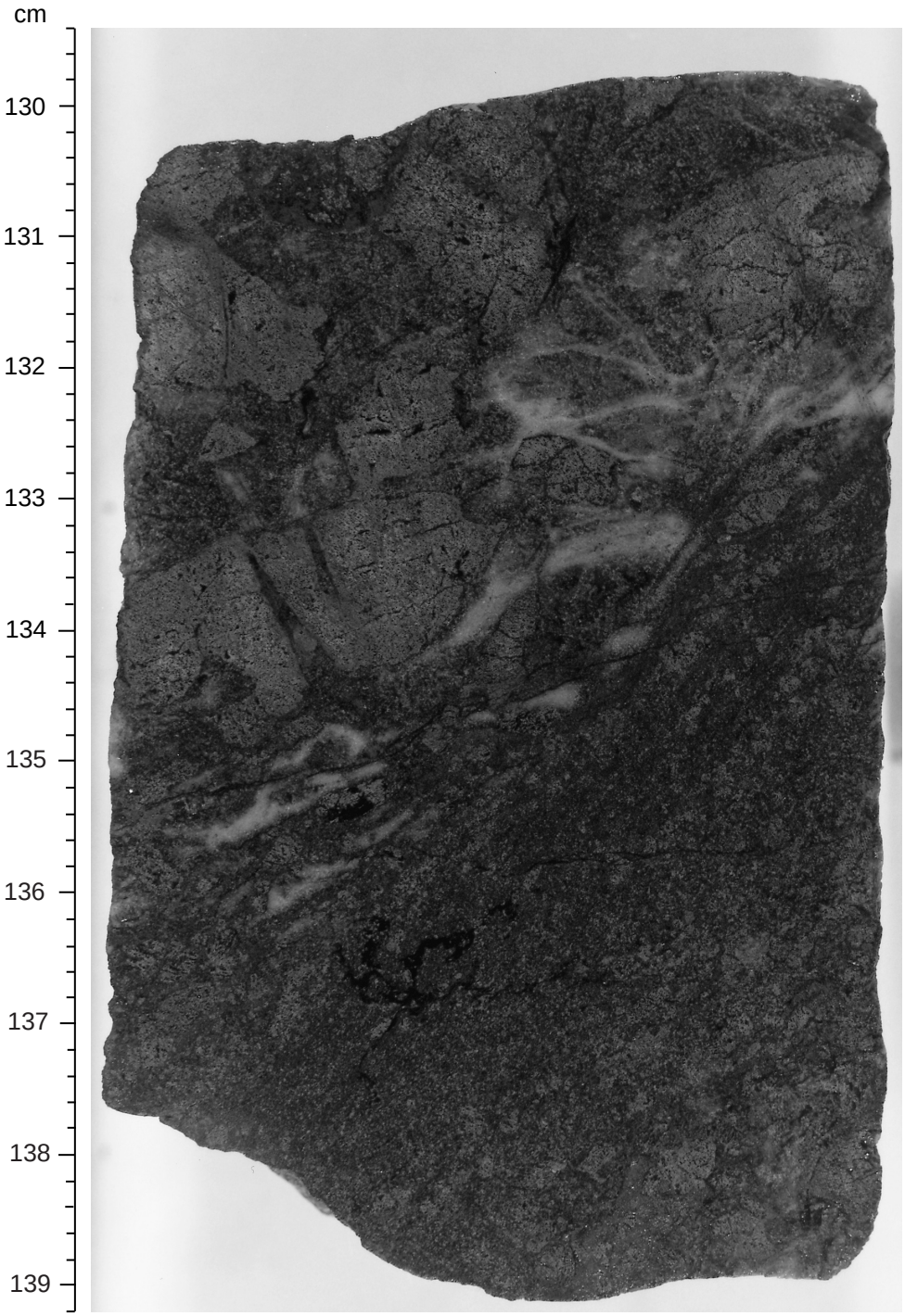

**Figure F69.** Digital photomicrograph of Sample 179-1105A-29R-1, 102–106 cm, showing an oxide-rich mylonitic domain with relatively strain-free small clinopyroxene porphyroclasts surrounded by fine-grained opaque oxide minerals and minor plagioclase neoblasts. Note two generations of fractures. One is truncated at the oxide-rich zone, and one crosscuts the boundary between the coarser porphyroclastic domain and the oxide-rich mylonite domain (cross-polarized light; field of view = 5.5 mm).

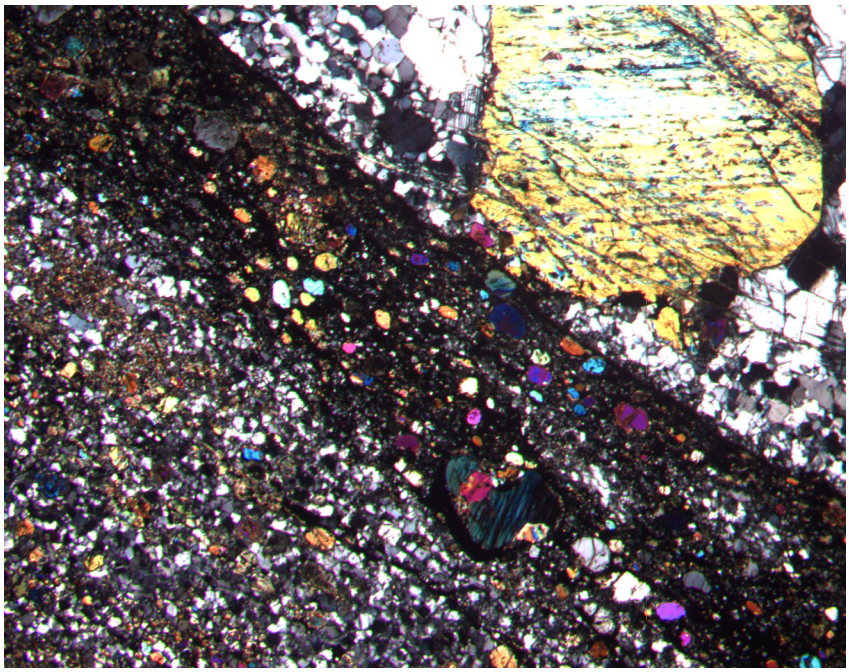

**Figure F70.** Leucocratic gabbro vein intruded into relatively undeformed gabbro. The vein gabbro is affected by crystal-plastic deformation of plagioclase and clinopyroxene. Note clinopyroxene porphyroclasts (dark) show slightly asymmetric tails of neoblastic clinopyroxene (close-up core photograph of interval 179-1105A-4R-1, 77–85 cm).

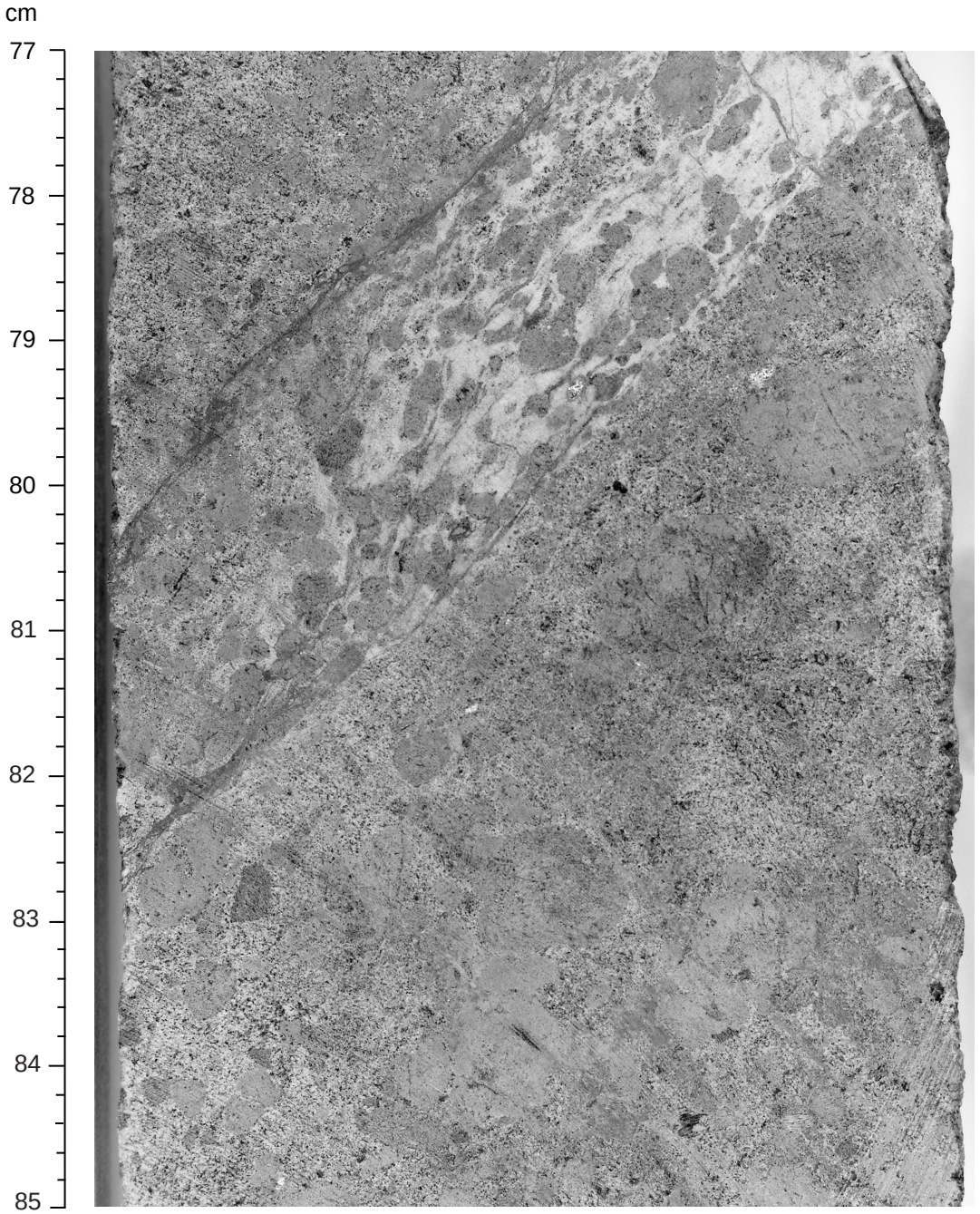

**Figure F71. A.** Close-up core photograph of smectite-clay veins within fractures in oxidized core face shown in interval 179-1105A-26R-2, 0–50 cm. (Continued on next two pages.)

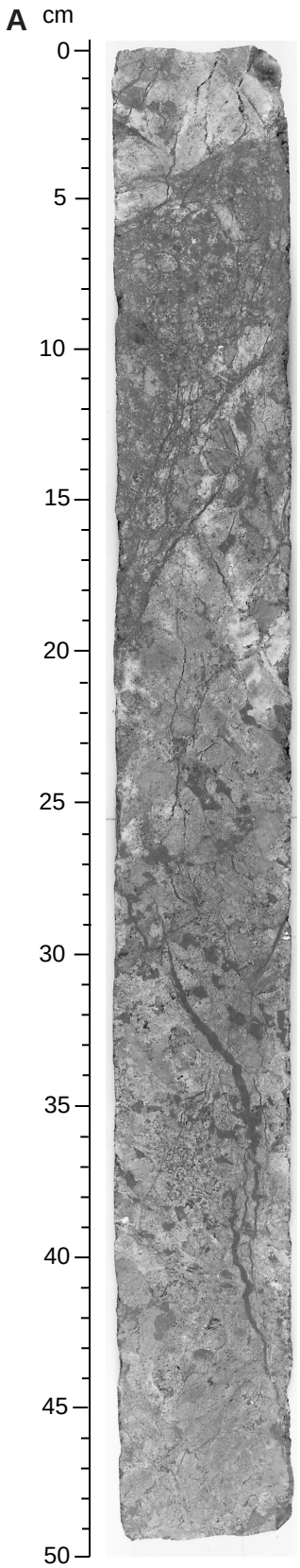

**Figure F71 (continued). B.** Close-up core photograph of smectite-clay veins within fractures in oxidized core facies shown in interval 179-1105A-26R-2, 1–22 cm.

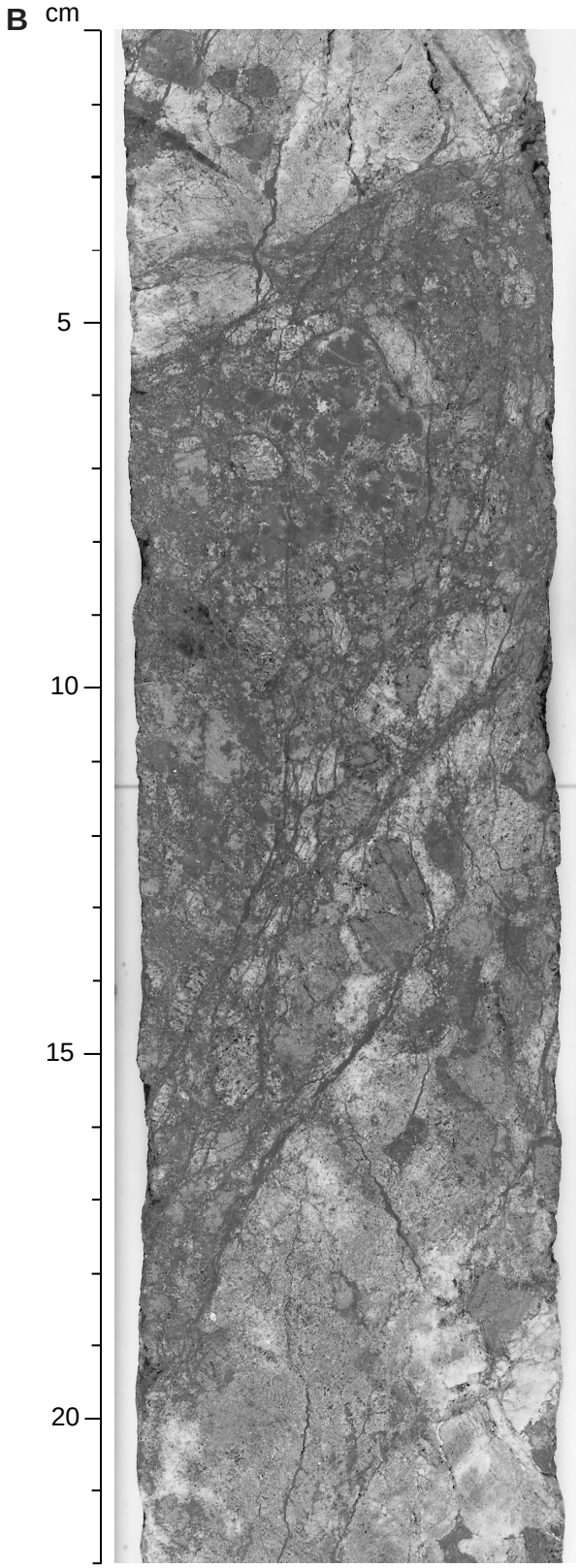

**Figure F71 (continued).** C. Close-up core photograph of smectite-clay veins within fractures in vuggy calcite veins in interval 179-1105A-30R-1, 1–9 cm.

**Figure F72.** Schematic model of unroofing and exposure of the Atlantis Bank along a low-angle detachment fault ~11.5 m.y. ago at the northern RTI of the Atlantis II Transform. Unroofing causes cooling of the gabbroic massif below the magnetic acquisition temperatures and subsequent clockwise rotation and steepening of the frozen-in magnetic inclination by ~19°–20°.

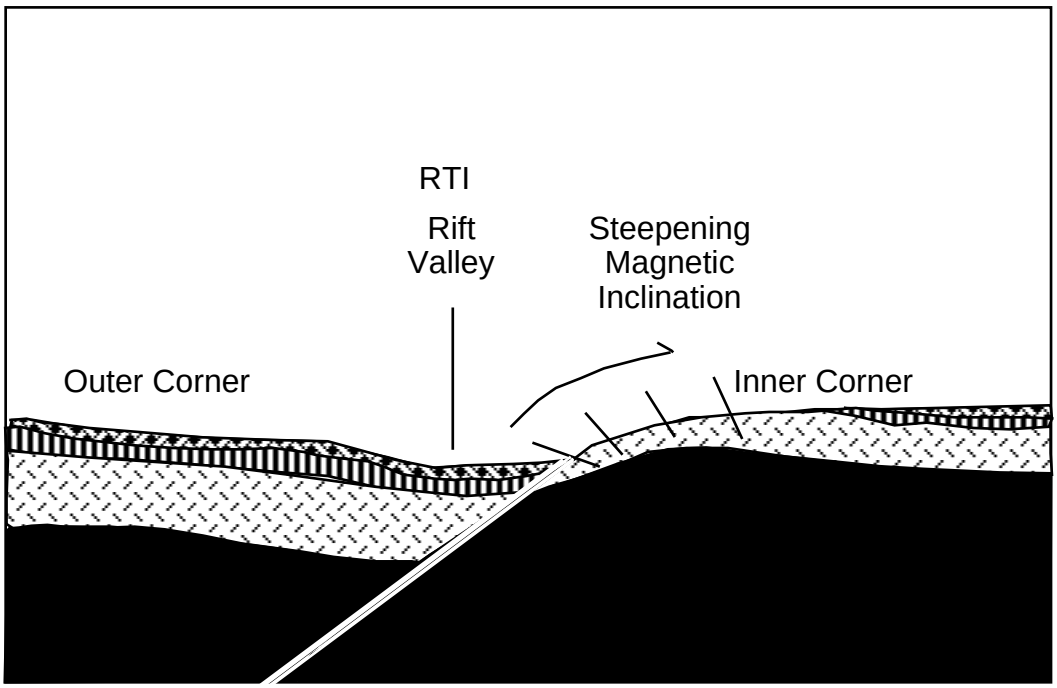

**Figure F73.** Whole-core magnetic susceptibility measurements. The only filter applied to these data is removal of over-range values caused by susceptibility meter saturation.

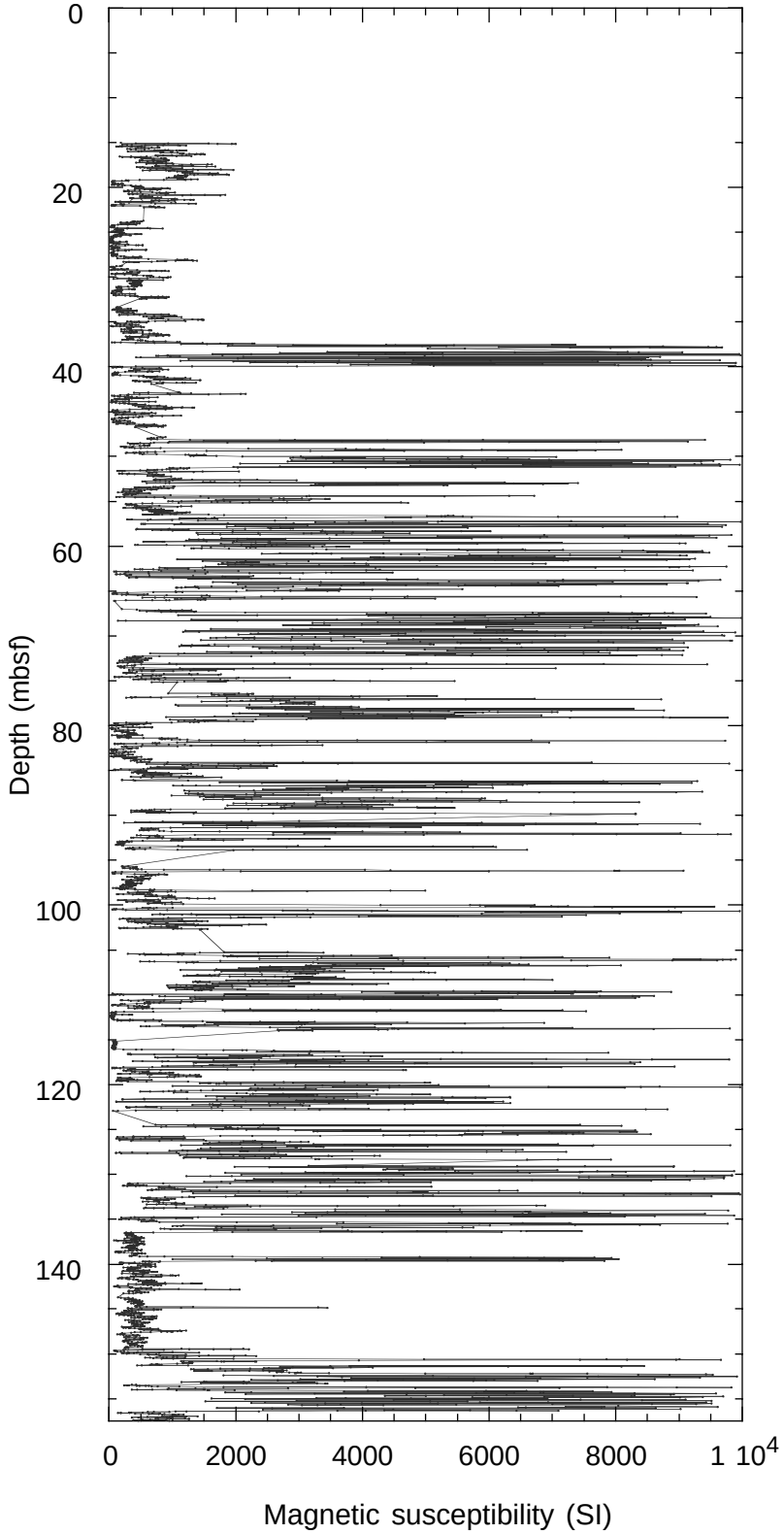

**Figure F74.** Filtered whole-core magnetic susceptibility measurements. All measurements of pieces smaller than the sensing interval of the susceptibility loop, as well as all measurements within 5 cm of the end of a piece, have been removed. A simplified graphic lithology column, highlighting only those intervals where Fe-Ti oxide has been reported, is plotted to the left. Lithologic unit boundaries are also shown adjacent to the graphic lithology plot and embedded in the magnetic susceptibility plot. The dashed line represents a weighted moving average through the magnetic susceptibility data. Lithologic unit average magnetic susceptibilities are Unit I, 828 SI; Subunit IIA, 3406 SI; Subunit IIB, 3010 SI; Unit III, 780 SI; Unit IV, 3472 SI.

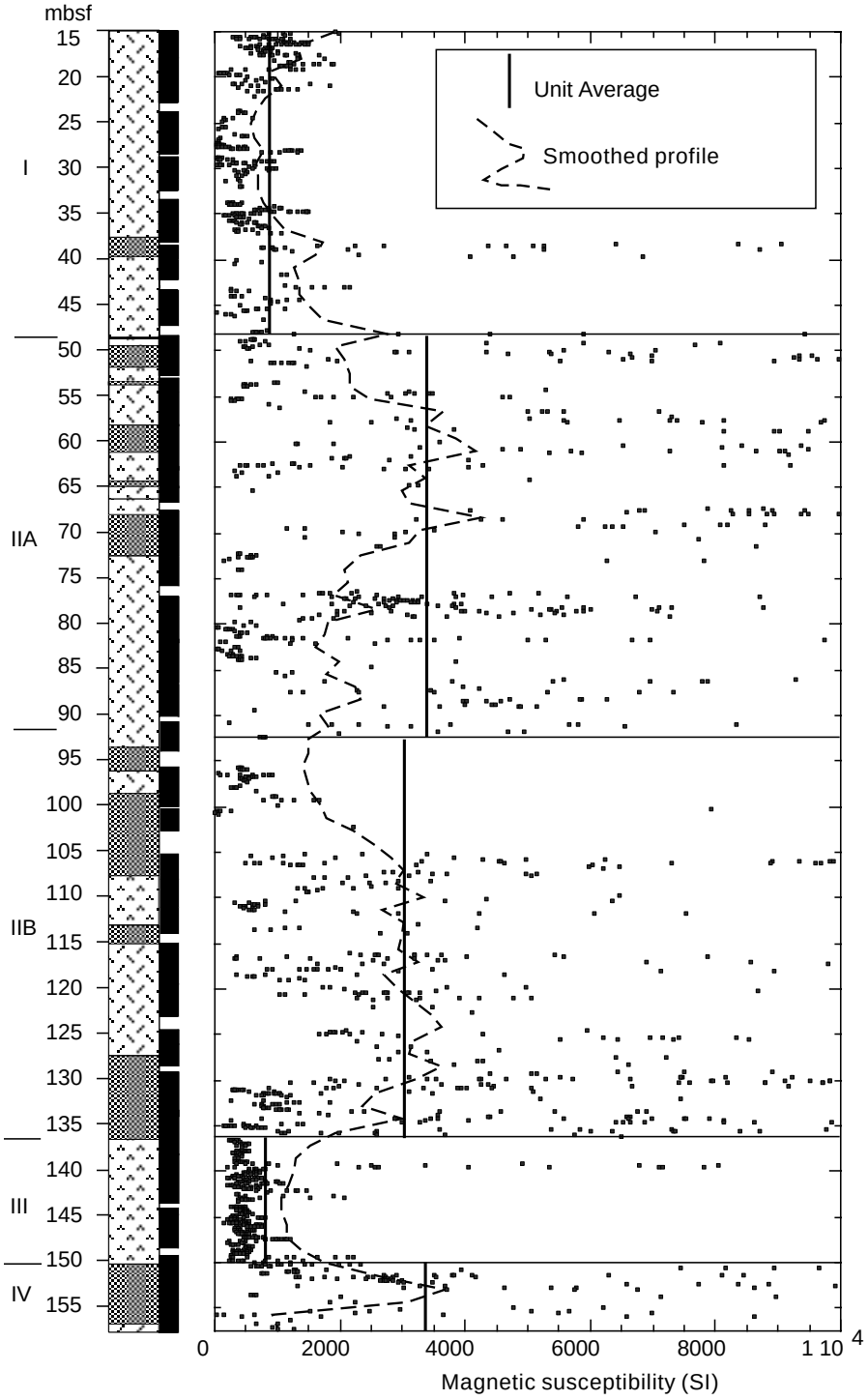

**Figure F75.** Split-core measurements of natural remanent magnetization showing downhole variation in declination, inclination, and intensity.

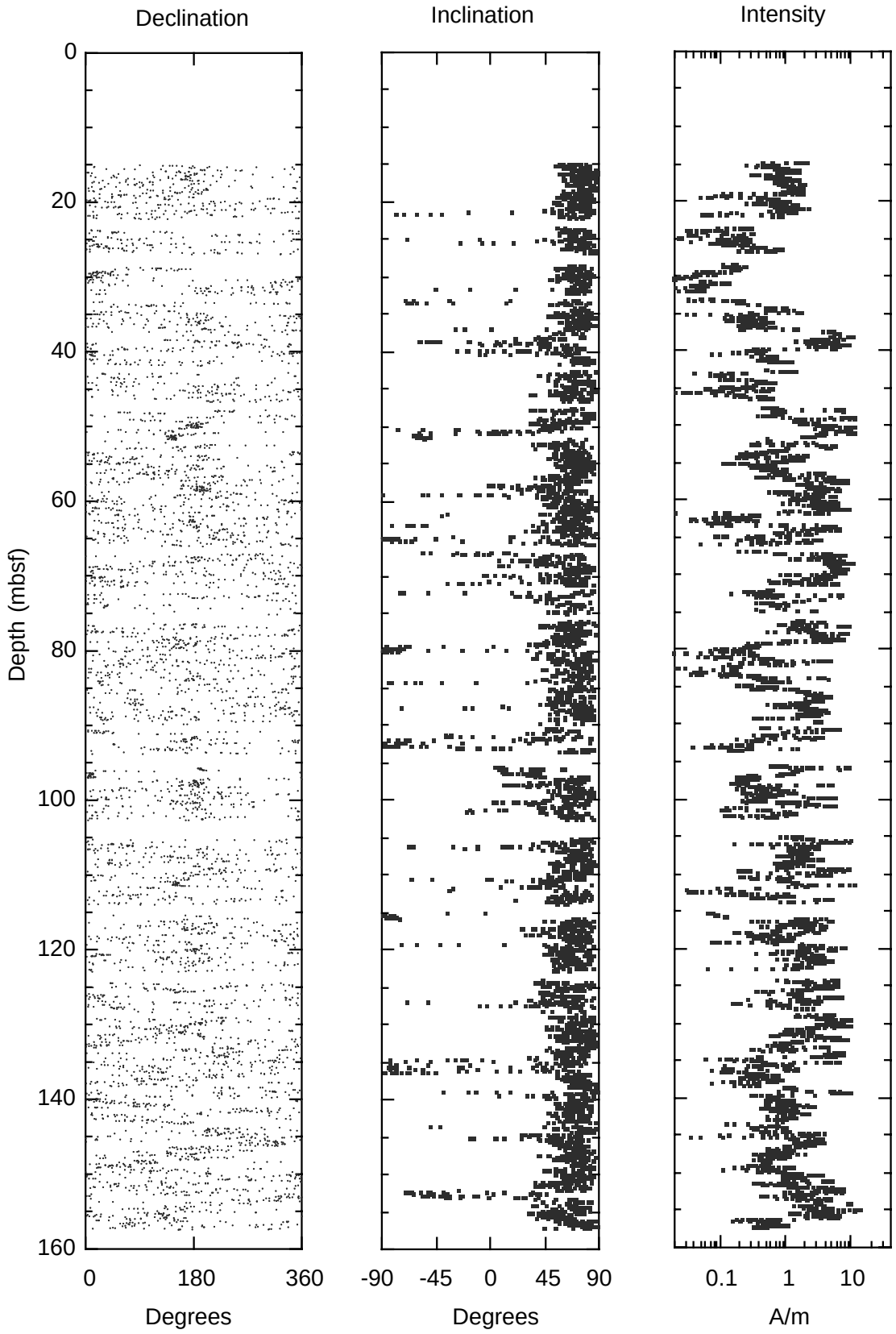

**Figure F76.** $V_p$ plotted as a function of depth for samples from Hole 1105A. Symbols distinguish the four major lithologies identified from macroscopic core description.

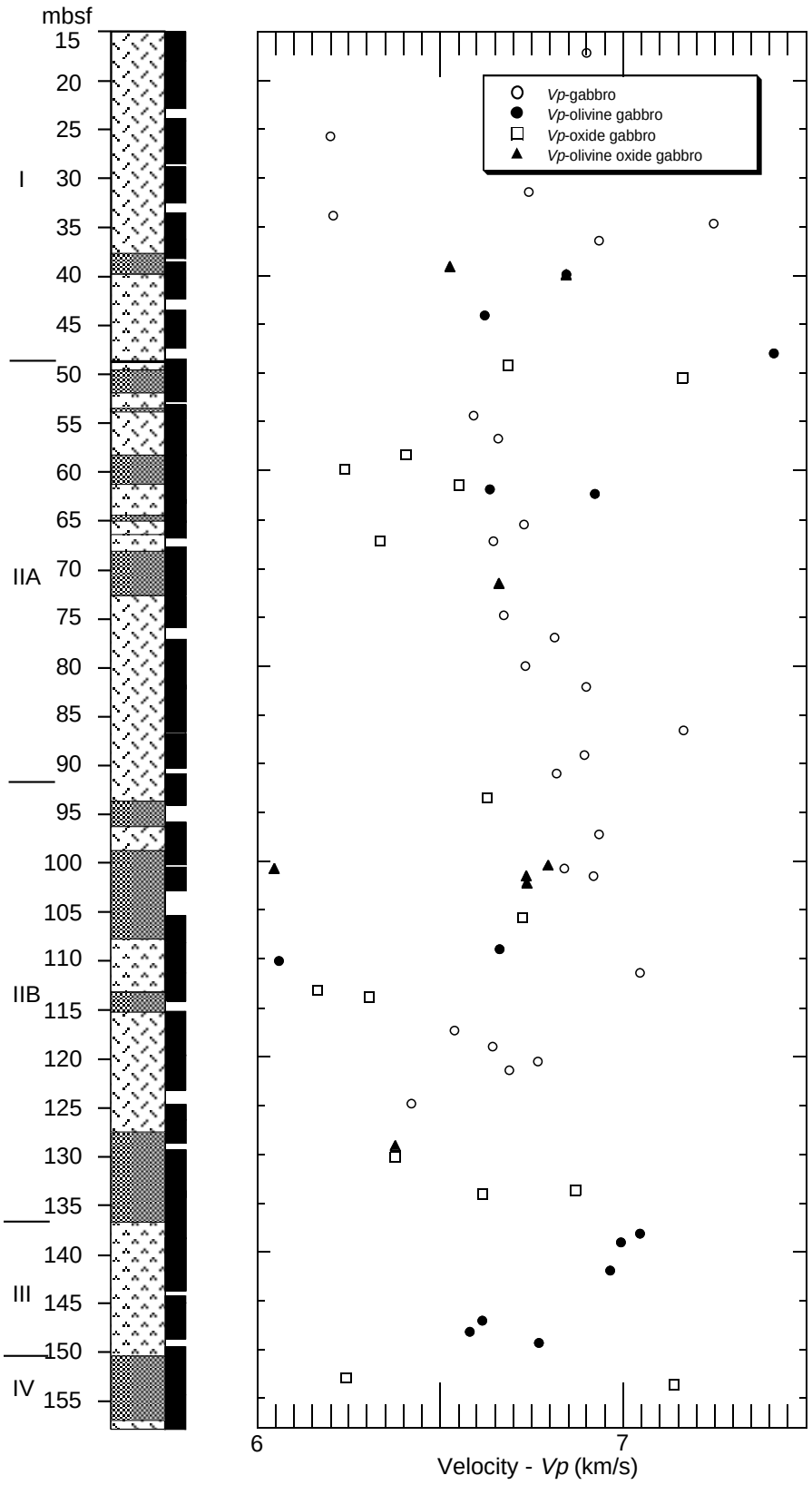

**Figure F77.** Downhole logs for Hole 1105A.Track 1: temperature curve and IPLT caliper data. Track 2: HSGR and HCGR data. Track 3: thorium, uranium, and potassium data. Tracks 4 and 5: resistivity data from the SFLU, IMPH, and IDPH.

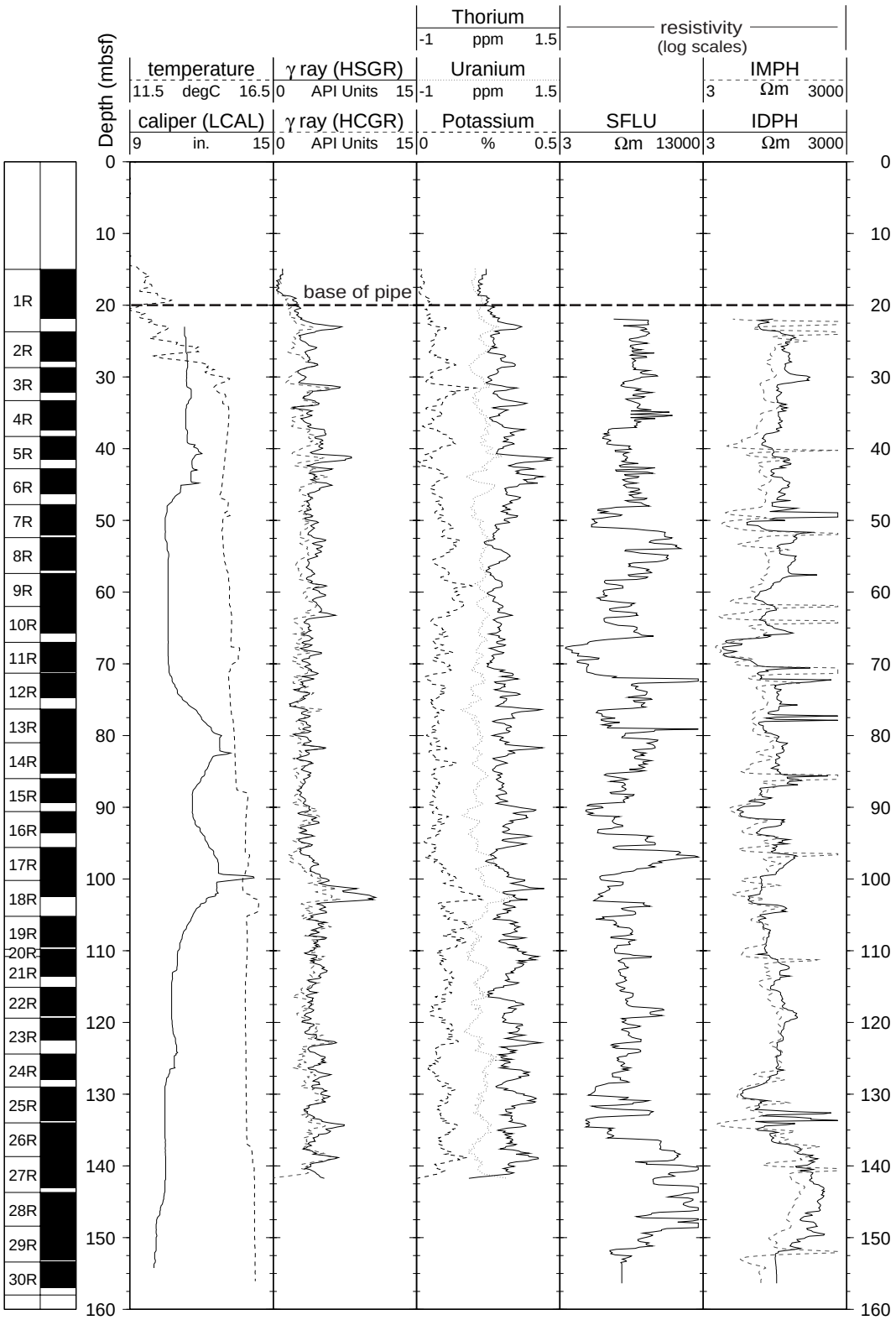

**Figure F78.** Downhole logs for Hole 1105A. Track 1: RHOM and discrete density laboratory measurements. Track 2: PEFL data. Track 3: APLC with discrete laboratory porosity measurements. Track 4: formation capture cross-section data of the SIGF. Track 5: calculated $V_p$.

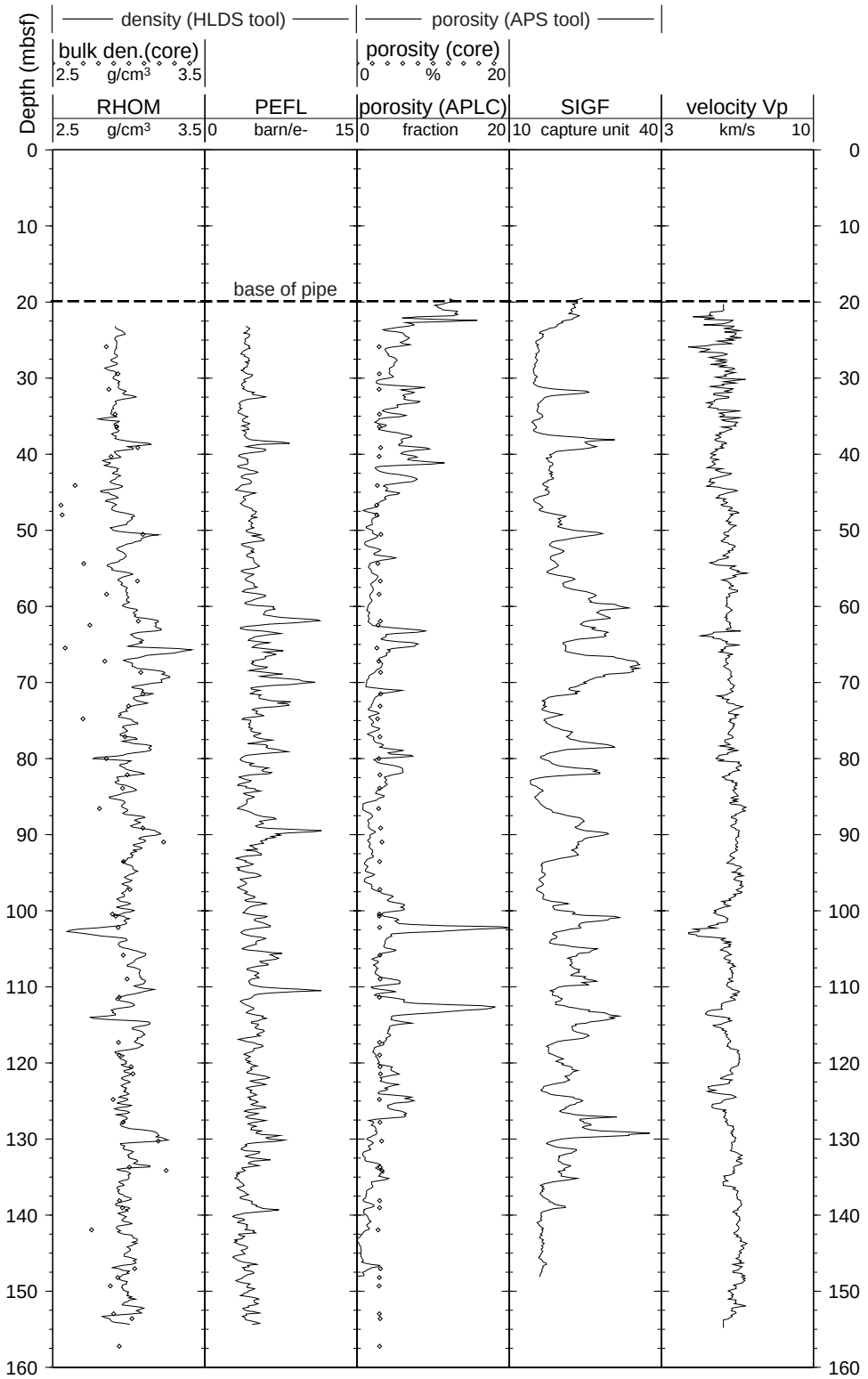

**Figure F79.** Downhole logs for Hole 1105A. HAZI 1 and 2 in track 2 are the computed hole azimuths based on magnetometer and accelerometer data from the GPIT and FMS tool string. Track 3 shows the magnetic field inclination. Track 4 shows the hole vertical deviation as measured by the GPIT during passes 1 and 2 of the FMS run. The rotation of the FMS is given in track 5 by the azimuth of pad 1 of the FMS as the tool proceeds through the borehole. The gamma-ray curve in track 1 is present for correlation with the other logs.

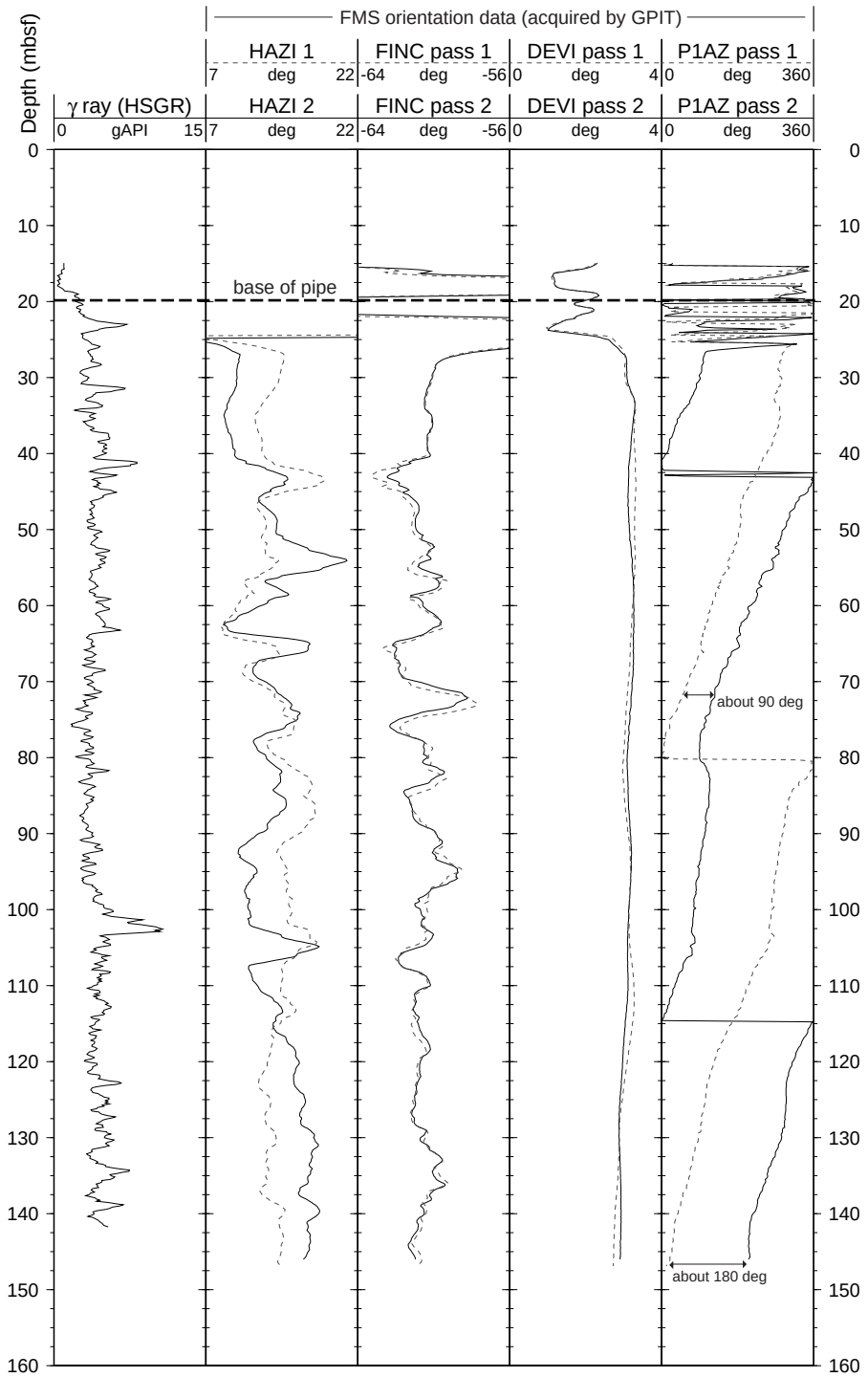

**Figure F80.** FMS image over the depth interval 93–100 mbsf in Hole 1105A with correlated lithologic units and oriented dips. Conductive areas appear in dark shades, whereas light shades are attributed to resistive zones.

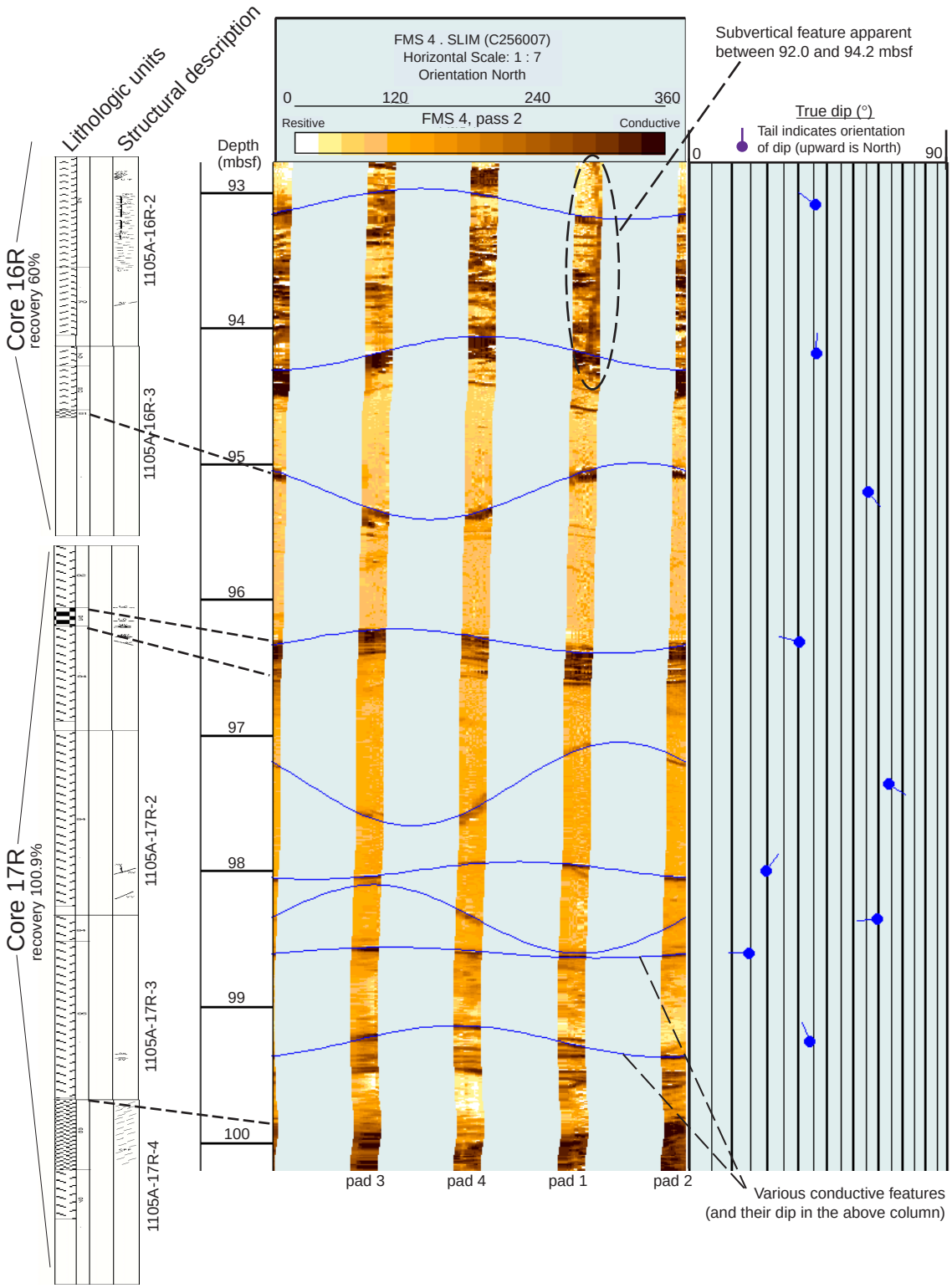

**Figure F81.** Composite diagram of the first 90 mbsf showing the relations between the SIGF from the APS tool, corresponding to the measure of the formation capture cross section of thermal neutrons and core geochemical analysis. In track 2, the RHOM is presented. High values of density are coherent with both the oxide gabbro intervals described in the cores and the SIGF high values.

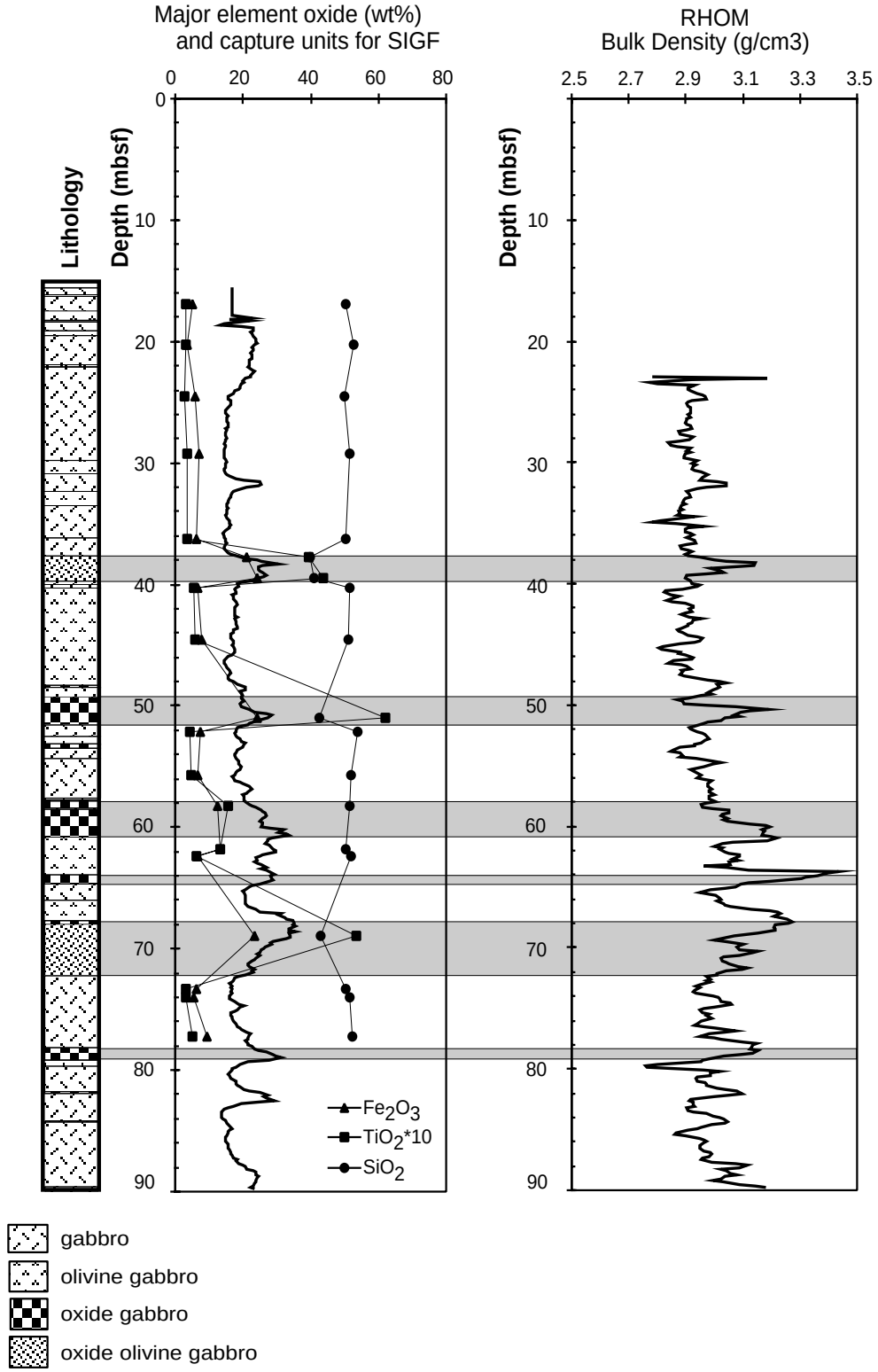

**Figure F82.** Vertical component of OBS A4's recording of the SDS 12-in fluid hammer drill with concentric winged bits. Each trace is 10 min; total recording shown is 80 min.

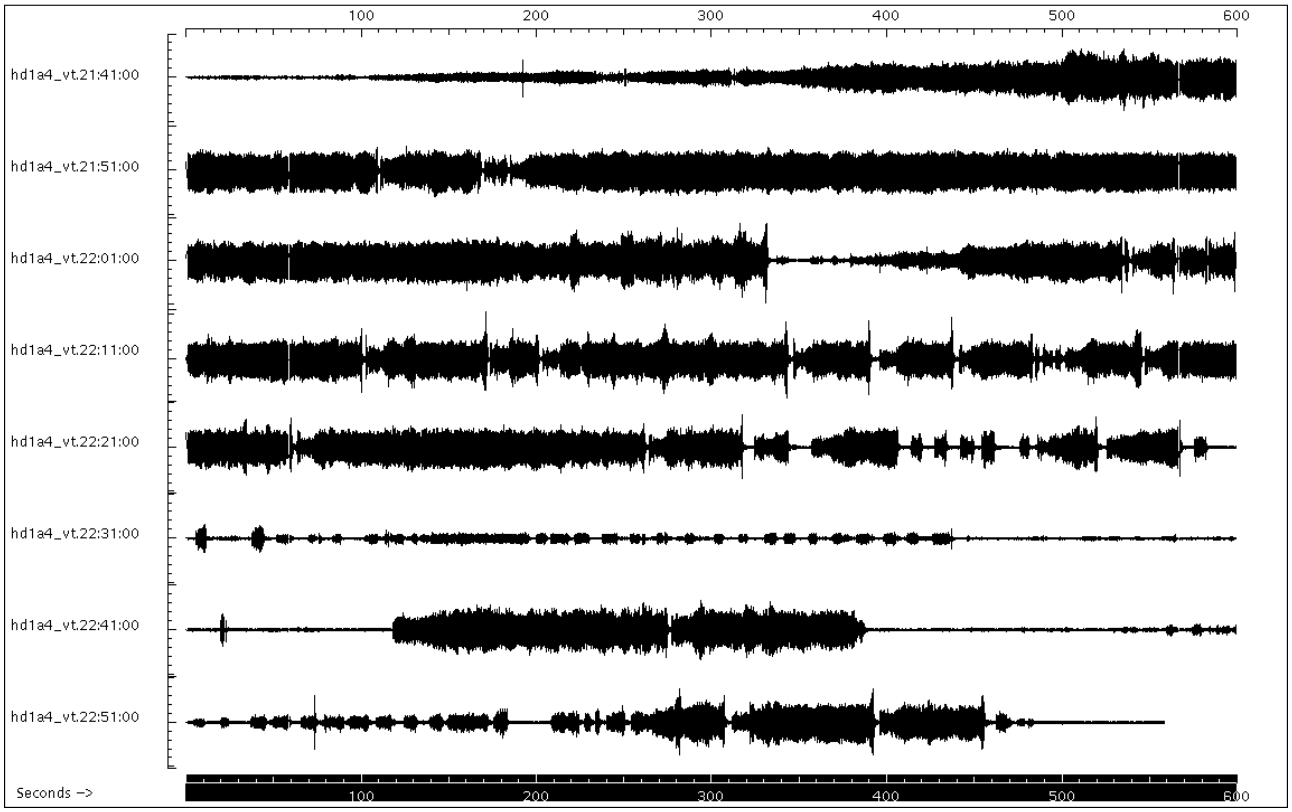

**Figure F83.** The waveform at 22:06:20 on Figure F82, when the hammer drill stalled, plotted on two expanded scales. Top trace is 15 s long; bottom trace is 1.7 s long.

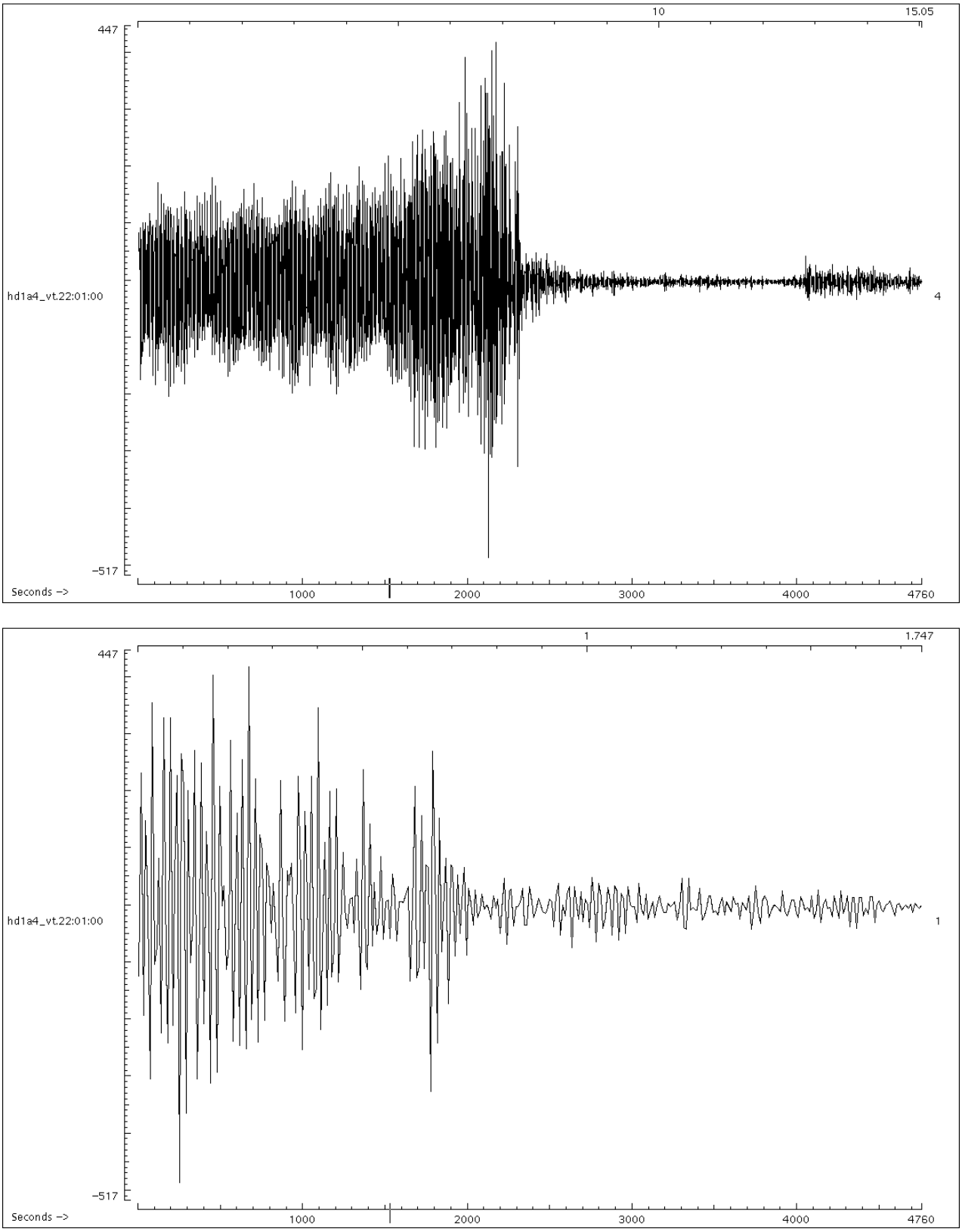

**Figure F84.** Amplitude spectra of drill-string accelerometer measurements at 35 mbsf. The upper trace is while the bit is off bottom during core recovery; the lower is while drilling rock. The value of the greatest spectral component is shown in the upper right.

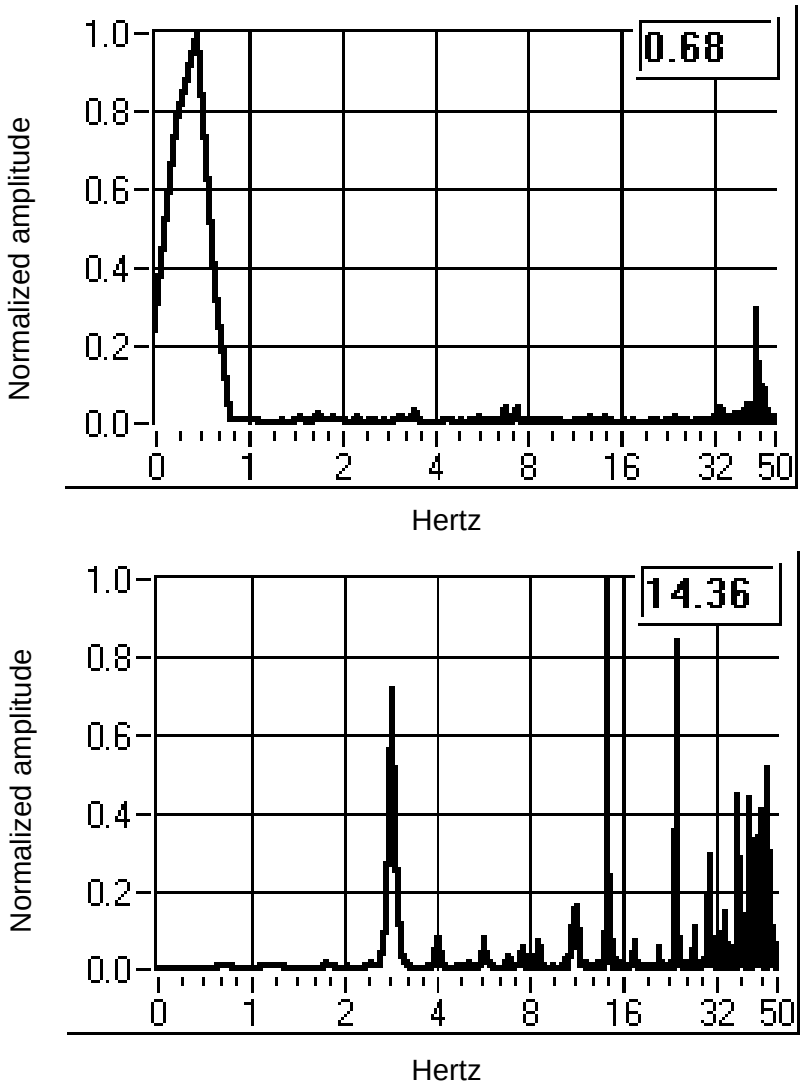

**Figure F85.** Time series (upper panel) and spectra (lower panel) for a 31-s sample while not drilling in Hole 1105A. In each case, the upper three traces are from the OBS nearer the hole, and the lower three from the far OBS. Note the differing amplitude scales for each trace.

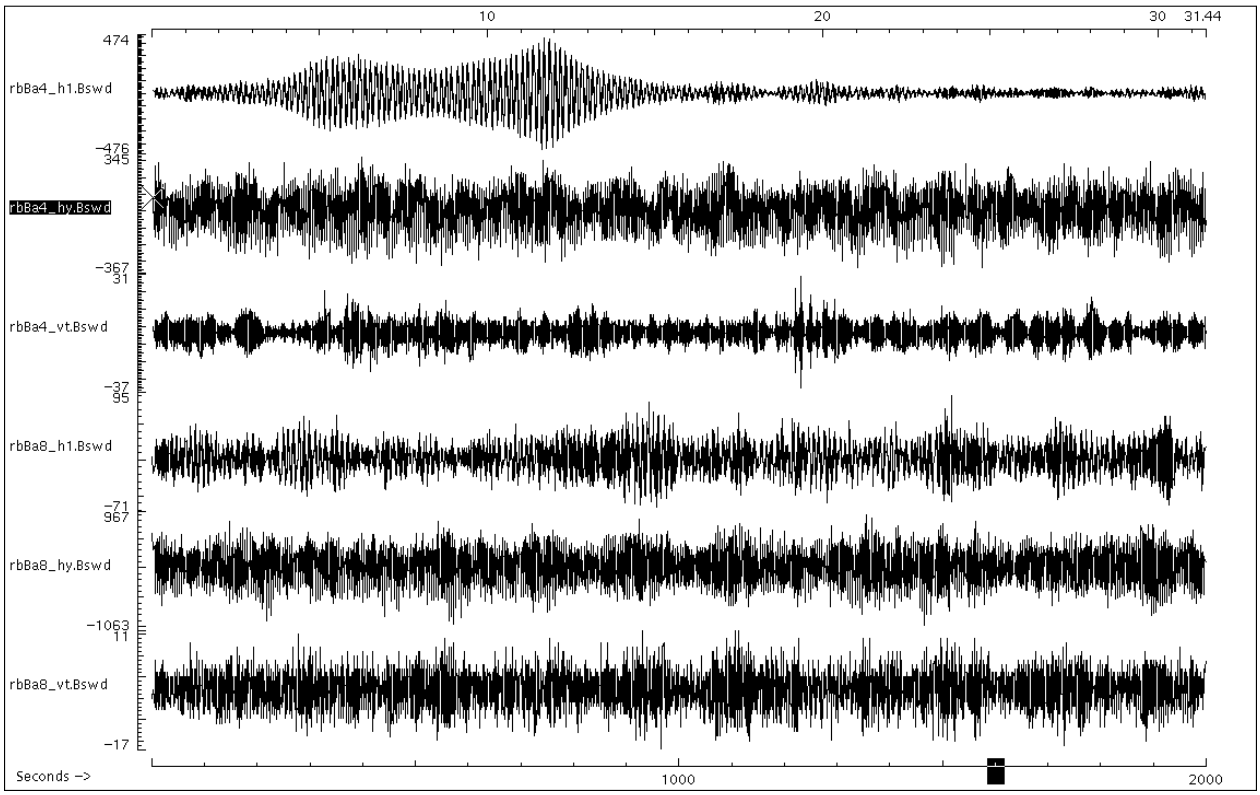


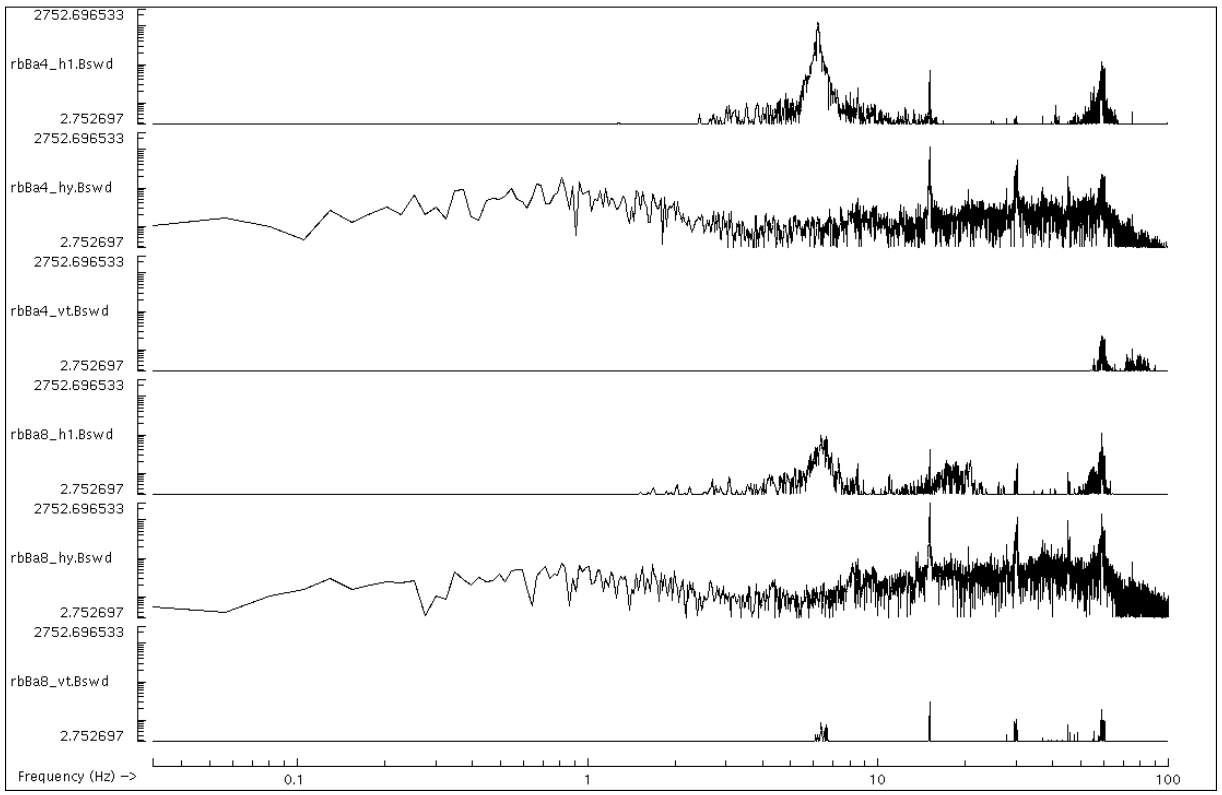

**Figure F86.** Time series (upper panel) and spectra (lower panel) for a 31-s sample while drilling in Hole 1105A. In each case, the upper three traces are from the OBS nearer the hole, and the lower three from the far OBS. Note the differing amplitude scales for each trace, and compare with Figure F85.

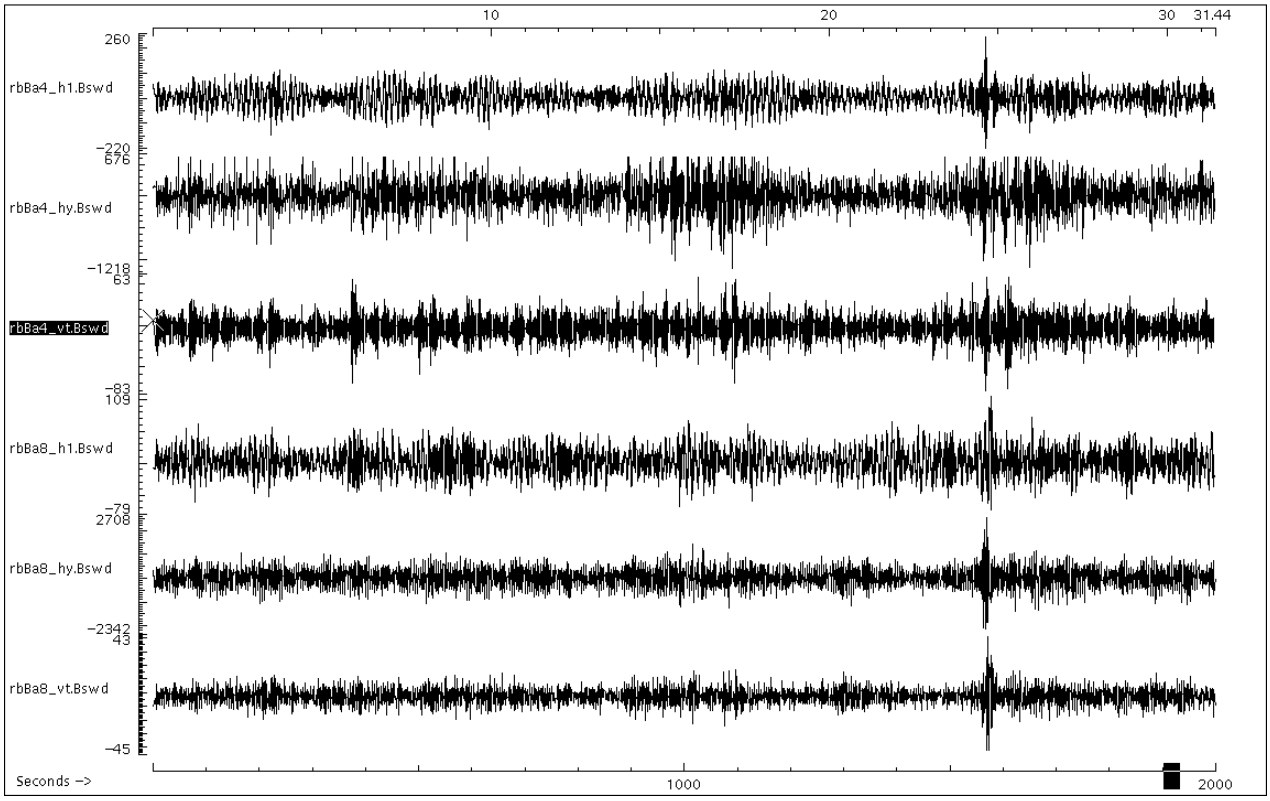


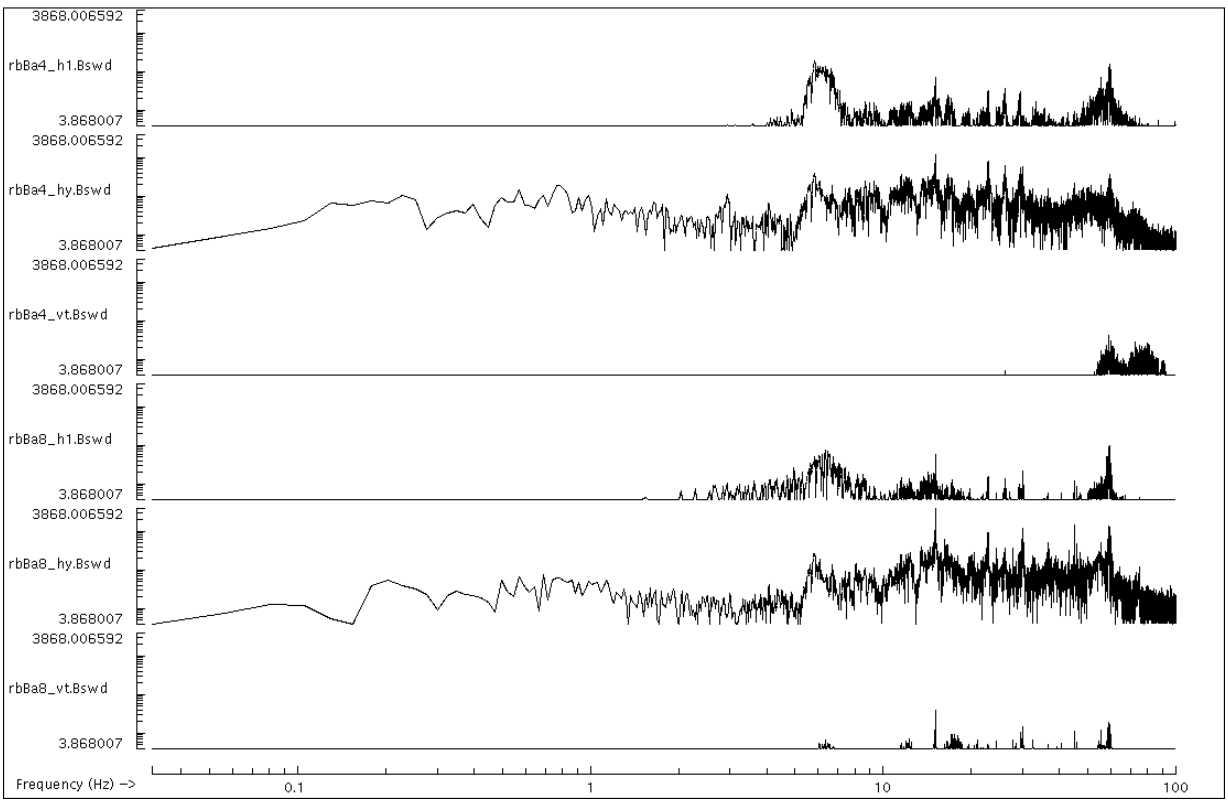

**Table T1.** Hammer deck test data, Site 1104.

| Flow rate (gpm) | Pressure (psi) | Comments |
|---|---|---|
| 75 | 270 | Hammer begins cycling smoothly |
| 150 | 360 | Hammer cycling smoothly at higher frequency |
| 200 | 560 | Hammer cycling smoothly at higher frequency |
| 250 | 820 | Hammer cycling smoothly at higher frequency |
| 300 | 1125 | Hammer cycling smoothly at higher frequency |

**Table T2.** Hammer drill spud test data, Site 1104.

| Flow rate (gpm) | Pressure (psi) |
|---|---|
| 1104 Spud test #1 | |
| 75 | 90 |
| 100 | 200 |
| 125 | 270 |
| 1104 Spud test #2 | |
| 100 | 175 |
| 125 | 295 |
| 150 | 450 |
| 175 | 570 |
| 100 | 170 |
| 1104 Spud test #3 | |
| 100 | 170 |
| 125 | 290 |
| 150 | 450 |
| 175 | 625 |
| 200 | 720 |
| 225 | 800 |
| 250 | 1090 |

Notes: Water depth = 740 mbrf; bit = SDS concentric.

**Table T3.** Hammer drill drilling test data, Hole 1104A.

| Time (UTC) | Flow rate (gpm) | Pressure (psi) | Weight on bit (lb) | Rotary speed (rpm) | Torque (ft-lb) | Notes |
|---|---|---|---|---|---|---|
| 0610 | 200 | 650 | 8000 | 10 | 2750 | Slight vibration in pumps and rig floor |
| | 225 | 820 | 8000 | 10 | 2750 | |
| | 250 | 1000 | 8000 | 10 | 2750 | Vibrations increasing |
| | 275 | 1190 | 8000 | 10 | 2750 | |
| | 300 | 1400 | 8000 | 10 | 2750 | Vibrations increasing |
| | 325 | 1590 | 8000 | 10 | 2750 | |
| | 350 | 1725 | 8000 | 10 | 5000 | Top drive stalled momentarily, torque erratic |
| | 375 | 1940 | 8000 | 20 | 5000 | Torque erratic |
| 0647 | 400 | 2125 | 8000 | 20 | 14000 | Torque erratic, top drive stalling |
| | 425 | 2255 | 8000 | 20 | 14000 | Torque erratic, top drive stalling |
| 0657 | NA | NA | NA | NA | NA | Lost all pressure, hammer drilled off opening by-pass |
| 0658 | NA | NA | NA | NA | NA | Pumps shut off, drill string lowered, pumps reengaged slowly |
| 0700 | NA | NA | NA | NA | NA | POOH with 10-15k overpull |

Notes: Water depth = 740 mbrf; bit = SDS concentric.

**Table T4.** Hammer drill drilling test data, Hole 1104B.

| Time (UTC) | Flow rate (gpm) | Pressure (psi) | Weight on bit (lb) | Rotary speed (rpm) | Torque (ft-lb) | Notes |
|---|---|---|---|---|---|---|
| 0830 | 100 | 170 | 10,000 | 20 | 1,000 | Hammer running smoothly |
| | 150 | 400 | 10,000 | 20 | 1,500 | |
| | 200 | 625 | 10,000 | 20 | 1,500 | |
| | 250 | 925 | 10,000 | 20 | 1,500 | |
| | 300 | 1,300 | 10,000 | 20 | 2,500 | Excessive vibration from pumps |
| | 350 | 1,650 | 10,000 | 20 | 2,500 | Top drive stalled, torque erratic up to 8,000 ft-lb |
| 0845 | 350 | 1,650 | 10,000 | 20 | 4,000 | Hammer running smoother, torque less erratic, making hole |
| 0845 | 125 | 200 | | 20 | | Pop-off valve on rig air failed, lost rig air, stopped drilling, stayed in hole, bit sticking |
| 0904 | | | | | | Rig air pop-off valve isolated, drilling resumed |
| | 350 | 1,575 | 10,000 | 20 | 4,000 | Continuous drill off, lose all pressure, heave closes hammer by-pass and dumps max flow to hammer piston/valve |
| | 375 | 1,780 | 10,000 | 20 | 8,000 | Torque erratic, slip stick rpm 0-50 |
| | 400 | 1,950 | 10,000 | 20 | 8,000 | Top drive stalling, slip stick, adjust heave compensator and WOB, pipe occasionally ringing, releasing torque upon stall hammer usually starts at 6,500 ft-lb |
| 1130 | 375 | 680 | 10,000 | 20 | 0 | Hammer not cycling, bit stuck, 3 m in hole |
| 1150 | | | | | | Bit freed, camera tripped to the seafloor observe Holes 1104A and 1104B. Both holes appear clean and smooth. Hole 1104B appears oblong as if spudded on a slope. Offset 20 ft south, set bit on seafloor, maintain WOB and recover camera |

Notes: Water depth = 739 mbrf; bit = SDS concentric.

**Table T5.** Hammer drill drilling test data, Hole 1104C attempt.

| Time (UTC) | Flow rate (gpm) | Pressure (psi) | Weight on bit (lb) | Rotary speed (rpm) | Torque (ft-lb) | Notes |
|---|---|---|---|---|---|---|
| 1310 | 100 | 90 | 10,000 | 15 | 2,000 | Hammer not cycling |
| | 125 | 150 | 10,000 | 15 | 2,000 | Hammer not cycling |
| | 175 | 250 | 10,000 | 15 | 2,000 | Hammer not cycling |
| | 200 | 290 | 10,000 | 15 | 2,000 | Hammer not cycling |
| | 250 | 400 | 10,000 | 15 | 2,000 | Hammer not cycling |
| | 190 | 10 | | | | Lift bit off bottom to open by-pass and flush hammer, lower bit back to seafloor |
| | 100 | 60 | 10,000 | 0 | 0 | Hammer not cycling |
| | 150 | 180 | 10,000 | 0 | 0 | Hammer not cycling |
| | 200 | 280 | 10,000 | 0 | 0 | Hammer not cycling |
| 1345 | | | | | | Switch to pump 1 to confirm downhole, POOH |

Notes: Water depth = 739 mbrf; bit = SDS concentric.

**Table T6.** Hammer drill drilling test data, Hole 1104C.

| Time (UTC) | Flow rate (gpm) | Pressure (psi) | Weight on bit (lb) | Rotary speed (rpm) | Torque (ft-lb) | Notes |
|---|---|---|---|---|---|---|
| 0115 | 100 | 170 | 8000 | 5-10 | | |
| | 150 | 400 | 8000 | 5-10 | | |
| | 200 | 620 | 8000 | 5-10 | | |
| | 250 | 930 | 8000 | 5-10 | | |
| | 300 | 1280 | 8000 | 15-20 | | |
| | 350 | 1480 | 8000 | 15-20 | | Pressure dropped off, 1 m penetration |
| 0124 | 100 | 130 | 8000 | 5-10 | | |
| | 150 | | 8000 | 25 | | |
| | 200 | 620 | 8000 | 25 | | Smooth rotation |
| | 250 | 920 | 8000 | 25 | | Smooth rotation |
| | 300 | 1260 | 8000 | 25 | | Smooth rotation |
| 0130 | 350 | 1590 | 8000 | 25 | | 0.5 m penetration |
| 0136 | 350 | 1630 | 8000 | 25 | | Slight slip stick |
| 0145 | | | | | | May have heaved out of the hole, stop pumps and restart hole |
| | 100 | 370 | 8000 | 25 | 11,000 | |
| | 200 | 580 | 8000 | 25 | | 1 m penetration |
| | 250 | 930 | 8000 | 25 | | |
| | 300 | 1220 | 8000 | 10-50 | | |
| 0150 | 350 | 1630 | 8000 | 20-25 | | |
| 0155 | 350 | 1630 | 8000 | 20-25 | 14,000 | Stop rotation, stop pumps, pick up to release torque, restart |
| 0200 | 150 | 380 | 8000 | 25 | | 1 m penetration |
| | 200 | 580 | 8000 | 25 | | |
| | 250 | 930 | 8000 | 25 | | |
| | 300 | 1240 | 8000 | 25 | | |
| | 350 | 1630 | 8000 | 25 | | Torque buildup, stop, release torque, restart |
| 0208 | 150 | 380 | 8000 | 25 | | |
| | 200 | 615 | 8000 | 25 | | |
| | 250 | 980 | 8000 | 25 | | |
| 0225 | | | | | | Shut down to repair 2-in pipe nipple on manifold, deploy camera to observe borehole |
| 0300 | | | | | | Observed four boreholes, appears bit has heaved out of the hole and restarted new holes, bit is approximately 0.5 m in the hole, recover camera while maintaining bit in hole |
| 0334 | 150 | 380 | 8000 | | | |
| | 200 | 600 | 8000 | | | |
| | 250 | 980 | 8000 | | 0-5000 | Occasional slip stick |
| | 300 | 1220 | 8000 | | 0-5000 | Occasional slip stick |
| 0343 | 350 | 1585 | 8000 | | | |
| 0348 | | | | | | Torque increased to 17,000 ft-lb, stop to release torque |
| 0350 | 110 | 175 | 8000 | | | Trouble restarting |
| | 200 | 620 | 8000 | | | |
| 0355 | 250 | 920 | 8000 | | | 1 m penetration |
| | 300 | 1235 | 8000 | | | |
| | 350 | 1540 | 8000 | | | Top drive stalled, slip stick on restart |
| 0400 | 350 | 1545 | 8000 | | 6000 | |
| 0405 | | | | | | Torque increase, reduce pumps, restart |
| 0410 | | | | | | 17,000 ft-lb torque, can't free torque, stop and restart hammer |
| | 350 | 1540 | 8000 | | | Stuck bit |
| 0415 | | | | | | May have heaved out of the hole, bit free |
| | 200 | 580 | 8000 | | | |
| | 350 | 1530 | 8000 | | | Pump off, restart |
| 0420 | 350 | 1545 | 8000 | | | |
| 0425 | 350 | 1510 | 8000 | | | Stand pipe pressure transducer failed, stopped test to repair, pull clear of seafloor, pressure transducer going to take time to be repaired, start new hole |

Notes: Water depth = 739 mbrf; bit = SDS concentric.

**Table T7.** Hammer drill drilling test data, Hole 1104D.

| Time (UTC) | Flow rate (gpm) | Pressure (psi) | Weight on bit (lb) | Notes |
|---|---|---|---|---|
| 0450 | 200 | 560 | 8,000 | |
| | 250 | 930 | 8,000 | Heave off bottom |
| | 350 | 1,620 | 8,000 | |
| | 350 | 1,590 | 8,000 | |
| | 350 | 1,565 | 10,000 | Torque erratic and increasing |
| 0505 | 350 | 1,589 | 10,000 | Top drive stalling |
| 0510 | | | | Deploy camera to observe bit and borehole, may have started several new holes |
| 0545 | | | | End Hole 1104D drilling test, recover camera, recover hammer |

Notes: Water depth = 739 mbrf; bit = Holte concentric.

**Table T8.** Hammer drill drilling test data, Hole 1104E.

| Time (UTC) | Flow rate (gpm) | Pressure (psi) | Weight on bit (lb) | Rotary speed (rpm) | Torque (ft-lb) | Notes |
|---|---|---|---|---|---|---|
| 0140 | 100 | 160 | 10,000 | 20-25 | | |
| | 150 | 300 | | | | |
| | 200 | 550 | | | | |
| | 250 | 820 | | | | |
| | 300 | 1080 | | | | |
| | 350 | 1480 | 10,000-12,000 | | | |
| 0150 | | 1420 | | | | |
| 0155 | 350 | 1520 | | | | |
| | | | | | | Stop-restart |
| | 355 | 1495 | | | | |
| 0200 | 355 | | | | | |
| 0205 | 355 | | | | | |
| | 100 | | | | | Torque up/stop |
| 0210 | 200 | | | | | |
| | 250 | 930 | | | | |
| | 350 | 1500 | | | | Torquing up |
| 0220 | 350 | 1470 | | | 8-11k | |
| 0226 | 350 | 1485 | | | | 1 m penetration |
| 0235 | | | | | | Torque up and stall, can't get bit to rotate, stuck 40 k over pull |
| | | | | | | Lower to bottom to see if hammering can free bit |
| 0245 | 400 | 1720 | | | 24k | 40 k overpull |
| 0300 | | | | | | Working pipe and hammering to free pipe |
| 0315 | | | | | | One-third left-hand rotation frees bit |
| 0320 | | | | | | Clear seafloor |
| 0350 | | | | | | Observe wings on bit have come unwelded, pull camera |

Notes: Water depth = 740 mbrf; bit = Holte concentric with arms welded shut.

**Table T9.** Hammer drill drilling test data, Hole 1106A.

| Time (UTC) | Flow rate (gpm) | Pressure (psi) | Weight on bit (lb) | Rotary speed (rpm) | Torque (ft-lb) | Notes |
|---|---|---|---|---|---|---|
| 1600 | 200 | 25 | | | | Off bottom |
| | 185 | 500 | | | | |
| 1605 | 200 | 550 | 10,000 | 10 | 2000 | |
| | 250 | 800 | 10,000-15,000 | 10 | | |
| | 400 | | | | | Heave off bottom |
| | 250 | 575 | 10,000-15,000 | 10 | 3000 | Heave off bottom |
| 1615 | 215 | 570 | 10,000-15,000 | 10 | | 2 m of heave |
| | 250 | 760 | 10,000-15,000 | 10 | 4000 | Heave off bottom |
| | 250 | 690 | 10,000-15,000 | 10 | 2500 | Heave |
| 1620 | 250 | 700 | 10,000-15,000 | 10 | 2500 | Heave |
| | 250 | 750 | 10,000-15,000 | 10 | 7000 | Heave |
| 1625 | 250 | 800 | 10,000-15,000 | 10 | 5000 | Heave |
| 1626 | 260 | 800 | 10,000-15,000 | 10 | 2500 | Heave, probably heaved out of hole |
| | 250 | 750 | 10,000-15,000 | 10 | 2500 | 0.5 m? penetration, heave |
| | 255 | 780 | 10,000-15,000 | 10 | 8000 | Heave |
| 1630 | 255 | 775 | 10,000-15,000 | 0 | 10,000 | Relieve torque, rotation free |
| | 260 | 810 | 10,000-15,000 | 10 | 2500 | Heave |
| 1636 | 260 | 810 | 10,000-15,000 | 10 | 4000 | Heave |
| 1640 | 280 | 940 | 10,000-15,000 | 10 | 4000 | |
| 1645 | | | | | | Stall still hammering, release torque, heave, stall, reduce wob. |
| | 275 | 930 | 10,000 | 10-40 | 5000-8000 | Heave, start rotation |
| 1650 | 280 | 920 | 10,000-15,000 | 10-40 | 2500-11000 | |
| | 300 | 1055 | 10,000-15,000 | 10-40 | 2500-11000 | |
| 1655 | 325 | 1160 | 10,000-15,000 | 10-40 | 1000-8000 | |
| 1700 | 325 | 1240 | 10,000-15,000 | 20-30 | 2500-5000 | |
| | 350 | 1400 | 10,000-15,000 | | 10000 | Stall |
| | | | | | | Heave free, stall, free |
| 1705 | 350 | 1400 | | | 10000 | Stall |
| | 350 | 1400 | 10,000-15,000 | | 10000 | Stall, slip stick torquing |
| 1725 | 450 | | | | | Hammer stopped - restart |
| | 350 | 1370 | 2500 | 20-50 | 12000 | Stall, hammer quit |
| 1730 | 400 | 1650 | | | | Stall |
| | 390 | 1600 | | | 8000 | Stall, hammer open |
| | | | | | | Hammer slams into bottom several times |
| | 390 | 1650 | | | | Slip stick, stall, hammer running |
| 1745 | | | | | | More of the same |
| 1810 | 400 | 1685 | | | | Slip stick, heaving over 2 m |
| 1815 | | | | | 11000 | Sticking |
| | | | 10,000-15,000 | | 11000 | Stick, slip, sticking |
| | | | | 0-60 | | Sticking more than rotating, running rough |
| 1845 | | | | | 0-11000 | Sticking |
| 1855 | | | | | | Yellow alert |
| | 395 | 1595 | 10,000-15,000 | | | |
| 1900 | 400 | 1650 | 10,000-15,000 | | | Running smoother without stalling |
| 1915 | 400 | 1645 | | | | Smoothing out without heaves, ~1.5-2 m penetration |
| 1935 | 400 | 680 | | | | Appears valve may have cracked again, loss of pressure |
| 1940 | | | | | | Try other mid pump to confirm not surface-related problem |
| 1945 | 300 | 500 | | | | Pull out of hole to repair hammer |
| 2245 | | | | | | All TC buttons on arms except the last trailing buttons are gone |

Notes: Water depth = 740 mbrf; bit = Holte concentric.

**Table T10.** Hammer drill drilling test data, Hole 1106B.

| Time (UTC) | Flow rate (gpm) | Pressure (psi) | Weight on bit (lb) | Rotary speed (rpm) | Torque (ft-lb) | Notes |
|---|---|---|---|---|---|---|
| 0635 | 150 | 15 | | | | Off bottom |
| 0640 | 140 | 215 | 10,000-12,000 | | | Tag bottom |
| | 200 | 500 | 10,000-12,000 | 20 | | |
| 0643 | 250 | 650-667 | 10,000-12,000 | 20 | | |
| 0646 | | 950 | | | | Looks like bit walked down hill |
| | 305 | 930 | 12,000 | 15-20 | | Running smooth |
| 0650 | 350 | 1,180 | | | 2,500 | |
| | 360 | 1,220 | | | 2,500-5000 | |
| 0653 | 400 | 1,520 | | | 5,000 | 2 m heave |
| | | | | | | Slight hesitation, stick, on each revolution |
| 0700 | | | | | | Heave out of hole and slide down hill |
| | 400 | 1,490 | 10,000-12,000 | 10-40 | 2,500-8,000 | |
| | | | | | | Hammer open |
| 0705 | 395 | 1,490 | | 10-60 | 2,500-5,000 | Sticking |
| | | | | | | Hammer running good |
| | | | | | | Heave open hammer |
| 0710 | 400 | 1,490 | 10,000-12,000 | 10-50 | 2,500-5,000 | |
| | | | | | | Hammer open |
| | | | | | | Hammer open |
| 0720 | | | | | | Stall, hammer off |
| 0722 | | | | | | Hammer on, stall |
| | 400 | 1,450 | 10,000-12,000 | 5-10 | 8,000 | |
| 0725 | 400 | 1,450 | 10,000-12,000 | 5-10 | 2,000-5,000 | Hammer noise affecting ASK–drifting around |
| 0730 | 395 | 1,470 | 10,000-15,000 | 10-20 | 7,000 | Stick slip |
| 0735 | 400 | 1,450 | 10,000-15,000 | 10-30 | 5,000 | Stick slip |
| | | | | | | Open hammer, start, open hammer |
| 0820 | | | | | | Heave out, start new hole |
| 0835 | 395 | 1,382 | | | | Heave off, stall rotary |
| | 400 | 1,350 | | 15-20 | 7,000 | Stall |
| | | | | | | POOH, no advancement being made |

Notes: Water depth = 741 mbrf; bit = Holte eccentric.

**Table T11.** Hammer drill drilling test data, Hole 1106C.

| Time (UTC) | Flow rate (gpm) | Pressure (psi) | Weight on bit (lb) | Rotary speed (rpm) | Torque (ft-lb) | Notes |
|---|---|---|---|---|---|---|
| 1830 | 150 | 55 | | | | Bit off seafloor |
| | 135 | 450 | 10,000-14,000 | 0 | 0 | |
| | 215 | 982 | 10,000-14,000 | 0 | 0 | |
| 1840 | 250 | 1,150-1,230 | 10,000-12,000 | 10 | | |
| 1843 | | | | | | Heaving and stopping hammer |
| | | | | | | May have heaved out of hole and skidded downslope |
| | 250 | 1,145 | | 0 | 0 | |
| 1845 | 250 | 1,243 | 10,000-12,000 | 10 | | |
| | 250 | 1,250 | | | | Stalled and restart |
| 1850 | 300 | 1,580-1,620 | 10,000-12,000 | 10 | | |
| | 350 | 1,940 | 10,000-12,000 | 15-20 | | |
| 1853 | | | | | | Heave and stall out |
| 1855 | 345 | 1,935 | 10,000-12,000 | 15-20 | | 1 m penetration |
| 1900 | 350 | 1,950 | 10,000-12,000 | 15-20 | | |
| | | | | | 2,500 | Sticking |
| 1905 | 225 | 1,455-2,300 | | | | Hammer running intermittently, bleed pressure off |
| | 225 | 2,300 | | | | Switch mud pumps to isolate source, bleed pressure off |
| | 150 | 650 | | | | |
| | 200 | 1,450 | | | | Pressure rising, running intermittently |
| | | | | | | Pick up off bottom and flush |
| 1912 | 115 | 15 | | | | Reset and try again |
| | 90 | 408 | | | | |
| | 150 | 680-750 | | | | |
| | 200 | 1,000-1,600 | | | | Intermittently running |
| 1915 | | | | | | POOH |

Notes: Water depth = 742.5 mbrf; bit = SDS flat-face.

**Table T12.** Hammer drill drilling test data, Hole 1106D.

| Time (UTC) | Flow rate (gpm) | Pressure (psi) | Weight on bit (lb) | Rotary speed (rpm) | Notes |
|---|---|---|---|---|---|
| 0340 | 140 | 475 | 10,000-12,000 | 0 | |
| | 210 | 915 | | | |
| | 250 | 1260 | 10,000-12,000 | 0 | Average 2 m of heave |
| 0348 | 300 | 2500 | | | Pressure continuing to climb |
| | | | | | Shut off pumps and bleed off pressure |
| | | | | | Restart pumps and try again |
| | 105 | 560 | | 0 | |
| | 150 | | | 0 | Pressure building |
| 0355 | 300 | | | 0 | Pick up and flush off bottom |
| | | | | | Lower to seafloor and retry start |
| | 80 | 550 | | 0 | |
| | 160 | 1374 | | 0 | 2-3 m of heave |
| | | | | 0 | Hammer firing intermittently |
| | 200 | 2000 | | | Same scenario as last run, appears piston is binding in bush |
| 0404 | | | | | POOH |

Notes: Water depth = 742.5 mbrf; bit = SDS flat-face.

**Table T13.** Hammer drill drilling test data, Hole 1106E.

| Time (UTC) | Flow rate (gpm) | Pressure (psi) | Weight on bit (lb) | Rotary speed (rpm) | Torque (ft-lb) | Notes |
|---|---|---|---|---|---|---|
| 1130 | 150 | 15 | | | | Flush air out of system above seafloor, 2-3 m of heave |
| 1132 | 150 | 15 | 0 | 0 | 0 | |
| 1135 | 150 | 70 | | | | Tag seafloor |
| | 250 | 1,200 | 10,000-12,000 | 0 | 0 | |
| 1145 | 250 | 1,130 | | 5 | 5,000 | |
| | | | | | | Hammer opened |
| 1147 | | | | | | Hammer opened, (valve chatter?) |
| | | | | | | Open hammer |
| 1150 | 250 | 1,100 | 15,000 | 0 | 2,500 | |
| 1153 | 310 | 1,610 | 15,000-18,000 | 5 | 5,000 | |
| 1154 | 310 | 1,775 | 18,000 | 5 | 7,000 | |
| | | 800-2,000 | | | | |
| | 305 | 1,730 | 18,000 | 0 | 8,000 | |
| 1157 | 300 | 1,300 | 18,000 | 10-40 | 1,000-5,000 | |
| | | | | | | Heaving, hammer open |
| 1200 | 310 | 1,570 | 10,00-15,000 | 5 | 5,000 | |
| | | | | | | Heaving, hammer open |
| 1204 | 300 | 1,610 | 10,000-12,000 | 0 | 8,000 | |
| | | | | | | Heaving, hammer open, 4-m heaves |
| 1207 | 300 | 1,570 | 12,000 | 10 | 5,000 | |
| | | | | | | Heaving, hammer open |
| 1210 | 305 | 1,520 | 12,000 | 5 | 2,500 | |
| | | | | | | Heaving, hammer open, open hammer, open hammer |
| 1217 | 305 | 1,400 | 12,000 | 5 | 5,000 | |
| | | | | | | Heaving, hammer open |
| 1222 | | | | | | Heaving, open hammer, stop hammer |
| 1224 | 310 | 1,530 | 15,000-20,000 | 0 | 11,000 | |
| | | | | | | Heaving, hammer open |
| 1225 | 310 | 1,490 | 15,000-20,000 | 10 | 8,000 | |
| 1230 | 325 | 1,615 | 15,000 | 10 | 8,000 | |
| 1235 | 325 | 1,600 | 18,000 | 2-5 | 8,000 | |
| 1240 | 320 | 1,560 | 18,000 | 1-2 | 2,500 | |
| | | | | | | Heaving, hammer open, heaving, hammer opening |
| 1245 | 325 | 1,625 | 18,000 | 2-5 | 11,000 | |
| | | | | | | Heaving, hammer open |
| 1247 | 360 | 2,000 | 18,000 | 2-5 | 5,000 | |
| | | | | | | Heaving, hammer open, heaving, hammer opening |
| | | | | | | Heaving, hammer open |
| 1250 | 360 | 1,810 | 18,000 | 2-5 | 7,000 | |
| 1255 | 360 | 1,760 | 18,000 | 1-2 | 6,500 | |
| 1300 | 390 | 1,925 | 12,000 | 2-5 | 5,000 | |
| | | | | | | Heave off bottom |
| 1310 | 385 | 1,800 | 15,000 | 2-3 | 8,000 | ~6 m penetration, ROP has slowed |
| 1315 | 390 | 1775 | 15,000-20,000 | 5-10 | 8,000 | Pick up off bottom |
| 1330 | | | | | | Shut down to replace leaking transducer in stand pipe |
| 1332 | 360 | 148 | 0 | 20 | 0 | Run back to bottom, no hammer |
| | 150 | 20 | 0 | 0 | 0 | No hammer |
| | | | | | | Check pumps |
| | | | | | | Can't find bottom of hole, pooh |
| 1400 | | | | | | Clear seafloor, run in hole with camera |
| | | | | | | Appears to have lost hammer at top of jet sub |
| 1500 | | | | | | POOH |

Notes: Water depth = 741 mbrf; bit = SDS flat-face.

**Table T14.** Summary of Leg 179 hammer drill drilling tests.

| Hole | Bit type | Bit manufacturer | Penetration (m) | Operating times (min) | Operating times (hr) | Comments |
|---|---|---|---|---|---|---|
| 1104A | Concentric | SDS | 1.5-2.5 | 50 | 0.83 | Lack of penetration |
| 1104B | Concentric | SDS | 2-3 | 200 | 3.33 | Lack of penetration |
| 1104C | Concentric | SDS | 0 | 35 | 0.58 | Valve cracked |
| 1104C | Concentric | SDS | 1-1.5 | 190 | 3.17 | |
| 1104D | Concentric | SDS | 0.5 | 55 | 0.92 | Lack of penetration |
| 1104E | Concentric | SDS | 0.5-1 | 95 | 1.58 | Arms welded shut, stuck in hole |
| 1106A | Concentric | Holte | 1.5-2 | 215 | 3.58 | Cracked valve |
| 1106B | Eccentric | Holte | 0.5-1 | 120 | 2.00 | Lack of penetration |
| 1106C | Flat face | SDS | 0.5-1 | 45 | 0.75 | New cartridge, piston binding, intermittently running |
| 1106D | Flat face | SDS | 0.25 | 15 | 0.25 | New cartridge, piston binding, intermittently running |
| 1106E | Flat face | SDS | 6 | 100 | 1.67 | Lost hammer assembly |
| Totals: | | | 14.25-18.75 | | 18.67 | |

**Table T15.** Major oxide and trace element analyses of gabbros from Hole 1105A. (Continued on next three pages.)

| Leg: | 179 | 179 | 179 | 179 | 179 | 179 | 179 | 179 | 179 | 179 | 179 | 179 | 179 | 179 |
|---|---|---|---|---|---|---|---|---|---|---|---|---|---|---|
| Site: | 1105 | 1105 | 1105 | 1105 | 1105 | 1105 | 1105 | 1105 | 1105 | 1105 | 1105 | 1105 | 1105 | 1105 |
| Hole: | A | A | A | A | A | A | A | A | A | A | A | A | A | A |
| Core: | 1 | 1 | 2 | 3 | 4 | 4 | 5 | 5 | 6 | 7 | 7 | 8 | 9 | 9 |
| Type: | R | R | R | R | R | R | R | R | R | R | R | R | R | R |
| Section: | 2 | 4 | 1 | 1 | 3 | 4 | 1 | 2 | 2 | 3 | 4 | 3 | 1 | 4 |
| Lithology: | Olivine gabbro | Gabbro | Gabbro | Olivine gabbro | Olivine gabbro | Oxide gabbro | Oxide olivine gabbro | Gabbro | Olivine gabbro | Oxide gabbro | Olivine gabbro | Gabbro | Gabbro | Olivine gabbro |
| Top (cm): | 88 | 141 | 79 | 51 | 46 | 57 | 115 | 55 | 32 | 31 | 30 | 47 | 82 | 12 |
| Bottom (cm): | 91 | 144 | 82 | 54 | 60 | 62 | 118 | 58 | 36 | 36 | 33 | 50 | 86 | 16 |
| Piece: | 2B | 8 | 6 | 3 | 3 | 7 | 7 | 6 | 2 | 2 | 7 | 4 | 7 | 1 |
| Depth (mbsf): | 16.96 | 20.31 | 24.49 | 29.21 | 36.28 | 37.79 | 39.45 | 40.33 | 44.58 | 50.94 | 52.12 | 55.69 | 58.22 | 61.81 |
| Major oxides (wt%): | | | | | | | | | | | | | | |
| $SiO_2$ | 50.45 | 52.50 | 49.90 | 51.43 | 50.28 | 39.70 | 41.05 | 51.47 | 51.22 | 42.45 | 53.79 | 51.88 | 51.65 | 50.41 |
| $TiO_2$ | 0.30 | 0.32 | 0.29 | 0.36 | 0.36 | 3.94 | 4.36 | 0.57 | 0.60 | 6.22 | 0.44 | 0.49 | 1.57 | 1.34 |
| $Al_2O_3$ | 18.14 | 20.64 | 17.37 | 16.38 | 15.40 | 11.50 | 11.21 | 17.17 | 16.42 | 9.95 | 16.73 | 15.39 | 13.96 | 13.69 |
| $Fe_2O_3$ | 5.00 | 3.34 | 5.96 | 7.10 | 6.28 | 21.16 | 24.36 | 6.82 | 7.89 | 24.05 | 7.54 | 6.70 | 12.30 | 13.40 |
| MnO | 0.09 | 0.08 | 0.09 | 0.13 | 0.12 | 0.31 | 0.32 | 0.13 | 0.14 | 0.34 | 0.14 | 0.14 | 0.23 | 0.25 |
| MgO | 9.35 | 5.47 | 10.76 | 9.00 | 11.87 | 3.54 | 3.85 | 7.84 | 8.70 | 5.92 | 7.13 | 9.50 | 6.02 | 7.35 |
| CaO | 14.22 | 13.98 | 13.32 | 12.02 | 14.05 | 11.93 | 9.64 | 12.91 | 12.44 | 9.48 | 10.90 | 13.85 | 10.81 | 10.55 |
| $Na_2O$ | 2.49 | 3.50 | 2.33 | 3.27 | 2.18 | 3.27 | 3.39 | 3.09 | 2.98 | 2.72 | 4.03 | 2.83 | 3.87 | 3.36 |
| $K_2O$ | 0.06 | 0.06 | 0.07 | 0.06 | 0.04 | 0.10 | 0.13 | 0.06 | 0.07 | 0.10 | 0.17 | 0.06 | 0.10 | 0.10 |
| $P_2O_5$ | 0.01 | 0.02 | 0.02 | 0.02 | 0.01 | 4.06 | 2.09 | 0.03 | 0.03 | 0.28 | 0.02 | 0.06 | 0.09 | 0.12 |
| Total | 100.09 | 99.89 | 100.10 | 99.76 | 100.58 | 99.49 | 100.38 | 100.07 | 100.48 | 101.49 | 100.87 | 100.87 | 100.59 | 100.54 |
| LOI: | 1.39 | 1.20 | 3.36 | 1.56 | 1.86 | 2.45 | 0.06 | 1.43 | 1.19 | –0.13 | 0.06 | 0.37 | 0.00 | –2.55 |
| Trace elements (ppm): | | | | | | | | | | | | | | |
| Nb | 2 | 1 | 1 | 1 | 1 | 10 | 8 | 2 | 1 | 5 | 1 | 1 | 3 | 3 |
| Zr | 31 | 24 | 21 | 19 | 19 | 73 | 88 | 29 | 38 | 106 | 31 | 41 | 44 | 72 |
| Y | 13 | 7 | 7 | 7 | 9 | 192 | 123 | 12 | 14 | 44 | 15 | 12 | 30 | 32 |
| Sr | 174 | 202 | 135 | 152 | 135 | 155 | 140 | 166 | 168 | 106 | 183 | 147 | 178 | 163 |
| Rb | 0 | 0 | 0 | 0 | 0 | 1 | 1 | 0 | 0 | 1 | 2 | 0 | 1 | 0 |
| Zn | 44 | 23 | 40 | 33 | 39 | 171 | 192 | 44 | 53 | 160 | 45 | 41 | 91 | 96 |
| Cu | 64 | 27 | 33 | 32 | 99 | 62 | 84 | 64 | 55 | 106 | 30 | 62 | 39 | 50 |
| Ni | 89 | 55 | 221 | 162 | 220 | 18 | 18 | 89 | 88 | 40 | 44 | 84 | 28 | 38 |
| Cr | 54 | 202 | 876 | 760 | 1066 | 0 | 0 | 100 | 75 | 0 | 2 | 143 | 0 | 41 |
| V | 167 | 146 | 142 | 142 | 172 | 169 | 197 | 181 | 167 | 864 | 184 | 207 | 318 | 182 |
| Ce | 39 | 50 | 41 | 44 | 36 | 40 | 0 | 35 | 36 | 0 | 28 | 35 | 0 | 3 |
| Ba | 116 | 165 | 136 | 144 | 135 | 0 | 0 | 106 | 97 | 0 | 99 | 122 | 0 | 0 |
| Mg# * | 0.81 | 0.79 | 0.81 | 0.75 | 0.81 | 0.28 | 0.27 | 0.73 | 0.72 | 0.36 | 0.69 | 0.77 | 0.53 | 0.56 |
| Mg# ** | 0.79 | 0.76 | 0.78 | 0.72 | 0.79 | 0.25 | 0.24 | 0.70 | 0.69 | 0.33 | 0.65 | 0.74 | 0.49 | 0.52 |

Notes: * = Fe calculated as 0.85 total iron. ** = Fe calculated as total iron. LOI = loss on ignition. This table is also available in ASCII format in the **TABLES** directory.

Table T15 (continued).

| Leg: | 179 | 179 | 179 | 179 | 179 | 179 | 179 | 179 | 179 | 179 | 179 | 179 | 179 | 179 |
|---|---|---|---|---|---|---|---|---|---|---|---|---|---|---|
| Site: | 1105 | 1105 | 1105 | 1105 | 1105 | 1105 | 1105 | 1105 | 1105 | 1105 | 1105 | 1105 | 1105 | 1105 |
| Hole: | A | A | A | A | A | A | A | A | A | A | A | A | A | A |
| Core: | 10 | 11 | 12 | 12 | 13 | 13 | 14 | 14 | 15 | 15 | 16 | 16 | 17 | 18 |
| Type: | R | R | R | R | R | R | R | R | R | R | R | R | R | R |
| Section: | 1 | 2 | 2 | 2 | 1 | 3 | 1 | 3 | 1 | 2 | 1 | 3 | 2 | 2 |
| Lithology: | Gabbro | Oxide olivine gabbro | Olivine gabbro | Gabbro | Olivine gabbro | Olivine gabbro | Olivine gabbro | Olivine gabbro | Olivine gabbro | Gabbro | Olivine gabbro | Olivine gabbro | Olivine gabbro | Olivine gabbro |
| Top (cm): | 38 | 51 | 50 | 123 | 87 | 38 | 42 | 91 | 113 | 71 | 91 | 22 | 23 | 60 |
| Bottom (cm): | 42 | 54 | 53 | 127 | 90 | 42 | 45 | 94 | 116 | 74 | 94 | 25 | 26 | 62 |
| Piece: | 3A | 7 | 5 | 15 | 3D | 3 | 3A | 7 | 13 | 9A | 10 | 3 | 2 | 7 |
| Depth (mbsf): | 62.38 | 68.91 | 73.27 | 74.00 | 77.17 | 79.42 | 81.42 | 84.55 | 87.13 | 88.21 | 91.51 | 93.56 | 97.25 | 102.22 |
| Major oxides (wt%): | | | | | | | | | | | | | | |
| $SiO_2$ | 52.04 | 43.09 | 50.33 | 51.32 | 52.46 | 52.72 | 50.12 | 50.78 | 50.66 | 52.05 | 52.63 | 49.69 | 50.07 | 52.16 |
| $TiO_2$ | 0.61 | 5.35 | 0.31 | 0.33 | 0.52 | 0.53 | 0.23 | 0.92 | 0.28 | 0.70 | 0.64 | 0.23 | 0.30 | 1.37 |
| $Al_2O_3$ | 17.89 | 9.32 | 17.10 | 17.15 | 15.37 | 15.67 | 17.31 | 15.95 | 16.33 | 15.39 | 15.44 | 16.62 | 15.78 | 16.22 |
| $Fe_2O_3$ | 6.64 | 23.51 | 6.39 | 5.66 | 9.33 | 9.40 | 6.13 | 9.03 | 6.08 | 10.17 | 9.71 | 6.63 | 6.21 | 10.56 |
| MnO | 0.13 | 0.37 | 0.11 | 0.12 | 0.19 | 0.19 | 0.11 | 0.16 | 0.11 | 0.19 | 0.19 | 0.11 | 0.11 | 0.16 |
| MgO | 6.90 | 5.99 | 10.39 | 9.45 | 7.53 | 7.17 | 10.18 | 7.92 | 10.59 | 7.64 | 7.25 | 12.02 | 11.39 | 5.31 |
| CaO | 12.75 | 9.86 | 13.07 | 13.72 | 11.19 | 11.25 | 13.25 | 12.23 | 13.77 | 10.87 | 11.29 | 12.68 | 13.68 | 10.26 |
| $Na_2O$ | 3.56 | 2.76 | 2.74 | 2.68 | 3.74 | 3.50 | 2.24 | 2.92 | 2.26 | 3.47 | 3.68 | 2.36 | 2.21 | 4.13 |
| $K_2O$ | 0.08 | 0.09 | 0.04 | 0.05 | 0.07 | 0.07 | 0.04 | 0.07 | 0.03 | 0.07 | 0.08 | 0.03 | 0.05 | 0.19 |
| $P_2O_5$ | 0.08 | 0.60 | 0.02 | 0.02 | 0.02 | 0.00 | 0.00 | 0.10 | 0.01 | 0.02 | 0.08 | 0.00 | 0.01 | 0.01 |
| Total | 100.67 | 100.92 | 100.49 | 100.48 | 100.39 | 100.48 | 99.59 | 100.07 | 100.10 | 100.55 | 100.98 | 100.35 | 99.79 | 100.36 |
| LOI: | 0.25 | –0.32 | 0.40 | 1.57 | –0.40 | 0.13 | –0.07 | –0.26 | –0.26 | –0.13 | 0.13 | 0.19 | 0.45 | –2.55 |
| Trace elements (ppm): | | | | | | | | | | | | | | |
| Nb | 1 | 6 | 1 | 0 | 0 | 2.2 | 1.1 | 4.0 | 2.3 | 2.7 | 3.5 | 1.4 | 1.1 | 2.2 |
| Zr | 64 | 80 | 20 | 34 | 29 | 29 | 17 | 71 | 20 | 43 | 66 | 18 | 24 | 30 |
| Y | 18 | 53 | 8 | 10 | 17 | 16 | 6 | 20 | 8 | 18 | 21 | 6 | 8 | 14 |
| Sr | 199 | 113 | 163 | 151 | 183 | 181 | 158 | 167 | 152 | 175 | 181 | 156 | 152 | 193 |
| Rb | 0 | 1 | 0 | 0 | 0 | 0 | 1 | 0 | 1 | 1 | 0 | 0 | 0 | 3 |
| Zn | 51 | 149 | 38 | 35 | 62 | 63 | 36 | 65 | 36 | 65 | 64 | 38 | 38 | 64 |
| Cu | 23 | 88 | 103 | 66 | 21 | 23 | 75 | 54 | 58 | 33 | 40 | 97 | 109 | 41 |
| Ni | 64 | 27 | 172 | 129 | 34 | 37 | 175 | 115 | 195 | 56 | 45 | 205 | 207 | 41 |
| Cr | 151 | 0 | 443 | 340 | 13 | 10 | 647 | 669 | 858 | 18 | 10 | 814 | 1041 | 0 |
| V | 162 | 300 | 138 | 166 | 204 | 207 | 128 | 155 | 150 | 204 | 149 | 114 | 146 | 303 |
| Ce | 37 | 0 | 37 | 40 | 22 | 23 | 40 | 25 | 39 | 27 | 30 | 41 | 47 | 6 |
| Ba | 108 | 0 | 113 | 137 | 79 | 72 | 127 | 46 | 124 | 64 | 72 | 116 | 128 | 0 |
| Mg#* | 0.71 | 0.37 | 0.79 | 0.80 | 0.65 | 0.64 | 0.79 | 0.67 | 0.80 | 0.64 | 0.64 | 0.81 | 0.81 | 0.54 |
| Mg#** | 0.67 | 0.34 | 0.76 | 0.77 | 0.62 | 0.60 | 0.77 | 0.63 | 0.78 | 0.60 | 0.60 | 0.78 | 0.78 | 0.50 |

Table T15 (continued).

| Leg: | 179 | 179 | 179 | 179 | 179 | 179 | 179 | 179 | 179 | 179 | 179 | 179 | 179 | 179 |
|---|---|---|---|---|---|---|---|---|---|---|---|---|---|---|
| Site: | 1105 | 1105 | 1105 | 1105 | 1105 | 1105 | 1105 | 1105 | 1105 | 1105 | 1105 | 1105 | 1105 | 1105 |
| Hole: | A | A | A | A | A | A | A | A | A | A | A | A | A | A |
| Core: | 19 | 19 | 21 | 22 | 22 | 23 | 23 | 24 | 25 | 25 | 26 | 27 | 27 | 28 |
| Type: | R | R | R | R | R | R | R | R | R | R | R | R | R | R |
| Section: | 2 | 3 | 1 | 2 | 3 | 1 | 2 | 1 | 1 | 1 | 3 | 1 | 3 | 1 |
| Lithology: | Gabbro | Olivine gabbro | Olivine gabbro | Gabbro | Olivine gabbro | Olivine gabbro | Oxide gabbro | Olivine gabbro | Oxide gabbro | Oxide gabbro | Olivine gabbro | Olivine gabbro | Gabbro | Olivine gabbro |
| Top (cm): | 98 | 94 | 49 | 74 | 130 | 94 | 98 | 32 | 23 | 133 | 76 | 28 | 94 | 95 |
| Bottom (cm): | 102 | 97 | 52 | 78 | 133 | 98 | 101 | 36 | 26 | 137 | 80 | 31 | 98 | 98 |
| Piece: | 8A | 8A | 6 | 5 | 8 | 8 | 11 | 3B | 2 | 5C | 5 | 1A | 2 | 3B |
| Depth (mbsf): | 107.68 | 108.99 | 111.29 | 117.24 | 118.98 | 120.34 | 121.88 | 124.72 | 129.23 | 130.33 | 137.52 | 138.98 | 141.96 | 144.65 |
| Major oxides (wt%): | | | | | | | | | | | | | | |
| $SiO_2$ | 52.32 | 47.42 | 49.85 | 52.59 | 52.33 | 50.82 | 46.10 | 52.17 | 48.08 | 45.63 | 51.12 | 50.94 | 50.57 | 49.58 |
| $TiO_2$ | 1.04 | 3.23 | 0.55 | 0.90 | 0.53 | 0.97 | 2.90 | 0.72 | 3.45 | 6.07 | 0.45 | 0.42 | 0.50 | 0.38 |
| $Al_2O_3$ | 15.16 | 12.53 | 17.01 | 16.31 | 15.60 | 14.37 | 11.19 | 17.15 | 12.32 | 11.21 | 13.90 | 16.24 | 17.73 | 15.70 |
| $Fe_2O_3$ | 10.01 | 17.52 | 6.30 | 10.60 | 7.97 | 12.61 | 19.68 | 8.49 | 16.66 | 19.18 | 6.59 | 6.35 | 9.60 | 8.43 |
| MnO | 0.18 | 0.24 | 0.11 | 0.18 | 0.15 | 0.22 | 0.26 | 0.14 | 0.25 | 0.29 | 0.13 | 0.12 | 0.16 | 0.14 |
| MgO | 6.23 | 6.42 | 9.38 | 5.04 | 7.89 | 7.67 | 7.89 | 6.25 | 5.93 | 5.44 | 11.11 | 9.55 | 8.60 | 11.89 |
| CaO | 10.90 | 10.20 | 13.48 | 9.94 | 11.74 | 9.73 | 8.82 | 10.54 | 9.96 | 9.47 | 14.80 | 13.78 | 9.48 | 11.93 |
| $Na_2O$ | 3.86 | 3.26 | 2.55 | 4.32 | 3.58 | 3.63 | 2.82 | 4.02 | 3.46 | 3.32 | 2.19 | 2.73 | 3.60 | 2.47 |
| $K_2O$ | 0.15 | 0.10 | 0.06 | 0.20 | 0.07 | 0.09 | 0.10 | 0.11 | 0.12 | 0.12 | 0.04 | 0.05 | 0.13 | 0.04 |
| $P_2O_5$ | 0.02 | 0.01 | 0.20 | 0.12 | 0.03 | 0.01 | 0.03 | 0.04 | 0.01 | 0.02 | 0.01 | 0.01 | 0.03 | 0.03 |
| Total | 99.84 | 100.91 | 99.48 | 100.20 | 99.89 | 100.11 | 99.78 | 99.61 | 100.21 | 100.74 | 100.32 | 100.18 | 100.37 | 100.58 |
| LOI: | 0.52 | 0.40 | 0.91 | 0.47 | 0.00 | 0.13 | 0.00 | 0.86 | 0.26 | 0.13 | 0.33 | 0.19 | 0.13 | –0.33 |
| Trace elements (ppm): | | | | | | | | | | | | | | |
| Nb | 2.5 | 2.6 | 3.5 | 3.4 | 2.4 | 2.3 | 1.8 | 2.5 | 2.2 | 5.2 | 1.8 | 2.0 | 3.5 | 2.3 |
| Zr | 39 | 44 | 82 | 61 | 43 | 33 | 51 | 51 | 38 | 78 | 26 | 35 | 48 | 33 |
| Y | 18 | 18 | 16 | 28 | 16 | 16 | 19 | 16 | 22 | 26 | 11 | 11 | 20 | 8 |
| Sr | 178 | 165 | 162 | 208 | 175 | 170 | 120 | 188 | 146 | 131 | 134 | 158 | 189 | 156 |
| Rb | 2 | 2 | 0 | 2 | 0 | 0 | 1 | 1 | 2 | 2 | 0 | 1 | 1 | 1 |
| Zn | 63 | 69 | 47 | 70 | 53 | 77 | 114 | 55 | 95 | 110 | 40 | 40 | 67 | 53 |
| Cu | 32 | 54 | 40 | 26 | 42 | 32 | 56 | 24 | 66 | 94 | 96 | 131 | 192 | 71 |
| Ni | 35 | 69 | 146 | 26 | 53 | 44 | 55 | 50 | 30 | 32 | 148 | 149 | 152 | 175 |
| Cr | 0 | 630 | 764 | 0 | 0 | 0 | 6 | 1 | 0 | 0 | 627 | 486 | 44 | 368 |
| V | 223 | 197 | 149 | 126 | 196 | 135 | 529 | 168 | 502 | 640 | 208 | 170 | 70 | 127 |
| Ce | 8 | 23 | 42 | 23 | 30 | 9 | 0 | 25 | 0 | 0 | 41 | 47 | 28 | 31 |
| Ba | 33 | 48 | 99 | 48 | 77 | 23 | 0 | 50 | 0 | 0 | 110 | 104 | 71 | 93 |
| Mg#* | 0.59 | 0.46 | 0.78 | 0.53 | 0.70 | 0.59 | 0.48 | 0.63 | 0.45 | 0.40 | 0.80 | 0.78 | 0.68 | 0.77 |
| Mg#** | 0.55 | 0.42 | 0.75 | 0.49 | 0.66 | 0.55 | 0.44 | 0.59 | 0.41 | 0.36 | 0.77 | 0.75 | 0.64 | 0.74 |

Table T15 (continued).

| | | | | |
|---|---|---|---|---|
| Leg: | 179 | 179 | 179 | 179 |
| Site: | 1105 | 1105 | 1105 | 1105 |
| Hole: | A | A | A | A |
| Core: | 29 | 30 | 30 | 30 |
| Type: | R | R | R | R |
| Section: | 3 | 1 | 2 | 3 |
| Lithology: | Oxide gabbro | Oxide gabbro | Oxide gabbro | Gabbro |
| Top (cm): | 109 | 27 | 109 | 102 |
| Bottom (cm): | 112 | 31 | 113 | 106 |
| Piece: | 3 | 3A | 8 | 9 |
| Depth (mbsf): | 152.18 | 153.67 | 155.85 | 157.12 |
| Major oxides (wt%): | | | | |
| $SiO_2$ | 49.07 | 47.98 | 46.86 | 52.77 |
| $TiO_2$ | 2.11 | 2.84 | 3.62 | 0.50 |
| $Al_2O_3$ | 13.31 | 13.12 | 11.94 | 15.48 |
| $Fe_2O_3$ | 14.97 | 16.93 | 18.11 | 7.80 |
| MnO | 0.22 | 0.23 | 0.25 | 0.15 |
| MgO | 7.41 | 6.54 | 6.31 | 8.48 |
| CaO | 10.53 | 9.93 | 10.46 | 11.68 |
| $Na_2O$ | 3.34 | 3.38 | 3.14 | 3.49 |
| $K_2O$ | 0.12 | 0.11 | 0.09 | 0.09 |
| $P_2O_5$ | 0.06 | 0.01 | 0.00 | 0.01 |
| Total | 101.12 | 101.05 | 100.77 | 100.43 |
| LOI: | –0.39 | –0.33 | 0.07 | 0.65 |
| Trace elements (ppm): | | | | |
| Nb | 2.4 | 2.1 | 2.3 | 3.4 |
| Zr | 52 | 37 | 33 | 39 |
| Y | 21 | 19 | 20 | 19 |
| Sr | 146 | 148 | 136 | 163 |
| Rb | 1 | 1 | 1 | 1 |
| Zn | 84 | 81 | 101 | 47 |
| Cu | 75 | 73 | 82 | 53 |
| Ni | 52 | 39 | 36 | 68 |
| Cr | 14 | 0 | 0 | 29 |
| V | 551 | 668 | 867 | 173 |
| Ce | 0 | 0 | 0 | 31 |
| Ba | 0 | 0 | 0 | 95 |
| Mg#* | 0.54 | 0.47 | 0.45 | 0.72 |
| Mg#** | 0.50 | 0.43 | 0.41 | 0.68 |

**Table T16.** Operations summary for Hole 1105A.

| | |
|---|---|
| Seafloor driller: | 714 mbrf |
| Drill pipe depth: | 733.9 mbrf |
| Total depth driller: | 872 mbrf |
| Seafloor logger: | 714 mbrf |
| Drill-pipe logger: | 733.5 mbrf |
| Total depth logger: | 870 mbrf |

| Event | Time | Depth (mbsf) | Logging speed |
|---|---|---|---|
| Tool string 1 DITE/SDT/NGT/TLT | | | |
| Start rig floor rigup | 0445 | | |
| Complete tool string rig-up | 0545 | | |
| Pass one | 0615 | 155.7-12.9 | 1800 ft/hr |
| Pass two | 0650 | 156.5-13.3 | 1800 ft/hr |
| Complete rig-down | 0800 | | |
| Tool string 2 FMS/NGT | | | |
| Complete rig-up | 0815 | | |
| Pass one begin | 0835 | 158-11.7 | 1700 ft/hr |
| Pass two begin | 0900 | 157.6-12.2 | 900 ft/hr |
| Complete rig-down | 1000 | | |
| Tool string 3 HLDS/APS/HNGS | | | |
| Complete rig-up | 1030 | | |
| Pass one begin (no HLDS) | 1110 | 157.0-15.5 | 900 ft/hr |
| Pass two begin (no APS) | 1155 | 157.0-12.3 | 1200 ft/hr |
| Complete rig-down | 1245 | | |
| Tool string 4 SDT-SLS-WA (BHC)/NGTC | | | |
| Complete rig-up | 1315 | | |
| Pass one begin | 1350 | 157.6-11.3 | 1200 ft/hr |
| Complete tool string rig-down | 1515 | | |
| Complete rig floor rig-down | 1600 | | |

Notes: For all runs, the pipe depth was 35.2 mbsf initially and pulled to 19.9 mbsf during logging. The WHC was used on all logging runs. The WHC was turned on following the tool's exit from the end of pipe and turned off prior to reentry into pipe. The date for all times listed = 10 May 1998.